Germanium pin Photodiodes on Silicon and Photonic Integrated Circuits:

Components for High-Speed Optical Data Communications

Von der Fakultät Informatik, Elektrotechnik und Informationstechnik
der Universität Stuttgart
zur Erlangung der Würde eines Doktor-Ingenieurs
(Dr.-Ing.) genehmigte Abhandlung

Vorgelegt von
Sandra Klinger
aus Stuttgart Bad Cannstatt

Hauptberichter:	Prof. Dr.-Ing. Manfred Berroth
Mitberichter:	Prof. Dr.-Ing. Joachim Burghartz
Tag der mündlichen Prüfung:	31.10.2011

Institut für Elektrische und Optische Nachrichtentechnik
der Universität Stuttgart
2011

Declaration of Authorship / Erklärung

I declare that this thesis and the work presented in it has been unassistedly generated by myself. The literature in use and any other resources are indicated completely.

Hiermit versichere ich, die vorliegende Arbeit selbstständig und ohne fremde Hilfe angefertigt zu haben. Die verwendete Literatur und sonstige Hilfsmittel sind vollständig angegeben.

Stuttgart, June 10, 2012

Contents

List of Abbreviations

Abbreviation	**Meaning**
AC	Alternating Current
ADC	Analogue-to-Digital Converter
ADS	Advanced Design System
Al	Chemical symbol for the element Aluminium
APD	Avalanche Photodiode
ARC	Anti-Reflexion Coating
B	Chemical symbol for the element Boron
BER	Bit Error Ratio
BERT	Bit Error Ratio Tester
BOX	Buried Oxide
BPG	Bit Pattern Generator
CAMFR	Cavity Modelling Framework
CCCS	Current Controlled Current Source
CDM	Code Division Multiplex
CMOS	Complementary Metal Oxide Semiconductor
CPW	Coplanar Waveguide
CW	Continuous Wave
CWDM	Coarse Wavelength Division Multiplex
DA	Differential Amplifier
DAC	Digital-to-Analogue Converter
DC	Direct Current
DFB	Distributed Feedback
D(B)PSK	Differential (Binary) Phase Shift Keying
DUT	Device Under Test
DWDM	Dense Wavelength Division Multiplex
E-O	Electro-Optical (conversion)
EDFA	Erbium Doped Fibre Amplifier
EEM	Eigenmode Expansion Method
EF	Emitter Follower
EIM	Effective Index Method
EM	Electromagnetic (wave)
FDTD	Finite Difference Time Domain
FEM	Finite Element Method
FET	Field Effect Transistor
GaAs	Chemical symbol for the compound semiconductor Gallium-Arsenide
GBP	Gain-Bandwidth-Product

Abbreviation	**Meaning**
GC	Grating Coupler
Ge	Chemical symbol for the element Germanium
GSG	Ground-Signal-Ground
HET	Heterodyne measurement setup
IAF	Fraunhofer Institute for Applied Solid State Physics (Fraunhofer Gesellschaft, Institut für Angewandte Festkörperphysik)
IC	Integrated Circuit
IEEE	Institute of Electrical and Electronics Institute
IHT	Institute for Semiconductor Engineering
InGaAs	Chemical symbol for the compound Indium-Gallium-Arsenide
InGaAsP	Chemical symbol for the compound Indium-Gallium-Arsenide-Phosphide
InP	Chemical symbol for the compound Indium-Phosphide
INT	Institute of Electrical and Optical Communications Engineering
IP	Inductive Peaking
JFET	Junction Field Effect Transistor
LA	Limiting Amplifier
LCA	Lightwave Component Analyser
LRRM	Line-Reflect-Reflect-Match
MBE	Molecular Beam Epitaxy
MM	Multi-Mode / Modal Method
MMF	Multi-Mode Fibre
MSM	Metal-Semiconductor-Metal
MUX	Multiplexer
NIR	Near Infrared
OC	Open Circuit structure
O-E	Opto-Electrical (conversion)
OOK	On-Off Keying
PD	Photodiode
PECVD	Plasma Enhanced Chemical Vapour Deposition
PIC	Photonic Integrated Circuit
POF	Polymeric Optical Fibre
PMF	Polarisation Maintaining Fibre
PRBS	Pseudo Random Bit Sequence
PSK	Phase Shift Keying
QPSK	Quadrature Phase Shift Keying
RCE	Resonant Cavity Enhanced
RCWA	Rigorous Coupled Wave Analysis
RF	Radio Frequency
RIE	Reactive Ion Etching
RPCVD	Reduced Pressure Chemical Vapour Deposition
Sb	Chemical symbol for the element Antimon
SC	Short Circuit structure
SCR	Space Charge Region
Si	Chemical symbol for the element Silicon

Abbreviation	**Meaning**
SiO_2	Chemical symbol for the compound Silicondioxide
SM	Single-Mode
SMF	Single-Mode Fibre
SMU	Source Measurement Unit
Sn	Chemical symbol for the element Tin
SOI	Silicon On Insulator
TDM	Time Division Multiplex
TE	Transverse Electric
TEM	Transverse Electromagnetic
TM	Transverse Magnetic
TIA	Transimpedance Amplifier
TL	Transmission Line
VCCS	Voltage Controlled Current Source
VCSEL	Vertical Cavity Surface Emitting Laser
VNA	Vector Network Analyser
WDM	Wavelength Division Multiplex
WG	Waveguide

List of Formula

Latin Symbols

Symbol	Unit	Meaning
A_{G}	–	normalisation factor of Gaussian beam
A_{j}	m^2	junction area
$\underline{a}_{1\|2}$	–	incident partial wave
$a_{\mathrm{TE\|TM}}$	–	summand in single mode criterion ($TE\|TM$ polarisation), $\in \mathbb{R}$
$\vec{B}$	Vsm^{-2}	magnetic flux density vector
$\underline{b}_{1\|2}$	–	reflected/transmitted partial wave
C_{j}	F	junction capacitance
C_{j0}	F	junction capacitance at zero biasing
$C_{\mathrm{P1\|P2}}$	F	parasitic capacitance (open circuit structure)
C_{S1}	F	parasitic capacitance (short circuit structure)
$\vec{D}$	Asm^{-2}	electric flux density vector
$D_{\mathrm{n\|p}}$	$\mathrm{cm}^2\mathrm{s}^{-1}$	diffusion constant of electrons|holes
d	m	thickness of dielectric layer in a stack / distance waveguide - lateral groove
d_{abs}	m	thickness of absorption region
d_{e}	m	etch depth of grating
d_{i}	m	thickness of intrinsic region of pin-photodiode
d_{pGe}	m	thickness of p-Ge-layer
d_{SCR}	m	thickness of space charge region
$d_{\mathrm{Si,t\|b}}$	m	thickness of Si top|bottom layer
$d_{\mathrm{SiO2,t\|b}}$	m	thickness of SiO_2 top|bottom layer
dc	–	duty cycle - ratio between grating ridge and grating period, also called filling factor
$\vec{E}$	Vm^{-1}	electric field vector
$E_{(1\|2)}$	Vm^{-1}	electric field
$E_{\mathrm{bw\|fw\|ref}}$	Vm^{-1}	electric field of backward|forward|reference wave
E_{F}	J, eV	Fermi level
E_{g}	J, eV	band gap energy
E_{hf}	J, eV	energy of one photon
E_{in}	Vm^{-1}	incident electric field
EQE	-	external quantum efficiency
F	–	Eigenvalue function (modal method)

Symbol	**Unit**	**Meaning**
f	Hz	variable of frequency
f_{RC}	Hz	RC frequency
f_{trans}	Hz	transit frequency
g	m	grating period
$\vec{H}$	Am^{-1}	magnetic field vector
H_{WG}	m	height of slab and rib (waveguide)
H_{slab}	m	height of slab (waveguide)
$I_{(\mathrm{i}\|\mathrm{layer}\|\mathrm{r}\|\mathrm{ref}\|\mathrm{t})}$	Wm^{-2}	intensity (incident|layer|reflected|reference|transmitted)
I_{dark}	A	dark current of photodiode
I_{high}	A	current component in DC photodiode model
I_{ph}	A	photo current of photodiode
I_{S}	A	saturation current
$\vec{J}$	Am^{-2}	electric current density vector
J_{dark}	Am^{-2}	dark current density of photodiode
$J_{\mathrm{SD1}\|\mathrm{SD2}}$	Am^{-2}	dark current density in DC photodiode model
$\vec{K}$	m^{-1}	reciprocal grating vector
$\vec{k}_{\mathrm{in}\|\mathrm{m}}$	m^{-1}	wave vector of incoming|diffracted wave of order m
k_0	m^{-1}	wave number
$k_{\mathrm{x,gg}\|\mathrm{gr}}$	m^{-1}	x component of wave vector in groove|ridge of grating
$k_{\mathrm{x,in}}$	m^{-1}	x component of wave vector of incoming wave
$k_{\mathrm{x,m}}$	m^{-1}	x component of wave vector of diffractied wave (order m)
k_{z}	m^{-1}	z component of wave vector
$k_{\mathrm{z,in}}$	m^{-1}	z component of wave vector of incoming wave
L_{corr}	m	correlation length
$L_{\mathrm{n}\|\mathrm{p}}$	m	diffusion length of electrons|holes
L_{S1}	H	parasitic inductance (short circuit structure)
l	–	continuous index, $\in \mathbb{Z}$
$\vec{M}$	Vm^{-2}	(fictitious) magnetic current density vector
M	–	exponent, $\in \left(\frac{1}{3} \ldots \frac{1}{2}\right)$
m	–	order of diffraction, $\in \mathbb{Z}$
N	–	continuous index, $\in \mathbb{N}$
$N_{\mathrm{A}\|\mathrm{D}}$	m^{-3}	acceptor|donor concentration
$n_{(\mathrm{in}\|\mathrm{t})}$	–	refractive index (medium of incident|transmitted light) (real part of complex refractive index)
n	m^{-3}	electron concentration
$n_{3\|\mathrm{D1}\|\mathrm{D2}}$	-	emission coefficient in DC photodiode model
n_{eff}	–	effective refractive index
$n_{\mathrm{eff,I}\|\mathrm{II}}$	–	effective refractive index of region $I\|II$
$n_{\mathrm{eff0}\|1}$	–	effective refractive index of mode 0|1
n_{e}	-	emission coefficient
n_{i}	m^{-3}	intrinsic carrier concentration
$n_{\mathrm{in}\|\mathrm{t}}$	–	refractive index (medium of incident|transmitted wave)

Symbol	**Unit**	**Meaning**
$\vec{P}$	$\mathrm{Asm^{-2}}$	polarisation vector
P_α	dB	dissipation power
p	$\mathrm{m^{-3}}$	hole concentration
p_t	–	saturation current temperature exponent
p_x	$\mathrm{kgms^{-1}}$	momentum of electron|hole in x direction
R	–	reflexion
$R_\mathrm{opt(,330nm\|max\|pd)}$	$\mathrm{AW^{-1}}$	optical *DC* responsivity (330 nm|maximum|photodiode)
$R_\mathrm{P1\|P2}$	Ω	parasitic resistance (open circuit structure)
R_S1	Ω	parasitic resistance (short circuit structure)
R_S	Ω	series resistance of photodiode
$\vec{S}$	$\mathrm{Jm^{-2}s^{-1}}$	Poynting vector
SD	–	standard deviation
T	–	transmission
T	K, °C	temperature
T_nom	K, °C	nominal temperature
t	s	variable of time
u	–	auxiliary quantity
V_bi	V	built-in voltage of a diode
V_bias	V	bias voltage of a diode
V_crit	V	voltage component in *DC* photodiode model
V_t	V	temperature voltage
$v_\mathrm{drift,e\|h}$	$\mathrm{ms^{-1}}$	drift velocity of electrons|holes
$v_\mathrm{ph,in\|t}$	$\mathrm{ms^{-1}}$	phase velocity in dielectric medium (incident|transmitted wave)
$v_\mathrm{sat(,Ge)}$	$\mathrm{ms^{-1}}$	saturation velocity (in *Ge*)
w_0	m	beam radius of Gaussian beam
x	–	Cartesian coordinate
x	–	portion of one element in a compound
y	–	Cartesian coordinate
$\underline{Z}_0$	Ω	system (reference) impedance
$\underline{Z}_\mathrm{in\|L}$	Ω	input|load impedance
$\underline{Z}_\mathrm{W}$	Ω	characteristic wave impedance
z	–	Cartesian coordinate

Greek Symbols

Symbol	Unit	Meaning
α	m^{-1}	absorption coefficient
Δf	Hz	difference frequency (heterodyne principle)
$\Delta\lambda_0$	m	difference wavelength (heterodyne principle)
ε_3	–	auxiliary quantity
$\varepsilon_{\mathrm{gg}\vert\mathrm{gr}}$	–	relative permittivity in grating grooves|ridges
$\underline{\varepsilon}_{\mathrm{r}}$	–	complex relative permittivity
ε_{r}	–	real part of complex relative permittivity
$\varepsilon''_{\mathrm{r}}$	–	imaginary part of complex relative permittivity
ζ	–	correction term for coupling efficiency of grating couplers
η_{coupl}	–	coupling efficiency
$\eta_{\mathrm{ext}\vert\mathrm{int}}$	–	quantum efficiency (external|internal)
θ_{B}	°, rad	Brewster angle
θ_{c}	°, rad	critical angle
$\theta_{\mathrm{in}\vert\mathrm{m}\vert\mathrm{r}\vert\mathrm{t}}$	°, rad	angle of incident|diffracted|reflected|transmitted wave
$\theta_{\mathrm{in,L}}$	°, rad	Littrow angle
κ	–	extinction coefficient imaginary part of complex refractive index
$\lambda_{(0)}$	m	wavelength (in vacuum)
$\lambda_{1\vert 2}$	m	wavelength of laser 1|2 (heterodyne principle)
$\mu_{\mathrm{e}\vert\mathrm{h}}$	$\mathrm{cm}^2(\mathrm{Vs})^{-1}$	mobility of electrons|holes
$\underline{\mu}_{\mathrm{r}}$	–	complex relative permeability
ρ	Asm^{-3}	electric charge density
σ	$\Omega^{-1}\mathrm{m}^{-1}$	electric conductivity
τ_{trans}	s	transit time constant
Φ_0	s^{-1}	photon flux
$\chi_{\mathrm{e}\vert\mathrm{m}}$	-	electric|magnetic susceptibility
ω	s^{-1}	angular frequency

Physical and Global Constants

Constant	Value	Unit	Meaning
c_0	$2.9979 \cdot 10^{8}$	ms^{-1}	velocity of light in vacuum
h	$6.626 \cdot 10^{-34}$	Js	Planck constant
	$4.13556 \cdot 10^{-15}$	eVs	
k	$1.3807 \cdot 10^{-23}$	JK^{-1}	Boltzmann constant
	$8.62 \cdot 10^{-5}$	eVK^{-1}	
q	$1.6022 \cdot 10^{-19}$	As	elementary charge
ε_0	$8.8542 \cdot 10^{-12}$	Fm^{-1}	permittivity in vacuum
μ_0	$4\pi \cdot 10^{-7}$	Hm^{-1}	permeability in vacuum

List of Figures

List of Tables

Abstract

Die glasfasergebundene Datenübertragung ist aus heutigen Weitverkehrs- und auch Metronetzen nicht mehr wegzudenken. Aufgrund der hohen Datenraten, die mithilfe der optischen Übertragung bewerkstelligt werden können, setzt sich der Siegeszug des Lichts inzwischen auch in den kleinsten Dimensionen fort: Bei der Kommunikation von Chip zu Chip und selbst zwischen Komponenten auf einem Chip wird ebenfalls auf hochbitratige optische Übertragung anstatt elektrischer Leitungen gesetzt.

Ein Großteil der Signalverarbeitung und vor allem die Speicherung von Daten erfolgt jedoch weiterhin im Elektrischen, so dass eine schnelle Wandlung elektrischer in optische Signale - und umgekehrt - an Sender und Empfänger notwendig ist. Der Fokus dieser Arbeit liegt daher auf diesen optischen Links, mit Schwerpunkt auf den Empfängerschaltungen.

Um die angestrebten hohen Datenraten von 100 Gbit/s und mehr mithilfe vorhandener Glasfasernetze zu erreichen, kommen höherstufige Modulationsverfahren und Multiplexverfahren zum Einsatz. Diese verlangen am Empfänger eine optische Signalmanipulation, welche durch integrierte photonische Schaltungen (*PICs*, engl. photonic integrated circuits) erreicht wird. Diese *PICs* werden am Institut für Elektrische und Optische Nachrichtentechnik (*INT*) entworfen und extern in dem Materialsystem *SOI* (Silizium-auf-Siliziumdioxid, engl. silicon on insulator) durch mehrere Ätzschritte gefertigt. *SOI* ist aufgrund des hohen Brechungsindexunterschieds zwischen Silizium und Siliziumdioxid sowie der Transparenz bei den Telekommunikationswellenlängen 1310 nm und 1550 nm bestens für die gewünschte kompakte Signalführung geeignet. Zudem ist es kompatibel zu der Silizium-basierten Komplementären Metall-Oxid-Halbleiter-Technologie (*CMOS*, engl. complementary metal oxide semiconductor), in der schnelle Mischsignalschaltungen realisiert werden können.

Zu den für schnelle integrierte optische Empfänger benötigten *PICs* gehören Einkoppelelemente und einfache Wellenleiterstrukturen, welche im Rahmen dieser Arbeit untersucht werden: Die Einkopplung des Lichts aus der Glasfaser in den Chip, auf dem sich die *PICs* befinden, muss auf einfache Weise und vor allem verlustarm erfolgen. Ein- und zweidimensionale Gitterkoppler, die im gleichen Ätzprozess wie die *PICs* selbst gefertigt werden, scheinen hier am erfolgversprechendsten. In der vorliegenden Arbeit werden eindimensionale binäre Gitter entworfen und ihr Transmissionsverhalten messtechnisch erfasst. Die vermessenen Gitterkoppler werden auf ihre Abhängigkeit von verschiedenen Gitterparametern, wie Gitterperiode und Füllfaktor, hin untersucht. Sie erreichen maximale Koppeleffizienzen von ca. 37%. Die Gitterkoppler sind für transversal-elektrische (*TE*) Polarisation und eine Wellenlänge von 1550 nm sowie 1310 nm optimiert.

Polarisations- und Wellenlängenabhängigkeit spielen bei diesen Kopplern eine große Rolle. Bei den Wellenleitern gehören zudem Einmodigkeit sowie Streu- und Biegeverluste zu den Aspekten, die zu berücksichtigen sind. Zudem können verschiedene Wellenleiterstrukturen wie Streifen- und Rippenwellenleiter miteinander verglichen werden. In dieser Arbeit werden theoretische Betrachtungen zu den genannten Punkten angestellt.

Nach der optischen Signalverarbeitung durch die *PICs* sind die optischen Signale zu wandeln. Mit Silizium als Basismaterial eignet sich für die Detektion des Lichts der Halbleiter Germanium: Der Absorptionskoeffizient ist bei den Telekommunikationswellenlängen ausreichend hoch, und außerdem lässt sich Germanium in Silizium integrieren. Dabei ist jedoch die Gitterfehlanpassung zwischen den beiden Halbleitermaterialien zu berücksichtigen. In einem gemeinsamen, von der Deutschen Forschungsgemeinschaft (*DFG*) geförderten Projekt mit dem Institut für Halbleitertechnik (*IHT*) können Fotodetektoren für den vertikalen Lichteinfall demonstriert werden, die eine 3 dB-Bandbreite von 49 GHz aufweisen. Die verwendete Struktur ist eine Germanium *pin*-Fotodiode mit vertikalem Doppel-Mesa-Aufbau; sie wird am *IHT* mithilfe eines dort entwickelten Wachstumprozesses, unter Verwendung eines virtuellen Substrats, auf Silizium aufgewachsen.

Das Hauptaugenmerk der vorliegenden Arbeit liegt bei dieser Kooperation auf der simulations- und messtechnischen Charakterisierung, vor allem im Hochfrequenzbereich, sowie der Untersuchung von layouttechnischen Optimierungsmöglichkeiten. Diese Optimierung bezieht sich in erster Linie auf die bisher noch niedrige Responsivität der Fotodioden, die in den geringen Abmessungen der Struktur zugunsten einer hohen Bandbreite begründet ist. Hierzu wird primär der Einsatz von Spiegelschichten und Beugungsgittern theoretisch untersucht. Mithilfe solcher Strukturen lässt sich die Responsivität theoretisch mehr als verdreifachen. Spiegel wie Gitter erweisen sich dabei jedoch als stark resonant.

Zudem beschäftigt sich die Arbeit mit der Ableitung von Simulationsmodellen für Schaltungssimulatoren wie *Advanced Design System* (*ADS*) von Agilent Technologies. Diese Modelle werden benötigt, um die Fotodioden gemeinsam mit nachfolgenden elektrischen Schaltungen simulieren und so das Gesamtverhalten charakterisieren zu können. Dabei stehen Gleichstrom- und Kleinsignalanalyse im Vordergrund. Der Vergleich von Messungen und

Simulationen zeigt hierbei gute Übereinstimmung für verschiedene Durchmesser der oberen Mesa der Diode.

Zur weiteren Charakterisierung der Fotodetektoren werden Messungen im Zeitbereich durchgeführt, die eine Bitrate von mindestens 25 Gbit/s bei einer Bitfehlerrate $< 10^{-12}$ belegen.

Das Signal, welches nach der opto-elektrischen Wandlung zur Verfügung steht, muss gegebenenfalls vor der eigentlichen Signalverarbeitung aufbereitet und zum Beispiel im Pegel angepasst werden. Für diesen Zweck wird im Rahmen dieser Arbeit ein einfacher differenzieller Begrenzungsverstärker in einer Silizium-Germanium-Bipolartechnologie entworfen und vermessen. Dank der hohen Transitfrequenz der verwendeten Technologie kann dabei eine Datenrate von 50 Gbit/s erzielt werden. Die Eingangsspannung von 1 mVpp an 50 Ω, was dem Ausgangssignal einer schnellen Fotodiode mit einem Durchmesser von 10 μm entspricht, wird dabei auf 300 mVpp verstärkt.

> „Siehst du, Momo“, sagte er zum Beispiel, „es ist so: Manchmal hat man eine sehr lange Straße vor sich. Man denkt, die ist so schrecklich lang; das kann man niemals schaffen, denkt man.“
>
> Er blickte eine Weile schweigend vor sich hin, dann fuhr er fort: „Und dann fängt man an sich zu eilen. Und man eilt sich immer mehr. Jedes Mal, wenn man aufblickt, sieht man, dass es gar nicht weniger wird was noch vor einem liegt. Und man strengt sich noch mehr an, man kriegt es mit der Angst, und zum Schluss ist man ganz außer Puste und kann nicht mehr. Und die Straße liegt immer noch vor einem. So darf man es nicht machen.“
>
> Er dachte einige Zeit nach. Dann sprach er weiter: „Man darf nie an die ganze Straße auf einmal denken, verstehst du? Man muss nur an den nächsten Schritt denken, an den nächsten Atemzug, an den nächsten Besenstrich. Und immer wieder nur an den nächsten.“
>
> Wieder hielt er inne und überlegte, ehe er hinzufügte: „Dann macht es Freude; das ist wichtig, dann macht man seine Sache gut. Und so soll es sein.“
>
> Und abermals nach einer langen Pause fuhr er fort: „Auf einmal merkt man, dass man Schritt für Schritt die ganze Straße gemacht hat. Man hat gar nicht gemerkt wie, und man ist nicht außer Puste.“ Er nickte vor sich hin und sagte abschließend: „Das ist wichtig.“

Michael Ende, „Momo“

> Nichts ist ein größerer Fehler ... als zu glauben, daß eine Aufgabe bis zur Erschöpfung behandelt werden müsse, um sie gut zu behandeln.

Max Eyth, Brief an die Eltern, Leeds, 16. August 1879

to my family

1 Introduction

1.1 Background

Fast optical communication systems are seen to spread at the expense of pure electrical communications: optical links are expected to replace electrical ones in areas where high transmission rates are required, as it is the case in distributed optical networks like Fibre-To-The-Home ($FTTH$), Local-Area-Network (LAN) and Ethernet.

For long haul applications, the C band around 1550 nm is the candidate of choice, using dense wavelength division multiplex ($DWDM$) with channel spacing of down to only 100 GHz [1]. In the Higher Speed Study Group ($HSSG$) of the Institute of Electrical and Electronics Institute ($IEEE$), standardisation for 40 Gbit/s Ethernet (server) and 100 Gbit/s Ethernet (core) has been ratified in June 2010 under the project number $802.3ba$. Even for shorter distances, like board-to-board, chip-to-chip or even on-chip connections, research on optical communications is ongoing.

This development is due to manifold reasons, including the inherent large bandwidth of optical components, low crosstalk, lack of electromagnetic interference (EMI) and low noise sensitivity. The attenuation of the electrical signal in a copper cable increases towards higher frequency. As it is larger than in glass fibres, fewer repeaters are needed for fibre communications. Furthermore, the low weight of the fibre is advantageous - as a cost factor in laying for long haul applications, but also for mobile communication media.

Nevertheless, also the optical transmission leads to problems: low attenuation and low dispersion are restricted to the so called optical windows of the glass fibre. In standard glass fibres, lowest attenuation occurs at 1550 nm and lowest material dispersion at 1310 nm. Therefore, fibres that optimise the dispersion effect around 1550 nm, like dispersion flattened, dispersion shifted or non-zero dispersion shifted fibres, are defined [1]. To some extent, they also consider non-linear effects that may appear due to dispersion shifting. These fibres are promising aspirants for upcoming projects. For long distance communications, however, the idea is to use the already existing dense network of standard glass fibres while increasing

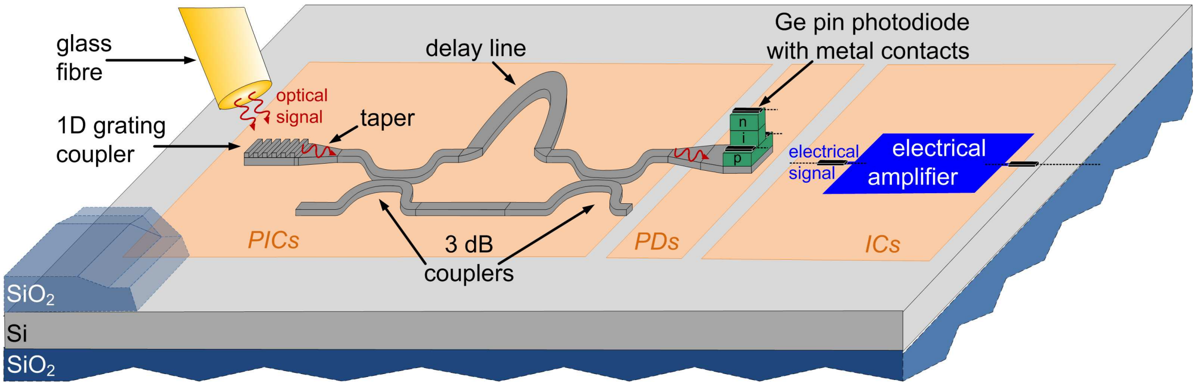

Figure 1.1: Building blocks of a differential binary *PSK* detector in a silicon on insulator material system, designed for one polarisation state. The light is coupled into the chip via a *1D* grating coupler and split at the 3 dB coupler. One output of the 3 dB coupler is delayed by one bit with the help of a simple delay line, before both outputs are combined again by a 3 dB coupler. Thus, the differentially *PSK* modulated optical input signal is demodulated by the *PICs*. At the evanescently coupled germanium *pin PD*, the opto-electrical conversion takes place. The electrical output signal is processed by an appropriate *IC*, here an electrical amplifier.

the data rate. Here, electrical compensation can take the load off the shoulders of the optics communications engineer, as sophisticated equalisers are at hand, like the Viterbi algorithm [2] that compensates for polarisation mode dispersion.

A closer look at the interconnects, at which optical data is transformed into electrical data and vice versa, reveals the three domains that the signals have to pass. For illustration purposes, Fig. 1.1 indicates the integrated solution of a simple differential binary phase shift keying (*PSK*) detector. The following description of the three domains is embedded in a short historical review:

At the very beginning, the light enters the chip and has to be guided and manipulated by photonic integrated circuits (*PICs*). First planar waveguiding structures aiming to participate in this task are examined in 1969 by E. A. J. Marcatili. - Then, the optical signal is converted into an electrical signal at the interface between photonic integrated circuits and electrical integrated circuits (*ICs*). This is possible by the inner photoeffect that is discovered in 1839 by A. E. Becquerel, while theoretical foundations are given by Einstein in 1905. Hence fast photodiodes (*PDs*) come into play. - Finally, the electrical signal at the output of the opto-electrical converter must be processed for further use. The most important element in this context is the transistor. It is theoretically predicted by J. E. Lilienfeld in the form of a field effect transistor (*FET*). In the year 1945, H. F. Mataré and H. Welker as well as, independently, W. B. Shockley, W. H. Brattain and J. Bardeen realise the first junction field effect transistor (*JFET*). But the breakthrough comes with the first integrated circuit, in which two bipolar transistors on a germanium (*Ge*) substrate are presented. This was done in 1958 by J. Kilby. It paved the way for today's high-speed analogue, digital and mixed-signal *ICs*.

In this work at hand, elements of all of these three areas are theoretically examined, partly designed and also measured. Some considerations on which this research is based on are given now, with the photodiode as central element.

One key factor is the choice of the proper material system that allows mass production with the combination of photonic, opto-electrical and electrical integrated circuits on one platform. In terms of the realisation of photodetectors in high-speed optical links, competition exists between group *III/V*-solutions and group *IV/IV*-solutions, like germanium on silicon. The latter approach enables direct integration of optical links in a complementary metal oxide semiconductor (*CMOS*) process. This alliance combines the comparatively high absorption coefficient of germanium in the near infrared (*NIR*) with the compactness and low-cost aspect of the well established *CMOS* technology, in which fast *ICs* are realised as well as silicon based *PICs*. One problem with integrating germanium into silicon is the mismatch of the lattice constants of the two materials. The growth of germanium on silicon can be managed in two ways: with a strained buffer layer between silicon and germanium, or a relaxed buffer layer.

Following characteristics of photodiodes have to be taken into account and optimised for the desired application: bandwidth, responsivity, integratability, power consumption and noise.

In telecommunications, the bandwidth of a system and the data rate that can be achieved are main aspects. Regarding photodiodes, they depend partly on the design of the device, which determines parasitic effects and delay times. However, also the kind of data and its modulation format have an influence on the speed of an optical link. For fast on-off keying (*OOK*) with direct detection on the receiver side, very fast photodiodes with vertical beam incidence are still a promising solution, e.g. for 40 Gbit/s. Advanced modulation formats based on *PSK* and/or coherent detection seem to be inevitable for aspired bit rates of 100 Gbit/s. Thus, waveguide photodiodes with lateral beam incidence are required that are accomplished by waveguide structures manipulating phase and polarisation information.

The waveguide photodiode is also beneficial regarding the responsivity of a photodiode [3]: for a *pin* photodiode with vertical or lateral light incidence, high velocity is gained by applying a thin intrinsic region of the photodiode, as this keeps the transit time short. For lateral coupling, the length of the device and thus the absorption area can be enlarged without increasing the capacitance of the photodiode. Therefore, the responsivity can become higher in this case without reducing speed. In addition, if a silicon on insulator (SOI) substrate is used, mirror effects below the waveguide photodiode are exploited. To be able to compete with these strengths, special measures for vertical incidence photodiodes have to be taken. One means is to properly choose the type and arrangement of the layers in the photodiode stack. Additionally, the implementation of effects based on diffraction can provide an improvement of the external quantum efficiency (EQE).

The photodiode shall be integrated together with the electrical elements of the entire receiver circuit and the photonic elements that are required for the use of advanced modulation formats. To achieve an integrated solution for $PICs$ and photodiode as shown in Fig. 1.1, a fibre-to-chip interface is needed for the optical signal to enter the planar lightwave circuits. There are several approaches to solve the problem of high coupling efficiency of light combined with simple fabrication and large adjustment tolerance of the glass fibre. First, the fibre can be placed laterally at the facet of the chip, and the electromagnetic wave is then further guided via waveguides that are integrated on the chip. However, the lateral placement with the help of V-grooves might become difficult for more complex chips where many electrical connections and bonds at the side of the chip are needed. The electromagnetic wave can also be forced into a waveguide by vertical fibre-to-chip coupling, via prisms, mirrors or grating couplers. The electromagnetic wave is coupled from the waveguide to the photodiode e.g. via evanescent coupling if the photodiode is placed on top of the waveguide [3], or it is coupled laterally if the photodiode is directly placed at the end of the waveguide [4]. In the case of photodiodes with direct vertical light incidence, the earlier mentioned measures to increase the overall efficiency, namely mirrors and diffractive elements, can advantageously be integrated in the layer stack and thus in the direct light path. The fibre is attached on top of the photodiode in this solution.

In total, the design and experimental examination of suitable photodiodes for fast interconnects must concentrate on mainly three aspects: the achievable bandwidth, a sufficiently high responsivity and the circumstances of integration. Bandwidth and responsivity requirements are the most competing aspects here. The applied bias voltage that has a direct impact on the power consumption of the device and the influence of noise have to be kept in mind, too.

The following sections summarise the status quo of fast germanium photodiodes on silicon and describe the topics and outline of this work.

Table 1.1: Status Quo of *Ge* photodiodes on *Si*.

1^{st} Author	Year	Substrate	Structure	Technology	Wave-length / nm	Bias Voltage / V	Band-width / GHz	*EQE* / %
Dehlinger [5]	2004	*SOI*	lateral *pin*	-	850	-4	29	34
Dosunmu [6]	2005	*SOI*	*RCE* Schottky	-	1540	-3	12.1	59
Rouvière [7]	2005	*SOI*	interdigitated *MSM*	-	1310/1550	-2	35	—
Jutzi [10]	2005	*Si*	vertical *pin*	*MBE*	1550	-2	39	2.8
Yin [3]	2007	*SOI*	vertical *nip* evanescent	-	1550	-2	31	
Masini [11]	2007	*Ge*	waveguide	-	1554	-1	>20	48
Vivien [4]	2008	*SOI*	vertical *pin* *SOI* waveguide	-	1550	-4	42	—
Suh [8]	2008	*Si*	vertical *pin*	*RPCVD*	1550	-3	35	37.6
This work [9]	2009	*Si*	vertical *pin*	*MBE*	1550	-2	49	4

1.2 Status Quo of Germanium Photodiodes on Silicon

A lot of research has been done in the area of germanium detectors on silicon in recent years, based on different approaches. In [5], a 3 dB-bandwidth of 29 GHz at a wavelength of 850 nm is announced. For 1540 nm, [6] reports a bandwidth of 12 GHz. Resonant cavity enhanced (*RCE*) Schottky photodiodes are applied in this example. 31 GHz are presented for a *nip* *Ge* photodiode on *SOI* [3]. With a metal-semiconductor-metal (*MSM*) photodiode structure, a bandwidth of 35 GHz at a reverse bias voltage V_{bias} of -2 V is achieved [7]. The same bandwidth is gained with a *Ge* on *Si* vertical photodiode in a reduced pressure chemical vapour deposition (*RPCVD*) process [8]. A bandwidth of 42 GHz is reported for a *Ge* on *Si* photodiode integrated in a *SOI* waveguide [4]. The highest bandwidth published so far is 49 GHz [9], applying a molecular beam epitaxy (*MBE*) process. The *Ge* on *Si* *pin* photodiodes with which this record value is achieved have been developed through the collaboration between the Institute for Semiconductor Engineering (*IHT*) and the Institute of Electrical and Optical Communications Engineering (*INT*), and according results are presented in this dissertation. Table 1.1 summarises chronologically the state of the art of fast *Ge* photodiodes, representing the work of different research groups.

1.3 Topics and Outline of this Work

This work covers two main topics. The first topic deals with the optimisation of vertical *Ge* *pin* photodetectors. The integration of these detectors on the electrical side is considered by the examination of electrical complements (Fig. 1.2a). The second topic is focusing on planar lightwave components that shall serve as building blocks for sophisticated photonic circuits, especially suited to receive signals based on advanced modulation formats (Fig. 1.2b).

The work is structured as follows: in Chapter 2, fundamentals of an optical transmission system, including important properties of carrier, signal and material in use, are summarised. Chapter 3 highlights the components that are elementary to this work: photodiodes, waveguides and gratings. Chapter 4 deals with photodiodes designed for light incidence from above. It is followed by Chapter 5 that summarises the work about a limiting amplifier, which is suitable as complement at the electrical output of the photodiode. In Chapter 6, grating couplers are presented. These *PICs* provide the interface between fibre and planar lightwave circuit and are useful as building blocks e.g. in a waveguide based phase detector. Thus, they are photonic complements at the optical input of a laterally coupled photodiode. For all of these three research topics - photodiode, electrical amplifier and grating coupler/*PICs* -, fabricated samples are at hand. Hence, in Chapter 4 to 6 theoretical aspects are as well covered as measurement techniques that are applied during this work and, finally, the corresponding measurement results are discussed. An overall summary in Chapter 7 concludes this work.

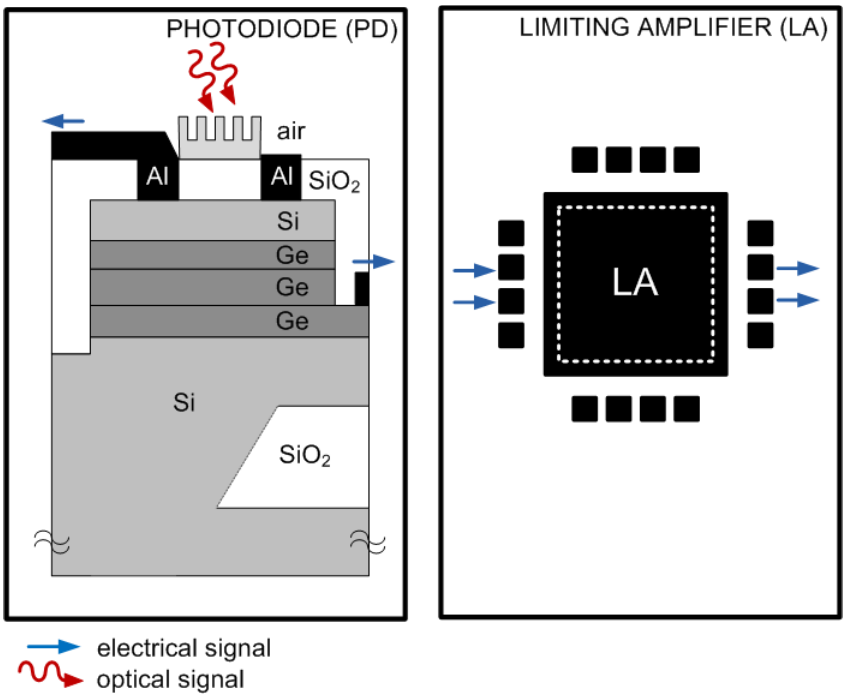

(a) *Ge pin* photodiode (*PD*) on *Si* (cross section) and limiting amplifier (*LA*) (top view).

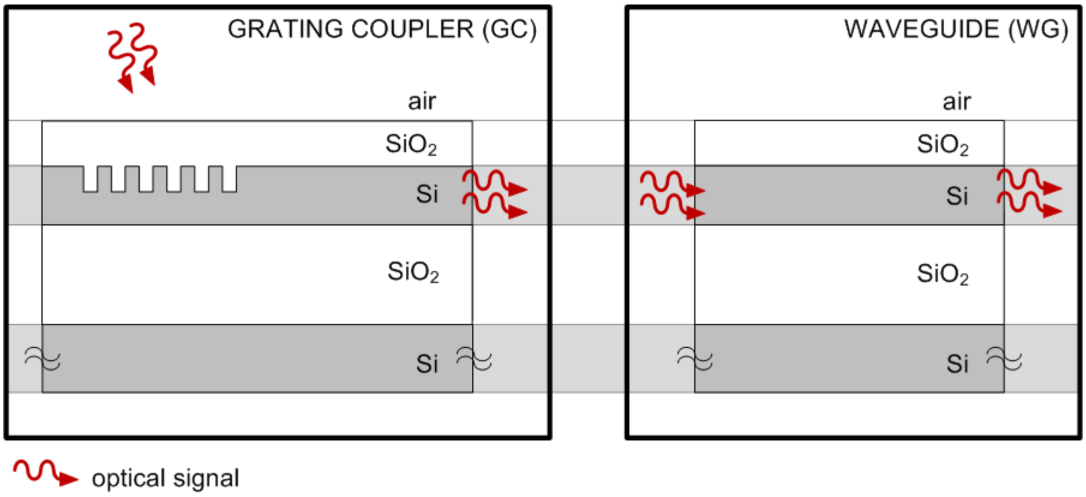

(b) Grating coupler (*GC*) and waveguide (*WG*).

Figure 1.2: Structures examined in this work: (a) *Ge pin* photodiodes on *Si* for direct light coupling from above, and limiting amplifier designed separately as electrical complement; (b) photonic building blocks constructed as supplements for a waveguide detector on *SOI*.

2 Fundamentals of Optical Data Transmission

At the beginning of this chapter, an optical transmission system and its requirements in terms of high-speed telecommunications are briefly described. In order to understand the nature of the optical and electrical signals in such a system, electromagnetic (EM) waves and their properties relevant to optical communications are introduced. At the end of this chapter, semiconductors, the backbone of *ICs* and *PICs*, are presented with respect to their application in the different building blocks of the transmission system.

2.1 Optical Transmission System

An optical transmission system mainly consists of an optical channel and optical links which the optical signal is sent from or received at. An integrated solution of the electrical circuit and the optical source (detector) on transmitter (receiver) side is aimed at. Two possible structures of an optical transmission system are shown in Fig. 2.1.

In the upper block diagram, light directly gets from the electro-optical (E-O) converter to the optical channel, the fibre, and then to the opto-electrical (O-E) converter. This is the case for vertical light coupling into the O-E converter with simple intensity modulation of the light. The lower block diagram includes *PICs* which transport the light between the E-O (O-E) converter and the fibre. The additional photonic building blocks are necessary if advanced modulation formats based on phase manipulation are applied.

Before the E-O and after the O-E conversion, the electrical signal usually needs some treatment, like predistortion and conversion by a digital-to-analogue converter (DAC) on the transmitter side and amplification, equalisation and conversion by an analogue-to-digital converter (ADC) on the receiver side. This is why, for an integrated solution, the electrical ICs for pre- and post-processing are also depicted in Fig. 2.1.

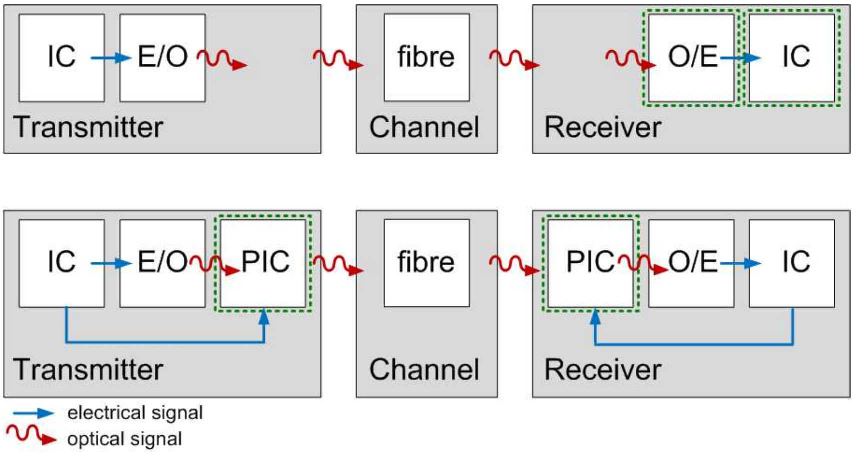

Figure 2.1: Elements of an optical transmission system - direct coupling from the *E-O* and to the *O-E* converter (top) and with coupling via *PICs* (bottom). Components examined in this work are marked with dashed green frames.

2.1.1 Building Blocks of an Optical Transmission System

In this section, some general considerations about the transmission channel and *PICs* are given. Then, the *E-O* and *O-E* converters of an optical transmission system are shortly presented. Of all these components, *PICs* and *O-E* converters are examined in this work.

The optical transmission channel is represented by **fibres**. Fibres are generally spoken cylindrical waveguides. Research on glass fibres for communications dates back to the midth of the last century. The importance of this research is reflected in the Nobel Prize Award in Physics in 2009 for Kao's work in this field [12]. Depending on the wavelength and the aspired bit rate, fibres made of different materials and with different diameters are available. For the work at hand, glass fibres are relevant. These fibre optic cables consist of fused silica, in contrast to e.g. polymeric optical fibres (*POF*) which are plastic fibres mainly used in short distance applications [13]. The two glass fibre types generally used in telecommunications are multi-mode fibres (*MMFs*) with a core diameter of 50/62.5 μm and single-mode fibres (*SMFs*) with a core diameter of 9 μm. The outer cladding around the core has a diameter of 125 μm in both cases. For spot sizes smaller than 9 μm, lensed *SMFs* are available with a beam waist down to 2 μm. Current standard glass fibres work best in the so called three optical windows around 850 nm, 1310 nm (O-Band) and 1550 nm (C-Band). The first one is dedicated to multi-mode operation, the latter two ones to single-mode operation. They are shown in Fig. 2.2.

At 1550 nm, the attenuation is lowest. At 1310 nm, the fibre has zero dispersion: dispersion in general describes a dependence of a physical variable on the wavelength. More concretely,

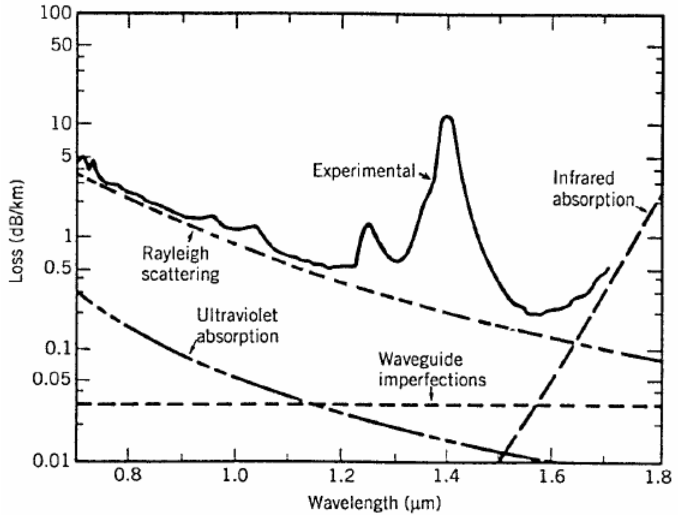

Figure 2.2: Attenuation of glass fibre versus wavelength λ_0 for current standard *SMFs* [14].

it shows the dependence of the propagation velocity of waves on their wavelength λ_0. An overview of different dispersion effects can be found e.g. in [15], pp. 21. The impact of dispersion can be reduced by tailoring the refractive index profile of the glass fibre appropriately for the desired wavelengths, which results in dispersion shifted or dispersion flattened fibres [16].

Next to attenuation and dispersion, which mainly depend on the preform making process [1], p. 3, non-linear behaviour becomes a greater issue if the power density in the fibre is increased, by increasing the power level itself or by reducing the effective area of the fibre. Non-linear effects caused by changes in the refractive index or by stimulated scattering are summarised e.g. in [15], pp. 27.

As stated above, glass fibres are commonly used in optical transmission to bridge long distances between transmitter and receiver. However, as soon as one reaches the destination point or wants to further distribute the light inside the transmitter or receiver itself, transmission can be taken over by planar waveguide structures on a substrate, the **photonic integrated circuits**. This means that there has to be coupling from the large-area fibre to small sized waveguides which automatically includes coupling losses. If coupling elements like mirrors or gratings are to be designed, one task is to keep the coupling efficiency of these elements high. The influence of fabrication and alignment tolerances on the coupling efficiency shall e.g. be held low for the sake of cost-effective production providing stable device performance.

Depending on the wavelength and bit rate in use, different **electro-optical converter** types on the transmitter side are available for high data rate transmission systems. At 850 nm,

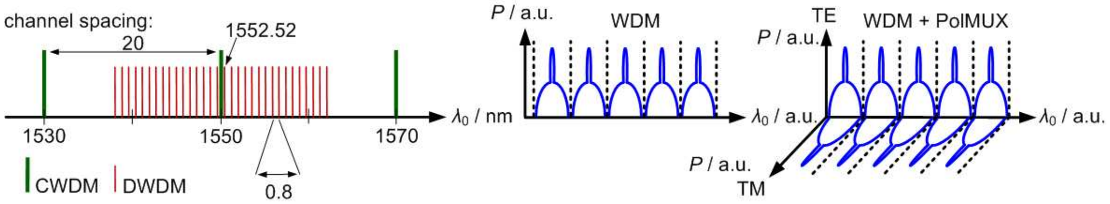

Figure 2.3: Multiplex schemes: spectrum of *CWDM* and *DWDM* (left), *WDM* (centre), *WDM* with *PolMUX* (right).

e.g. vertical cavity surface emitting lasers (*VCSELs*) are used for this purpose [17]. *VCSELs* are also investigated for the telecommunication wavelengths around 1550 nm [18]. Standard lasers at these wavelengths are, however, distributed feedback (*DFB*) lasers with a small spectral bandwidth. Such lasers are also used in the experimental setup in this work.

The **opto-electrical conversion** of light on the receiver side is done by one or more photodiodes. The choice of material, structure and design of the photodiode strongly depends on the application which is aimed at, and is topic of the ongoing sections.

2.1.2 Multiplexing and Modulation Formats

The modulation format describes how the data signal is combined with the carrier signal [19]. Pre-distortion and post-correction of transmission errors can be implemented by coding, which might be part of the modulation process itself. If the signals that are in use are orthogonal to each other, they can be transported in the same transmission medium without interfering with each other [19]. At the receiver, the signals can be separated again if no cross talk occurs in the transmission medium. Because of this fact, orthogonality is essential for the application of multiplexing schemes.

2.1.2.1 Multiplexing

The overall data rate can be increased by multiplexing: one channel is used to submit several bundled data streams simultaneously. Typical multiplex operations are frequency (*FDM*), time (*TDM*), code (*CDM*) and wavelength divison multiplex (*WDM*). They are summarised graphically e.g. in [19]. For optical transmission, the *WDM* method is applied in several standards: coarse *WDM* (*CWDM*) in the ITU-Recommendation G.694.2 and dense *WDM* in the ITU-Standard G.604.1 as well as the ITU-Recommendation G.694.1. According to these recommendations, *CWDM* has a channel spacing of 20 nm, and for *DWDM*, four grids are defined: 12.5 GHz, 25 GHz, 50 GHz and 100 GHz [1], p. 136. An example for *CWDM*

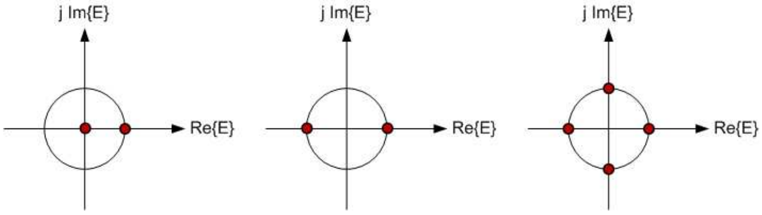

Figure 2.4: Modulation formats - *OOK*, (differential) *BPSK* and *QPSK*.

and *DWDM* grids around 1550 nm is given in Fig. 2.3, left. Also applicable in optics is the polarisation multiplexing (*PolMUX*), where two orthogonal polarisation states transport different information via a *SMF*. For these multiplex operations, wavelength and polarisation sensitive filters are needed at the receiver frontend, which should be low-loss, insensitive to changes in temperature and slightly tunable in the optimum case. *WDM* and *PolMUX* can be also combined as shown in Fig. 2.3, centre and right.

2.1.2.2 Modulation Formats

In [20][21], some advanced modulation formats are summarised with special emphasis on transmitter and receiver schemes. They are also compared there in terms of noise, dispersion and non-linear behaviour. The simplest modulation scheme is the **on-off keying** where the laser is just switched on and off to produce binary signals. Another method that results in binary signals is the external on-off modulation of continuous wave (*CW*) lasers. The data rate can be doubled by using duobinary signals, where three voltage levels are used instead of two as for binary signals. This is realised by precoding of the binary signal, e.g. using an *XOR*-gate: one input of the *XOR*-gate consists of the inverted binary data stream, the other one is the feedback of the output of the *XOR*-gate with a time delay of one bit duration.

Phase shift keying based modulation formats are advantageous as they are e.g. less sensitive to damping on the channel as the information is coded in the phase of the optical signal, not in the amplitude. To realise phase detectors, *PICs* are additionally needed, which provide a phase shift to regain the signal information with intensity detectors (*PDs*). With differential *PSK*, the difference in phase carries the data: in contrast to the pure *PSK*, the phase of the carrier does not have to be known. In the case of differential (binary) phase shift keying (*D(B)PSK*), only one interferometric structure, a delay line with a delay of one bit duration, is necessary. Regarding the quadrature phase shift keying (*QPSK*) format, optical hybrids and delay lines in front of the actual receivers have to be realised and two pairs of balanced receivers are implemented. Thus, the complexity of the receiver increases with higher modulation formats. This is why it is still of interest to examine very fast photodetectors usable for *OOK* in the case of implementation-constrained applications [19].

The mostly favoured higher oder modulation format at present is the *QPSK* modulation. Combined with *PolMUX*, it provides 4-fold improvement of the spectral efficiency. Other promising modulation formats are a combination of phase and amplitude shift keying as e.g. the Star quadrature amplitude modulation (*Star-QAM*)[21].

2.1.2.3 Detection Schemes

For demodulation, two basic detection techniques are in use. With **direct detection**, the photodiode as a square-law device directly delivers a photo current proportional to the intensity of the optical input signal. The phase information is lost if not recovered e.g. by a delay line interferometer (*DLI*) as is the case with differential *PSK* demodulation. The second detection technique is the **coherent detection**. With coherent detection, all information provided by the optical signal is passed on to the electrical domain [21], p. 79. A local oscillator in form of a laser is crucial for this configuration. The photodetector receives input and oscillator signal, both with the same phase but slightly different frequency, and works as a mixer then. This is the same principle as with radio frequency (*RF*) homodyne/heterodyne receivers. If the resulting intermediate frequency (*IF*) is unequal to 0, one talks about a heterodyne receiver; if the *IF* is equal to 0, this is called a homodyne receiver.

2.2 Electromagnetic Waves

Of the broad frequency spectrum of *EM* waves, two regimes are of interest in this work. First, there is the spectrum of the data carrier, which lies in the *NIR*, covering frequencies from 190 THz to 350 THz. This corresponds to the wavelength range from 1550 nm to 850 nm. The other one is the modulation bandwidth that lies in the *RF* segment, restricted in this work to 100 GHz or 3 mm. At this point, fundamental equations, like the Maxwell's equations that describe the formation of electric and magnetic fields and the interaction between them, are summarised. Of the relevant properties of *EM* waves, polarisation is presented first. The impact of material properties on *EM* waves is discussed afterwards. The interaction between *EM* waves and material is crucial to optical communications, as it can e.g. cause losses and can limit the achievable transmission rate. The section closes with a deeper insight into interference that is e.g. responsible for scattering and effects that are related to it. These are refraction, reflexion and diffraction. Interference itself and the phenomena that are involved with it are to some extent investigated by the mathematical model of ray tracing where this appears to be more illustrative.

2.2.1 Maxwell's and Continuity Equations

Field simulators are based on solving the Maxwell's equations in order to calculate field distribution and wave propagation of *EM* waves. This is why they are shortly presented in the following, together with the continuity and the wave equation.

2.2.1.1 Maxwell's Equations

The four partial differential equations listed here represent the differential form of the time-varying Maxwell's equations [22]:

$$\nabla\times \vec{E} = -\vec{M} - \tfrac{\partial \vec{B}}{\partial t} \quad \text{Gauss's Law,} \tag{2.1}$$

$$\nabla\times \vec{H} = \vec{J} + \tfrac{\partial \vec{D}}{\partial t} \quad \text{Gauss's Law for Magnetism,} \tag{2.2}$$

$$\nabla\cdot \vec{D} = \rho \quad \text{Faraday's Law of Induction,} \tag{2.3}$$

$$\nabla\cdot \vec{B} = 0 \quad \text{Ampere's Circuital Law with Maxwell's Correction.} \tag{2.4}$$

The Nabla operator ∇ represents $(\frac{\partial}{\partial x}, \frac{\partial}{\partial y}, \frac{\partial}{\partial z})$ [23], p. 528. It is applied to the *EM* fields which are represented by $\vec{E}$ as the electric and $\vec{H}$ the magnetic field vector. They are physical values that can be directly measured. $\vec{D}$ is the electric and $\vec{B}$ the magnetic flux density which are related to the *EM* fields via the material equations. The electric current density is denoted with $\vec{J}$. Its counterpart is $\vec{M}$, an only theoretically existent magnetic current density. The charge density is given by ρ, which in optical applications is commonly regarded to be zero.

If harmonic fields with sinusoidal time-dependence under steady-state condition are regarded, the phasor form of the *EM* fields can be used, shown here for the electric field in Cartesian coordinates x, y, z:

$$\vec{E}(x, y, z, t) = \vec{E}(x, y, z) \cdot e^{+j\omega t}. \tag{2.5}$$

Thus, time and space dependence are given in different factors. Under the assumption of lossless propagation in z-direction, the equation above becomes:

$$\vec{E}(x,y,z,t) = \vec{E}(x,y) \cdot e^{+j\omega t} \cdot e^{-jk_z z}, \tag{2.6}$$

where k_z[1] is the component of the wave vector $\vec{k}$ in the z-direction.

2.2.1.2 Continuity Equation

If the first derivation is applied to the second of the Maxwell's equations (Eq. 2.2), this leads to:

$$\nabla \cdot \left(\nabla \times \vec{H}\right) = \nabla \cdot \left(\vec{J} + \frac{\partial \vec{D}}{\partial t}\right) = \nabla \cdot \vec{J} + \frac{\partial}{\partial t}\left(\nabla \cdot \vec{D}\right) = 0, \tag{2.7}$$

using [23], p. 528

$$\nabla \cdot \left(\nabla \times \vec{H}\right) = 0 \tag{2.8}$$

and

$$\nabla \cdot \left(\frac{\partial \vec{D}}{\partial t}\right) = \frac{\partial}{\partial t}\left(\nabla \cdot \vec{D}\right). \tag{2.9}$$

With the third of Maxwell's equation (Eq. 2.3) inserted in Eq. 2.7, this results in:

$$\nabla \cdot \vec{J} + \frac{\partial \rho}{\partial t} = 0, \tag{2.10}$$

which is the continuity equation. It describes the relation between the sources of electromagnetic waves, namely $\vec{J}$ and ρ, in a given point in space: the drain of current, represented by the divergence of $\vec{J}$, is equalled by the time-dependent generation of current, indicated by $\frac{\partial \rho}{\partial t}$.

2.2.2 Polarisation

Polarisation is a resonance event and describes the direction of oscillation of a transverse wave. If there is no preferred direction, one talks about unpolarised light. In a material,

---

[1] k_z is equivalent to the propagation constant β that is an expression used in some references.

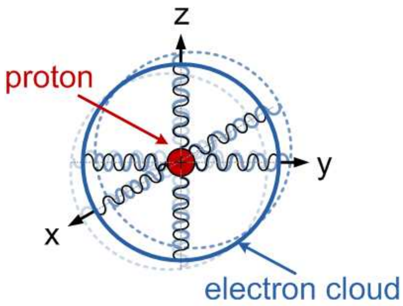

Figure 2.5: Atomic oscillator - the electrons of an orbit can oscillate around the proton. In a dielectric, the mean value of the oscillations of all atoms are summed up. Polarisation describes the preferred direction.

the oscillation of the wave is superposed by the oscillation of the atoms. In an isotropic material, the atoms can oscillate with the same frequency in all directions, as shown by the spring-mass-analogon in Fig. 2.5 [24], pp. 121.

Regarding transverse electromagnetic (TEM) waves, the electric and magnetic field vectors are orthogonal to the propagation direction, and polarisation indicates the direction of the electric field vector. The number of polarisation states is infinite, but three of them are the most important ones. These are the linear, circular and elliptic polarisation[2]. Each of them can be composed by the sum of two orthogonal linear polarised waves [24], p. 526, of which the electric field looks like [24], p. 190:

$$\vec{E} = \vec{E}_0 \cdot e^{j\left(\omega t - \vec{k}\,\vec{r}\right)}. \tag{2.11}$$

In the linear case, the polarisation vector points in the same direction as the electric field vector [25]:

$$\vec{P} = \chi_e \cdot \varepsilon_0 \, \vec{E}, \tag{2.12}$$

with χ_e the electric susceptibility that defines the ratio of the created dipole density to the applied electric field.

In standard glass fibres, the polarisation of light is not stable and changes along the fibre. Polarisation maintaining fibres (PMF) have been developed that can keep the incoming polarisation state.

If an EM wave is incident on the interface between two materials, where both are isotropic and homogeneous, its electric and magnetic field vectors are split in two components and

---

[2] Strictly spoken, linear and circular polarisation are a special case of elliptic polarisation.

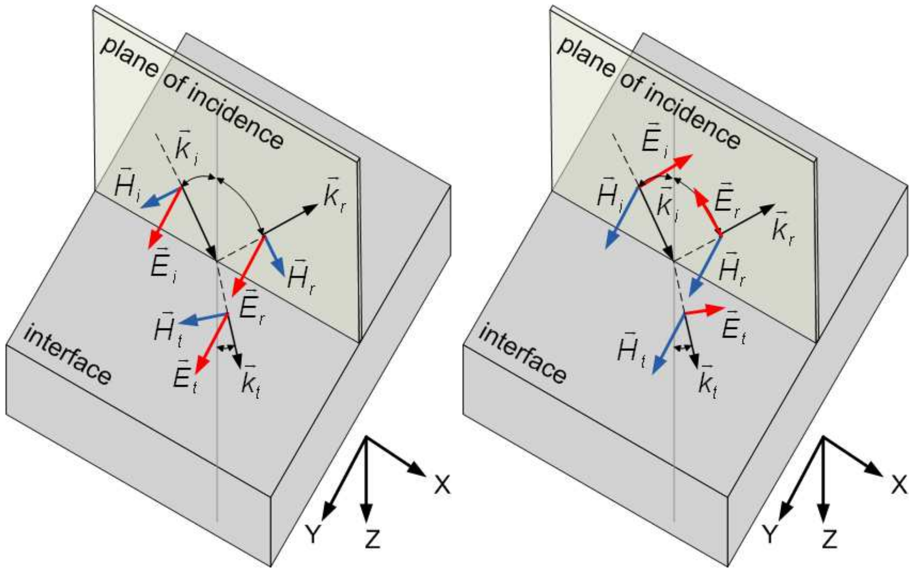

(a) *TE* or orthogonal polarisation. (b) *TM* or parallel polarisation.

Figure 2.6: Polarisation at an interface: incident plane and orientation of field vectors for *TE* and *TM* polarisation. The index i stands for the incident, r for the reflected and t for the transmitted part of the wave.

two separate cases can be regarded. Both are illustrated in Fig. 2.6, where the index i refers to the incident, r to the reflected and t to the transmitted part of the wave. In the case of transverse electric (*TE*) polarisation, the electric field vector is orthogonal to the plane of incidence and parallel to the interface. In the case of transverse magnetic (*TM*) polarisation, the magnetic field vector is orthogonal to the plane of incidence and parallel to the interface. The electric field vector is parallel then to the plane of incidence[3].

If *EM* waves are guided in a medium other than air, as it is the case e.g. for the transport of light via glass fibres, or if they pass stacks of different materials, e.g. when light gets on and off chip level, some material properties and their influence on *EM* waves become crucial. These are presented now.

2.2.3 Relative Permittivity and Refractive Index

Though this section is dedicated to *EM* waves, some material parameters are examined here more closely, as they are dependent on the frequency of the *EM* waves, and as they can,

---

[3] The *TE* polarisation is also called orthogonal or s-polarisation, and the *TM* polarisation has the aliases parallel or p-polarisation.

furthermore, cause losses. These effects are represented by different parameters that can be transformed one into the other.

In the frequency domain, the complex relative permittivity $\underline{\varepsilon}_{\mathrm{r}}$ is commonly used to account for the phenomena mentioned aforehead. In anisotropic material, it is represented by a tensor. In optics, isotropic materials are used in most cases. Therefore, following equations assume isotropy of the materials.

The relative permittivity is defined via the electric susceptibility $\underline{\chi}_{\mathrm{e}}$:

$$\underline{\varepsilon}_{\mathrm{r}}(\omega) = 1 + \underline{\chi}_{\mathrm{e}}(\omega) . \tag{2.13}$$

As can be seen from the equation above, the relative permittivity depends on the frequency ω and makes thus a material dispersive.

The relative permeability $\underline{\mu}_{\mathrm{r}}$ is expressed by the magnetic susceptibility $\underline{\chi}_{\mathrm{m}}$:

$$\underline{\mu}_{\mathrm{r}} = 1 + \underline{\chi}_{\mathrm{m}}, \tag{2.14}$$

and is only mentioned here for completeness. In non-magnetic material, $\underline{\chi}_{\mathrm{m}} = 0$ and thus $\mu_{\mathrm{r}} = 1$. This case is assumed throughout this work as optical materials are usually dielectrica or semiconductors.

The relative permittivity decomposed into real and imaginary part is:

$$\underline{\varepsilon}_{\mathrm{r}}(\omega) = \varepsilon_{\mathrm{r}}(\omega) - j\varepsilon_{\mathrm{r}}''(\omega) = \varepsilon_{\mathrm{r}}(\omega) - j\frac{\sigma}{\varepsilon_0\omega}. \tag{2.15}$$

The real part ε_{r} describes the storage effect of the material if an external electric field is applied, the imaginary part $\varepsilon_{\mathrm{r}}''$ accounts for losses, composed of dielectric losses and changes in the electric conductivity σ. Dielectric losses occur due to different polarisation effects that are caused by the applied field and depend strongly on the frequency of this field [26].

The dispersion relation in terms of the wavelength λ_0 is expressed by the complex refractive index $\underline{n}$. It is given by:

$$\underline{n}(\lambda_0) = n(\lambda_0) - j\kappa. \tag{2.16}$$

The real part n is called refractive index and describes the impact of the material on the phase of the wave. The imaginary part κ is the extinction coefficient and represents the damping properties of a material [24].

Both complex numbers, $\underline{n}$ and $\underline{\varepsilon}_\mathrm{r}$, are linked as follows:

$$\sqrt{\underline{\varepsilon}_\mathrm{r}\underline{\mu}_\mathrm{r}} \overset{\underline{\mu}_\mathrm{r}=1}{=} \sqrt{\underline{\varepsilon}_\mathrm{r}} = \underline{n}, \tag{2.17}$$

$$\varepsilon_\mathrm{r} = n^2 - \kappa^2 \qquad \text{and} \qquad \varepsilon''_\mathrm{r} = 2n\kappa, \tag{2.18}$$

$$n = \Re\{\sqrt{\underline{\varepsilon}_\mathrm{r}}\} = \sqrt{\frac{1}{2}\left(\sqrt{\varepsilon_\mathrm{r}^2 + \varepsilon_\mathrm{r}''^2} + \varepsilon_\mathrm{r}\right)} \qquad \text{and} \qquad \kappa = \Im\{\sqrt{\underline{\varepsilon}_\mathrm{r}}\} = \sqrt{\frac{1}{2}\left(\sqrt{\varepsilon_\mathrm{r}^2 + \varepsilon_\mathrm{r}''^2} - \varepsilon_\mathrm{r}\right)}. \tag{2.19}$$

2.2.4 Material and Wave Equations

2.2.4.1 Material Equations

As mentioned before, $\underline{\varepsilon}_\mathrm{r}$ and $\underline{\mu}_\mathrm{r}$ are scalars for isotropic material. The material equation for the electric field is hence given for by:

$$\vec{D} = \vec{P} + \varepsilon_0 \vec{E}\,. \tag{2.20}$$

For a linear relation between polarisation and electric field vector as in Eq. 2.12, this results in:

$$\vec{D} = \vec{E}\,\varepsilon_0\left(1 + \underline{\chi}_\mathrm{e}\right) = \varepsilon_0\underline{\varepsilon}_\mathrm{r}\,\vec{E}, \tag{2.21}$$

with ε_0 the free space permittivity. Analogously, the material equation for magnetic fields in the linear case is:

$$\vec{B} = \mu_0\underline{\mu}_\mathrm{r}\,\vec{H}, \tag{2.22}$$

with μ_0 the free space permeability. The Ohmic Law makes allowance for absorption losses in the medium with the help of a proportional factor between current density and electric field vector, the electric conductivity σ:

$$\vec{J} = \sigma\,\vec{E}\,. \tag{2.23}$$

2.2.4.2 Wave Equation

The wave equation is used to mathematically describe the propagation of waves. In order to derive one form of the wave equation, the following assumptions are made: the region of interest is source-free, isotropic and homogeneous, and the material equations are linear. Furthermore, the material is non-magnetic, so $\mu_r = 1$, and it is lossy. This means that the electric current density $\vec{J}$ is unequal zero. Starting again from the Maxwell's equations, Eq. 2.1 and Eq. 2.2 become then:

$$\nabla\times \vec{E} = -\mu_0 \frac{\partial \vec{H}}{\partial t}, \tag{2.24}$$

$$\nabla\times \vec{H} = \sigma \vec{E} + \varepsilon_0 \varepsilon_r \frac{\partial \vec{E}}{\partial t}. \tag{2.25}$$

Thus, two equations with two variables are given. The resulting equation which only contains the electric field can be found by first applying the Nabla-operator to Eq. 2.24:

$$\nabla \times \left(\nabla\times \vec{E}\right) = -\mu_0 \frac{\partial}{\partial t}\left(\nabla\times \vec{H}\right), \tag{2.26}$$

using Eq. 2.9 on the right side of the equation. Applying the vector identity on the term on the left of the equal sign, this one becomes:

$$\nabla \times \left(\nabla\times \vec{E}\right) = \nabla \times \nabla\times \vec{E} = \nabla \cdot \left(\nabla \vec{E}\right) - \nabla^2 \vec{E} = -\nabla^2 \vec{E} \tag{2.27}$$

with $\nabla \vec{E} = \frac{1}{\varepsilon_0 \varepsilon_{\mathrm{r}}} \nabla \vec{D} = 0$, as the region under consideration is assumed to be source-free. Inserting Eq. 2.25 in Eq. 2.26, the wave equation for arbitrary waveforms turns out to be:

$$\nabla^2 \vec{E} - \mu_0 \sigma \frac{\partial \vec{E}}{\partial t} - \varepsilon_0 \varepsilon_r \mu_0 \frac{\partial^2 \vec{E}}{\partial t^2} = 0. \tag{2.28}$$

For lossless material with $\sigma = 0$, the wave equation is:

$$\nabla^2 \vec{E} - \varepsilon_0 \varepsilon_r \mu_0 \frac{\partial^2 \vec{E}}{\partial t^2} = 0. \tag{2.29}$$

For a time-harmonic electric field with $\underline{\vec{E}} \propto e^{+j\omega t}$, Eq. 2.28 for lossy material results in:

$$\nabla^2 \vec{E} - j\omega\mu_0\sigma \vec{E} + \varepsilon_0 \varepsilon_r \mu_0 \omega^2 \vec{E} = 0. \tag{2.30}$$

This can be rewritten to:

$$\nabla^2 \vec{E} + \omega^2 \varepsilon_0 \mu_0 \underbrace{\left(\varepsilon_r - j\frac{\sigma}{\omega\varepsilon_0}\right)}_{\underline{\varepsilon_r}} \vec{E} = 0, \tag{2.31}$$

and this wave equation for harmonic waves is the so called Helmholtz equation [24]. In order to show this equation in dependence on $\underline{n}$, the wave number k_0 of free space is introduced here, which represents the length of the wave vector $\vec{k}$:

$$k_0 = \frac{2\pi}{\lambda_0} = \frac{2\pi f}{c_0} = \frac{\omega}{c_0} = \omega\sqrt{\varepsilon_0\mu_0}. \tag{2.32}$$

The re-arrangement of the wave number is achieved with the following definitions of the velocity of light in vacuum:

$$c_0 = f\lambda_0 = \frac{1}{\sqrt{\varepsilon_0\mu_0}}, \tag{2.33}$$

where f and λ_0 are the frequency and wavelength of the wave, respectively. The wave equation is then:

$$\nabla^2 \vec{E} + k_0^2 \underline{n}^2 \vec{E} = 0. \tag{2.34}$$

For a harmonic wave travelling only in z direction as described in Eq. 2.6, this expression becomes:

$$\frac{\partial^2 \vec{E}}{\partial x^2} + \frac{\partial^2 \vec{E}}{\partial y^2} - k_z^2 \vec{E} + k_0^2 \underline{n}^2 \vec{E} = 0. \tag{2.35}$$

This can be rewritten to:

$$\frac{\partial^2 \vec{E}}{\partial x^2} + \frac{\partial^2 \vec{E}}{\partial y^2} + k_0^2 \left(\underline{n}^2 - \frac{k_z^2}{k_0^2}\right) \vec{E} = 0. \tag{2.36}$$

The ratio $\frac{k_z}{k_0}$ is also known as the effective refractive index n_{eff} that a wave sees in its propagation direction and is discussed more deeply later on.

2.2.5 Interference and Scattering

2.2.5.1 Interference

Interference is the interaction between waves according to the principle of superposition. This means that the amplitudes of the waves that are involved add up or are subtracted from each other. Interference can only occur with coherent waves which are waves that have a fixed phase relation and the same frequency. If interference leads to an increase of the amplitude, this is called constructive interference, while the extinction effect is named destructive interference. Inteference causes a redistribution of energy in space [24] pp. 157, so it can also change the direction of waves carrying energy.

One phenomenon regarding the interaction of *EM* waves and material is scattering, which can be explained by interference [24]. Scattering is a collective term for several physical processes comprising refraction, reflexion and diffraction, that change direction, phase or frequency of an *EM* wave. These processes and the scattering phenomenon in general are discussed next in this section[4].

2.2.5.2 Scattering

If a photon collides with an atom, it is redirected from its original propagation direction. Additionally, also the frequency and phase of the photon can be changed due to scattering, depending on the original energy of the photon. One can distinguish two cases of scattering - the one where energy and frequency of the photon remain unchanged, and the one where they are changed, namely elastic and inelastic scattering.

In the case of **elastic scattering** or so called Rayleigh scattering, the energy of the incoming photon is not large enough to excite the colliding atom, so the energy and frequency of the scattered photon is not changed. The length of the original wave vector equals the length of the scattered wave vector. As the Rayleigh scattering is proportional to $\frac{1}{\lambda_0^4}$, with λ_0 the wavelength in free space, light of the short wavelength range is scattered more strongly than infrared light. This is one reason why (near) infrared light is used in optical data transmission.

If the energy of the photon is large enough to get over an excitation level, **inelastic scattering** occurs: the exchange of energy between photon and the material is permanent. One example for inelastic scattering is the so called Raman scattering: with the change in its

---

[4] To understand these phenomena from a different perspective, namely for light being a particle, see e.g. [27].

energy, the scattered photon is also frequency-shifted[5]. This kind of scattering is relevant in indirect semiconductors, where the energy is exchanged with the lattice vibrations, the phonons. Another effect relevant for this work is the so called photoeffect: the photon is absorbed, that means it passes all its energy to an electron that is thereby freed from the atom in the lattice. In the next subsections, scattering processes that play a role in this work are dealt with.

2.2.6 Diffraction and Refraction

2.2.6.1 Diffraction

Diffraction is the interference effect if a wavefront meets an obstacle: new elementary waves are generated behind and in the shadow regions of the obstacle, based on the Huygens principle. This holds also true for very small openings. Diffraction strongly depends on the ratio between the size of the obstacle and the wavelength of the incident *TEM* wave. The meaning of the diffraction effect is elaborately discussed in Sec. 3.3, where the periodic arrangement of obstacles is considered.

2.2.6.2 Refraction

If a wave under oblique angle of incidence reaches the interface of two materials with different refractive index, part of this wave is transmitted into the second material, part is reflected back, as depicted in Fig. 2.7a. The angle of the transmitted wave θ_t through the second material is determined by the incident angle θ_{in} and the refractive indices n_{in} and n_{t} of both materials:

$$\frac{n_{\mathrm{in}}}{n_{\mathrm{t}}} = \frac{c_0}{v_{\mathrm{ph,in}}} \cdot \frac{v_{\mathrm{ph,t}}}{c_0} = \frac{\sin\theta_{\mathrm{t}}}{\sin\theta_{\mathrm{in}}}. \tag{2.37}$$

This is the so called Snell's Law. $v_{\mathrm{ph,in}}$ and $v_{\mathrm{ph,t}}$ are the phase velocities of the wave in the respective materials. The angle of the reflected wave θ_{r} is equal to θ_{in}, which is due to the conservation of momentum of the tangential electric field components at the interface [22].

If one considers the case that $n_{\mathrm{in}} > n_{\mathrm{t}}$, the transmitted wave is refracted away from the vertical reference line. If the incident angle is further increased, total reflexion occurs, as

---

[5] Stokes-Raman: lower energy and lower frequency, Anti-Stokes-Raman: higher energy and higher frequency

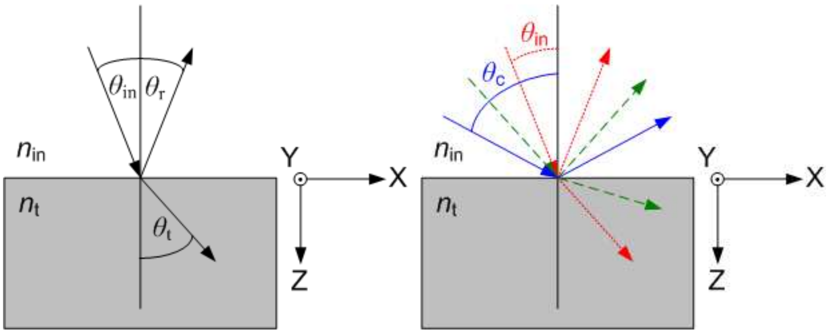

(a) Refraction at an interface of two materials with different refractive index ($n_{in} > n_t$) (cross section).

(b) Increase of θ_{in} above θ_c leads to total reflexion for $n_{in} > n_t$ (cross section).

Figure 2.7: Refraction at an interface that leads with increasing incident angle θ_{in} to total reflexion.

depicted in Fig. 2.7b. To make this happen, the incident angle θ_{in} must be larger than the critical angle θ_c:

$$\theta_{in} \overset{!}{>} \theta_c = \frac{n_t}{n_{in}}. \tag{2.38}$$

Snell's Law reveals the direction into which transmitted and reflected waves travel. Furthermore, it is of interest which portion of the incident light is transmitted and which portion is reflected. Energy that is lost due to absorption in the material is disregarded so far.

2.2.7 Reflexion and Transmission

The reflexion R is defined as the ratio of reflected to incident intensity, I_r and I_{in}, respectively. The transmission T is given by the ratio of transmitted intensity I_t to incident intensity I_{in}:

$$R = \frac{I_r}{I_{in}} = \left(\frac{E_r}{E_{in}}\right)^2 \quad \text{and} \quad T = \frac{I_t \cos\theta_t}{I_{in}\cos\theta_{in}} = \frac{n_t \cos\theta_t}{n_{in}\cos\theta_{in}} \left(\frac{E_r}{E_{in}}\right)^2. \tag{2.39}$$

Lossless material is assumed here, hence only the real part of the complex refractive index is used.

R and T can be calculated separately for both polarisations, TE and TM, with the help of the Fresnel reflexion and transmission coefficients r and t, respectively [24], pp. 192:

$$\begin{aligned}
r_{\mathrm{TE}} &= \left(\tfrac{E_{\mathrm{r\,TE}}}{E_{\mathrm{in\,TE}}}\right) = \tfrac{n_{\mathrm{in}}\cos\theta_{\mathrm{in}} - n_{\mathrm{t}}\cos\theta_{\mathrm{t}}}{n_{\mathrm{in}}\cos\theta_{\mathrm{in}} + n_{\mathrm{t}}\cos\theta_{\mathrm{t}}} \\
t_{\mathrm{TE}} &= \left(\tfrac{E_{\mathrm{t\,TE}}}{E_{\mathrm{in\,TE}}}\right) = \tfrac{2n_{\mathrm{in}}\cos\theta_{\mathrm{in}}}{n_{in}\cos\theta_{\mathrm{in}} + n_t\cos\theta_t} \\
r_{\mathrm{TM}} &= \left(\tfrac{E_{\mathrm{r\,TM}}}{E_{\mathrm{in\,TM}}}\right) = \tfrac{n_{\mathrm{t}}\cos\theta_{\mathrm{in}} - n_{\mathrm{in}}\cos\theta_{\mathrm{t}}}{n_{\mathrm{in}}\cos\theta_{\mathrm{t}} + n_{\mathrm{t}}\cos\theta_{\mathrm{in}}} \\
t_{\mathrm{TM}} &= \left(\tfrac{E_{\mathrm{t\,TM}}}{E_{\mathrm{in\,TM}}}\right) = \tfrac{2n_{\mathrm{in}}\cos\theta_{\mathrm{in}}}{n_{\mathrm{in}}\cos\theta_{\mathrm{t}} + n_{\mathrm{t}}\cos\theta_{\mathrm{in}}}.
\end{aligned} \tag{2.40}$$

These equations can be derived from Maxwell's equations taking into account the boundary conditions for *EM* waves at an interface [24], pp. 194. The reflexion R and the transmission T are then given by:

$$\begin{aligned}
R_{\mathrm{TE}} &= r_{\mathrm{TE}}^2, \\
R_{\mathrm{TM}} &= r_{\mathrm{TM}}^2,
\end{aligned} \tag{2.41}$$

$$\begin{aligned}
T_{\mathrm{TE}} &= t_{\mathrm{TE}}^2 \cdot \tfrac{n_{\mathrm{t}}\cos\theta_{\mathrm{t}}}{n_{\mathrm{in}}\cos\theta_{\mathrm{in}}}, \\
T_{\mathrm{TM}} &= t_{\mathrm{TM}}^2 \cdot \tfrac{n_{\mathrm{t}}\cos\theta_{\mathrm{t}}}{n_{\mathrm{in}}\cos\theta_{\mathrm{in}}}.
\end{aligned} \tag{2.42}$$

For vertical incidence of the wave with $\theta_{\mathrm{in}} = 0°$, the reflection R for *TE* and *TM* polarised light is identical and is given by

$$R_{\mathrm{TE,TM}} = r_{\mathrm{TE,TM}}^2 = \left(\frac{n_{\mathrm{t}} - n_{\mathrm{in}}}{n_{\mathrm{t}} + n_{\mathrm{in}}}\right)^2. \tag{2.43}$$

It can be seen from $r_{\mathrm{TE,TM}}$ in Eq. 2.43 that a phase shift of π occurs for the electric field amplitude if $n_{\mathrm{in}} > n_{\mathrm{t}}$. For $n_{\mathrm{in}} < n_{\mathrm{t}}$, no phase shift arises.

If the angle of the incident beam is increased, the reflexion at an interface between two media changes as can be seen in Fig. 2.8. In this figure, an interface between air and Germanium (*Ge*) is considered, with $n_{\mathrm{in}} = 1.0 < n_{\mathrm{t}} \approx 4.0$. For *TE* polarisation, the reflexion increases with increasing incident angle. For *TM* polarisation, the reflexion becomes zero at the so called Brewster angle θ_{B}:

$$\tan\theta_{\mathrm{B}} = \frac{n_{\mathrm{t}}}{n_{\mathrm{in}}}. \tag{2.44}$$

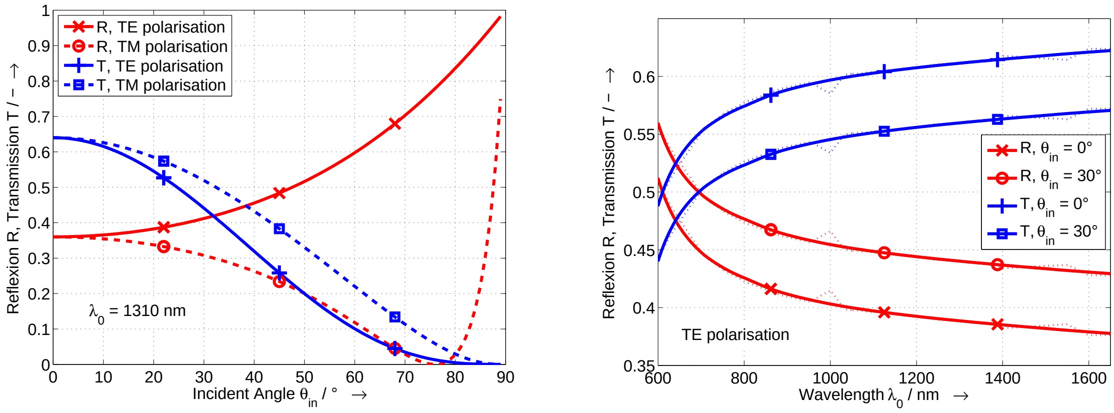

(a) Reflexion R and transmission T and reflexion at air-Ge interface versus incident angle θ_{in} - TE and TM polarisation ($\lambda_0 = 1310\,\text{nm}$).

(b) Reflexion R and transmission T at air-Ge interface versus wavelength λ_0 for TE polarisation and $\theta_{\text{in}} = 0°$, $\theta_{\text{in}} = 30°$. The dahsed lines refer to measured data from literature [28]. For the solid lines, this data is fitted with the Herzberger dispersion formula [29].

Figure 2.8: Reflexion and transmission at interface between air and Ge. The incident angle θ_{in} and the wavelength λ_0 are swept.

This means that the reflected part of an unpolarised wave, incident onto the interface under the Brewster angle, becomes TE-polarised. Thus, the angle of incidence is a means to influence the polarisation state.

In Fig. 2.9, the relevance of reflexion throughout this project is visualised: it comes into play in the optical regime regarding reflexion losses at the layers of a photodiode stack as well as in the task to create waveguiding structures. In terms of electrical circuits, the reflexion helps to determine the input impedance of the photodiodes under consideration.

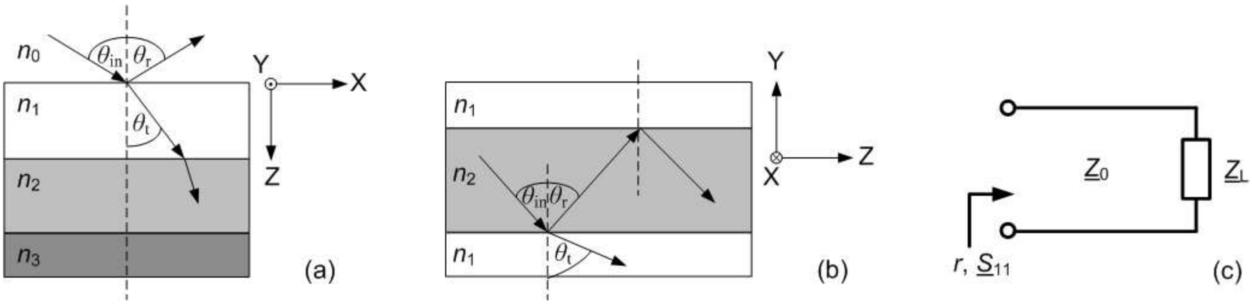

Figure 2.9: Where reflexion becomes important throughout this project: (a) Reflexion losses at surface of photodiode stack. (b) Total reflexion used to keep waves in waveguides. (c) Determination of the input impedance of a photodiode.

2.3 Semiconductors

A short introduction into some fundamentals and important parameters of semiconductors is presented in this section. More detailed information is given elsewhere [30]. Afterwards, properties of some semiconductor materials are listed. These materials are compared in respect to their potential application in optical transmission systems. The final subsection describes the most important aspects about diodes, necessary to understand later on the design of photodiodes.

2.3.1 General Considerations

The periodic crystal structure of a semiconductor is described by its (Bravais) lattice in space and the according translation vector [31]. The translation vector is composed of the three base vectors of the lattice. In the case of a cubic lattice, their common length is called the lattice constant. Via the Fourier transformation of such a space lattice, one retrieves the reciprocal lattice. Together with the reciprocal lattice vector, which depends on the wave vector $\vec{k}$, the reciprocal lattice provides the same information as the space lattice, but in the k- or momentum space. The unit cell in the k-space is the so called 1^{st} Brillouin zone or Wigner-Seitz elementary cell. Due to the periodic potential of the crystal, it is sufficient to consider this unit cell alone [32], especially in dispersion diagrams.

2.3.1.1 Energy Diagrams

The energy dependence is regarded in both, the original and the reciprocal domain: the band or E-x diagram as shown in Fig. 2.10b describes the spatial dependence of the energy E in a semiconductor and will be used to show the working principle of diodes and photodiodes. Other than with free atoms, in a crystal structure, where identical atoms are forced close together, only discrete energy levels are allowed [30], p. 54. The energy level where the occupation probability for electrons and holes is one half is called the Fermi level with the energy E_{F} [32].

The E-k-diagram of Fig. 2.10a depicts the relationship between the wave vector $\vec{k}$ and the energy E in the k-space. The wave vector component k_{x} pointing into x direction is proportional to the momentum p_{x} of electron and hole, pointing into the same direction. Thus the E-k-diagram also informs about the energy-momentum-relation. The parabolic shape of the E-k relation in this figure is a simplification based on the free electron/carrier-gas model: the kinetic energy is proportional here to the square of the momentum [30], p. 64.

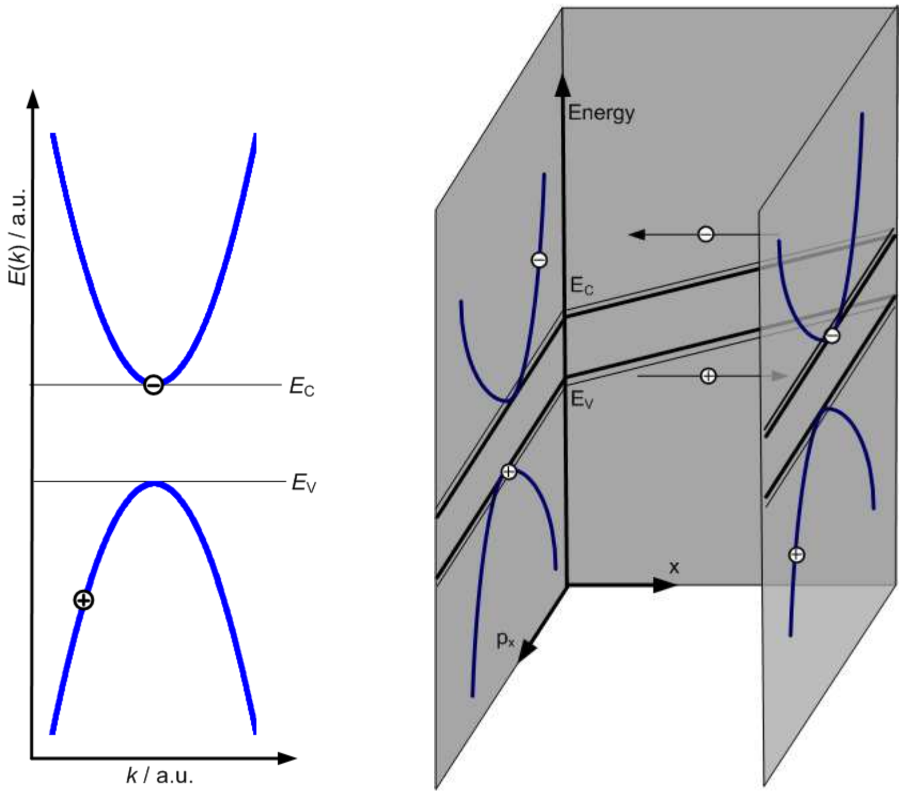

(a) Parabolic E-k diagram.

(b) Combined parabolic E-k and E-x diagram.

Figure 2.10: Parabolic E-k diagram and combined E-k and E-x diagram [30], p. 65. E_C is the so called conduction band, E_V the valence band.

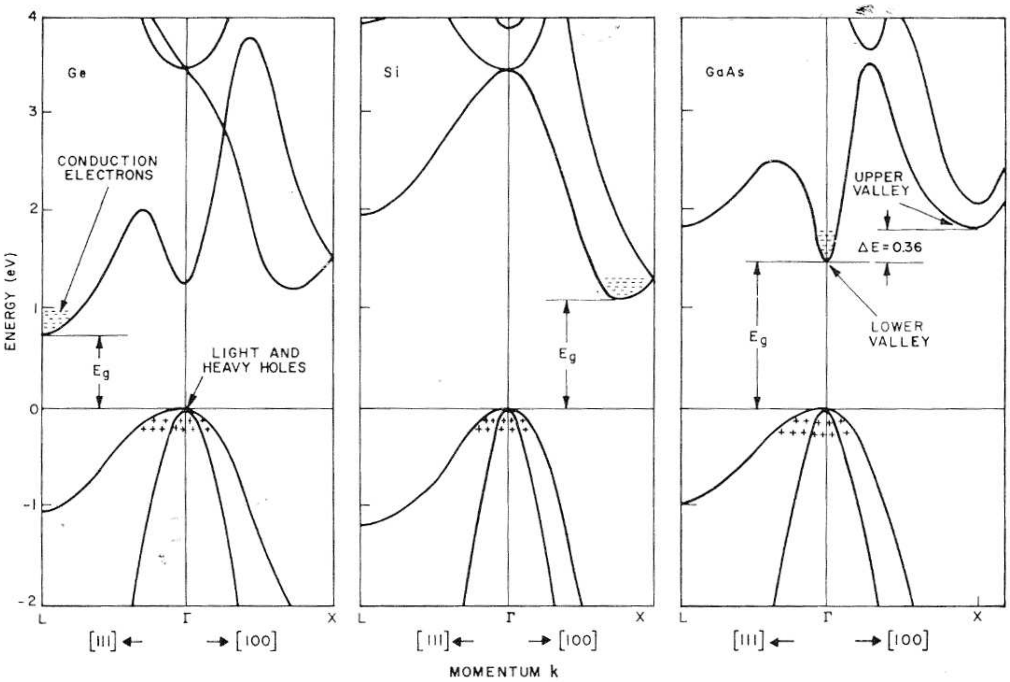

Figure 2.11: *E*-*k* diagram for *Ge* (left), *Si* (centre) and *GaAs* (right) [33], p. 22.

For periodic potentials, steps in the *E*-*k* relation occur due to diffraction, thus resulting in forbidden bands [31]. Fig. 2.10b shows the connexion between the movement of the carriers in *x*-space and *k*-space [30], p. 65.

Fig. 2.11 shows the 1^{st} Brillouin zone of the three materials *Ge*, *Si* and gallium-arsenide (*GaAs*) [33], p. 22. This diagram reveals that *GaAs* is a direct semiconductor of which the lowest energy level of the conduction band occurs at the same k-value as the highest energy level of the valence band. *Ge* and *Si* are, on the contrary, indirect semiconductors. As recombination processes in indirect semiconductors depend strongly on the defect concentration [31], very pure indirect semiconductors are not suitable for light sources: the purer the material, the longer the lifetime of the carriers. The diagram further reveals the gap between valence and conduction band, and the according band gap energy that will be discussed next.

2.3.1.2 Band Gap Energy

In a semiconductor, the energy that is needed to move a bound electron into the state of a free electron where it can contribute to electrical current is the so called band gap energy E_g. A photon can be absorbed and thereby create an electron-hole pair if its energy E_hf is

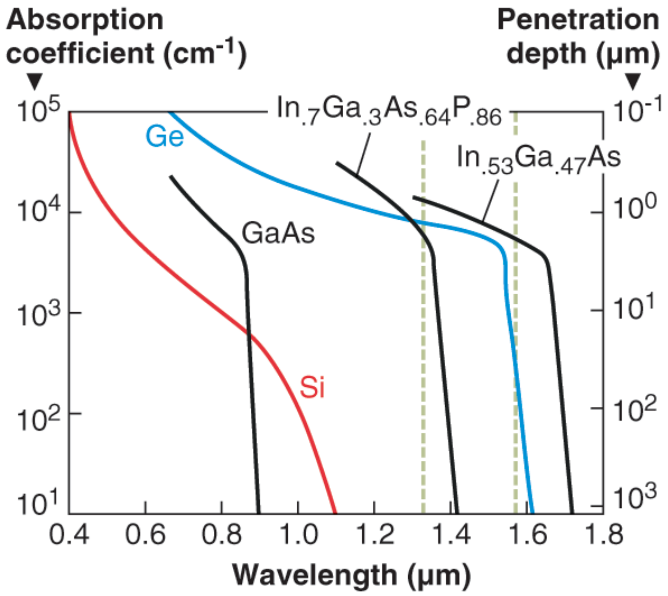

Figure 2.12: Absorption coefficient α versus wavelength λ_0 for different materials [34].

equal to or larger than this band gap energy E_g:

$$E_\mathrm{hf} = hf \overset{!}{=} E_\mathrm{g}, \tag{2.45}$$

where h is the Planck constant and f the frequency of the photon. Hence, the higher the frequency of the photon or, equivalently, the lower its wavelength, the larger is its energy. The wavelength below which the photon has an energy higher than the band gap energy is the so called critical wavelength.

2.3.1.3 Absorption Coefficient

The capability of a material to absorb light is expressed by the absorption coefficient α. The absorption coefficent for different materials is plotted versus the wavelength λ_0 in Fig. 2.12 [34]. α is proportional to the extinction coefficient κ, which depends on λ_0, and antiproportional to the wavelength itself:

$$\alpha(\lambda_0) = \frac{\kappa(\lambda_0)4\pi}{\lambda_0} = \kappa(\lambda_0)2k_0. \tag{2.46}$$

For increasing wavelength, α is reduced as the photon energy becomes too small to overcome the bandgap energy E_g. Simultaneously, κ becomes smaller for longer wavelengths [28], [35].

The absorption coefficient can also be described as a power dissipation P_α in dB:

$$P_\alpha = 10 \cdot \log_e \alpha. \tag{2.47}$$

The values for the wavelength dependent complex refractive index $\underline{n}$ for different materials have been derived elsewhere from measurements and polynomial curve fitting: values used in this work for n and κ/α are based on [28] for Ge and on [35] for Si.

2.3.1.4 Mobility

The mobilities μ_e and μ_h describe the relation of the drift velocity of electrons and holes, respectively, to the applied electric field $\vec{E}$:

$$\begin{aligned} \vec{v}_\mathrm{drift,e}\,(\vec{E}) &= \mu_\mathrm{e}(\vec{E})\;\vec{E}, \\ \vec{v}_\mathrm{drift,h}\,(\vec{E}) &= \mu_\mathrm{h}(\vec{E})\;\vec{E}\;. \end{aligned} \tag{2.48}$$

In indirect semiconductors, the drift velocity is directly proportional to the electric field at low electric field values. Therefore, the mobility is then independent of the electric field. For large electric field values, the mobility can become nonlinear and the drift velocity saturates to the saturation velocity v_sat [32].

2.3.2 Comparison of Semiconductor Materials

In this section, elements and compounds are evaluated in terms of their usability for different tasks in the design of transceivers: substrate, waveguiding structures and light detectors. The emitter is not included in these considerations. The usability of the alloys to process the resulting fast electrical signals is shortly mentioned, too.

2.3.2.1 Material Properties

Some relevant material properties have been presented in the preceding passages. They are summarised and complemented in Table 2.1 for the group IV elements Ge and Si, the III/V compounds $GaAs$, indium-gallium-arsenide ($InGaAs$) and indium-phosphide (InP). These materials can fulfil different tasks in a high-speed optical link as will be discussed later on in this section.

Table 2.1: Material Properties[6].

Property at 300 K	Unit	*Ge* [28]	*Si* [35]	*GaAs* [36]	$In_{0.53}Ga_{0.47}As$ [37][38]	*InP* [37][38][39]
Crystal Structure	-	diamond	diamond	zinc blende	zinc blende	zinc blende
Lattice Constant	Å	5.64613	5.43095	5.6533	5.8688	5.8688
Bandgap	-	indirect	indirect	direct	direct	direct
Energy Gap [direct]	eV	0.66[0.8]	1.12	1.424	0.73	1.27/1.33
Critical Wavelength	nm	1880/1551	1108	871.3	1650	976.9
Absorption Coefficient @ 1310 nm	m^{-1}	$7.486 \cdot 10^{5*}$	$2.61 \cdot 10^{-3}$	*transparent*	$11.6 \cdot 10^5$	*transparent*
Absorption Coefficient @ 1550 nm	m^{-1}	$4.6 \cdot 10^4$	$8.32 \cdot 10^{-10*}$	*transparent*	$6.8 \cdot 10^5$	*transparent*
Dielectric Constant	-	16.0	11.9	13.1/12.85	13.85	12.61
Refractive Index @ 1310 nm	-	4.304*	3.504*	≈ 3.4	3.78	3.21
Refractive Index @ 1550 nm	-	4.275 4.219*	3.476*	3.374	3.59	3.17
Mobility, electrons	$cm^2V^{-1}s^{-1}$	3900	1500	8500	8000	5400
Mobility, holes	$cm^2V^{-1}s^{-1}$	1900	475	400/500	300	300

---

[6] Values marked with ”*” stem from interpolated data.

Germanium is a group *IV* element and well known from the early days of transistor technology. Together with *InGaAs*, it absorbs at the telecommunication wavelengths, as becomes obvious from Fig. 2.12. Around 1550 nm, however, the slope of the absorption coefficient α of *Ge* is very steep, and measures to improve the absorption in this wavelength range are sought for. One solution is the incorporation of Tin (*Sn*) in *Ge* [40]: the alloy *GeSn* has a reduced bandgap compared to pure *Ge*, and thus provides increased absorption at longer wavelengths.

Silicon is the substrate material for *CMOS* processes. This is due to manifold reasons. One of them is the cost factor: it is easier to fabricate large *Si* wafers than wafers of other materials. Today, a wafer diameter as large as 450 mm can be realised. From Fig. 2.12, one can see that *Si* absorbs only for wavelengths up to around 1100 nm, so it cannot be used at telecommunication wavelengths as a detector material.

In order to make use of the transparency of *Si* at the telecommunication wavelengths, the **silicon on insulator** technology is implemented: the high difference in the refractive index between *Si* and silicondioxide (SiO_2) allows them to be used as waveguiding structures. *SOI* is also already in use in *CMOS* processes as highly insulating layer, reducing parasitic capacitances and thus increasing speed of the electrical circuits.

Due to the omnipresence of *CMOS* in the design of fast digital and mixed-signal *IC*s, it is worthwhile to find adequate materials that can be monolithically integrated into *Si*. Thus, photodetectors and electrical circuits can be combined on one platform, and fast optical links can be built.

One promising approach is the combination of **silicon** and **germanium**, both group *IV* elements. *Ge* has a lattice constant that is 4% larger than the lattice constant of *Si* (5.64613 Å and 5.43095 Å, respectively). In order to adjust this lattice mismatch to grow *Ge* on *Si*, ultrathin virtual substrates can be applied [41][42]. The alloy *SiGe* is also used for bipolar processes. These processes provide a very high transit frequency and are, therefore, ideal for analogue high-speed applications.

Though **indium-gallium-arsenide** is a *III/V*-alloy and not investigated in this work, some aspects of this compound are outlined at this point, as it is a direct competitor to *Ge* in the area of telecommunications. The absorption coefficient α of *InGaAs* is above $1 \cdot 10^4\,\mathrm{m}^{-1}$ for the telecommunication wavelengths $\lambda_0 = 1310\,\mathrm{nm}$ and almost $0.7 \cdot 10^4\,\mathrm{m}^{-1}$ at $\lambda_0 = 1550\,\mathrm{nm}$ (see Table 2.1). For both of these wavelengths, α of *InGaAs* is larger than α of *Ge*, which makes *InGaAs* the more suitable detector material at these wavelengths. One advantage of

Ge, however, lies in its integratability. Though efforts have been made, *InGaAs* cannot be grown on *Si* so far, which hinders it to be integrated into *CMOS*.

The compound **indium-phosphide** is used as a substrate material for *InGaAs*, as lattice matched epitaxially growth of *InGaAs* is possible on *InP*. For *InGaAs* grown on *InP*, 53 % of *In* and 47 % of *Ga* are used. This combination achieves a lattice constant of 5.8688 Å, which fits to the lattice constant of *InP* [37].

The group *III/V* alloy **gallium-arsenide** is applied as active material for semiconductor lasers and detectors in the visible spectral range. Because it only works at wavelengths up to 850 nm as obvious from Fig. 2.12, it is no candidate as active material for the desired telecommunication wavelengths.

2.3.2.2 Application of Materials

As a summary of the considerations about material properties as described above, the application of these materials in fast optical links is shown graphically in Fig. 2.13. Taken into account are monolithic as well as hybrid integration. Three different tasks on the receiver side of an optical transceiver are regarded in the optical regime, namely substrate material for electrical and photonic *IC*s, materials suitable for detectors and materials that can be used for waveguiding structures. It is furthermore depicted how the different materials can be used in the pure electrical regime for post-processing of the converted signals. Possible combinations are also indicated and examples from literature are notated.

2.3.3 Diodes

Detailed explanations about diodes can be found e.g. in [30][32]. In general, a diode represents a valve, conducting current in one direction under defined conditions, and blocking the current otherwise. For semiconductors, this valve is realised by a potential barrier that can be overcome by applying a positive external voltage V_{bias}, the so called forward bias, such that current can flow in one direction. For negative external voltage, namely reverse bias, almost no current is conducted in this direction [30], p. 177. The most relevant parameters of a diode are shown for the case of a *pn*-junction diode in the next subsection.

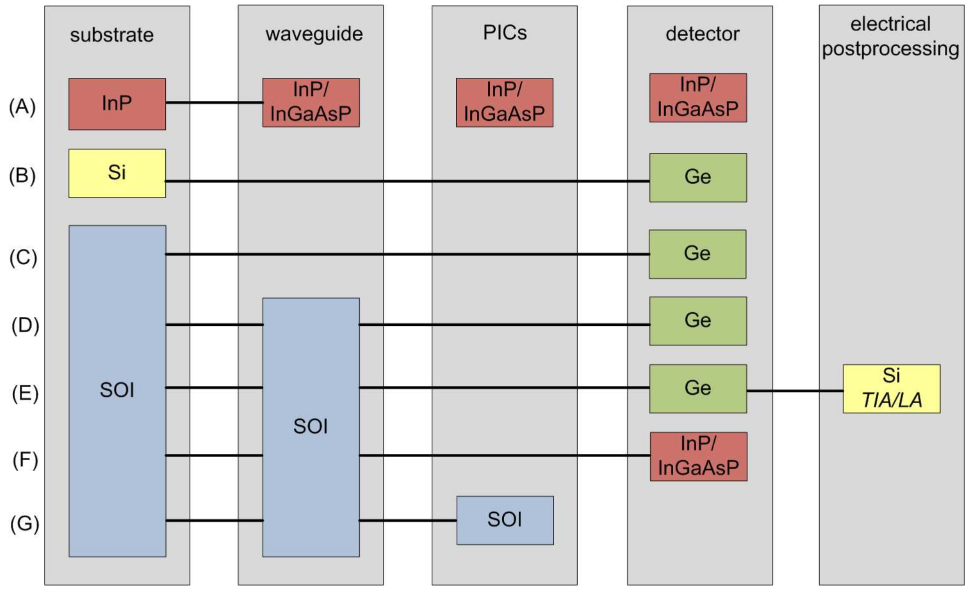

Figure 2.13: Application of different materials in an optical link on the receiver side using monolithic integration: (A): u2t Photonics AG/*HHI* [43]; (B): *IHT/INT* [9]; (C): *IHT/INT* [44]; (D): *IEF/CEA-LETI* [4]; (E): Luxtera [11], (F): Alcatel Lucent Bell Labs [45]; (G): *INTEC*/Eindhoven [46]; (H): *INTEC* [47].

2.3.3.1 *pn*-Junction Diode

Pure semiconductors can be selectively doped with impurity atoms that have an amount of electrons in the outer electron shell different from the original semiconductor material. If the impurity atom has more electrons, it is called a donator and the doped material is *n*-doped. If the impurity atom has less electrons it is called acceptor and the material is *p*-doped.

For a *pn*-junction, or a *pn*-diode, a *p*-doped area and an *n*-doped area are brought together. At the interface of the two doped materials, diffusion of carriers, electrons and holes, occurs.

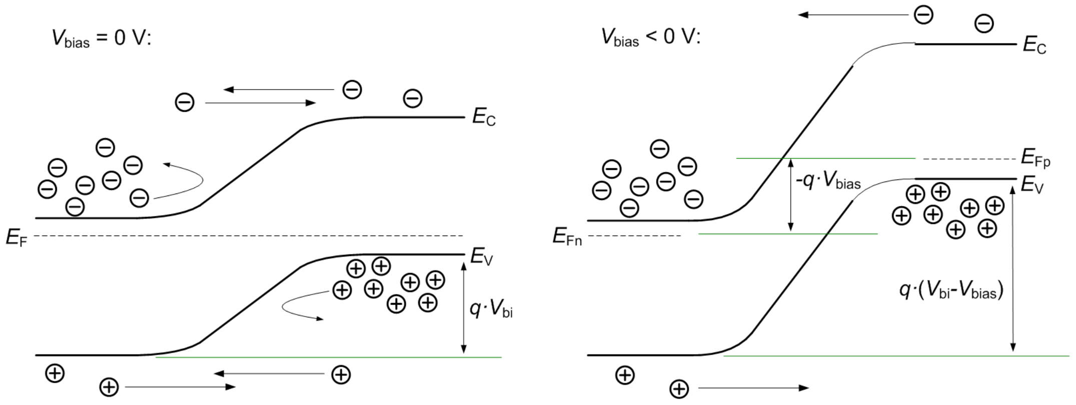

Figure 2.14: Band diagram of *pn*-junction for zero bias ($V_{\text{bias}} = 0\text{V}$) and reverse bias ($V_{\text{bias}} < 0\text{V}$). E_{F} is the so called Fermi level, E_{Fn} and E_{Fp} the quasi Fermi levels.

They recombine and leave ionised atomic cores. Between these oppositely charged atomic cores, a region without free carriers, the so called space charge region (SCR), is created. Across this region, a voltage is built up, the built-in voltage V_{bi}, see Fig. 2.14. This voltage causes an electric field across the SCR that works against the diffusion of carriers at the borders of the SCR. It is given by:

$$V_{\mathrm{bi}} = V_{\mathrm{t}} \cdot \ln \frac{N_{\mathrm{D}} N_{\mathrm{A}}}{n_{\mathrm{i}}^2}. \tag{2.49}$$

Here, n_{i} is the intrinsic carrier concentration of the given material, N_{A} is the acceptor and N_{D} the donator concentration. The so called temperature voltage V_{t} is defined as

$$V_t = \frac{kT}{q}, \tag{2.50}$$

where k is the Boltzmann constant, T the ambient temperature and q the elementary charge.

In the following, the electrical properties of a pn-diode are described for direct current (DC) and alternating current (AC).

2.3.3.2 Current-Voltage Characteristics

Across the diode, an external voltage V_{bias} can be applied to set the bias point of the diode. The current that flows due to this voltage drop is introduced here. Derivations are mainly left out here and can be found e.g. in [30]. In Fig. 2.15, the described phenomena are summarised.

The so called Shockley equation describes the unsymmetric and non-linear dependence of the diffusion current I_{dark} on the applied external diode voltage V_{bias}:

$$I_{\mathrm{dark}} = I_{\mathrm{S}} \left(e^{\frac{V_{\mathrm{bias}}}{V_{\mathrm{t}}}} - 1 \right). \tag{2.51}$$

At reverse bias, $I_{\mathrm{dark}} \approx I_{\mathrm{S}}$. The saturation current I_{S} is proportional to the junction area A_{j} of the diode. It is defined by the minority carriers and thus depends on the doping levels N_{A} and N_{D} of p- and n-region, respectively:

$$I_{\mathrm{S}} = Aqn_{\mathrm{i}}^2 \left(\frac{D_{\mathrm{n}}}{L_{\mathrm{n}} N_{\mathrm{A}}} + \frac{D_{\mathrm{p}}}{L_{\mathrm{p}} N_{\mathrm{D}}} \right). \tag{2.52}$$

L_{n} and L_{p} are the diffusion lengths of both carrier types, and D_{n} and D_{p} the respective

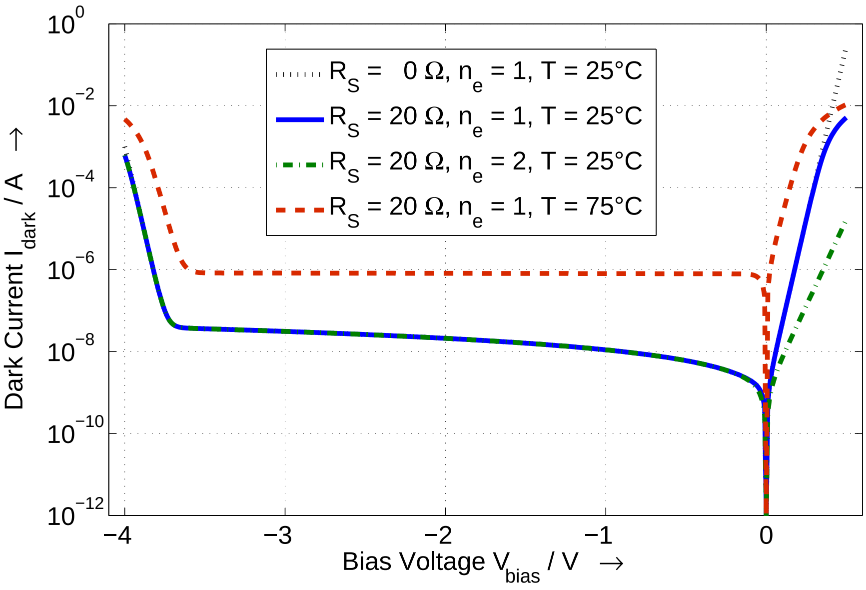

Figure 2.15: IV-characteristic for an ideal diode in logarithmic scale. Shown is the breakdown effect at large reverse bias, the influence of temperature at reverse and forward bias and the influence of a series resistance at forward bias. The increase in current at low negative bias is due to an assumed leakage to the substrate.

diffusion constants: D_n and D_p are proportional to the mobility μ_e of electrons and μ_h of holes, respectively, according to the Einstein relation:

$$\begin{aligned} D_\mathrm{n} &= \frac{\mu_\mathrm{e} kT}{q} = V_\mathrm{t}\mu_\mathrm{e}, \\ D_\mathrm{p} &= \frac{\mu_\mathrm{h} kT}{q} = V_\mathrm{t}\mu_\mathrm{h}. \end{aligned} \tag{2.53}$$

The considerations above are valid under two assumptions, namely that no electron-hole recombination takes place in the depletion layer and that the electric field in the n- and p-region can be neglected [30], p. 155. In reality, however, some second order effects occur that are not covered by the form of the Shockley equation introduced so far.

Firstly mentioned shall be the recombination current in the *SCR*. The maximum recombination current is proportional to $e^{\frac{V_\mathrm{bias}}{2V_\mathrm{t}}}$, while the diffusion current of the Shockley equation is proportional to $e^{\frac{V_\mathrm{bias}}{V_\mathrm{t}}}$ [30], p. 155. These dependencies are quite similar, so that they can be combined in the Shockley equation by the so called emission coefficient n_e:

$$I_\mathrm{dark} = I_\mathrm{S}\left(e^{\frac{V_\mathrm{bias}}{n_\mathrm{e}V_\mathrm{t}}} - 1\right). \tag{2.54}$$

This emission coefficient reaches values between 1 and 2, according to the dependencies mentioned above.

Another important second order effect is the parasitic resistance which is represented by a resistance R_S of the diode in series to the *pn*-junction, with which the equation for I_dark becomes implicit:

$$I_\mathrm{dark} = I_\mathrm{S}\left(e^{\frac{V_\mathrm{bias}-I_\mathrm{dark}R_\mathrm{S}}{n_\mathrm{e}V_\mathrm{t}}} - 1\right). \tag{2.55}$$

The resistance R_S is thereby composed of contact resistances and resistances in the neutral *p*- and *n*-region [30], p. 157.

The static parameter that depends on temperature T in Eq. 2.55 is the saturation current I_S. Its temperature dependence is described by the following equation [30], p. 169:

$$I_\mathrm{S}(T) = I_\mathrm{S}\cdot\left(\frac{T}{T_\mathrm{nom}}\right)^{p_\mathrm{t}/n_\mathrm{e}} \cdot e^{-\frac{qE_\mathrm{g}}{kT}\left(1-\frac{T}{T_\mathrm{nom}}\right)}. \tag{2.56}$$

T_nom is the nominal temperature and p_t the saturation current temperature exponent.

In Fig. 2.15, another second order effect is revealed that occurs at higher negative voltages: for a bias voltage $V_\mathrm{bias} < V_\mathrm{B}$, with V_B the so called breakdown voltage, the negative current increases exponentially [30], p. 160:

$$I_\mathrm{dark} = -I_\mathrm{S}\left(e^{-\frac{V_\mathrm{B}+V_\mathrm{bias}}{V_\mathrm{t}}} - 1 + \frac{V_\mathrm{B}}{V_\mathrm{t}}\right). \tag{2.57}$$

This effect is known as the breakdown effect of a diode. The value of V_B varies in a large range for different diode types [30], p. 159, and depends on the doping concentration of *n*- and *p*-region, [30], p. 175. One can distinguish between avalanche and tunneling breakdown [30], pp. 171: the tunneling breakdown occurs at lower reverse biasing than the avalanche breakdown and the according *IV* curve is flatter in the breakdown region.

The next subsection deals with parameters determining the *AC* characteristica of the diode.

2.3.3.3 Junction Capacitance

The small signal behaviour of the diode is mainly determined by the junction capacitance C_j across the *SCR*. For a *pn* junction, this capacitance can be approximated as a parallel plate capacitor for which the equation is:

$$C_\mathrm{j}(d_\mathrm{SCR}) = \frac{A\varepsilon_0\varepsilon_\mathrm{r}}{d_\mathrm{SCR}}. \tag{2.58}$$

Here, A_j is the area of the cross section of the *SCR* and d_SCR its thickness, ε_0 is the dielectric constant in vacuum and ε_r is the relative permittivity of the regarded material (homogeneous material assumed).

The thickness of the *SCR* changes with the applied bias voltage: if higher reverse voltages are applied, more atoms close to the *pn*-junction get ionised, and the thickness d_SCR increases. With larger d_SCR, the junction capacitance becomes smaller, as can be seen from Eq. 2.58. This bias dependence can be expressed by solving the Poisson equation for different transitions at the *pn*-junction [30], pp. 87. A general expression for a *pn*-diode results to be:

$$C_\mathrm{j}(V_\mathrm{bias}) = C_\mathrm{j0} \cdot \left(1 - \frac{V_\mathrm{bias}}{V_\mathrm{bi}}\right)^{-M}, \tag{2.59}$$

where C_j0 is the capacitance at zero biasing. M determines if the *pn*-junction is abrupt ($M = 1/2$) or linear ($M = 1/3$) [30], pp. 87. For real diodes, M lies in between these two values.

3 Opto-Electrical Converters and Photonic Structures

The basics of the *O-E* converters and photonic structures examined in this work are presented in the following sections. Firstly discussed are the photodiodes. The next elements to be talked about are simple waveguide structures that guide and manipulate the light on its way to the *O-E* converter. The final elements that are dealt with are grating structures that couple light from outside the chip into the waveguide structures or directly into the photodiode. These structures provide coupling based on diffraction.

3.1 Photodiodes

A photodiode is basically a diode junction that is illuminated. The illumination results in the generation of electrons and holes due to absorption, if the photon energy is large enough. This effect is known as the inner photoeffect. It is assumed that the bandwidth of the incident *TEM* wave is very small so that we can talk about quasi-monochromatic electromagnetic waves. Additionally, the electromagnetic waves under consideration will be called light further on, though light is striktly speaking only the visible wavelength spectrum between 380 nm and 780 nm.

The photodiode examined in this work is the *pin* photodiode, which is covered first in the next subsection. There are mainly three parameters that determine the overall performance of photodiodes, namely noise, responsivity and bandwidth. The summary of the last two of these parameters that is given here refers first and foremost to the *pin* photodiode. A short comparison of three different photodiode structures, including the *pin* structure, closes this subsection.

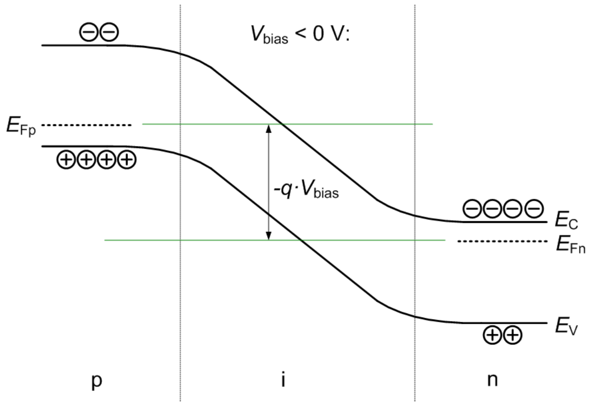

Figure 3.1: Band diagram of a *pin* photodiode with reverse bias voltage V_{bias} applied.

3.1.1 The pin-Photodiode

The current in simple *pn*-photodiodes is dominated by diffusion, which is a very slow carrier transport mechanism. To achieve faster carrier transport, essential for high bandwidth devices, an intrinsic or weakly doped semiconductor material is sandwiched between the *p*- and *n*-doped layers, as shown in Fig. 3.1. The carrier transport in this area is dominated by the drift mechanism: carriers that are generated in this intrinsic region because of the photoeffect are separated due to the field across the region and are accelerated to the n^+- and p^+-regions and the metal contacts there. If the field is strong enough, recombination processes are prevented. The use of this additional intrinsic region increases speed, and it simultaneously increases responsivity, as the volume where photons are absorbed is enlarged.

Depending on the direction from which the photodiode is illuminated, additional absorption may take place outside the *i*-region, in the n^+- and p^+-region. This absorption is determined by the thickness, the carrier concentration, and the materials of these regions.

If the thickness of the intrinsic region is chosen to be equal to the width of the *SCR*, the junction capacitance of the *SCR* should be independent of the applied bias voltage. Precondition is that all free carriers are removed from the intrinsic region at zero bias so that the *SCR* is completely depleted. Otherwise, a voltage dependence is given for lower reverse voltages.

3.1.2 Responsivity

The responsivity of a photodiode is a kind of efficiency that is determined by several criteria. These are explained first, before the term responsivity is completely described.

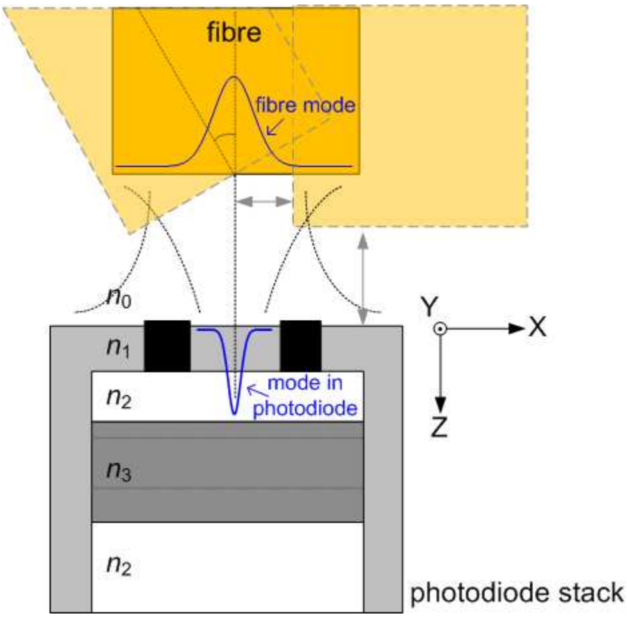

Figure 3.2: Schematic cross section of the photodiode stack used in this work with fibre in different positions above it.

3.1.2.1 Coupling Losses

The coupling losses in this context are losses that result from a mismatch between two waveguiding elements - the one from which a wave is coupled out, and the one which this wave shall be coupled into. Coupling losses occur for different reasons; in the following, reflexion losses and alignment mismatch are discussed. They are indicated in Fig. 3.2.

Reflexion at the interface between fibre and surface of the photodiode is due to the difference in the refractive index of the materials of which the elements consist. The reflexion can be reduced by carefully choosing the thickness of the single material layers of the photodiode, such that in total a destructive interference takes place at the surface of the photodiode layer stack. Not all layers can be adapted freely due to their influence on other parameters. One layer of which the thickness usually can be chosen more flexibly is the top passivation layer. It can be changed in thickness in a wide range, so that a mirror layer working as an anti-reflexion coating (ARC) can be realised. If the fibre is tilted, as happens during measurements, reflexion losses increase even further for TE polarsation, as shown in Fig. 2.8. For fabrication purposes, however, the fibre tip is fixed to the surface of the photodiode by a glue. This glue can be chosen to have a refractive index lying between the one of the fibre and the one of the passivation material.

In order to gain higher bandwidth, the photodiode junction area must become smaller, thus reaching a diameter close to the core diameter of the fibre. This means that losses due to lateral alignment mismatch increase. The vertical alignment is also critical, as the intensity reduces with increasing distance between fibre and surface of the photodiode. For lensed fibres, the distance between fibre and surface of the photodiode should coincide with the focal length of the focussed beam. For fibres with a flat polished surface, the beam diverges directly behind the tip of the fibre: the further away the fibre, the broader the area that is illuminated. For photodiodes with a diameter close to the fibre diameter, light is lost laterally even for perfect lateral alignment. The beam waist of a standard *SMF* is assumed to be $9\,\mu$m at the fibre tip: $20\,\mu$m away from the tip, the beam waist broadens to $10\,\mu$m. These values are retrieved from the spatial intensity profile of a Gaussian beam in air [48].

3.1.2.2 Quantum Efficiency

The internal quantum efficiency η_{int} describes the ratio of absorbed to incident photons, assuming that all photons emitted from the light source enter the absorption region. This ratio of absorbed to incident photons depends exponentially on the wavelength dependent absorption coefficient α of the material and the thickness of the absorption region d_{abs}. Hence η_{int} is given by the Beer-Lambert Law:

$$\eta_{\text{int}} = 1 - e^{-\alpha d_{\text{abs}}}. \tag{3.1}$$

If the absorption region is very thick and the absorption strong, all incident photons generate an electron-hole pair and $\eta_{\text{int}} \to 1$. The external quantum efficiency η_{ext} takes additionally into account coupling losses at the surface of the device due to reflexion. With the according coupling efficiency η_{coupl}, η_{ext} becomes:

$$\eta_{\text{ext}} = \eta_{\text{coupl}} \cdot \eta_{\text{int}}. \tag{3.2}$$

One can define the coupling efficiency η_{coupl} by:

$$\eta_{\text{coupl}} = 1 - R, \tag{3.3}$$

with R the reflexion losses, so that η_{ext} becomes:

$$\eta_{\text{ext}} = (1 - R)\,\eta_{\text{int}}. \tag{3.4}$$

The reflexion losses are calculated with the help of the Fresnel reflexion coefficients.

In Fig. 3.3, the internal and external quantum efficiency as well as the coupling efficiency are

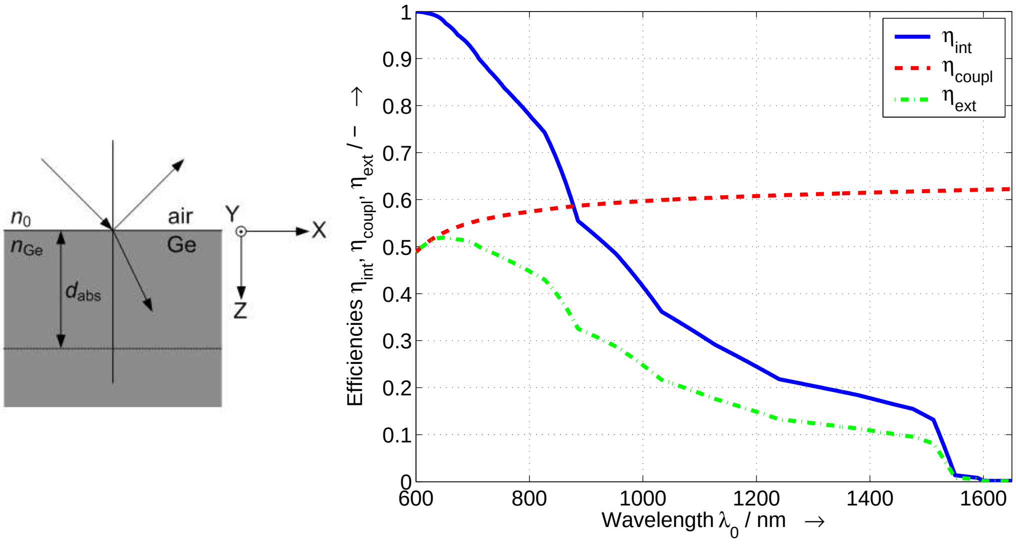

(a) Interface between semi-infinite *Ge* and air, indicating absorption area.

(b) Efficiencies η_{ext}, η_{int} and η_{coupl} versus wavelength λ_0. The incident angle $\theta_{\text{in}} = 0°$.

Figure 3.3: Cross section of examined layer stack (a). Efficiencies η_{ext}, η_{int} and η_{coupl} versus wavelength λ_0 for a *Ge* layer of thickness $d_{\text{abs}} = 330\,\text{nm}$ and a *Ge*-air interface. The incident angle $\theta_{\text{in}} = 0°$ (b).

plotted versus the wavelength λ_0 for a *Ge* layer of thickness 330 nm with an air-*Ge* interface. This thickness corresponds to the thickness of the intrinsic region of one of the photodiode samples examined in this work.

3.1.2.3 Responsivity - General Considerations

The photo current of a photodiode is proportional to the magnitude of the electric field to the square and, therefore, to the power of the optical input signal. A proportionality factor is introduced, the so called responsivity R_{opt}. It states how much photo current I_{ph} is produced due to the inner photo effect when applying a defined amount of optical power P_{opt} to the photodiode:

$$R_{\text{opt}} = \frac{I_{\text{ph}}}{P_{\text{opt}}}. \tag{3.5}$$

With $I_{\text{ph}} = \eta_{\text{ext}} q \Phi_0$ and $P_{\text{opt}} = hf\Phi_0$, where Φ_0 is the incident photon flux, R_{opt} is given by:

$$R_{\text{opt}} = \frac{\eta_{\text{ext}} q \Phi_0}{hf\Phi_0} = \eta_{\text{ext}}(f)\frac{q}{h}\frac{1}{f} = \eta_{\text{ext}}(\lambda_0)\frac{q}{hc_0}\lambda_0. \tag{3.6}$$

The responsivity is thus directly proportional to the external quantum efficiency. R_{opt} depends directly and indirectly, namely via η_{ext}, on the wavelength λ_0 in use. Regarding the geometry of the photodiode, R_{opt} depends on the thickness of the intrinsic region of the device due to η_{ext}.

The maximum *DC* responsivity $R_{\mathrm{opt,max}}$ that is theoretically achievable is given for $\eta_{\mathrm{ext}} = 1$, i.e. no reflexions occur at the interface and all the photons entering the device generate an electron-hole pair:

$$R_{\mathrm{opt,max}} = \frac{q}{h}\frac{1}{f} = \frac{q}{h \cdot c_0}\lambda_0. \tag{3.7}$$

$R_{\mathrm{opt,max}}$ depends only on the wavelength. It increases linearly with the wavelength, and resulting values are $R_{\mathrm{opt,max}} \approx 685\,\mathrm{mA/W}$ at $850\,\mathrm{nm}$, $R_{\mathrm{opt,max}} \approx 1056\,\mathrm{mA/W}$ at $1310\,\mathrm{nm}$ and $R_{\mathrm{opt,max}} \approx 1250\,\mathrm{mA/W}$ at $1550\,\mathrm{nm}$.

3.1.2.4 Responsivity - Multilayer Stack

The photodiode structure as shown in Fig. 3.2 can be regarded as a multilayer stack. For the consideration of its transmission, reflection and absorption behaviour, the layers can be assumed to be infinite into x- and y-direction. The reflexions at each interface and in both directions, upwards and downwards, have to be considered. These multipath reflexions can increase the responsivity of the photodiode if the thickness of the layers allows the light to get back into the absorption region. This happens if the reflected waves interfere constructively. In order to estimate the achievable responsivity of the photodiode including reflexion losses and multipath phenomena in the photodiode stack, one dimensional field simulations are done. Software based on the eigenmode expansion method (*EEM*) is used for this purpose [49]. With the knowledge of the electric field at the upper and lower boundary of the absorption region, the intensity inside the absorption region can be determined. Following calculations refer to perpendicular light incidence.

The intensity I is given by the averaged value of the power density in terms of time, which is the absolute value of the real part of the complex Poynting vector $\underline{\vec{S}}$ [50]:

$$I = \left|\Re\left\{\underline{\vec{S}}\right\}\right| = \frac{1}{2}\left|\Re\left\{\underline{\vec{E}} \times \underline{\vec{H}}^*\right\}\right| = \frac{1}{2}\left|\Re\{\underline{E} \cdot \underline{H}^*\}\right| = \frac{1}{2}\frac{|\underline{E}|^2}{\Re\{\underline{Z}_W\}}, \tag{3.8}$$

where $\underline{E}$ and $\underline{H}^*$ are complex field amplitudes, and $\underline{Z}_{\mathrm{W}}$ is the characteristic wave impedance

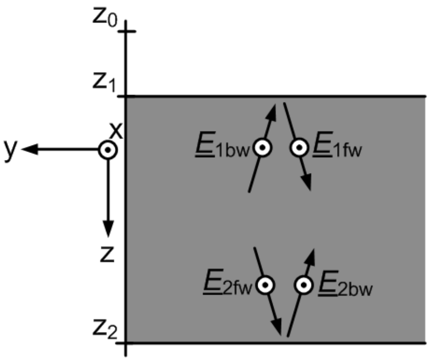

Figure 3.4: Field contributions to calculate the absorbed intensity for a layer of thickness d, extended along the z axis from z_1 to z_2. The extension in x- and y-direction is infinite.

of the given material:

$$\underline{Z}_{\mathrm{W}} = \frac{\underline{\mu}}{\underline{\varepsilon}} = \frac{\mu_0\underline{\mu}_{\mathrm{r}}}{\varepsilon_0\underline{\varepsilon}_{\mathrm{r}}}. \tag{3.9}$$

With this definition of $\underline{Z}_{\mathrm{W}}$ and considering isotropic material, the intensity I becomes

$$I = \frac{1}{2}\sqrt{\frac{\varepsilon_0}{\mu_0}}\Re\{\sqrt{\underline{\varepsilon}_{\mathrm{r}}}\} \cdot |\underline{E}|^2. \tag{3.10}$$

From now on, oblique light incidence and lossy material are considered. According to [22], p. 30, the ansatz above cannot directly be used for lossy material. If a wave is travelling in a lossy material from z_1 to z_2 along the axis z, see Fig. 3.4, its intensity is reduced due to absorption. The distance d that is passed hereby is in our case the thickness of the active layer in the photodiode. The intensity that is absorbed in this layer is given by the difference of the intensities at point z_1 and z_2, shortly after entering and shortly before leaving the layer [51], p. 156. At these interfaces, both, forward and backward waves, contribute to the intensities, as shown in Fig. 3.4. This is why four field contributions have to be taken into account for the calculation of the absorbed intensity [51], p. 156:

$$I_{\mathrm{layer}} = \sqrt{\frac{\varepsilon_0}{\mu_0}} \cdot u \cdot \left(|\underline{E}_{1\,\mathrm{fw}}|^2 - |\underline{E}_{2\,\mathrm{fw}}|^2 + |\underline{E}_{2\,\mathrm{bw}}|^2 - |\underline{E}_{1\,\mathrm{bw}}|^2\right). \tag{3.11}$$

These fields lie inside the considered layer, beyond the interfaces (right of z_1 along the z-axis and left of z_2). The auxiliary quantity u represents the impact of the material in use in form of the relative permittivity ε_{r} [51], p. 156:

$$u = \frac{1}{2}\sqrt{\varepsilon_{\mathrm{r}} - \varepsilon_3 + \sqrt{(\varepsilon_{\mathrm{r}} - \varepsilon_3)^2 + \varepsilon_{\mathrm{r}}''^2}}, \tag{3.12}$$

with ε_3 being an auxiliary quantity that contains information about the incident angle θ_{in} and the surrounding material with the refractive index n_0:

$$\varepsilon_3 = \left(n_0 \sin\theta_{\mathrm{in}}\right)^2 . \tag{3.13}$$

In the case of vertical light incidence, u results to be identical with $\Re\left\{\sqrt{\underline{\varepsilon}_{\mathrm{r}}}\right\}$.

The plane through z_0 marks the surface of the photodiode and, therefore, the reference plane for the following considerations. The ratio of the absorbed intensity in the dielectric layer of interest to the intensity at z_0 provides us with the desired external quantum efficiency. The medium above the reference plane is air, with the refraction index $n_0 = 1$.

$$\eta_{\mathrm{ext}} = \frac{I_{\mathrm{layer}}}{I_{\mathrm{ref}}} = u \cdot \frac{|\underline{E}_{1,\mathrm{fw}}|^2 - |\underline{E}_{2,\mathrm{fw}}|^2 + |\underline{E}_{2,\mathrm{bw}}|^2 - |\underline{E}_{1,\mathrm{bw}}|^2}{|\underline{E}_{\mathrm{ref}}|^2} . \tag{3.14}$$

$\underline{E}_{\mathrm{ref}}$ is the electric field strength at the reference plane positioned at z_0 and is assumed to be 1 as a reference value.

Three different material stacks with the according responsivities are illustrated in Fig. 3.5. The responsivity of a *Ge* layer with thickness $d = 330\,\mathrm{nm}$ is shown for different loss stages versus the vacuum wavelength λ_0. The solid line shows the maximum achievable responsivity $R_{\mathrm{opt,max}}$ for *Ge* under the assumption that the material is infinitely extended and there are no additional losses, so $\eta_{\mathrm{ext}} = 1$ because $\eta_{\mathrm{int}} = 1$ and $\eta_{\mathrm{coupl}} = 1$. For the solid line with ×-markers, the thickness becomes finite, 330 nm in this case, hence the internal quantum efficiency is unequal 1. For increasing wavelength, the penetration depth becomes larger, and thus less and less light is absorbed in the thin *Ge*-layer. The solid line with ∘-markers adds to the former situation a coupling efficiency unequal 1.

The final two curves show the responsivity of a *Ge*-layer of the same thickness in a photodiode stack: for the dashed line, only the intrinsic *Ge*-layer absorbs. For the dotted line, the p^+- and n^+-layer are also made of *Ge*, so these layers absorb, too. At lower wavelengths, the upper *Ge*-n^+-layer absorbs most of the light with short penetration depth. For larger wavelengths, the influence of these additional absorbing layers becomes smaller.

Comparing the single layer with the thickness of $d = 330\,\mathrm{nm}$ and the same layer in the photodiode stack, the responsivity of the latter one is larger even for *Ge* n^+- and p^+-layer for wavelengths larger than 900 nm due to the reflexions that occur inside the stack.

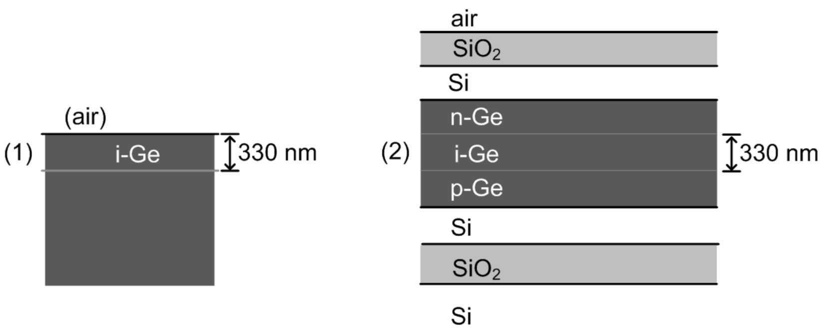

(a) Material stacks: *Ge* layer with thickness 330 nm (1), photodiode stack with intrinsic *Ge* layer of thickness 330 nm (2).

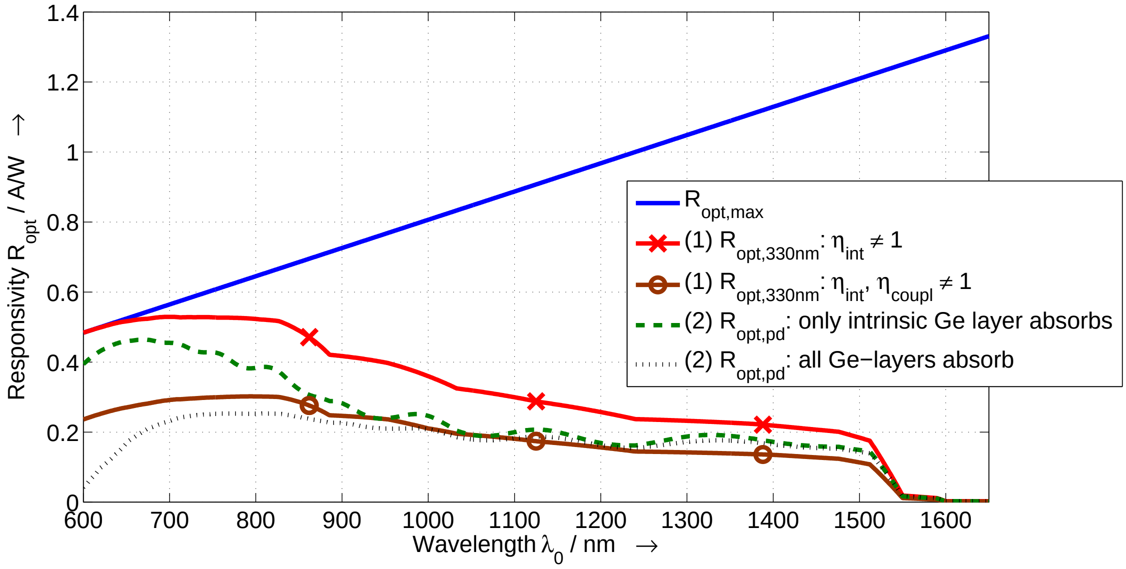

(b) Simulated responsivities: theoretical maximum responsivity $R_{\text{opt,max}}$; R_{opt} for single *Ge* layer with a thickness of 330 nm (1), with and without coupling losses; and R_{opt} of the same *Ge* layer in the photodiode stack (2) with and without additional absorption losses in n^+- and p^+-layer.

Figure 3.5: Two different material stacks (a) and corresponding responsivities plotted versus wavelength λ_0 at an incident angle of $\theta_{\text{in}} = 0°$, *TE* polarisation (b).

3.1.3 Bandwidth

The influencing parameters on the bandwidth are determined by the different mechanisms that transport the photogenerated charges to the contacts. These mechanisms are mainly drift and diffusion, of which both are defined by material parameters and the geometry of the photodiode. Regarding a *pin* photodiode as investigated theoretically and experimentally in this work, the time constants and frequencies of drift and diffusion components are given as follows.

3.1.3.1 Transit Time

The transit time is the time the carriers need to pass the *SCR* with the thickness d_{SCR}. It is assumed that the electric field is large enough to make them travel at maximum velocity, the saturation velocity v_{sat}:

$$\tau_{\mathrm{trans}} = \frac{d_{\mathrm{SCR}}}{v_{\mathrm{sat}}}. \tag{3.15}$$

The value of the transit frequency depends on the type of absorption, weak or strong [52]:

$$f_{\mathrm{trans,weak}} = 0.55 \cdot \frac{v_{\mathrm{sat}}}{d_{\mathrm{SCR}}}, \qquad f_{\mathrm{trans,strong}} = 0.44 \cdot \frac{v_{\mathrm{sat}}}{d_{\mathrm{SCR}}}. \tag{3.16}$$

The expression used in this work is taken from [33]:

$$f_{\mathrm{trans}} = \frac{\sqrt{2}}{\pi} \cdot \frac{v_{\mathrm{sat}}}{d_{\mathrm{SCR}}} \approx 0.45 \cdot \frac{v_{\mathrm{sat}}}{d_{\mathrm{SCR}}}. \tag{3.17}$$

3.1.3.2 *RC* Time

The junction capacitance C_{j} across the *SCR* must be reloaded. This causes, together with resistive losses, an *RC* time constant of the device, resulting in the *RC* frequency f_{RC}:

$$f_{\mathrm{RC}} = \frac{1}{RC_{\mathrm{j}}} = \frac{d_{\mathrm{SCR}}}{\left(R_{\mathrm{S}} + \Re\{\underline{Z}_0\}\right) A\varepsilon_0\varepsilon_{\mathrm{r}}}. \tag{3.18}$$

R_{S} summarises the resistive losses in the device itself. The system impedance $\underline{Z}_0$ is usually real and has a value of $50\,\Omega$ in most setups. Obviously, with increasing resistance values, the *RC* frequency reduces. The same holds true for increasing capacitance values. As f_{RC} contributes to the overall 3 dB frequency, one means to increase the bandwidth of the device is to reduce resistance and capacitance values adequately, without impairing other parameters.

3.1.3.3 Diffusion Time

The diffusion occurs in the contact regions, the p^+- and the n^+-layer. The diffusion time constant for electrons and holes are defined as

$$\tau_{\mathrm{diff,n}} = \frac{L_{\mathrm{n}}^2 q}{\mu_{\mathrm{e}} kT}, \qquad \tau_{\mathrm{diff,p}} = \frac{L_{\mathrm{p}}^2 q}{\mu_{\mathrm{h}} kT}. \tag{3.19}$$

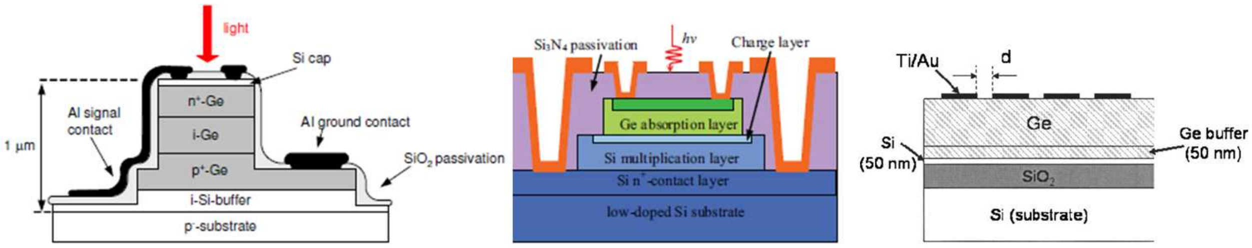

Figure 3.6: Cross sections of high-speed *Ge* photodiodes presented in literature - *pin* photodiode [53] (left), *APD* [54] (centre), and *MSM* photodiode [7] (right).

L_n (L_p) is the diffusion length of electrons (holes). If the p^+- and the n^+-layer are very thin, the impact of the diffusion process on the overall 3 dB frequency can be neglected.

3.1.4 Comparison of Photodiode Structures

Next to the *pn*-junction and *pin*-junction photodiode, avalanche photodiodes (*APDs*) and *MSM*/Schottky photodiodes are promising structures for fast optical communications. Fig. 3.6 shows possible schematic cross sections of these structures for high-speed *Ge* photodiodes based on literature [53][54][7]. One can distinguish between lateral and vertical photodiode structures, where the involved layers are arranged next to each other or in a vertical stack, respectively. The optical coupling into the structures can also be different, namely vertical or lateral. In all examples given in Fig. 3.6, stack structure and light incidence are vertical.

In the following, the different structures are shortly described and compared to each other according to performance and application.

The responsivity of an *APD* is very high compared to *pn*- or *pin*-junction photodiodes due to a multiplication layer where electrons are accelerated. By collision with atoms, more excitons are generated, leading to the avalanche effect. In the material system *SiGe*, *Ge* can be chosen as the absorption region and *Si* as the multiplication region as it is done in [54]. Thus *APDs* get high bandwidth and high responsivity simultaneously, resulting in gain-bandwidth-products (*GBPs*) larger than 300 GHz [54]. This is, however, only possible at very high reverse bias voltages ($V_\mathrm{bias} < -25\,\mathrm{V}$ in [54]). Due to the high responsivity, *APDs* are not only suitable for high-speed communications applications, but also in e.g. single photon detection where the *APD* is operated in Geiger mode.

Integrated *MSM* photodiodes are easy to be fabricated as only one lithography mask is needed which is typically applied to the most upper metal layer. *MSM* photodiodes are usually realised as interdigitated metal contacts. Thus, the distance between the two electrodes remains short. Furthermore, the active area is increased. As usually the capacitance of the *MSM* photodiode is low, these devices have an inherent large bandwidth. On the other hand, the responsivity is comparably low, mainly due to reflexions at the metal contacts. This can be avoided by using transparent contact material like Indium Tin Oxide (*ITO*). However, by doing so, the advantage of easy integration into a standard *CMOS* process is lost. Furthermore, the bandwidth might be reduced due to larger resistive loss with this contact material.

Considerations about the *pin* photodiode in general can be found in Section 3.1.1. In summary, the *pin* photodiode structure provides a higher bandwidth than the pure *pn* junction. It can operate at lower bias voltage than the *APD* photodiode, which is beneficial in terms of integration into low power electrical *CMOS* circuits. A lower responsivity can be balanced by using a waveguide photodiode structure. For direct vertical light incidence, however, additional means have to be taken to increase the responsivity and to compete with other photodiode structures.

3.2 Waveguides

Detailed information about waveguides can be found e.g. in [55][56][57]. In general, a waveguide consists of a core and a surrounding cladding. The core has a higher refractive index than the cladding. Thus, a waveguide mode can be guided inside the core due to total internal reflexion at the core-cladding-interface. The glass fibre is a representative of a cylindrical waveguide and is not in the focus of this work: main emphasis is set on planar rectangular dielectric waveguides. These waveguides can be structured by etching a high refractive index material on a low refractive index wafer. In this work, *SOI* wafers are used, with an additional SiO_2 passivation layer deposited after etching. The cross section of the unetched wafer is similar to the one in Fig. 3.7a. The rectangular waveguides can be further subdivided into different types, of which three are presented here.

After the introduction of waveguide types, the single-mode condition for strip and rib waveguides is derived. Under this condition, only the fundamental mode is able to propagate in the waveguide. At the end of this section, loss mechanisms related to waveguides are summarised.

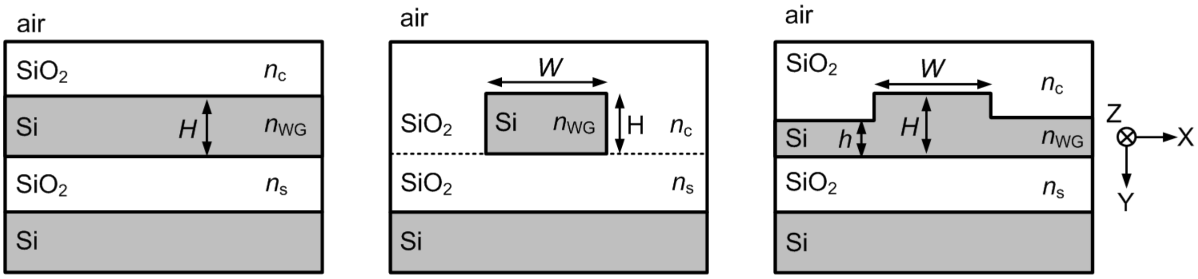

(a) Planar/slab waveguide. (b) Strip waveguide. (c) Rib/ridge waveguide.

Figure 3.7: Cross sections of three waveguide types in a *SOI* material system: planar, strip and rib waveguide.

3.2.1 Types of Waveguides

In the following pages, three types of waveguides are shortly introduced, namely planar/slab, strip and rib/ridge waveguides. The cross sections of these waveguide types are shown in Fig. 3.7. In this figure, n_c (n_{WG}, n_s) refers to the refractive index of the cladding (waveguide layer, substrate). H is the height of the unetched waveguide layer and h the height of this layer after partial etching. The **planar waveguide** in Fig. 3.7a consists of a layer with refractive index n_{WG} that is sandwiched between two layers, called cladding and substrate, with the refractive indices n_c and n_s, respectively. The substrate layer is assumed to be thick enough to prevent leakage of the waves into the next lower layers. In the figure, cladding and substrate consist of SiO_2, while waveguide and the carrier below the substrate consist of Si. If the conditions for total internal reflexion at the upper and lower cladding are fulfilled [57], a wave is guided in the sandwiched layer. As the planar waveguide is infinite in the x direction, an infinite number of lateral modes can propagate. To reduce the number of these modes, lateral confinement is needed.

For a **strip waveguide** as shown in Fig. 3.7b, the lateral extension of the core is limited by lower refractive index material: the number of lateral modes can be controlled by the width w of the core. This structure can most easily be achieved by etching the waveguide layer down to the substrate layer. The cladding layer has to be deposited afterwards then. The simulated fundamental mode for a strip waveguide in a *SOI* material system is shown in Fig. 3.8 for quasi *TE* and *TM* polarisation.

The *SOI* material system provides a large refractive index contrast between the relevant layers. Thus, the core size of a strip waveguide is only a few hundred nanometres for single-mode operation, as shown later on and in [58]. Such small structures are also called nanophotonic waveguides, and the fabrication of them is still quite challenging with standard technologies. Very compact structures can be realised using these waveguides. However, the coupling of

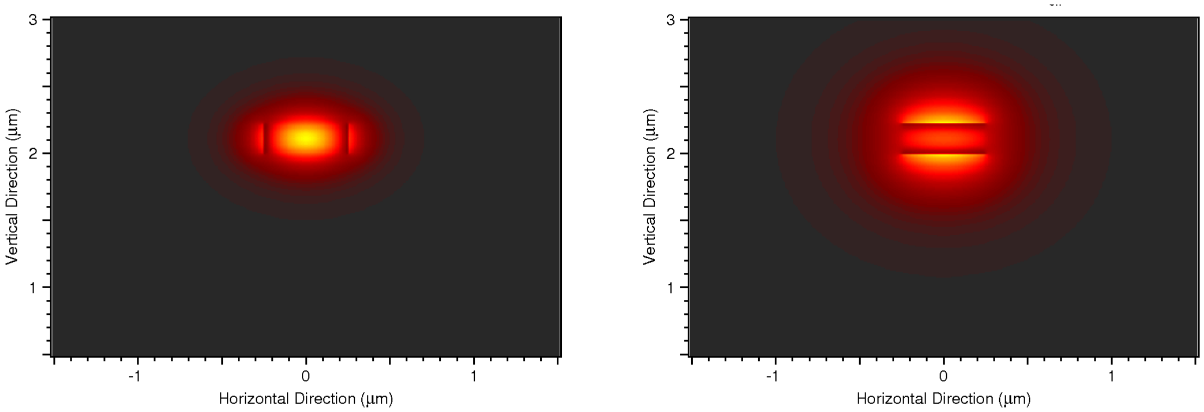

(a) Quasi *TE* mode in a strip waveguide. (b) Quasi *TM* mode in a strip waveguide.

Figure 3.8: Mode profile in a strip waveguide: fundamental quasi *TE* (a) and *TM* (b) mode in a *SOI* material system. $H = 220\,\mathrm{nm}$, $W = 500\,\mathrm{nm}$, wavelength $\lambda_0 = 1550\,\mathrm{nm}$. (bright = high intensity; dark = low intensity)

light into and out of the waveguide remains an ambitious task: the structures that have to be coupled to from these waveguides, like e.g. *SMFs* or photodiodes, have dimensions in the μm-range. Therefore, tapers are needed that serve as mode converters by appropriately broadening the cross section of the waveguide up to the coupling point. This is why waveguide structures that fulfil the single-mode condition while simultaneously having a larger width are of interest.

If the waveguiding layer of the planar waveguide is only etched partially, the so called **rib waveguide** of Fig. 3.7c emerges. For this waveguide, part of the wave is guided in the slab, not in the rib itself as can be seen for the fundamental quasi *TE* and *TM* mode in Fig. 3.9. Thus, the lateral guidance is weak for this kind of waveguide, compared to the strip waveguide, which becomes noticeable e.g. in increased bending losses.

3.2.2 Single-Mode Condition

The single mode condition is fulfilled if the dimensions of a waveguide are such that only the fundamental mode can propagate inside the waveguide for a given wavelength. The fulfilment of the single-mode condition is crucial for the design of phase detectors. In the following, the single-mode criterion for strip and rib waveguides are presented for a *SOI* material system as used in this project. The chosen wavelength is $\lambda_0 = 1550\,\mathrm{nm}$.

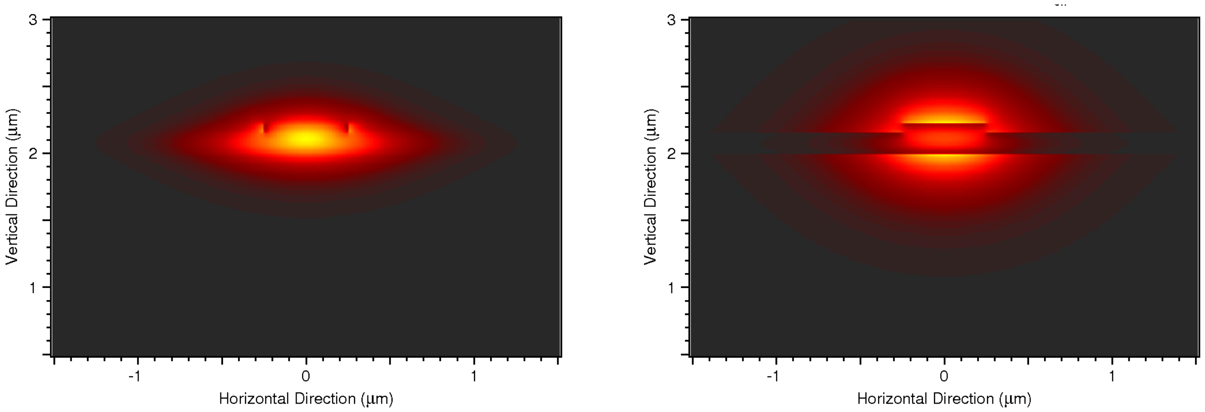

(a) Quasi *TE* mode in a rib waveguide.
(b) Quasi *TM* mode in a rib waveguide.

Figure 3.9: Mode profile in a rib waveguide: fundamental quasi *TE* (a) and *TM* (b) mode in a *SOI* material system. $H = 220\,\mathrm{nm}$, $h = 150\,\mathrm{nm}$, $W = 500\,\mathrm{nm}$, wavelength $\lambda_0 = 1550\,\mathrm{nm}$. (bright = high intensity; dark = low intensity)

3.2.2.1 Strip Waveguides

It has been demonstrated for *SOI* strip waveguides that the core dimensions must be clearly below 1 μm for single-mode operation [59]. For large cross sections, the strip waveguide can be split in horizontal and vertical direction and the mode cut-off for each direction can be calculated separately with the effective index method (*EIM*) [59].

An aproximation for the single-mode condition for small cross section *SOI* strip waveguides based on *2D* finite element method (*FEM*) simulations is given in [58], pp. 29:

$$W \leq -1.405H + 0.746, \tag{3.20}$$

with W and H in μm. This result has been derived in [58] for *TM* polarisation. For the *SOI* process in use, this single-mode criterion is depicted in Fig. 3.10. It is also valid for *TE* polarisation, as the conditions for the latter one are less restrictive. This can be seen in Fig. 3.10 where additionally the single-mode criterion for *TE* polarisation as defined in [60], p. 28, is plotted:

$$W \times H < 0.13\mu\mathrm{m}^2. \tag{3.21}$$

With high refractive index contrast of core and cladding, the waveguide has to become smaller in order to keep its single-mode operation [59]. This means, on the contrary, that high index contrast materials allow for compact structures as the light confinement is very

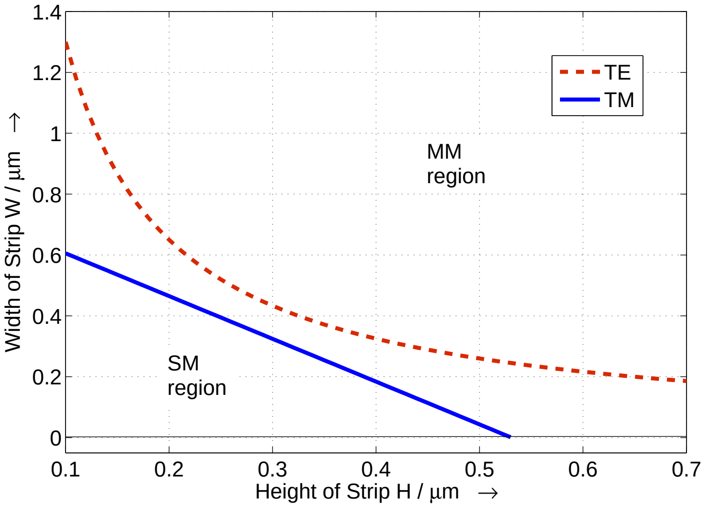

Figure 3.10: Single-mode criteria for a *SOI* strip waveguide at 1550 nm for *TE* and *TM* polarisation. The single-mode region is always below, the multi-mode region always above the plotted separation lines.

strong. On the other hand, the optical power density of these waveguides can be very high so that nonlinear optical effects become more probable [58], p. 28.

3.2.2.2 Rib Waveguides

Three different approaches to define multi-mode and single-mode regions of a rib waveguide in dependence on its geometric parameters are outlined here:

According to the analytical Soref citerion [61], the following relationships between geometrical parameters can be used to define a single-mode criterion:

$$\frac{W}{H} \leq 0.3 + \frac{r}{\sqrt{1-r^2}}, \tag{3.22}$$

where W is the width of the rib and $r = \frac{h}{H}$ defines the ratio between H, the total height of the waveguide consisting of slab and rib, and h, the height of the slab (see Fig. 3.11 for the geometrical parameters). This condition mainly has an impact on the horizontal modes, as with this condition, their effective refractive index is held below the index of the core [59]. In order to prevent vertical modes [59], r is restricted to:

$$0.5 \leq r \leq 1.0. \tag{3.23}$$

Pogossian et al. [62] derive an unequation based on the *EIM* which determines the cut-

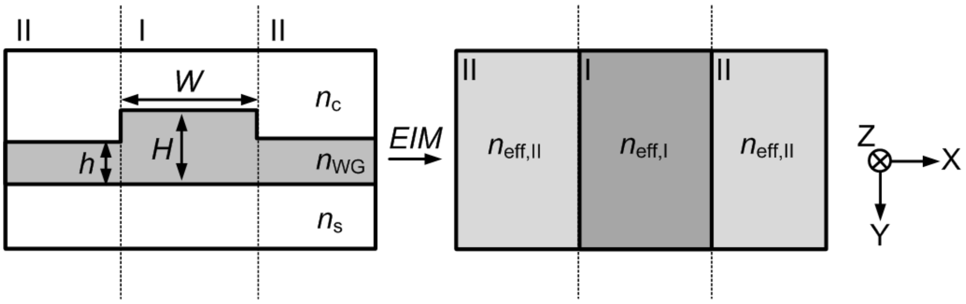

Figure 3.11: Cross section of a rib waveguide and its division into regions by the *EIM*.

off condition of the first higher mode [63]: the condition for the width of the rib to keep single-mode operation derived with the *EIM* is

$$w \leq \frac{\pi}{k_0\sqrt{n_{\text{eff,I}}^2 - n_{\text{eff,II}}^2}}, \tag{3.24}$$

where $n_{\text{eff,I}}$ and $n_{\text{eff,II}}$ are the effective indices of region I and II, respectively. These regions are depicted in Fig. 3.11. They have a slab height of $H_{\text{slab,I}} = H$ and $H_{\text{slab,II}} = h$.

Dividing this equation by H and using $n_{\text{eff,I|II}}^2 \approx n_{\text{WG}}^2 - \frac{\pi^2}{k_0^2 H_{\text{slab,I|II}}^2}$ for mode 0 [63], Eq. 3.24 becomes the modified Soref criterion with $a = 0$:

$$\frac{W}{H} \leq \frac{r}{\sqrt{1-r^2}}. \tag{3.25}$$

This condition is more restrictive to the geometrical parameters than Soref's criterion.

The single-mode criteria given above hold true for rib waveguides with large cross sections, where [61]:

$$H \geq \frac{\lambda_0}{\sqrt{n_{\text{WG}}^2 - n_{\text{c}}^2}}. \tag{3.26}$$

According to [64], however, higher modes in vertical extension can still propagate in large cross section rib waveguides, even if the mentioned single mode criteria are fulfilled.

A modification of Soref's criterion and the *EIM* is also valid for rib waveguides with small cross section [63]. It is a semi-analytical approach and uses the following ansatz:

$$\frac{W}{H} \leq a + \frac{\pi}{k_0 H\sqrt{n_{\text{eff,I}}^2 - n_{\text{eff,II}}^2}}, \quad \text{with parameter } a \in \mathbb{R}. \tag{3.27}$$

The effective refractive indices $n_{\text{eff,I}}$ and $n_{\text{eff,II}}$ of region I and II, respectively, are calculated

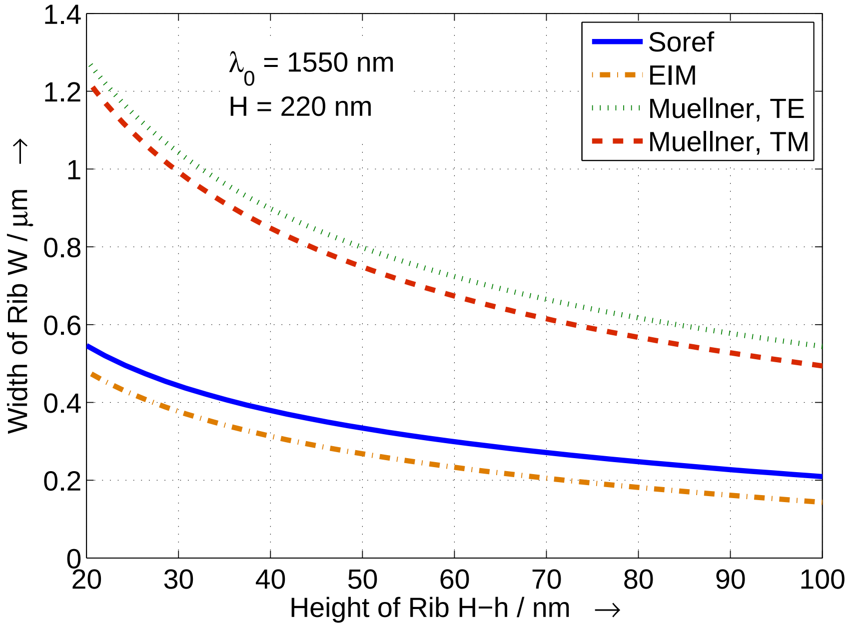

Figure 3.12: Single-mode criteria for a *SOI* rib waveguide at 1550 nm for *TE* and *TM* polarisation. The single-mode region is always below, the multi-mode region always above the plotted separation lines.

by solving the mode equation for a slab waveguide for the fundamental mode [63] and the height H_{slab} of a slab:

$$\pi - \arctan\left(k_{\mathrm{c}}\frac{\sqrt{n_{\mathrm{WG}}^2 - n_{\mathrm{eff}}^2}}{\sqrt{n_{\mathrm{eff}}^2 - n_{\mathrm{c}}^2}}\right) - \arctan\left(k_{\mathrm{s}}\frac{\sqrt{n_{\mathrm{WG}}^2 - n_{\mathrm{eff}}^2}}{\sqrt{n_{\mathrm{eff}}^2 - n_{\mathrm{s}}^2}}\right) - H_{\mathrm{slab}}\sqrt{n_{\mathrm{WG}}^2 - n_{\mathrm{eff}}^2} \overset{!}{=} 0. \quad (3.28)$$

In Eq. 3.28, k_{c} and k_{s} are 1 for *TE* polarisation and $k_{\mathrm{c}} = \frac{n_{\mathrm{c}}^2}{n_{\mathrm{wg}}^2}$ and k_{s} for *TM* polarisation. By matching the resulting curve for Eq. 3.27 with *FEM* based simulations, following values for a for the *TE* and *TM* polarisation are found in [63]:

$$\begin{aligned} a_{\mathrm{TE}} &= 0.31 \pm 0.02, \\ a_{\mathrm{TM}}(H) &= 0.28 \cdot \left(1 - e^{-\frac{H}{360}}\right) \pm 0.03. \end{aligned} \quad (3.29)$$

It can be seen that the condition for the *TM* polarisation depends on the height of the rib. This can be understood by having a closer look at the cross sectional field distribution for *TM* polarisation in a rib waveguide as shown in Fig. 3.9. These single-mode criteria are graphically summarised in Fig. 3.12 for the *SOI* process in use.

3.2.3 Losses in Waveguides

There are different loss mechanisms in waveguides, which are attributed to the type of waveguide in use, the coupling method, the material of the guiding structure and the quality of fabrication. More detailed considerations can be found e.g. in [57].

3.2.3.1 Coupling Losses

Two types of coupling are of importance in this work: the front-to-front coupling represents the coupling from glass fibre to photodiode while the coupling from fibre to grating coupler is essential for the considerations about *PICs*. For both cases, the coupling efficiency can be calculated by the overlap integral, which is [65]:

$$\eta_{\text{coupl}} = \frac{|\iint E_1(x,y)E_2^*(x,y)dxdy|^2}{\int |E_1(x,y)|^2 dxdy \int |E_2(x,y)|^2 dxdy}. \tag{3.30}$$

In the case of front-to-front coupling, E_1 is the electric field of the outcoupling waveguide, and E_2 is the electric field of the waveguide into which is coupled. In reality, there is always a small gap, filled with air or a refractive index matched oil or glue, between the out-coupling waveguide (glass fibre) and the in-coupling waveguide (photodiode). This gap transforms the waveguide mode into a Gaussian beam [66]. In the case of a grating coupler, E_1 represents the electric field of a Gaussian beam, sent out from the glass fibre, and E_2 is the electric field of the waveguide mode.

3.2.3.2 Bending Losses

If a waveguide is bent, losses occur because the mode field inside the waveguide is forced to the outer part of the waveguide: leakage in form of radiation to the outer material occurs.

For low loss refractive index contrast between core and cladding, the bending losses become very high as the guiding of the wave is weak. Only bends with a large bend radius can be used then, which means that a large area has to be covered to realise curved waveguide structures. Strip waveguides are preferable to rib waveguides for complex structures as the refractive index contrast is much higher in this case and thus smaller bend radii are possible, down to the μm range [58], p. 28. The loss due to bends is exponentially proportional to the bending radius. In Fig. 3.13, bending losses of a 500 nm wide rib and strip waveguide are shown for *TE* and *TM* polarisation.

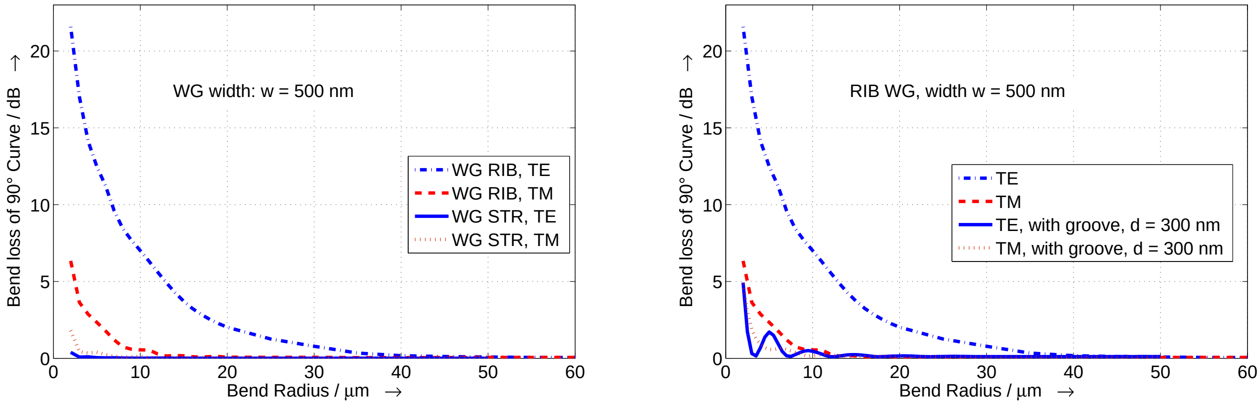

(a) Rib and strip waveguide.

(b) Rib waveguide, with and without groove.

Figure 3.13: Comparison of bending losses of rib and strip waveguide (a) as well as comparison of bending losses of rib waveguides with and without adjacent groove (b). The waveguide (rib) has a width of 500 nm. Simulations are shown for both, *TE* and *TM* polarisation.

One measure to keep the field inside the rib waveguide when the wave passes through a bend is a groove that runs in parallel to the bend on the outward side [59]. In Fig. 3.14 (left), the *SOI* rib waveguide has a width of 500 nm and a height of 70 nm while the slab has a height of 150 nm. The bend radius is 30 μm.

Fig. 3.14, left, shows the bending losses in a rib waveguide for *TE* and *TM* polarised light. In Fig. 3.14, right, a groove is added in parallel to the outer curve of the waveguide. The groove has a width of 500 nm and is placed at a distance d of 300 nm to the waveguide. Bending losses are strongly reduced in this configuration for *TE* polarisation, hence bending radii can be reduced for this polarisation compared to the solution without groove.

The *TM* polarised light, on the contrary, is not such as strongly affected by the bending losses, which means that the groove does not have a big influence on waves of this polarisation. Hence this figure reveals a polarisation dependence of the bending losses which is confirmed by literature [59]. This fact can be exploited for polarisation splitters, consisting of curved lateral couplers: the *TE* mode can be coupled out of the waveguide into another waveguide or directly into a detector, while the *TM* polarised light is further guided in the original waveguide.

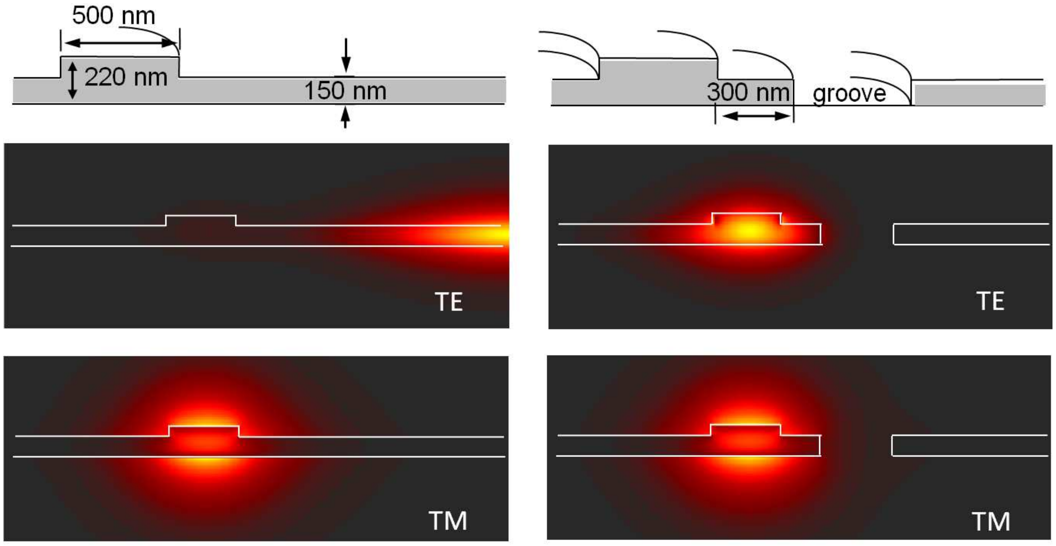

Figure 3.14: Cross section of a bent rib waveguide, with (left) and without groove (right). (bright = high intensity; dark = low intensity)

3.2.3.3 Propagation Losses

Of the different propagation losses, losses due to surface roughness play the most important role with *SOI* waveguides, as it is generally the case in high index contrast material systems [67]. The roughness of a surface causes surface scattering which leads to radiation and thereby attenuates the guided mode. For a strip or rib waveguide, roughness of the horizontal planes as well as roughness of the sidewalls has to be regarded. If the material is very pure, the roughness of the horizontal planes can be neglected. The roughness of the sidewalls depends on the fabrication process. It can be approximated in most of the cases by [67]:

$$R\left(x_0\right) = (SD)^2 e^{\frac{x_0}{L_{\text{corr}}}}, \tag{3.31}$$

with x_0 the position in x-direction on the waveguide, L_{corr} the correlation length and SD the standard deviation.

Propagation losses due to absorption can be neglected in *Si* in the *O*- and *C*-band because of the very small absorption coefficient of *Si* at these wavelengths.

3.3 Gratings

In order to understand the operating principle of diffractive elements, some considerations about the most important properties of gratings will be given in the next paragraphs. As

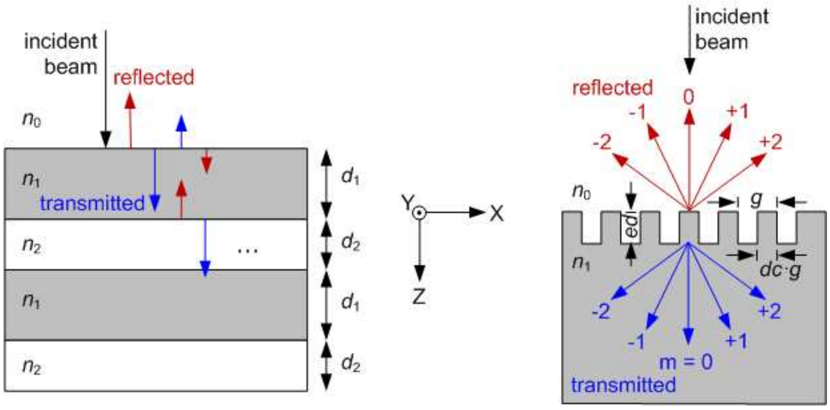

Figure 3.15: Cross section of *0D* (left) and *1D* (right) gratings. The order of diffraction is denoted by m; g is the grating period, dc the duty cycle and d_e the etch depth of the grating.

there exist several ways to analyse these gratings, a short overview of some calculation methods is presented afterwards. Most of the following considerations are based on [68][69]. Some applications of diffractive elements in *PICs* are summarised afterwards.

3.3.1 Basic Grating Properties

In this work, zero- and one-dimensional (*0D* and *1D*) gratings such as those in Fig. 3.15 are examined. For both, *0D* and *1D* gratings, the dimensioning of the grating structures depends on the wavelength in use as well as on the refractive index of the materials which the grating is built of. The *0D* gratings are stacked uniform layers that are homogeneous in all three directions of space. They are used as mirrors, so called Bragg reflectors. For constructive interference, the layer thicknesses (d_1 and d_2 in Fig. 3.15, left) have to be chosen appropriately.

For *1D* gratings, the refractive index profile changes periodically in one direction (Fig. 3.15, right). The shape of the grating, its grating period g, the duty cycle dc (also called fill factor) and etch depth d_e have an influence on the properties of the grating like diffraction angle and coupling efficiency. A coupling efficiency as high as possible for the chosen diffraction order and angle must be aimed at. In terms of fibre coupled gratings, the performance is further influenced by external parameters like the position of the fibre above the grating in horizontal and lateral direction and the tilt of the fibre. Of the different cross sectional shapes that exist for *1D* gratings, only binary gratings are dealt with in this document. They are the ones that can most easily be fabricated by only one etch step. The influence of the

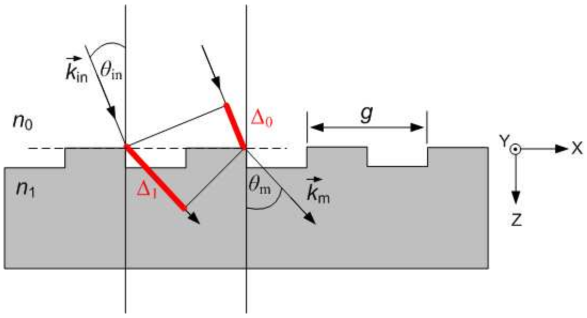

Figure 3.16: Cross section of grating coupler illustrating Bragg condition by means of the optical path difference of adjacent partial waves.

fabrication process on the shape of the gratings, like a trapezoidal cross section [70] p.50, is not examined here. Instead, perfect orthogonal sidewalls are assumed.

A structure as shown in Fig. 3.16 is regarded for the following considerations: a grating is etched into the semi-infinite layer 1 with refractive index n_1. The superstrate is semi-infinite in the negative z-direction and has the refractive index n_0. It is assumed that $n_1 > n_0$. In x-direction, the grating structure is periodic and infinite. As the structure is infinite in y-direction, the *3D* problem that has to be solved can be reduced to a *2D* problem. The incident wave is represented by its wave vector $\vec{k}_{\mathrm{in}}$, the wave propagating below the grating by its wave vector $\vec{k}_{\mathrm{m}}$.

In order to get constructive interference inside layer 1, the optical path difference between adjacent partial waves must be a multiple of λ_0:

$$n_1\Delta_1 - n_0\Delta_0 \overset{!}{=} l\lambda_0, \tag{3.32}$$

where Δ_0 and Δ_1 are the geometrical path differences in in the superstrate and in the grating material, respectively, and the continuous index $l \in \mathbb{Z}$. With

$$\Delta_0 = \sin\theta_{\mathrm{in}} \cdot g, \quad \Delta_1 = \sin\theta_{\mathrm{m}} \cdot g, \tag{3.33}$$

the grating equation results to be:

$$g \cdot (n_1 \sin\theta_{\mathrm{m}} - n_0 \sin\theta_{\mathrm{in}}) = l\lambda_0. \tag{3.34}$$

In this equation, g is the grating period, θ_{in} the incident angle and θ_{m} the diffracted angle. If the grating period is infinite, which means that no grating is present, this equation reduces to Snell's Law.

The grating equation and thus the relation between incident and diffracted angle of a given diffraction order only depends on one grating parameter, namely the grating period g. The different configurations that are possible for a grating can be defined via the ratio between g and the effective wavelength. One of these configurations provides symmetric propagation for the waves of order $m = 0$ and $m = -1$. This is the so called Littrow Mounting. The ratio of grating period and effective wavelength is then dependent on the incident angle and the material of region 1 [70] p. 25:

$$\frac{g}{\lambda_0/n_0} = \frac{1}{2\sin\theta_{\mathrm{in}}}. \tag{3.35}$$

The following relations hold true for the x components of the incident and diffracted wave vectors for plane waves:

$$k_{\mathrm{in,x}} = k_0 n_{\mathrm{eff0}} = k_0 n_0 \sin\theta_{\mathrm{in}}, \quad k_{\mathrm{m,x}} = k_0 n_{\mathrm{eff1}} = k_0 n_1 \sin\theta_{\mathrm{m}}, \tag{3.36}$$

where n_{eff0} (n_{eff1}) is the effective refractive index of the wave in material layer 0 (1). If these relations are inserted into the grating equation, the scalar Bragg Condition is defined by

$$k_{\mathrm{m,x}} - k_{\mathrm{in,x}} = l\frac{2\pi}{g} = l \cdot K. \tag{3.37}$$

Here K is the length of the (reciprocal) grating vector $\vec{K}$:

$$K = \frac{2\pi}{g}. \tag{3.38}$$

In general form, re-written for vectors, this equation becomes [31]:

$$\vec{k}_{\mathrm{m}} - \vec{k}_{\mathrm{in}} = l \cdot \vec{K}. \tag{3.39}$$

For coupling between fibre and waveguide via a grating coupler, $\vec{k}_{\mathrm{m}}$ and $\vec{k}_{\mathrm{in}}$ are the wave vectors of the Gaussian beam emitted from the fibre and the mode guided inside the waveguide. For the waveguide, the effective refractive index can be determined by applying appropriate software like *BeamPROP*.

The Bragg condition carries information only about the direction, not the intensity of the diffracted waves. The duty cylce dc and the etch depth d_{e} as depicted in Fig. 3.15 are grating parameters that have an impact on the coupling efficiency of the grating: for a given grating period g, dc and d_{e} manipulate the effective refractive index n_{eff} of the grating. In the following, calculation methods to determine the coupling efficiency of gratings in different applications are shortly presented.

3.3.2 Calculation Methods to Retrieve Coupling Efficiency

The size of the grating period g in relation to the wavelength λ_0 determines which kind of calculation method is applicable. If the grating period is much larger than the wavelength of the wave in the grating material, scalar calculation methods are sufficient. If the grating period is in the sub wavelength range, the effective medium theory can be applied: in this method, the wave sees the grating as a homogenous material with an effective refractive index [70], p. 2. If the grating period lies in the range of the wavelength in the material, i.e. the grating period is equal to the wavelength or up to 1.5 times larger, rigorous calculation methods have to be used. These methods are also valid outside this range of wavelength values, but can be replaced there by the aforementioned calculation methods which are more simple and require less calculation time.

Before a short introduction into some of the commonly used rigorous calculation methods, a more physical approach to predict the behaviour of transmission gratings is presented. This is the so called modal method (MM) which is based mainly on interference effects of the light when it is travelling through a grating.

3.3.2.1 Modal Method

For gratings with a simple rectangular form and a large aspect ratio, that means deeply etched gratings with a comparatively short grating period, one can interpret the grating walls as the cavity of a waveguide [65][71][72]. The waves propagating through the grating are regarded as waveguide modes. If the grating period lies in the range of the incident wavelength, only few modes contribute to the energy transport through the grating [69]. For the calculations that follow, two modes are considered. On that condition and the further restriction that a Littrow mounting of the grating is used [72], one can calculate the efficient refractive indices of these two modes propagating symmetrically in the grating. With the knowledge of the effective refractive indices, excitation and coupling efficiency can be determined. Both depend on the overlap integral [65] and the matching between the wave of excitation and the excited waveguide mode. The coupling efficiency of one diffraction order of the grating is the sum of the energy of all modes that are coupled to the considered diffraction order, which are two modes in the considered case. The structure and parameters referred to during the next paragraphs are depicted in Fig. 3.17. The next paragraphs are mainly based on [70].

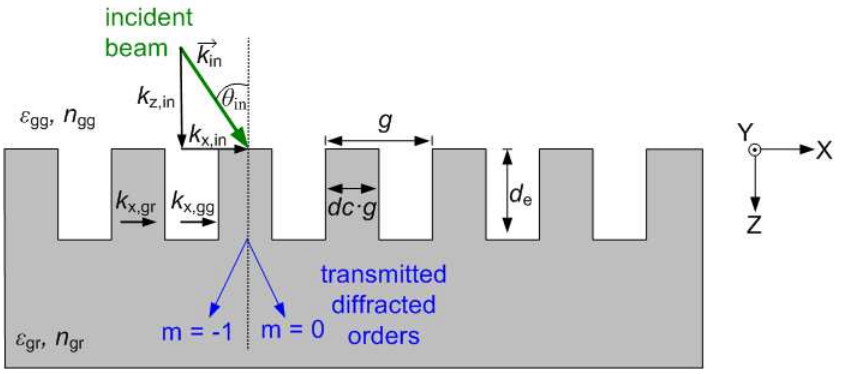

Figure 3.17: Structure and parameters as considered for the calculations with the modal method. Here, k_{gr} (k_{gg}) refers to the x component of the wave vector in the ridges (grooves). Shown is the case of Littrow mounting.

Following Eigenvalue equation in respect to the squared effective refractive index n_{eff}^2 results from the fact that the field continuity of the tangential field components must be fulfilled at the transition from ridge to groove [71][70], p. 19:

$$F(n_{\text{eff}}^2) = \cos\left(k_{\text{in,x}} \cdot g\right), \tag{3.40}$$

with $k_{\text{in,x}}$ the x component of the incident wave vector $\vec{k}$. The z component of the wave vector $\vec{k}$ is given by

$$k_{\text{in,z}} = k_0 \cdot \cos\left(\theta_{\text{in}}\right). \tag{3.41}$$

Eq. 3.40 describes all modes that can propagate inside the grating region [69], p. 50. Hence with this equation, the effective refractive indices of the two propagating modes under consideration can be determined.

The term left of the equal sign in Eq. 3.40, $F(n_{\text{eff}}^2)$, is different for *TE* and *TM* polarisation and is defined as:

$$\begin{aligned} F_{\text{TE}}(n_{\text{eff}}^2) \quad = \quad & \cos\left(k_{\text{gr,x}} \cdot dc \cdot g\right) \cdot \cos\left(k_{\text{gg,x}}(1-dc) \cdot g\right) \\ & -\tfrac{\beta_{\text{r}}^2+\beta_{\text{gg}}^2}{2k_{\text{gr,x}}k_{\text{gg,x}}} \cdot \sin\left(k_{\text{gr,x}} \cdot dc \cdot g\right) \cdot \sin\left(k_{\text{gg,x}}(1-dc) \cdot g\right) \end{aligned} \tag{3.42}$$

$$\begin{aligned} F_{\text{TM}}(n_{\text{eff}}^2) \quad = \quad & \cos\left(k_{\text{gr,x}} \cdot dc \cdot g\right) \cdot \cos\left(k_{\text{gg,x}}(1-dc) \cdot g\right) \\ & -\tfrac{\varepsilon_{\text{gr}}^2 k_{\text{gr,x}}^2+\varepsilon_{\text{gg}}^2 k_{\text{gg,x}}^2}{2\varepsilon_{\text{gr}}\varepsilon_{\text{gg}}k_{\text{gr,x}}k_{\text{gg,x}}} \cdot \sin\left(k_{\text{gr,x}} \cdot dc \cdot g\right) \cdot \sin\left(k_{\text{gg,x}}(1-dc) \cdot g\right) \end{aligned} \tag{3.43}$$

It can be seen that this part of the equation depends on following geometric parameters of the grating: the period g and the duty cycle dc. Furthermore, $k_{\text{x,gr}}$ ($k_{\text{x,gg}}$) is the x component of the k vector in the ridges (grooves) of the grating:

$$k_{\mathrm{gr,x}} = k_0\sqrt{n_{\mathrm{gr}}^2 - n_{\mathrm{eff}}^2}, \qquad k_{\mathrm{gg,x}} = k_0\sqrt{n_{\mathrm{gg}}^2 - n_{\mathrm{eff}}^2}. \tag{3.44}$$

Here, $\varepsilon_{\mathrm{gr}}$ and $\varepsilon_{\mathrm{gg}}$ are the according relative permittivities, while n_{gr} and n_{gg} are the according refractive indices in ridges and grooves.

The term right of the equal sign in Eq. 3.40 is determined by the grating period and the x component of the k vector of the incident wave, $k_{\mathrm{in,x}}$, as given in Eq. 3.37:

$$k_{\mathrm{in,x}} = k_0 \cdot \sin\left(\theta_{\mathrm{in}}\right) = \frac{2\pi}{\lambda_0} \cdot \sin\left(\theta_{\mathrm{in}}\right). \tag{3.45}$$

The surrounding material is assumed to be air, thus $n_{\mathrm{gg}} = n_0 = 1$. Eq. 3.40 can be re-written to:

$$F(n_{\mathrm{eff}}^2) = \cos\left(2\pi\frac{g}{\lambda_0}\sin\theta_{\mathrm{in}}\right). \tag{3.46}$$

It is obvious from this equation that the ratio of grating period and wavelength plays a role in this equation as well as the incident angle, and thus the kind of grating mounting. Let us consider the so called Littrow mounting now. For this arrangement, one higher diffraction order is reflected or transmitted symmetrically to the order $m = 0$. This results in:

$$\sin\left(\theta_{\mathrm{in}}\right) = \frac{\lambda_0}{2g}, \tag{3.47}$$

and $k_{\mathrm{in,x}}$ becomes then:

$$k_{\mathrm{in,x}} = \frac{\pi}{g}. \tag{3.48}$$

This finally leads to:

$$F(n_{\mathrm{eff}}^2) \overset{!}{=} -1. \tag{3.49}$$

This equation is solved for a defined grating period g but for different filling factors dc, resulting in pairs of $n_{\mathrm{eff0}}(dc)$ for mode 0 and $n_{\mathrm{eff1}}(dc)$ for mode 1. As all higher diffraction orders, reflected as transmitted ones, shall be suppressed except for $m = -1$, a limited range of values is available for the grating period g:

$$\frac{\lambda_0}{2n_{\mathrm{gr}}} < g < \frac{3\lambda_0}{2n_{\mathrm{gg}}}. \tag{3.50}$$

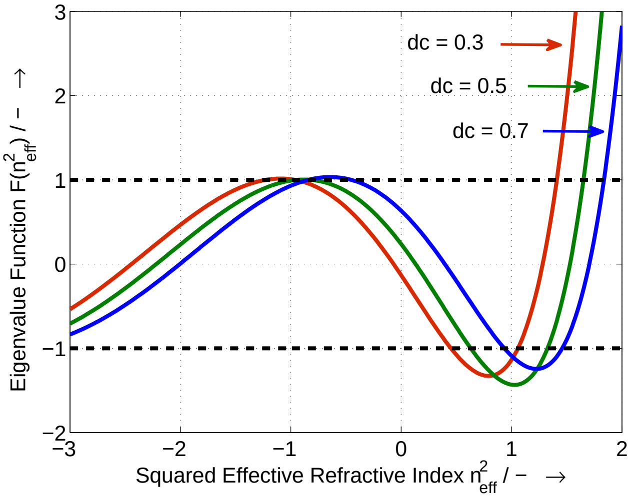

Figure 3.18: Eigenvalue function versus squared effective refractive index n_{eff}^2.

Fig. 3.18 shows the Eigenvalue function for a wavelength of $\lambda_0 = 1550\,\mathrm{nm}$ and a grating period of $g = 1000\,\mathrm{nm}$. The material of the grating is SiO_2 with a refractive index of $n_{\mathrm{gg}} = 1.45$. The surrounding material is air. Three duty cycles are plotted, namely $dc = 0.3$, $dc = 0.5$, and $dc = 0.7$. The coupling efficiency η_{coupl} into the order $m = -1$ is then calculated in dependence on the duty cycle dc and the etch depth d_{e} as:

$$\eta_{\mathrm{coupl}} = \sin^2\left(\frac{\pi}{\lambda_0}|n_{\mathrm{eff0}}(dc) - n_{\mathrm{eff1}}(dc)|d_{\mathrm{e}}\right). \tag{3.51}$$

As reflexion losses are neglected in this approach, a theoretical coupling efficiency of $\eta_{\mathrm{coupl}} = 1$ is possible.

In the following subsections, a very short summary of two rigorous calculation methods that are used to solve the Maxwell's equations is given. These are the finite difference time domain method ($FDTD$) and the rigorous coupled wave analysis ($RCWA$).

3.3.2.2 Finite Difference Time Domain

The $FDTD$ has been developed by Taflove [73]. It is based on a uniform spatial discretisation of Maxwell's equations in the time domain: derivatives in Maxwell's equations become thus finite differences [68], p. 41. The finer the grid is, the more accurate the results are. A fine grid requires, however, long calculation times. The software utilised in this work for $FDTD$ simulations is called $FullWAVE$ and is part of the $RSoft$ software suite.

3.3.2.3 Rigorous Coupled Wave Analysis

The *RCWA* was developed by M.G. Moharam, and a review of this method can be found in [74]. With the *RCWA*, the electromagnetic fields are given by a sum over coupled waves. The calculations are done in the frequency domain. The complex device structure is divided into blocks with constant refractive indices in terms of the propagation direction. The package *DiffractMOD* of the *RSoft* software suite implements a form of the *RCWA* [75]. This package is applied in this work.

Both methods, *FDTD* and *RCWA*, are used in this context to simulate coupling into photodiodes, with and without gratings. For the simulation of grating couplers between fibre and waveguide, a software based on the eigenmode expansion method is applied.

3.3.2.4 Eigenmode Expansion Method

The freely available software Cavity Modelling Framework (*CAMFR*) has been developed at the Ghent University [76]. A manual is included in the package with simulation examples [49]. Following short overview of the theory behind the (bidirectional) *EEM* is mainly extracted from [68][76]. The *EEM* works in the frequency domain. The structure under consideration is divided into sections, which are, in the $2D$ case, slab waveguides. In each section, the eigenmodes, guided and radiated modes, are calculated. All these sections form a stack, and the scattering matrix of this stack is calculated by applying a mode-matching technique at the interfaces of the sections. Thus, reflexion and transmission of the entire stack are retrieved. Fields and radiated power can be calculated at each point of the stack, which is helpful when this software is used to calculate the external quantum efficiency of a photodiode stack.

With the *EEM*, the simulation space must be confined in the vertical direction by appropriate boundaries, the perfectly matched layers (*PMLs*). They attenuate radiated waves so that they are not reflected back into the structure, thus emulating the scenario for an open structure. This is the same principle as used in an anechoic chamber: there, absorbers cover the wall of the chamber to prevent reflexions. The structure that is considered in the following is the one in Fig. 3.19. The coupling efficiency from fibre to waveguide is the same as from waveguide to fibre, as the reciprocity condition is fulfilled [68]. The calculation of the coupling efficiency is based on the overlap integral as presented in Eq. 3.30. In the case of the grating coupler, the overlap between the field in the waveguide and the fibre mode is calculated. If the coupling from waveguide to fibre is regarded and the power that is coupled

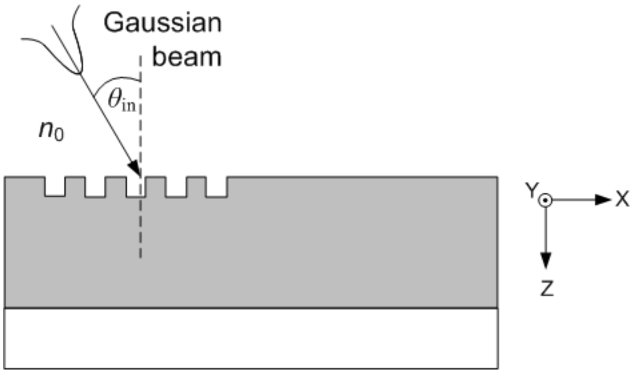

Figure 3.19: Grating coupler structure with grating parameters as applied in Eq. 3.52.

into the fibre is known, multiplication of the overlap integral by this power results in the coupling efficiency.

According to [68], some simplifications are made before calculating the coupling efficiency. The coupler itself is a *3D* structure, but is reduced to a *2D* problem spreading into direction x and z. The influence of the lateral extension y of the waveguide is taken into account by a correction factor ζ. This is possible only if the waveguide is wide enough not to strongly perturbate the lateral field extension in the waveguide. Furthermore, a Gaussian beam profile is assumed for the fibre mode. The coupling efficiency is then given by [68], p. 48:

$$\eta_{\mathrm{coupl}} = \zeta \cdot \left| \int E(x, z = z_0) A_{\mathrm{G}} e^{(x-x_0)^2} w_0^2 e^{j \cdot n_0 \frac{2\pi}{\lambda_0} \sin(\theta_{\mathrm{in}}) x} dx \right|^2 . \tag{3.52}$$

The reference position on the x (z) axis is x_0 (z_0), n_0 is the refractive index of the material between fibre and waveguide. The fibre mode is approximated as a Gaussian beam with the beam radius w_0 and the normalisation factor A_{G}. Reflexions at the grating surface or the fibre facet are not yet included in this equation.

3.3.3 Application of Gratings in Photonic Integrated Circuits

There are different applications for diffraction gratings in combination with photodiodes and planar lightwave circuits. Fig. 3.20 illustrates the applications that have been examined in this work:

Simple Bragg reflectors are realised by alternating layers with a refractive index difference as high as possible, Fig. 3.20, left. In the given configuration of the photodiode with vertical light incidence, the *Si*- and SiO_2-layers already at hand in a *SOI* stack can be used to work as such reflectors.

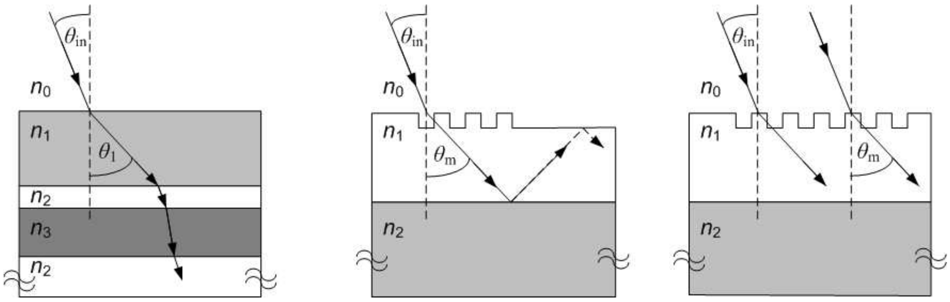

Figure 3.20: Cross sections of gratings investigated in this work: Bragg grating as reflector (left), binary grating used as grating coupler on top of a waveguide (centre) and on top of a photodiode (right).

For waveguide photodiodes, v-shaped grooves are a common solution for the coupling from fibre to waveguide [66]. These grooves are etched or sawn into the chip directly in front of the waveguide. The fibres are placed horizontally into these grooves. Hence the light of the fibres is directly butt-coupled into the waveguide. This horizontal coupling can be replaced by vertical coupling using a grating coupler [77], Fig. 3.20, centre. This is especially useful if the chip must be very compact and has many (optical as electrical) in- and outputs. The grating is placed on top of a waveguide and the fibre is positioned orthogonally or in an oblique angle above the grating. The light that is incident on the grating is redirected by the coupler so that it is conducted horizontally into the waveguide. For this purpose, the grating is designed as an efficient transmission grating. Such gratings can simultaneously work as a filter, e.g. as wavelength demultiplexer or polarisation splitter, as e.g. demonstrated in [70][68].

By using diffraction gratings on top of a vertical photodiode stack with vertical light incidence, the angle under which the light enters the layers below the grating can be changed, Fig. 3.20, right. With increasing angle, the optical path of the light through the active region becomes longer and, therefore, the absorption stronger. This causes an increase of the quantum efficiency. For this operation, a high-efficient transmission grating is needed. The light has to pass several layers with different refractive indices before it reaches the active region. The diffraction angle of the grating can, however, not be chosen arbitrarily, as total internal reflexion can occur if the diffraction angle becomes too large.

4 Photodetectors for Oblique Light Incidence

In this chapter, first the device structure of the examined photodiodes is focused on. With the knowledge of this structure and the associated parasitic effects in mind, equivalent DC and small signal circuits are derived. In a second part, means to improve two of the key parameters of the detector, namely responsivity and bandwidth, are discussed. The last three parts of this chapter summarise the measurement techniques applied in this work and the corresponding measurement results for DC, small signal and time domain characterisation.

4.1 Photodiodes under Examination

In this work, photodiodes with vertical and oblique light incidence are examined. The general device structure of these detectors can, however, also be applied for waveguide photodiodes [78], which make use of lateral light incidence and are suitable for integrated phase detectors. This section comprises the device structure of the photodiodes that have been examined, the contact structure and the detailed dimensions of the samples that have been simulated and measured.

4.1.1 Device Structure

The Ge pin-structure is realised in an MBE process developed and run at the IHT. The most challenging part is the growth of Ge on Si due to the different lattice constants of both materials. The IHT uses an ultrathin virtual substrate for the adjustment of the lattice mismatch: a strain-relaxed Ge buffer layer is grown on a Si substrate by a low temperature process [41][42]. The thin Ge layer is annealed at $850\,°C$ to reduce threading dislocation densities [79]. Onto the buffer layer, the pin diode is grown.

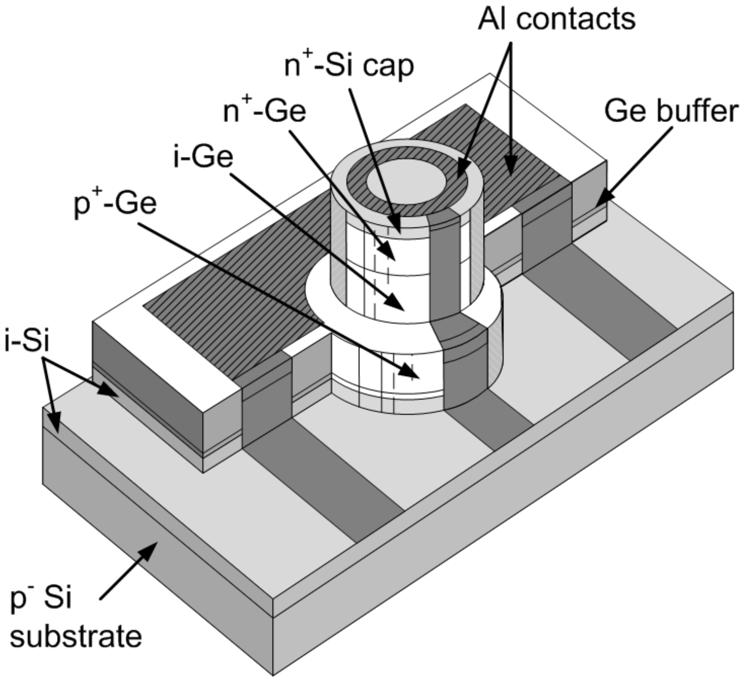

Figure 4.1: Device structure of vertical *Ge* on *Si pin* photodiode indicating part of contact structure (not to scale). The SiO_2 passivation layer is not shown in this figure for clearness. Where the metal is hatched, it lies in an oxide window for contacting.

The whole device process of the *IHT* is described in detail in e.g. [42][80] and is only shortly outlined here. The resulting device structure is schematically shown in Fig. 4.1: on a *Si* substrate, the virtual substrate is grown, followed by *Ge* layers, forming the vertical *pin* diode, and a *Si* cap layer. The p^+-region is doped with the group-III-element Boron (B) at a doping concentration of $10^{20}\,\mathrm{cm}^{-3}$. The doping concentration of the intrinsic region has a steep transmission from $10^{20}\,\mathrm{cm}^{-3}$ down to $10^{16}\,\mathrm{cm}^{-3}$. The n^+-layer is doped with the group-V-element Antimon (Sb) at a doping concentration of $10^{20}\,\mathrm{cm}^{-3}$. On top of the n^+-layer, a strained *Si* cap with a doping concentration of $10^{20}\,\mathrm{cm}^{-3}$ is used as the ohmic top contact.

The processing starts with the etch step to structure the n^+i-mesa. A second etch step for the p^+-buried layer follows. For passivation, a SiO_2-layer is deposited. Therefore, plasma enhanced chemical vapour deposition ($PECVD$) is used. Afterwards, the contact windows are opened for aluminium (Al) metallisation. This is done with reactive ion etching (RIE) and, for the last 50 nm, wet etching. The metallic n^+-contact is ringlike or discoid. For the p^+-contact, the metal shape is rectangular with an open area for the n^+i-mesa.

Photodiodes with different geometries and thicknesses are examined. In Table 4.1, the samples under examination are listed with the according layer thicknesses (data as provided by

Table 4.1: Samples examined in this work with according wafer material, layer thicknesses and contact material.

Sample	Substrate	Layer Thickness / nm							Contact
		Si buffer	*Ge* buffer	*p-Ge*	*i-Ge*	*n-Ge*	*Si* cap	SiO_2	Material
A2044_1/2	*Si*	152	50	297	426	106	25	330	*Al*
A2045_1/2	*Si*	138	50	300	331	83	25	320	*Al*

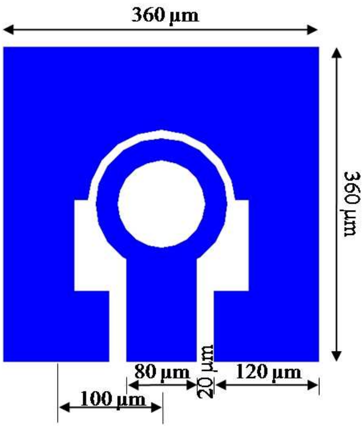

Figure 4.2: Layout and dimensions of the contact structure of the photodiodes under examination [51], p. 59. In this example, the upper mesa has a diameter of $D = 160\,\mu$m.

the *IHT*). Each sample has a size of $35 \times 35\,$mm^2. The diameter D of the upper mesa of the single photodiodes lies in the range of 10 to 160 μm.

4.1.2 Contact Structure

The photodiode has an *Al* contact structure with a thickness of $1.3 - 1.6\,\mu$m [81]. It is designed to allow contacting by ground-signal-ground (*GSG*) *RF* probes with a pitch of 100 μm. The contact structure as shown in Fig. 4.2 starts from the pads with a symmetric coplanar line. The distance between signal contact and ground contacts as well as the width of the signal contact are chosen to provide a characteristic impedance of 50 Ω. The simulation of the scattering parameters of such a transmission line is shown in Fig. 4.3 at 50 GHz. The length of the line is swept in this simulation from 100 μm to 1000 μm.

If the area of the pad becomes too small, *RF* probe contacting as well as bonding becomes difficult. The signal pad in use has a size of $80 \times 80\,\mu$m^2, the dimensions of the ground pads are $120 \times 80\,\mu$m^2. The contacts are covered with Alumina. The oxide has to be penetrated by the tips of the *RF* probe to ensure a proper contact. This is why the measured resistance that includes the contact resistance can vary for different measurements.

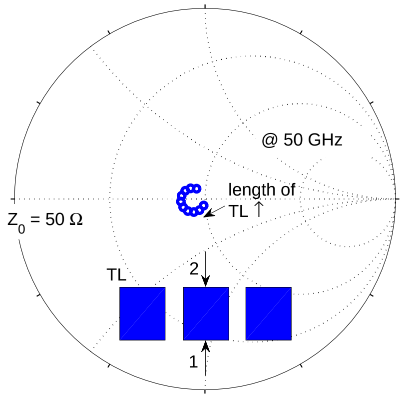

(a) Reflexion coefficient S_{11} of transmission line, length swept.

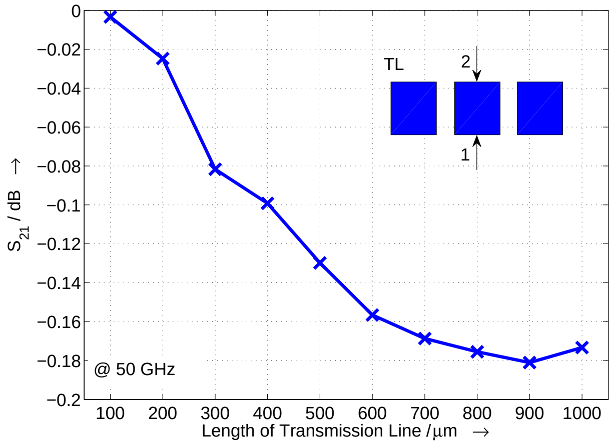

(b) Transmission factor S_{21} of transmission line, length swept.

Figure 4.3: Reflexion coefficient (a) and transmission factor (b) of transmission line (*TL*), simulated at 50 GHz. The length of the *TL* is swept from 100 μm to 1000 μm. The width of the signal line is 80 μm, the distance between signal and ground line is 20 μm.

4.2 Circuit Simulator Models

This section deals with the equivalent circuit of the photodiode as used in a circuit simulator. In this work, the photodiode model is realised in the circuit simulator *Advanced Design System* (*ADS*) from Agilent Technologies. In order to keep the model flexible and adaptable to different environmental conditions, the behaviour of the device is represented by lumped elements and controlled sources. The values of the parameters in use are extracted from measurements using *ADS* implemented optimisation routines.

In *ADS*, the parameters that are adjustable outside the model, e.g. for the purpose of scaling a device, are called design parameters. The design parameters in this model are the geometric dimensions d_{i}, which is the thickness of the intrinsic *Ge* region, and D, which is the diameter of the upper mesa. With the latter one, the scaling parameter A_{j}, which is the junction area, is calculated inside the model und applied for the area dependent parameters.

The model consists of a separate description of *DC* and small signal behaviour. For both models, the characteristics of photodiodes with and without illumination are considered.

4.2.1 DC Simulation Model

Fig. 4.4 shows the *DC* model of the photodiodes under examination. The general behaviour of the diode without illumination is described by the dark current block as marked in the figure. Dependence on geometry is included here. The influence of light is represented by the photo current block that is also enframed in the figure. Both parts of the overall *DC*-model are presented in the subsequent subsections.

4.2.1.1 Dark current

The *pn*-junction of the photodiode is represented by a pre-implemented diode model as available in *ADS*. Detailed information about such models, like *SPICE* models, can be found in e.g. [30], pp. 159. These models are based on the Shockley-equation as defined in Eq. 2.51. The temperature dependence without illumination is also implemented in most of these models, using Eq. 2.56. The *pn*-junction diode is denoted with D_1 in Fig. 4.4. The applied device parameters of this diode are also listed in this figure. These are the emission coefficient n_{D1}, the saturation current I_{SD1}, which scales with the junction Area A_{j}, and the series resistance R_{S}.

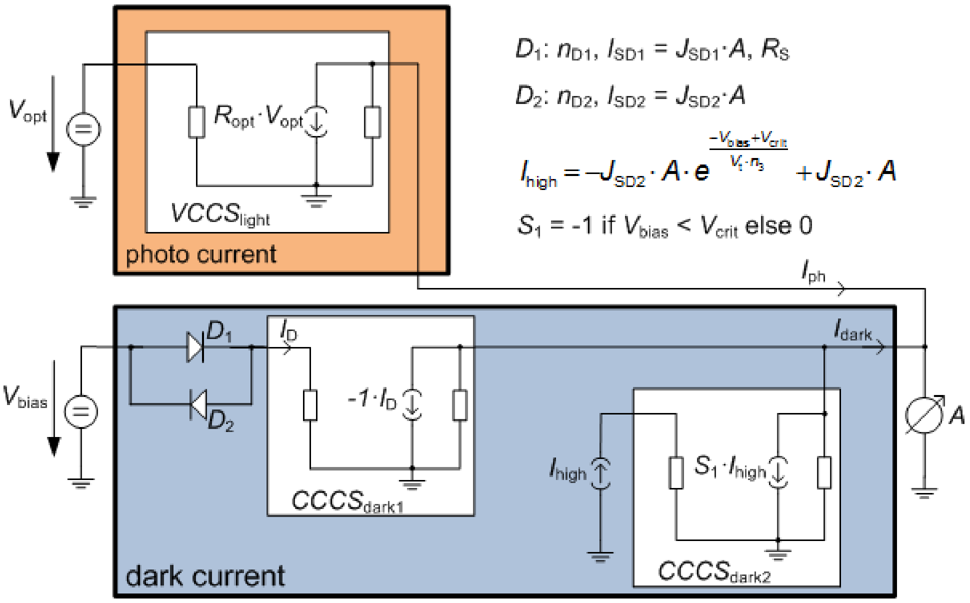

Figure 4.4: Equivalent *DC* circuit.

Due to the overlay of several physical aspects, the dark current of the examined *Ge* photodiodes is not completely described by a constant saturation current I_S at reverse bias: the dark current rather becomes non-linear and increases exponentially. This exponential increase already starts close to zero biasing. In the model derived in this work, inspired by [82], a diode D_2 is placed anti-parallel to the pn-junction diode D_1 to describe this behaviour. The device parameters used of the diode model are here the emission coefficient n_{D2} and the saturation current I_{SD2}, also scaling with the area A_j. The current of both diodes is summed up by a current controlled current source ($CCCS$), $CCCS_{dark1}$, which ensures that the voltage at the diodes really is V_{bias}.

At higher reverse bias, the slope of the exponential increase becomes even steeper for some of the examined photodiodes. A current source providing the current I_{high} is applied to represent this phenomenon. A $CCCS$ named $CCCS_{dark2}$ makes the current I_{high} start at the negative voltage V_{crit}.

These non-linear contributions are assumed to mainly represent tunneling effects [83].

In Fig. 4.5, a simulation is depicted for the dark current of a diode with diameter $D = 20\,\mu$m, indicating the impact of the single contributions mentioned above. The measurement used for curve fitting and parameter extraction is additionally shown. This model only provides a rough mapping of the diode behaviour that is based on the fitting of measurement curves. Nevertheless, this part of the model is a means for further interpretation of the complex processes inside the photodiode.

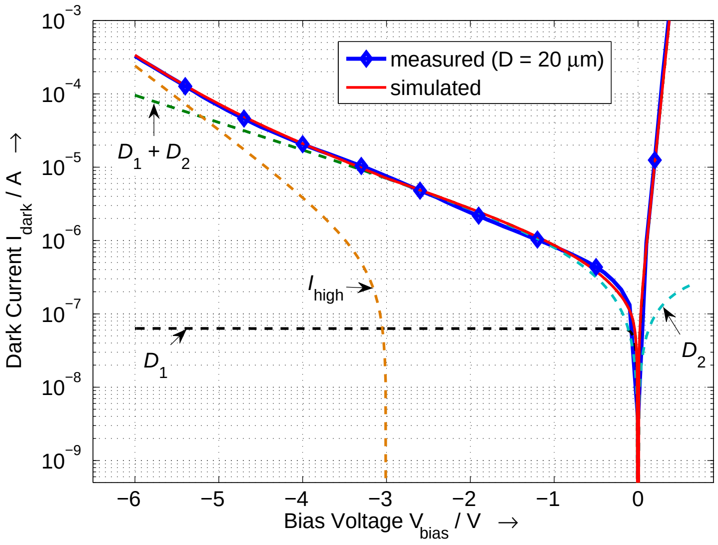

Figure 4.5: Simulation of *DC* dark model with the current contributions of the single blocks as defined in Fig. 4.4. The measurement of a photodiode with diameter $D = 20\,\mu$m is additionally shown (sample: *A*2045_2).

4.2.1.2 Photo Current

The conversion from light to current is modeled by a voltage controlled current source (*VCCS*), namely $VCCS_{\text{light}}$: the applied voltage V_{opt} stands for the optical power that is incident into the photodiode, thus the unit [V] has to be interpreted as [W] in this model. The transconductance of the *VCCS* represents the responsivity R_{opt}. Consequently, the unit [A/V] has to be read [A/W]. The responsivity is assumed to be constant over the whole reverse voltage range in the given model. As the responsivity varies with wavelength, several *VCCS*s can be placed in parallel to account for light sources of different wavelengths that simultaneously illuminate the photodiode, each with its own responsivity and thus transconductance value.

4.2.2 Small Signal Simulation Model

In the small signal model of the photodiode, the relationship of optical input power and electrical output power is regarded to be linear. This is assumed for Fig. 4.6 which shows the perspective view of the photodiode structure indicating the location of ohmic, inductive and capacitive parasitic elements.

One can see that not only the *pin* diode itself, but also the metallic contact structure contributes to parasitic effects. From this figure, a small signal equivalent ciruict of the photodi-

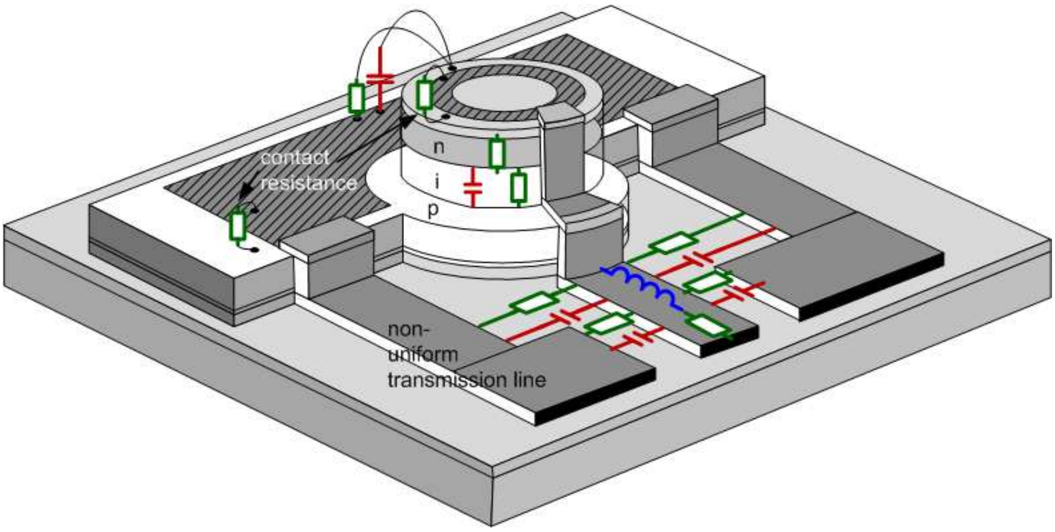

Figure 4.6: Photodiode with contact structure indicating parasitic elements used in the equivalent circuit (structure not to scale). Where the metal is hatched, it lies in an oxide window for contacting. Else, SiO_2 is placed below the metal for isolation.

ode as shown in Fig. 4.7 can be derived. The contact structure, the inner diode representing the photodiode without illumination and a low pass filter accounting for the transit time of the photogenerated carriers are dealt with separately in the following subsections.

4.2.2.1 Contact Structure

The contact structure in this simulation model consists of a transmission line in form of a coplanar waveguide (CPW), that is extracted from layout simulations, and several lumped elements. In reality, this structure is a network consisting of distributed resistances, con-

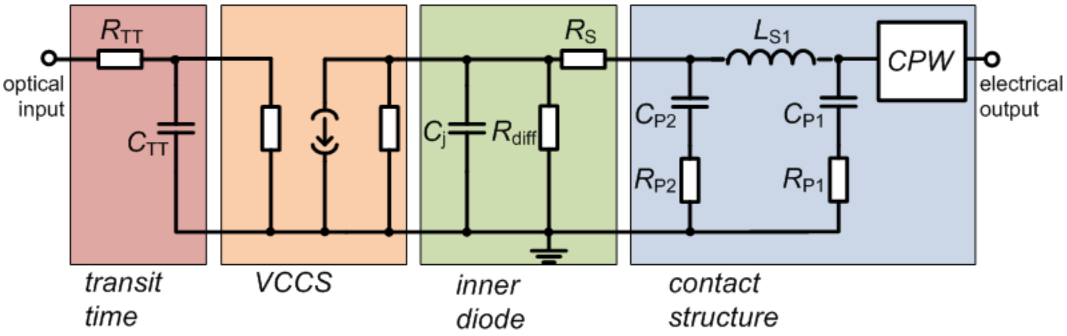

Figure 4.7: Small signal equivalent circuit of the overall photodiode with illumination. The single elements are: low pass filter representing the transit time, the $VCCS$ to represent the responsivity, the inner diode and the contact structure.

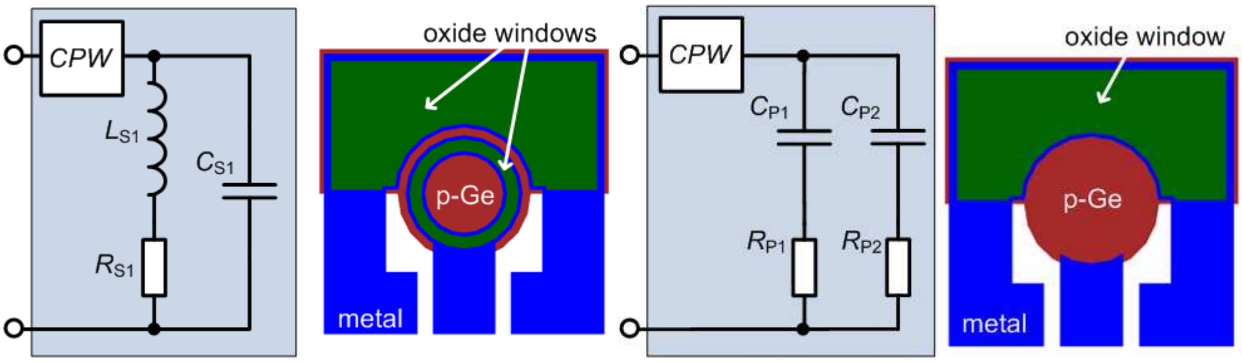

(a) Short circuit (*SC*). (b) Open circuit (*OC*).

Figure 4.8: Small signal equivalent circuit and layout [51], p. 85, of de-embedding structures - short circuit (a) and open circuit (b).

ductances, inductances and capacitances. As an approximation, the structure can be split into two parts - one that accounts for the ohmic-capacitive character of the contact structure, and one that accounts for the ohmic-inductive behaviour. The first one is called open circuit structure (*OC*) in the following, the second one short circuit structure (*SC*). Their equivalent circuits [51] are shown in Fig. 4.8.

The short circuit consists of an inductance L_{S1} in series with a resistance R_{S1}. This resistance mainly accounts for the resistance of the p^+-mesa, which is not removed in this layout. L_{S1} accounts for the inductive behaviour of the short circuited contact structure. In parallel to these two elements, a capacitance C_{S1} is situated, representing stray losses.

The open circuit is represented by two *RC* elements in parallel. The first *RC* element consists of the capacitance C_{P1} and the resistance R_{P1}. They account for the capacitive influence of the contact structure. According to [51], the second *RC*-element with C_{P2} and R_{P2} represents the overlap capacitance between the central signal contact and the p^+-mesa, separated by an oxide layer.

In addition to these elements as used in [51] and confirmed by circuit simulations, a *CPW* is placed in front of open and short circuit structure. Its scattering parameters have been extracted from layout simulations with the *EM* simulator Momentum from *ADS*.

The presence of the contact structure prevents from direct measurement of the diode parameters. This is why, in order to retrieve the values of the diode elements, de-embedding has to be done. Therefore, de-embedding structures representing the introduced *OC* and *SC* are processed on the same wafer as the photodiode. In Fig. 4.8, the layout of these structures [51] is depicted next to the corresponding equivalent circuit. By measuring the input impedance of these de-embedding structures, their element values can be extracted with the help of the

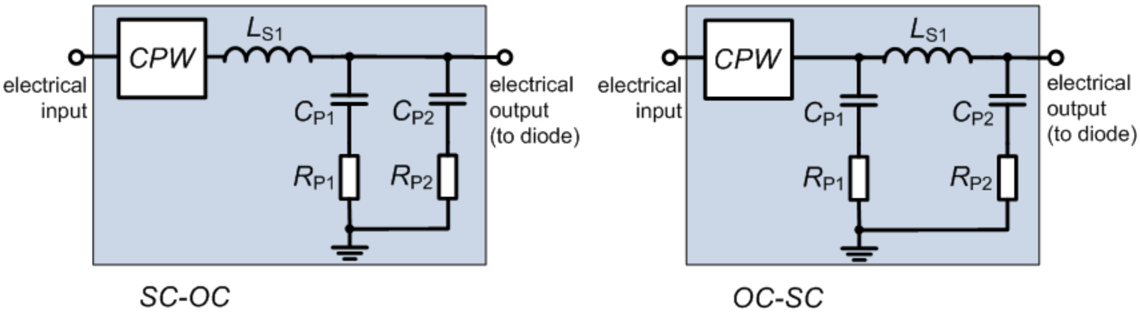

Figure 4.9: Equivalent small signal circuit for contact structure: transmission line with short-open (*SC*-*OC*) circuit (left) and open-short circuit (*OC*-*SC*) (right). R_{S1} is left out here because it has to be included into the series resistance of the inner diode.

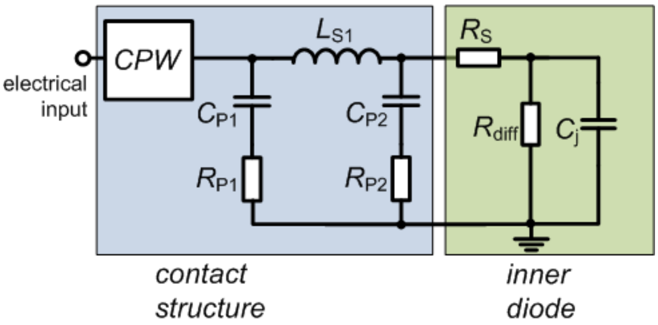

Figure 4.10: Equivalent small signal circuit of the overall photodiode without illumination. For the contact structure, the *OC*-*SC* configuration is depicted. R_{S1} is included in R_S.

optimisation option in *ADS*. For the equivalent circuit of the contact structure, *OC* and *SC* elements can be arranged in different ways, e.g. [84][51]. The two configurations of Fig. 4.9, *OC*-*SC* and *SC*-*OC*, are examined.

4.2.2.2 Inner Diode

An *RC*-subcircuit with a resistance in parallel is assumed to represent the inner diode. The *RC*-element consists of the series resistance R_S present in the neutral regions and the depletion capacitance C_j of the *SCR*. The parallel resistance R_{diff} is the differential resistance of the diode. To retrieve the parameter values of these components, the extracted values for *OC* and *SC* elements are inserted into the overall circuit of the photodiode without illumination as shown in Fig. 4.10. The element values of the inner diode can be retrieved from the measurement of the overall input impedance of the photodiode by again using the optimisation routine of *ADS*, now in the equivalent circuit of Fig. 4.10.

4.2.2.3 Illumination and Transit Time

In the overall equivalent circuit as shown in Fig. 4.7, which considers illumination of the photodiode and hence an optical input signal, the CW light source is represented by a voltage source, controlling a $VCCS$ that adjusts the responsivity of the photodiode. Thus, these elements have the same functionality as explained for the DC model. The input resistance of the $VCCS$ is set to $50\,\Omega$ to prevent back reflexions at the optical input of the circuit. The output resistance of the $VCCS$ is set to infinity. This adds an open to the electrical input impedance of the photodiode, and thus the input impedance remains unchanged by these additional elements. To represent the influence of the transit time on the overall bandwidth of the circuit, an additional RC lowpass filter has been included [85] in front of the $VCCS$.

The next sections deal with the key parameters of the photodiode and the question how to improve them.

4.3 Enhancement of Responsivity

There are several ways to increase the responsivity of the photodiode under consideration. First of all, the absorption outside the intrinsic region of the pin photodiode can be minimised. Furthermore, reflexion losses can be reduced, and measures to force the light to prolong its way through the intrinsic region can be chosen.

Three aspects implementing these approaches are examined theoretically in this work: the choice of material of specific layers, the thickness of some of these layers and, finally, the application of diffraction gratings. Technological aspects that have to be dealt with in this context are not covered here. The same holds true for investigations on waveguide photodiodes, though they are promising candidates for high $GBPs$ [86]. For the following considerations, the structure and dimensions of sample $A2045\_2$ as listed in Table 4.1 are taken as initial values.

4.3.1 Choice of Material

The penetration depth of light increases with increasing wavelength, thus an assumption can be made for the given photodiode stack: of all waves that reach the active layer with a wavelength below the critical wavelength of Ge, part of the photons is absorbed in the upper

n-Ge-layer. This reduces the responsivity of the device. As the n-Ge-layer is 83 nm thick, the minimum wavelength to reach the active area is 645 nm, according to the penetration depth of Ge shown in Fig. 2.12. For the attenuated waves that still get beyond the active layer, photons are additionally absorbed in the p-Ge-layer. The choice of material for the n- and p-layer can, therefore, improve the responsivity of the photodiode for different wavelength ranges. According to Fig. 2.12, the absorption in Si-layers is less than for Ge-layers in the whole considered wavelength range that starts at 600 nm. Furthermore, for wavelengths above the Si cut-off wavelength 1100 nm, there is no absorption at all in the Si layers. Hence one means to improve responsivity is to make the n- and p-layer of Si instead of Ge. One should keep in mind, however, that, with the usage of another material, the effective thickness of the single layers and thus the overall reflexion behaviour changes.

Fig. 4.11 shows the external quantum efficiency for the stack of sample $A2045\_2$ in the original configuration, with p- and n-layer made of Ge, as well as for a configuration with n-Si/p-Ge and for one with n-Si/p-Si. As expected, the EQE strongly increases at shorter wavelengths if n-Si is used. Also at longer wavelengths the EQE becomes higher than for the original configuration, with 23.30% increase at 1310 nm and 16.13% increase at 1550 nm. But a further improvement with both, n-Si and p-Si, is not really given: the two curves representing the EQE lie very close to each other, and one provides alternatingly higher EQE than the other.

The small oscillations of these curves between 700 nm and 1400 nm are due to the wavelength dependent reflexions at the Si/Ge interfaces. At shorter wavelengths, the two curves are identical, as the p-layer is out of reach for these waves and has, therefore, no influence on the absorption behaviour.

4.3.2 Mirrors and Antireflexion Coatings

In the photodiode stack, waves are reflected back at the interface between layers with different refractive index. Depending on the thickness of the layer, the interference of the waves reflected at the upper and lower interface of the layer is constructive or destructive. Thus, by optimising the thickness of the layers in the photodiode stack, dielectric mirrors or so called Bragg reflectors can be created. According to Bragg's Law, the total path length difference of the two rays in Fig. 4.12a must be $l \cdot \lambda$ for constructive interference, where $\lambda = \frac{\lambda_0}{n}$ is the wavelength in the material with refractive index n and $l \in \mathbb{Z}$. For destructive interference, the path length difference must be an odd multiple of $\frac{\lambda}{2}$. Table 4.2 summarises the relevant

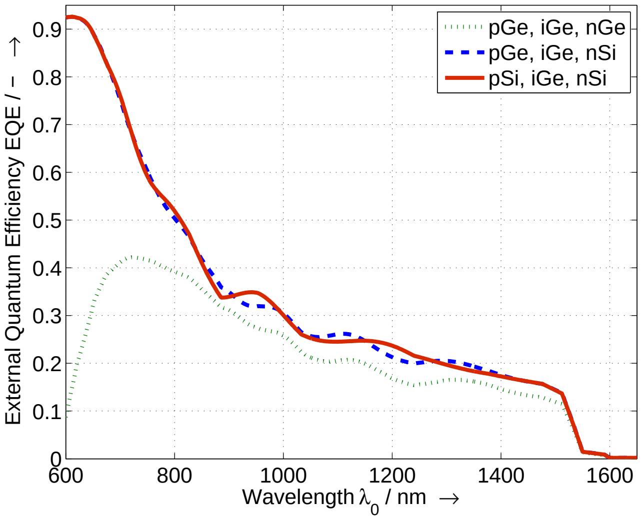

Figure 4.11: External quantum efficiency EQE versus wavelength λ_0 for three different configurations of p- and n-layer: Both made of Ge, n-Si/p-Ge and both made of Si.

Table 4.2: Thickness of different materials equivalent to $\frac{1}{4}\frac{\lambda_0}{n}$ and $\frac{1}{2}\frac{\lambda_0}{n}$. The refractive index n of Ge is interpolated based on the data of [28].

	SiO_2	Si	Ge
$\frac{1}{4}\frac{\lambda_0}{n}$ / nm	267.2	111.5	91.85
$\frac{1}{2}\frac{\lambda_0}{n}$ / nm	534.5	223	183.70
n @ $\lambda_0 = 1550\,\text{nm}$ / -	1.45	3.476	4.219

thicknesses of the materials SiO_2, Si and Ge at $\lambda_0 = 1550\,\text{nm}$.

The thickness of the layer under consideration contributes to the overall path length, as does any phase shift occuring at the interface between layers and also the incident angle into the layers. Fig. 4.12b indicates these phase shifts of the given photodiode stack when a SOI substrate is used. The existence of the phase shift of 0 or π, depending on inner or outer reflexion, has been stated in the presentation of Fresnel's reflexion coefficients. TE polarisation and vertical light incidence are considered in the following. Fig. 4.12c reveals the reflectivity at the interfaces of the photodiode stack. It is obvious that reflectivity is strongest at the SiO_2-Si interface, as the refractive index difference is largest for these two layers.

If a mirror is placed very close below the absorption layer, light that has not yet been absorbed can be reflected back and pass the active region a second time. Depending on the thickness of the layer of the active region and on the penetration depth of the light, a doubling of the

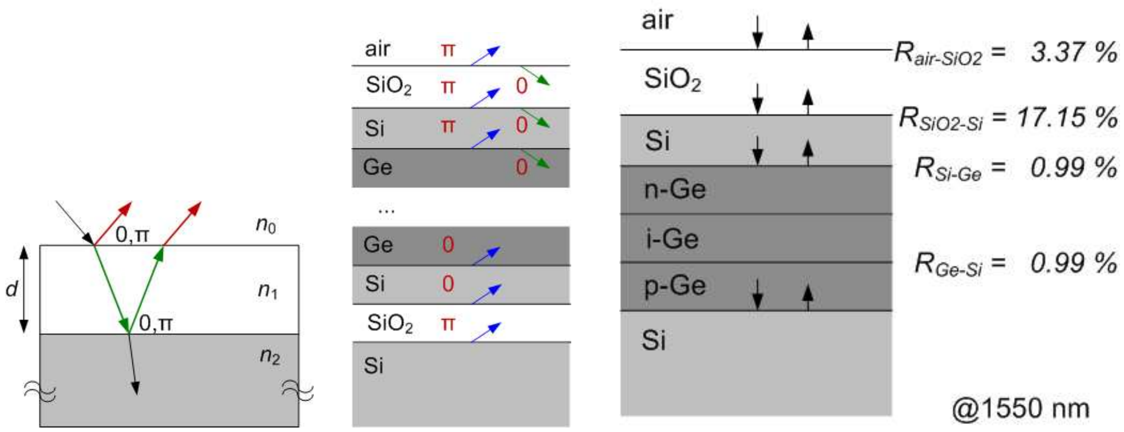

(a) Reflexion at interface due to one layer. Oblique light incidence is shown only to highlight the ray tracing.

(b) Phase shift of reflected electric field in photodiode stack.

(c) Reflectivity at interfaces in the considered layer stack.

Figure 4.12: Reflexion at interfaces of one layer and in the considered layer stack (b) with according reflectivity values at $\lambda_0 = 1550\,\mathrm{nm}$ (c).

quantum efficiency is possible. With an additional mirror above the absorption region, the light on its way up can be reflected back into the absorption region once again. This further increases the external quantum efficiency EQE.

Depending on the refractive index difference of the layers involved, more than only one mirror layer might be necessary to achieve a complete reflexion of the waves. One material combination for a mirror in the given stack is p-doped $Si_{1-x}Ge_x$-Si, replacing the p-Ge layer. Several piles of $Si_{1-x}Ge_x$-Si mirror layers below the pin-layer stack are necessary to reach high reflectivity of the mirror. For a reflecitivy of 100%, almost 30 periods are needed, as becomes obvious from Fig. 4.13. The Si-SiO_2 material system, on the contrary, has a large refractive index difference of 2.05 at $\lambda_0 = 1550\,\mathrm{nm}$, and it is sufficient to regard only four Si-SiO_2 sub-stacks for 100% reflectance. Therefore, the case of the Si-SiO_2 material system is considered from now on. For a bottom mirror consisting of one Si-SiO_2 period, a SOI substrate can be used. If no additional growing steps are added to gain more periods, the maximum reflectivity that can be realised is about 60%. The same holds true if one Si-SiO_2 period is placed on top of the stack.

Starting from the original stack on Si bulk as shown again in Fig. 4.14a, different scenarii are investigated. They are depicted in Fig. 4.15. For the given device structure, one Si-SiO_2 transition is already available in form of the Si cap on top of the n^+-doped Ge-layer and the top cladding of SiO_2 serving as passivation layer. This can be used as mirror or ARC

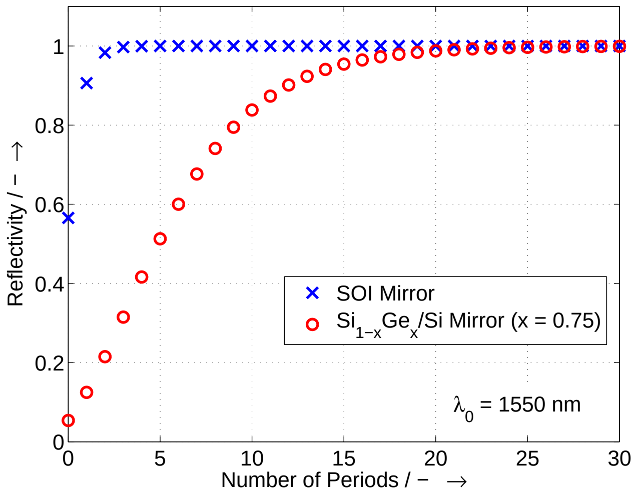

Figure 4.13: Reflectivity of $Si_{1-\mathrm{x}}Ge_{\mathrm{x}}$ and SOI mirror versus number of sub-stacks (periods).

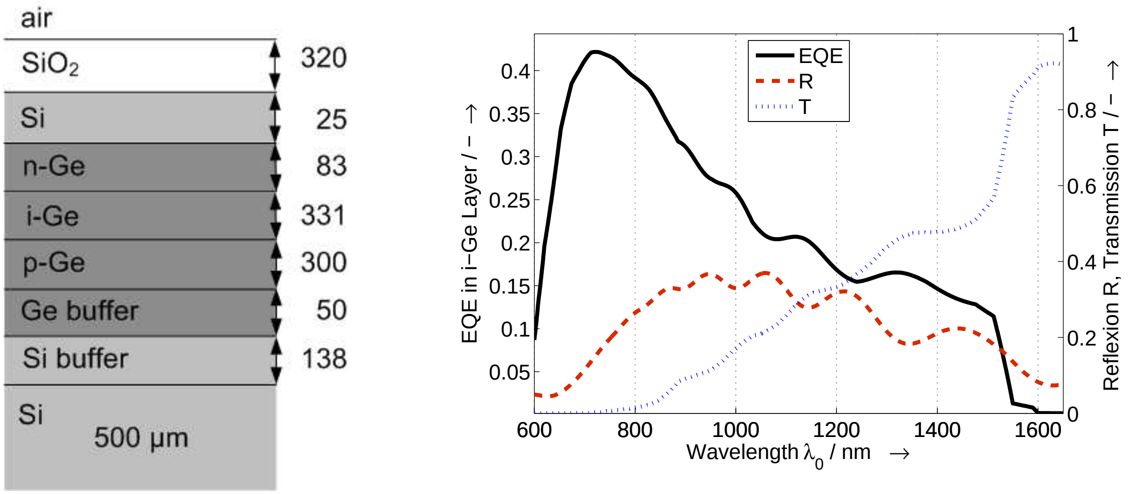

(a) Original $A2045\_2$ photodiode stack. Thicknesses in nm.

(b) External quantum efficiency EQE, reflexion R and transmission T versus wavelength λ_0.

Figure 4.14: Original stack $A2045\_2$ as starting point for the investigations (a) and according external quantum efficiency, reflexion and transmission (b).

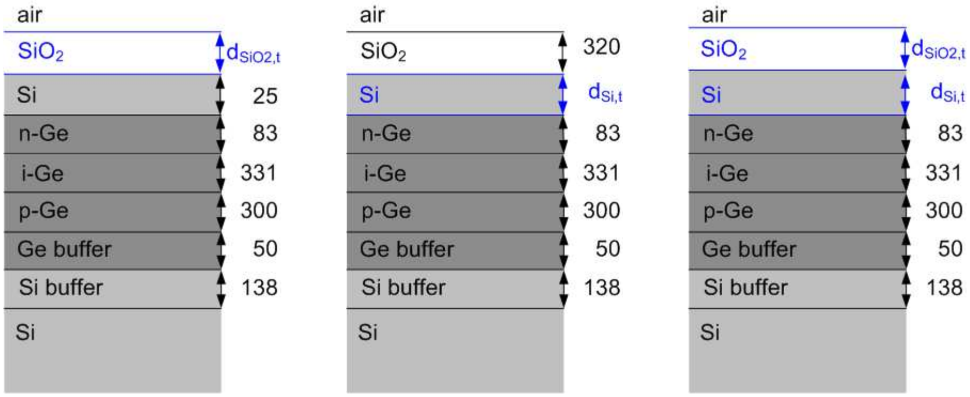

(a) Top SiO_2 layer. (b) Top Si layer. (c) Top SiO_2-Si layers.

Figure 4.15: Modifications of top SiO_2 and Si layers of photodiode stack on Si bulk substrate (thicknesses in nm): the tickness of the SiO_2 passivation layer $d_{\mathrm{SiO2,t}}$ is swept (a). The thickness of the Si cap layer $d_{\mathrm{Si,t}}$ is swept (b). Both, $d_{\mathrm{SiO2,t}}$ and $d_{\mathrm{Si,t}}$, are simultaneously swept (c).

above the photodiode. First of all, the impact of the SiO_2 passivation layer thickness $d_{\mathrm{SiO2,t}}$ is studied (Fig. 4.15a). Its influence on the external quantum efficiency EQE is shown in Fig. 4.16. This layer is the one that can be adapted most easily, as it is the last one to be deposited. At $\lambda_0 = 1550\,\mathrm{nm}$, the external quantum efficiency is $EQE = 0.0131$ for 300 nm and $EQE = 0.0093$ for 500 nm thickness of the SiO_2. The minimum thickness with maximum $EQE = 0.0133$ is $d_{\mathrm{SiO2,t}} = 270\,\mathrm{nm}$. This is approximately $\lambda_0/4n$ in the case of SiO_2.

Then, the thickness of the Si top layer $d_{\mathrm{Si,t}}$ is swept while the other layers keep the dimensions of the original stack (Fig. 4.15b). The minimum thickness for maximum EQE is here $d_{\mathrm{Si,t}} = 140\,\mathrm{nm}$, which is not exactly $\lambda_0/4n$. Here is one explanation for the different optimum thicknesses of SiO_2 and Si: most of the light is reflected at the SiO_2-Si interface. Thus, for the interference effects at the SiO_2-Si/SiO_2-air interfaces and hence the SiO_2-thickness, the influence of the lower layers are neglectable. Below the Si layer, two Si-Ge transistions occur, both with the same low reflectivity. In this case, the lower layers do count for the overal reflexion at the SiO_2-Si interface, and the interference effect is determined by the thicknesses of Si and Ge together. A comparison of the influence on the responsivity for swept SiO_2 thickness and Si thickness is given in Fig. 4.17. As the other layers are set to the values of the original stack and are consequently not optimised, the maxima shown for the responsivity do not necessarily coincide with the global maximum.

In a next step, both, the thickness of the SiO_2 passivation and the Si cap layer, are swept simultaneously (Fig. 4.15c). The minimum best values for SiO_2 and Si are $d_{\mathrm{SiO2,t}} = 270\,\mathrm{nm}$ and $d_{\mathrm{Si,t}} = 140\,\mathrm{nm}$, respectively, which could be expected from the results aforehead obtained.

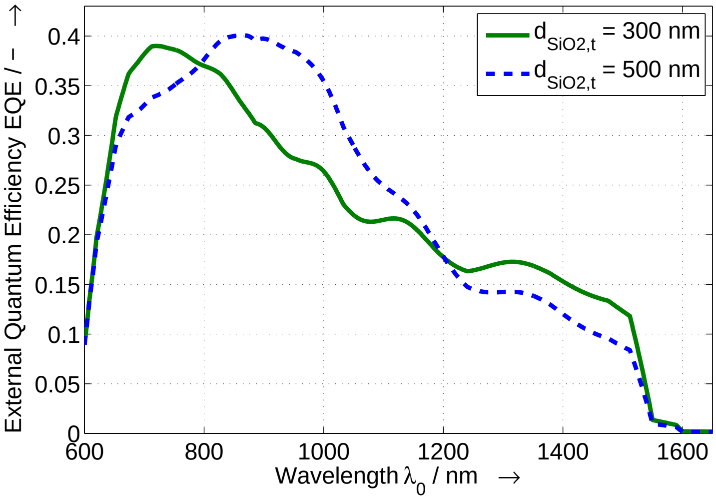

Figure 4.16: External quantum efficiency EQE versus wavelength λ_0 for two different thicknesses of the SiO_2 passivation layer in the photodiode stack: $d_{\mathrm{SiO2,t}} = 300\,\mathrm{nm}$ and $d_{\mathrm{SiO2,t}} = 500\,\mathrm{nm}$.

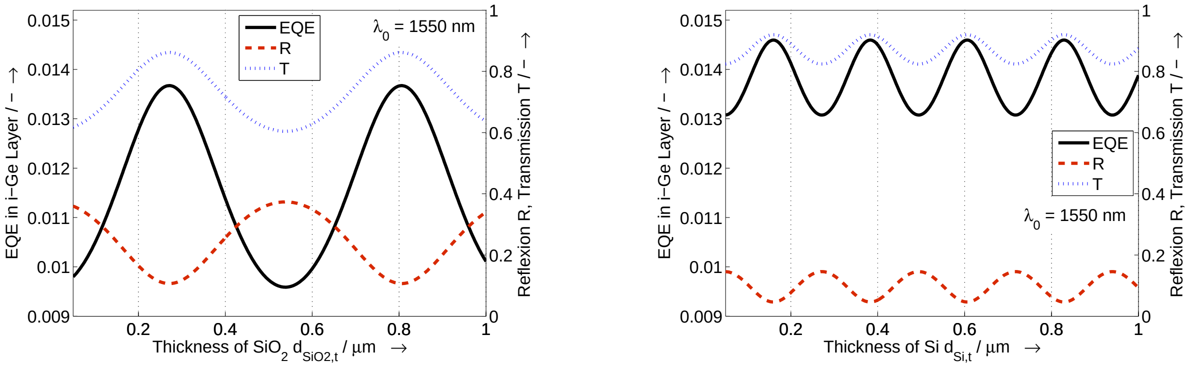

(a) EQE, R and T versus the thickness of the SiO_2 passivation layer.

(b) EQE, R and T versus the thickness of the Si cap layer.

Figure 4.17: External quantum efficiency EQE, reflexion R and transmission T versus the thickness of the SiO_2 passivation layer (left) and the Si cap layer (right) in the photodiode.

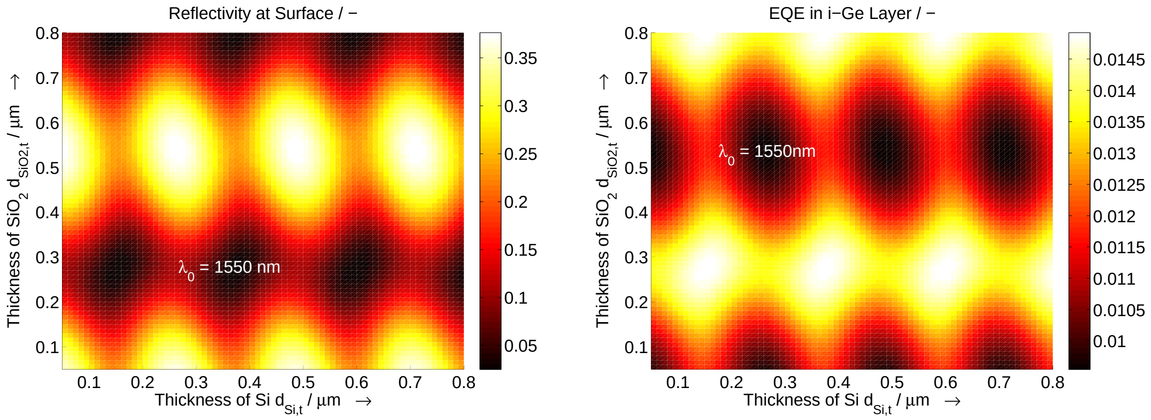

(a) R versus $d_{\mathrm{Si,t}}$ and $d_{\mathrm{SiO2,t}}$.

(b) EQE versus $d_{\mathrm{Si,t}}$ and $d_{\mathrm{SiO2,t}}$.

Figure 4.18: Reflectivity R and external quantum efficiency EQE versus thickness of SiO_2 passivation, $d_{\mathrm{SiO2,t}}$, and Si cap-layer, $d_{\mathrm{Si,t}}$. The incident angle is $\theta_{\mathrm{in}} = 0°$, and the wavelength is $\lambda_0 = 1550\,\mathrm{nm}$.

Fig. 4.18 shows the reflectivity R at the surface of the stack and the external quantum efficiency EQE in the intrinsic Ge layer versus both thicknesses. It can clearly be seen that the maximum EQE coincides with the minimum R. The maximum EQE to be achieved at $\lambda_0 = 1550\,\mathrm{nm}$ is 1.49%.

Below the photodiode, the mirror can be realised as already mentioned, namely by a SOI substrate with optimised thicknesses of the Si-layer and the buried oxide (BOX). The cross section of the layer stack is shown in Fig. 4.19a. The corresponding values for the thicknesses of the relevant layers are also listed. The different additional modifications are depicted in Fig. 4.19b - Fig. 4.19d. The resulting reflexion R and external quantum efficiency EQE are plotted for the photodiode stack with optimised bottom mirror in Fig. 4.20. It is obvious that minimum R and maximum EQE do not coincide, which is due to the other layers in the stack that are not optimised in terms of constructive/destructive interference.

For the combination of simultaneously optimised top and bottom mirror as suggested in Fig. 4.19b, the EQE at 1550 nm becomes 4.56%.

In a next step, the thickness of the Ge layers is optimised: in total, the thickness of these layers must be a multiple of $\frac{\lambda}{2}$. The thickness of the iGe-layer is not changed as it is optimised in terms of a maximum 3 dB frequency f_{3dB}. The nGe-layer should not become thicker due the absorption losses involved, hence it is the pGe-layer of which the thickness is swept. The thickness of the SOI top and bottom mirrors are chosen for this sweep to achieve maximum reflexion back into the Ge layer stack. EQE can be increased to 4.76% by this measure. The overall thickness of the Ge layers for this result is 554 nm. This corresponds to $3 \cdot \frac{\lambda}{2}$ in

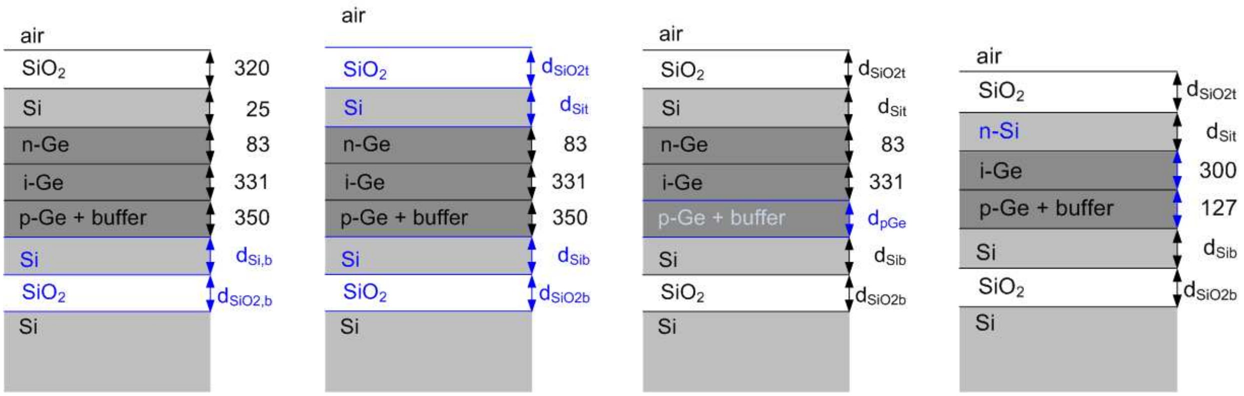

(a) Bottom Si-SiO_2 layers.

(b) Bottom and top Si-SiO_2 layers.

(c) Bottom and top Si-SiO_2 layers and Ge layers.

(d) Bottom and top Si-SiO_2 layers, Ge layers and nSi layer.

Figure 4.19: Modifications of layers in photodiode stack on a *SOI* substrate (thicknesses in nm): the bottom *SOI* mirror is optimised (a). (Both, top and bottom *SOI* mirrors, are simultaneously optimised (b). The thickness of the p-Ge layer is swept to optimise the thickness of the overall Ge layer stack (c). Dimensions of top and bottom mirrors are set for maximum reflexion into the Ge layers. Optimised top and bottom mirrors are used together with optimised overall Ge layer thickness and n-Si instead of n-Ge (d).

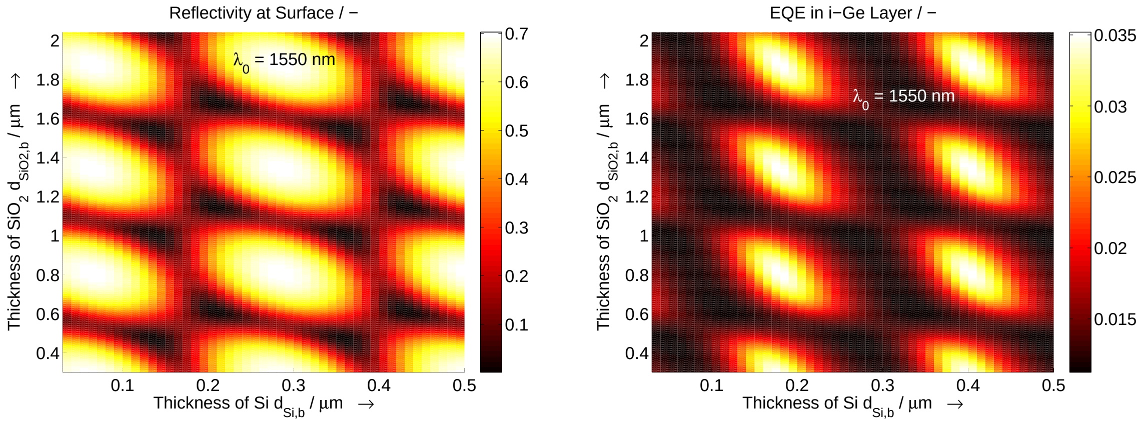

(a) R versus $d_{\mathrm{Si,b}}$ and $d_{\mathrm{SiO2,b}}$.

(b) EQE versus $d_{\mathrm{Si,b}}$ and $d_{\mathrm{SiO2,b}}$.

Figure 4.20: Reflectivity R and external quantum efficiency EQE versus thickness of Si bottom layer, $d_{\mathrm{Si,b}}$, and SiO_2 BOX, $d_{\mathrm{SiO2,b}}$. The incident angle is $\theta_{\mathrm{in}} = 0°$, and the wavelength is $\lambda_0 = 1550\,\mathrm{nm}$.

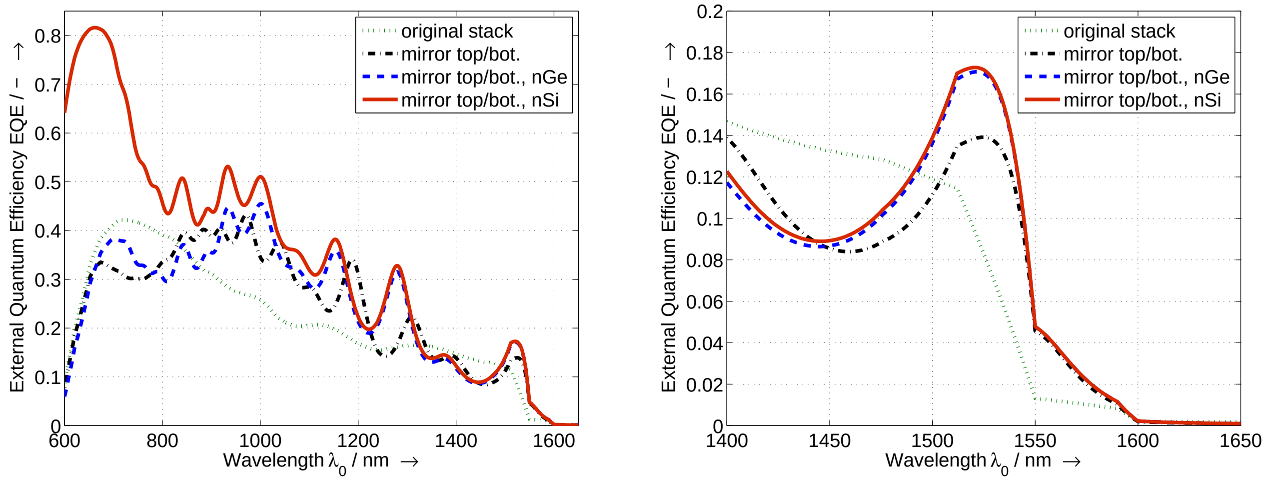

(a) EQE versus λ_0.

(b) EQE versus λ_0 - zoom around 1550 nm.

Figure 4.21: External quantum efficiency EQE versus wavelength λ_0 of photodiode stack with different optimised layer dimensions: optimised top and bottom *SOI* mirror; additionally optimised *Ge* layer thickness (with *nGe*); and, for this latter case, the scenario with *nSi* instead of *nGe*. The wavelength dependent behaviour of the original structure is also plotted for comparison (a). A zoom around $\lambda_0 = 1550\,\text{nm}$ is also displayed (b).

Ge.

Finally, as indicated in Fig. 4.19d, the mirror layer thicknesses are kept at their optimum values, the overall thickness of the *i-Ge* and *p-Ge* layers is set to 554 nm as found in the last paragraph, and the *n-Ge* is replaced by *n-Si*. This layer simultaneously serves as the upper *Si* mirror layer. EQE at $\lambda_0 = 1550, \text{nm}$ results to be 4.77%.

For the modifications of Fig. 4.19b - 4.19d, the EQE is plotted versus the wavelength λ_0 for comparison in Fig. 4.21. The EQE of the original structure is also added to this figure.

Table 4.3 summarises the results of the modifications described above. It can be seen that the use of a bottom mirror is more efficient at the desired wavelength than the application of an *ARC* on top of the *Ge* stack. A simultaneous optimisation of top and bottom mirror can more than triple the external quantum efficiency compared to the original stack. Best result is obtained with optimising additionally the *Ge* thickness. Replacing the *n-Ge* by *n-Si* and adapting the *Ge* layer thicknesses appropriately still slightly improves the result. For these two cases, it can also be seen that the thicknesses of the mirror layers correspond to the theoretically expected ones: $l \cdot \lambda/2$ for $d_{\text{Si,t}}$, $d_{\text{SiO2,t}}$ and $d_{\text{Si,b}}$, and $(2l-1)\cdot\lambda/4$ for $d_{\text{SiO2,b}}$. These values lead to constructive interference and thus maximum reflexion back into

Table 4.3: Configurations of the photodiode stack to increase responsivity - layer thicknesses, material and resulting EQE.

	original stack	SiO_2 top	Si top	SiO_2-Si top	SiO_2-Si bottom	SiO_2-Si top/bottom	d_{pGe}	n_{Si}
EQE / -	0.0132	0.0137	0.0146	0.0149	0.0352	0.0456	0.0476	0.0477
x EQE_{org} / -	1.0	1.04	1.11	1.13	2.67	3.45	3.61	3.61
d_{SiO2t} / nm	320	270	320	270	320	550	540	540
d_{Sit} / nm	25	25	160	140	25	190	220	220
d_{Sib} / nm	-	-	-	-	400	210	220	220
d_{SiO2b} / nm	-	-	-	-	800	1880	1870	1870
$d_{\text{Ge,all}}$ / nm	764	764	764	764	764	764	554	554
$d_{\text{Ge,p}}$ / nm	350	350	350	350	350	350	140	223
$d_{\text{Ge,n}}$ / nm	83	83	83	83	83	83	83	-

the Ge layer from both, bottom and top mirror. The reflexion losses at the surface of the photodiode stack are maximised then, too. But this is compensated by the fact that the light can pass the absorption region several times.

The optimum design is strongly wavelength dependent: for one thing, the thickness of layers for constructive/destructive interference is determined by wavelength and refractive index. Secondly, the penetration depth of light is defined by the wavelength for a given material. For $\lambda_0 = 1550\,\text{nm}$, the penetration depth is $21\,\mu\text{m}$, which means that several transitions through the absorption region are possible. For smaller wavelengths, it is more useful to reduce reflexion losses at the surface (and replace n-Ge by n-Si), as the second mirror below the absorption region might not even be reached by the waves. Due to the strong dependence on the wavelength, these structures are very resonant ones, and small changes in e.g. the layer thicknesses or the refractive index cause an according shift of the wavelength for which maximum EQE is found.

4.3.3 Diffraction Gratings

A grating structure placed on top or inside the photodiode stack can help to increase the absorption in the active layer in several ways: the grating can increase the optical path length of the light through the active region if it is diffracted under large diffraction angles. This is depicted in Fig. 4.22a. In Fig. 4.22b, the resulting EQE due to the increased path length is plotted for a layer thickness of $d_{\text{i}} = 330\,\text{nm}$, excluding any reflexions. A comparison is made based on $RCWA$ simulations where the absorption in a Ge layer with this thickness is recorded for swept incident angle θ_{in}. Up to $\theta_{\text{in}} = 80°$, the agreement of both curves is quite good.

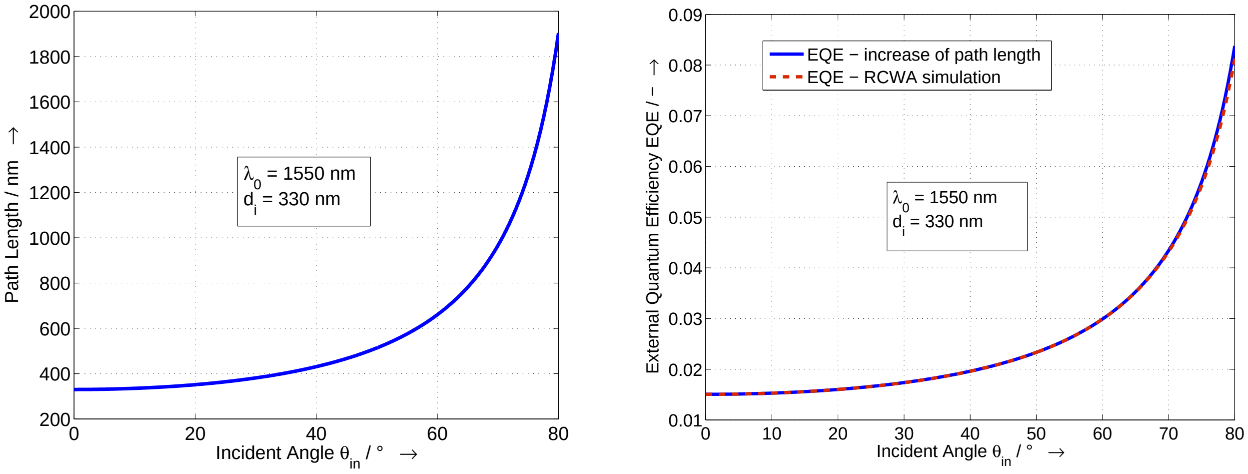

(a) Increase of optical path length.

(b) Increase of EQE.

Figure 4.22: Increased path length versus incident angle θ_{in} (a) and EQE versus incident angle θ_{in} simulated with $RCWA$ (b).

The increase of the optical path length strongly depends on the material system, as the incident angle into each layer is determined by Snell's Law. If the refractive index is increasing in the direction of light propagation inside the stack, the angle decreases simultaneously and the optical path length is reduced again. This is the case for the given photodiode stack.

An increase of the optical path length through the active region of the photodiode can enhance the absorption in this region and thus the responsivity of the photodiode. There is, however, a trade off between the gain due to the increased path length and the coupling and reflexion losses of the grating which has to be kept in mind. Furthermore, there is usually more than only one diffraction order involved, and each order has a different diffraction angle and thus a different increase in the path length. The transmitted power is divided into all diffraction orders, hence the contribution of each has to be calculated separately or simulated with appropriate tools.

4.3.3.1 SiO_2 Grating in Littrow Mounting

Based on the MM, a thick grating in SiO_2 is simulated. The duty cycle dc and the etch depth d_{e} as shown in Fig. 4.24 are swept. The grating period g is set to a fixed value. The choice of this value is not decisive for a high coupling efficiency as with d_{e} and dc all values for a coupling efficiency between 0 and 1 can be theoretically achieved. The period decides, however, about the incident angle, the Littrow angle $\theta_{\mathrm{in,L}}$. The larger the period, the smaller the incident angle. Furthermore, the minimum etch depth d_{e} that is necessary for maximum

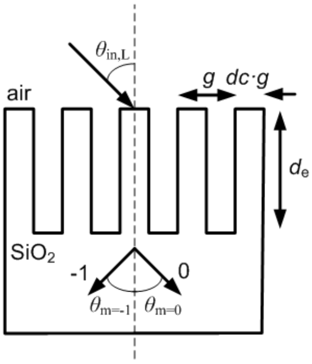

Figure 4.23: Simulated grating structure.

coupling efficiency η_{coupl} is influenced by the period. Therefore, the choice of the period depends on the application, e.g. if a small incident angle is more crucial than a small etch depth. According to Eq. 3.50, the condition $775\,\mathrm{nm} < g < 1600\,\mathrm{nm}$ must be fulfilled to ensure that only two diffracted modes are excited for a wavelength of $\lambda_0 = 1550\,\mathrm{nm}$. Hence for the design, g is arbitrarily set to be $g = 1000\,\mathrm{nm}$. The corresponding incident angle for Littrow mounting is $\theta_{\mathrm{in,L}} = 50.81°$. According to the *MM*, the minimum etch depth for a coupling efficiency of 100% into diffraction order $m = -1$ results to be $d_\mathrm{e} = 2.024\,\mu\mathrm{m}$, with a duty cycle of $dc = 0.374$ and a wavelength of $\lambda_0 = 1550\,\mathrm{nm}$.

The simulation results of the *MM* are compared in Fig. 4.24 with simulation results using the *RCWA*. The *RCWA* simulations show an overall maximum coupling efficiency of 95.93% including reflexion losses. The according minimum etch depth is $d_\mathrm{e} = 2.3\,\mu\mathrm{m}$ and the duty cycle is $dc = 0.55$. For the *MM*, the coupling efficiency η_{coupl} is still 100% for this combination of parameters due to the neglected reflexion losses. The effective refractive indices of the waves diffracted into order $m = 0$ and $m = -1$ are then $n_{\mathrm{eff0}} = 0.835$ and $n_{\mathrm{eff1}} = 1.171$, respectively.

The diffraction angle of order $m = -1$ is $\theta_\mathrm{m} = -32.31°$. If the grating is placed on top of the photodiode stack, this angle is reduced due to refraction into the *Si* and *Ge* layer to $\theta_\mathrm{m} = -10.44°$. Thus, the increase of the path length is also reduced: the increase is then 1.7%. Up to an incident angle of $\theta_{\mathrm{in}} = 70°$, the increase of absorption depends linearly on the increase of the path length. This is why the absorption in all three *Ge* layers can also only increase by 1.7%. As reflexion losses at the surface of the photodiode stack are larger with grating than without, the overall absorption in the whole *Ge* stack is smaller with grating ($\approx 2.9\%$) than without ($\approx 3.0\%$), according to *RCWA* simulations.

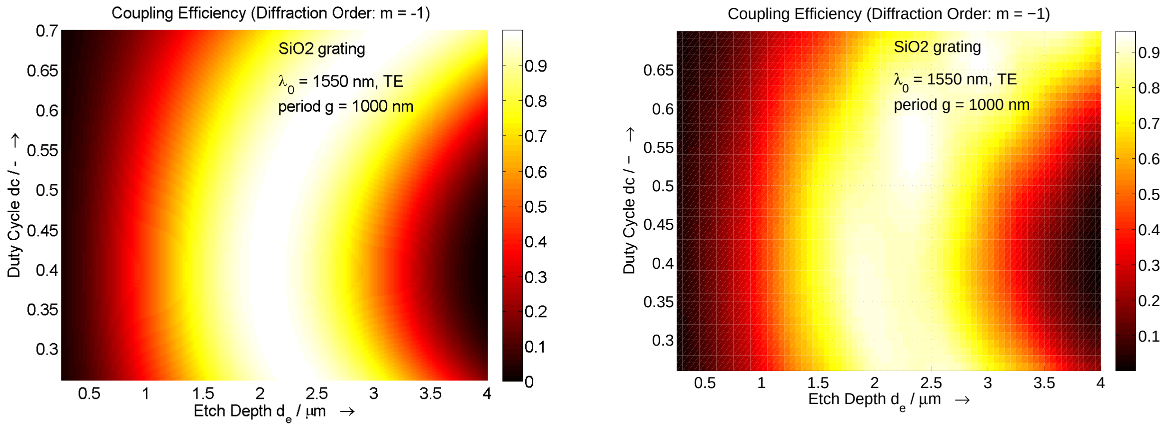

(a) Modal Method.

(b) *RCWA*.

Figure 4.24: Coupling efficiency of grating in SiO_2 versus etch depth d_e and duty cycle dc. Simulation based on the MM and on the $RCWA$. The grating period $g = 1000\,\mathrm{nm}$.

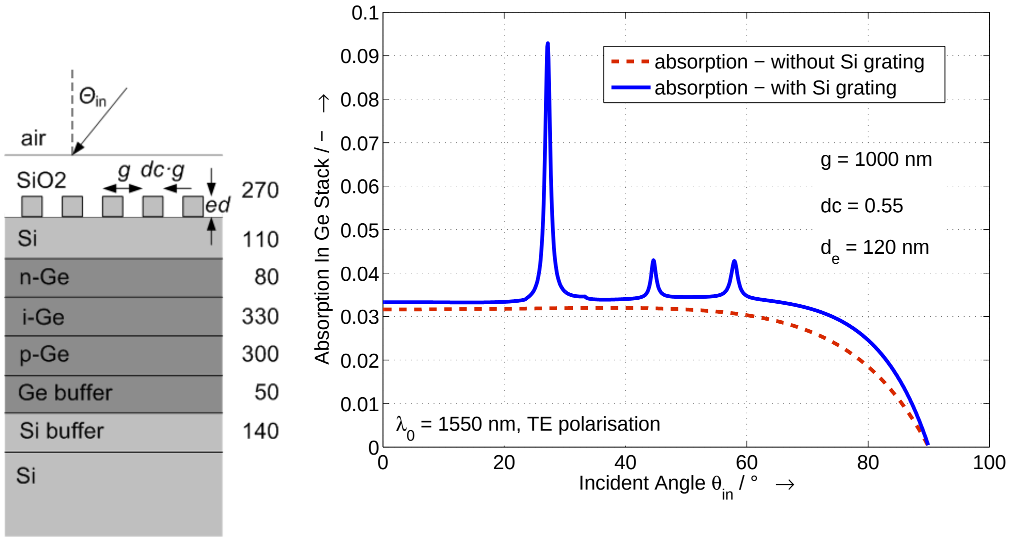

(a) Grating Structure.

(b) Overall absorption versus incident angle.

Figure 4.25: Overall absorption in photodiode stack with Si grating on top versus θ_{in} for $\lambda_0 = 1550\,\mathrm{nm}$. The simulation is based on the $RCWA$.

4.3.3.2 Si Grating with Oblique Light Incidence

The use of grating structures in the top layer of the photodiode stack does not provide higher increase in efficiency than the implementation of mirror layers. Furthermore, mirror layers can be realised by optimisation of the available layer thicknesses and by using *SOI* substrates. Grating structures, on the contrary, have to be realised by additional etch steps. Therefore, the benefit of these structures must justify the effort. The grating can also be placed more closely to the *Ge* stack, by structuring the *Si* on top of the *Ge*. Fig. 4.25 shows *RCWA* based simulations of such a grating. The overall absorption is tripled for this grating compared to simulations without grating. This is a very resonant structure and only works well for an incident angle of $\theta_{\mathrm{in}} = 27.2°$.

All gratings presented here are optimised for *TE* polarisation. Polarisation insensitive structures can be realised by circular concentric arrangement of the grating stripes.

4.4 Increase of Bandwidth

As indicated in the introductory part of this work, different aspects have an impact on the bandwidth of the photodiodes. In the following sections, approaches on the design level are presented, which are the essential geometric structure of the photodiode itself and the influence of electrical circuits in a possible integrated solution. Further measures to increase the bandwidth refer to technological aspects where e.g. the contact resistance of the device is reduced. Such measures have been successfully taken by the *IHT* [9].

4.4.1 Optimisation of the Diode Design

Neglecting the contribution of the diffusion time constant, the 3 dB frequency $f_{3\mathrm{dB}}$ of the photodiode structure is calculated as follows [86]:

$$f_{3\mathrm{dB}} = \frac{1}{\sqrt{\frac{1}{f_{\mathrm{RC}}^2} + \frac{1}{f_{\mathrm{TT}}^2}}}, \tag{4.1}$$

with f_{RC} and f_{TT} as defined in Section 3.1.3. In Fig. 4.26, the *RC* frequency f_{RC}, the transit frequency f_{TT} and the resulting 3 dB frequency $f_{3\mathrm{dB}}$ are plotted versus the thickness of the intrinsic region d_{i}. The diameter D of the upper photodiode mesa is used as a sweep parameter. The resistance R is assumed to be the real system impedance of 50 Ω, neglecting the diameter dependent series resistance of the photodiode. It can be seen that there is

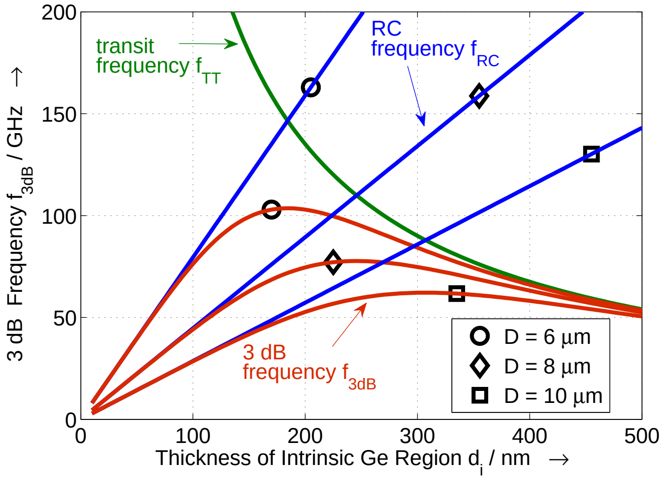

Figure 4.26: 3 dB frequency $f_{3\mathrm{dB}}$ versus the thickness d_i of the intrinsic *Ge* region [87][88]. Also depicted are the *RC* frequency f_RC, with $R = 50\,\Omega$, and the transit frequency f_TT. The sweep parameter is the diameter D of the photodiode.

always an optimum combination of the geometric parameters where $f_{3\mathrm{dB}}$ has a maximum. According to the graphical representation, the optimal thickness of the intrinsic region for a maximum 3 dB frequency is the one where the drift frequency is equal to the *RC* frequency.

4.4.2 Exploitation of Integration

In an integrated solution where the electric circuit is directly connected with the photodiode on chip via short transmission lines, a matching to 50 Ω is not necessary anymore. The 3 dB-frequency is increased significantly then, as only the resistance of the photodiode contributes to the *RC*-frequency. Fig. 4.27 shows the theoretical 3 dB-frequency versus the resistance R. The diameter D is swept here. The thickness of the intrinsic region d_i is once kept fixed (Fig. 4.27a), once it is set to the optimum thickness for the corresponding diameter D (Fig. 4.27b). These figures show that a low resistance value is crucial especially for devices with large diameter.

Thus with integration, one more degree of freedom is gained in the design process. The interconnexion between photodiode and electrical complement can be additionally used to manipulate the signal, e.g. by forming a resonant structure for inductive peaking by appropriately dimensioned transmission lines.

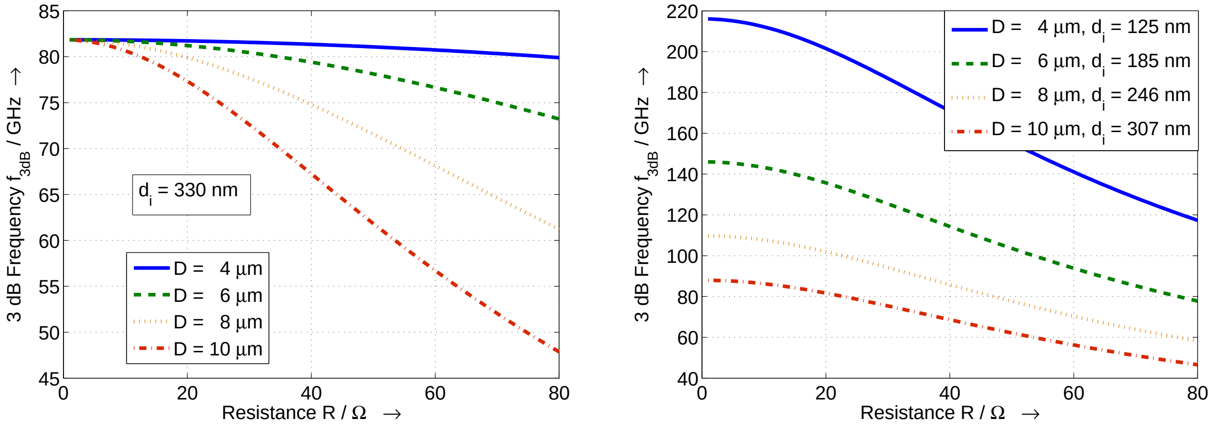

(a) d_i is kept fixed.

(b) d_i is optimised.

Figure 4.27: 3 dB frequency f_3dB and RC frequency f_RC versus the resistance$R$ of the photodiode. The diameter D of the photodiode is thereby swept. The thickness of the intrinsic region d_i is kept fixed (a) and set to the optimum value for the considered diameter D (b).

4.5 DC Characterisation

4.5.1 Dark Current

The saturation current I_S and the emission coefficient n_e can be retrieved from measurements on basis of the Shockley equation as defined in Eq. 2.55. In the forward region, the summand $-I_\text{S}$ is small compared to the majority current and can, therefore, be neglected. In the voltage range where the influence of R_S is not dominant, one can thus use the equation:

$$I_\text{dark} = I_\text{S} \cdot e^{\frac{V_\text{bias}}{V_\text{t} n_\text{e}}}. \tag{4.2}$$

Taking the logarithmic representation of this latter expression, which is

$$\log\left(I_\text{dark}\right) = \log\left(I_\text{S}\right) + \frac{V_\text{bias}}{V_\text{t} n_\text{e}}, \tag{4.3}$$

I_S and n_e can be derived from measurements by linear curve fitting, see Fig. 4.28a. These values serve as initial data for the derived *ADS DC* model. I_S and n_e are adjusted in the model by the built-in optimisation algorithms, taking into account the complete measured IV-characteristic.

The series resistance of the photodiode can be derived from *DC* four-wire measurements as described in the following. Assuming again that the term $-I_\text{S}$ can be neglected, one can use

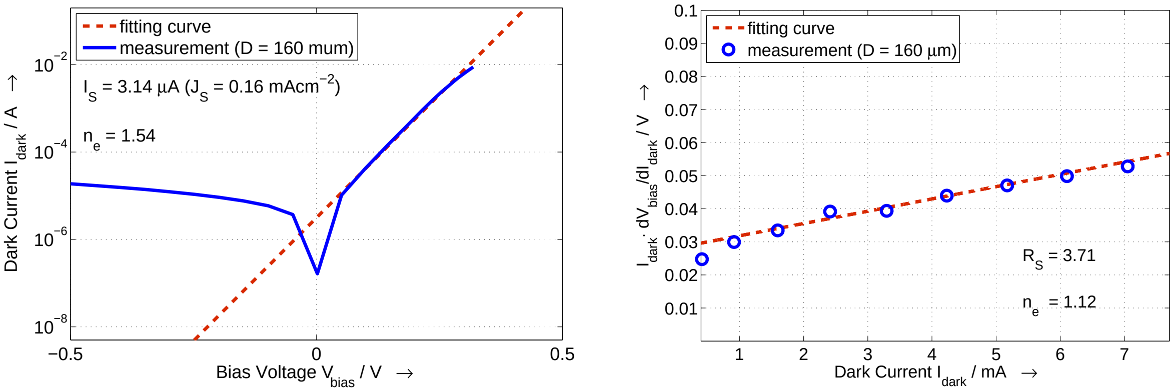

(a) Curve fitting to retrieve saturation current I_S and emission coefficient n_e.

(b) Curve fitting to retrieve series resistance R_S and emission coefficient n_e.

Figure 4.28: Curve fitting to retrieve saturation current I_S and emission coefficient n_e, and curve fitting to retrieve series resistance R_S and emission coefficient n_e. The measured photodiode has a diameter of $D = 160\mu$m.

the logarithmic form of Eq. 2.55 and differentiate the resulting equation with respect to the bias voltage V_bias [89][90], for what one gets:

$$I_\mathrm{dark} \cdot \frac{dV_\mathrm{bias}}{dI_\mathrm{dark}} = I_\mathrm{dark} \cdot R_\mathrm{S} + V_\mathrm{t} n_\mathrm{e}. \tag{4.4}$$

With the use of a linear fit, n_e and R_S can be extracted by axis intercept and slope, respectively. The curve fitting is exemplatory shown in Fig. 4.28b for a photodiode with mesa diameter $D = 160\,\mu$m.

As can be seen comparing results for the emission coefficient n_e in Fig. 4.28 for both fitting procedures, the extracted values are not identical. Fine tuning is hence done in the *ADS* simulation model on the basis of different diameters.

In Fig. 4.29, the measured dark current I_dark and the dark current density J_dark are plotted for different diameters D of the upper mesa of the photodiode. The thickness of the intrinsic region d_i is hereby 330 nm (sample *A*2045_2). It is obvious from the plot that the dark current scales with the junction area A_j, because the dark current density is almost identical for all measured diameters.

The temperature dependence is determined by placing the device under test (*DUT*) on a chuck that is connected to a temperature control unit. As at this setup only *GSG* probes can be mounted, precise four-wire measurements are not possible. However, for the examination of the general temperature dependence in the reverse bias region, the influence of an increased resistance due to probe and cables is regarded to be neglectable.

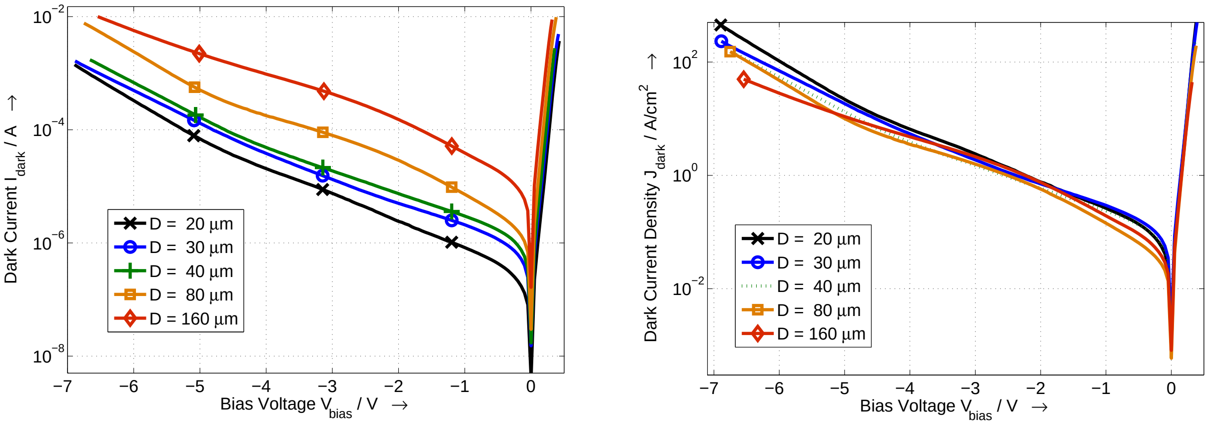

(a) Dark current I_{dark} versus V_{bias}.

(b) Dark current density J_{dark} versus V_{bias}.

Figure 4.29: Dark current I_{dark} and dark current density J_{dark} versus bias voltage V_{bias} for different mesa diameters D (20 to 160 μm). The sample which is characterised is $A2045\_2$.

In Fig. 4.30, the IV characteristic of the dark current I_{dark} at different temperatures is shown. The dark current increases with higher temperature as expected. Self-heating effects cannot be determined by the setup, because the temperature of the chuck is measured and not the temperature of the DUT itself.

In Fig. 4.31, the differential resistance R_{diff} is plotted versus the junction area A_{j} for two values of the intrinsic thickness d_{i}, namely 330 nm and 420 nm. Next to the values extracted from measurements, fitting curves are shown. It can be seen that R_{diff} is inverse proportional to A_{j}. The proportionality factor is denoted as a_0. Furthermore, Fig. 4.31 reveals that R_{diff} increases with increasing d_{i}. For $d_{\mathrm{i}} = 330\,\mathrm{nm}$, the extracted proportionaliy factor is $a_0 = 0.13\,\mathrm{m}\Omega$, for $d_{\mathrm{i}} = 420\,\mathrm{nm}$, it is $a_0 = 0.63\,\mathrm{m}\Omega$.

4.5.2 DC Responsivity

To extract the DC responsivity R_{opt} from measurements, the IV-curve at the desired wavelength is measured at different optical input power levels P_{opt}. For one selected voltage, the measured current is plotted versus the input power, and linear curve fitting is applied. The resulting slope of the fitting line corresponds to the responsivity:

$$R_{\mathrm{opt}} = \frac{dI}{dP_{\mathrm{opt}}} = \frac{d\left(I_{\mathrm{dark}} + I_{\mathrm{ph}}\right)}{dP_{\mathrm{opt}}} = \frac{d\left(I_{\mathrm{ph}}\right)}{dP_{\mathrm{opt}}}. \tag{4.5}$$

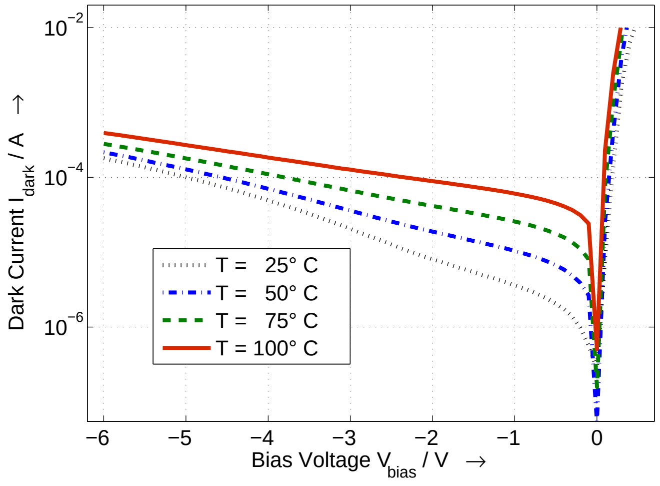

Figure 4.30: Dark current I_{dark} versus bias voltage V_{bias} at different temperatures T (25°C to 100°C) for a photodiode with a diameter of the upper mesa of $D = 80\,\mu\mathrm{m}$ (sample: $A2044\_2$).

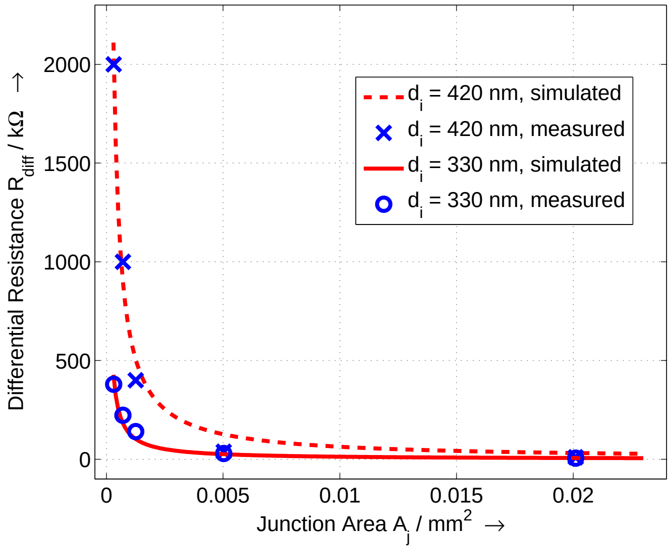

Figure 4.31: Extracted differential resistance R_{diff} versus junction area A_{j} for $d_{\mathrm{i}} = 330\,\mathrm{nm}$ (sample: $A2045\_2$) and $d_{\mathrm{i}} = 420\,\mathrm{nm}$ (sample: $A2044\_2$).

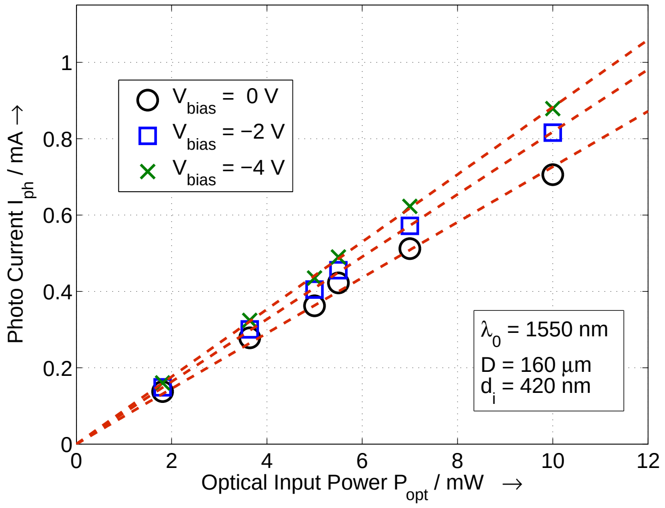

Figure 4.32: Extracted photo current I_{ph} versus input power P_{opt}. Measured (markers) and fitted (dashed line) results are shown. The wavelength $\lambda_0 = 1550\,\text{nm}$, the diameter of the upper mesa $D = 160\,\mu\text{m}$ and the thickness of the intrinsic region $d_{\text{i}} = 330\,\text{nm}$. Several bias voltages V_{bias} are considered.

The influence of the dark current is taken from the result due to the differentiation, for I_{dark} does not change with the optical input power.

In Fig. 4.32, the photo current extracted from measurements under illumination, $I_{\text{ph}} = I - I_{\text{dark}}$, is plotted versus the optical input power P_{opt}. A photodiode with diameter $D = 160\,\mu\text{m}$ from sample A2044_1 is examined in this case. The markers show the measured results while the dashed lines are fitting curves. They cross the origin as expected, as no photo current can be available without illumination. The slope and thus the responsivity increases with increasing negative bias voltage.

Fig. 4.33 shows the bias dependence of the responsivity for a photodiode from sample *A*2045_2. The diameter $D = 40\,\mu\text{m}$, and measurements are taken at two wavelengths, $\lambda_0 = 1310\,\text{nm}$ and $\lambda_0 = 1550\,\text{nm}$. At zero bias, the responsivity is 200 mA/W and 50 mA/W at $\lambda_0 = 1310\,\text{nm}$ and $\lambda_0 = 1550\,\text{nm}$, respectively. The increase of the responsivity at higher reverse bias can be seen here, too. This is attributed to the assumption that the *SCR* is not completely depleted at zero biasing.

The measured values of R_{opt} are higher than the simulated values, which are 175 mA/W and 16 mA/W at 1310 nm and 1550 nm, respectively. There might be different reasons for this discrepancy.

At 1550 nm, the voltage dependence of R_{opt} can be attributed to the Franz-Keldysh-effect

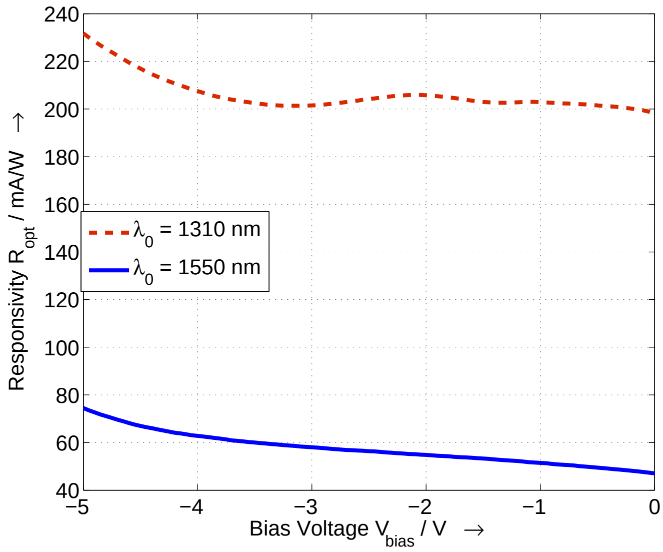

Figure 4.33: Extracted responsivity R_{opt} versus bias voltage V_{bias} for $\lambda_0 = 1310\,\text{nm}$ and $\lambda_0 = 1550\,\text{nm}$. The sample is A2045_2, the diameter of the photodiode is $D = 40\,\mu\text{m}$.

and thus explain the difference between measurement and simulation [44].

One further reason could be that the transition from p- to i-region and from i- to n-region is not abrupt. If this is the case, electron-hole pairs generated in the transition area might contribute to the overall photo current.

Another aspect refers to the thickness of the fabricated layers that might differ from the ones expected in simulations: as shown in Section 4.3.2, changes in the layer thicknesses also affect the responsivity.

Furthermore, the wavelength dependence of the external quantum efficiency EQE has to be reconsidered, see e.g. Fig. 4.14: at $\lambda_0 = 1550\,\text{nm}$, the negative slope of the simulated EQE is very steep. This means that if the operating laser in the measurements is slightly detuned, the change in the responsivity can become quite large.

But one must also be aware of the influence of the measurement setup: the distance between fibre and surface of the photodiode can be such that Fabry-Pérot resonances occur. This phenomenon is not included in the reference simulations presented so far, where the surrounding material is air and no fibre is included.

For the results of *2D* simulations shown in Fig. 4.34, the fibre is taken into account. The refractive index of the fibre is hereby set to $n = 1.46$. To represent the impact of the fibre, the distance between fibre tip and photodiode surface is swept as well as the tilt of the fibre.

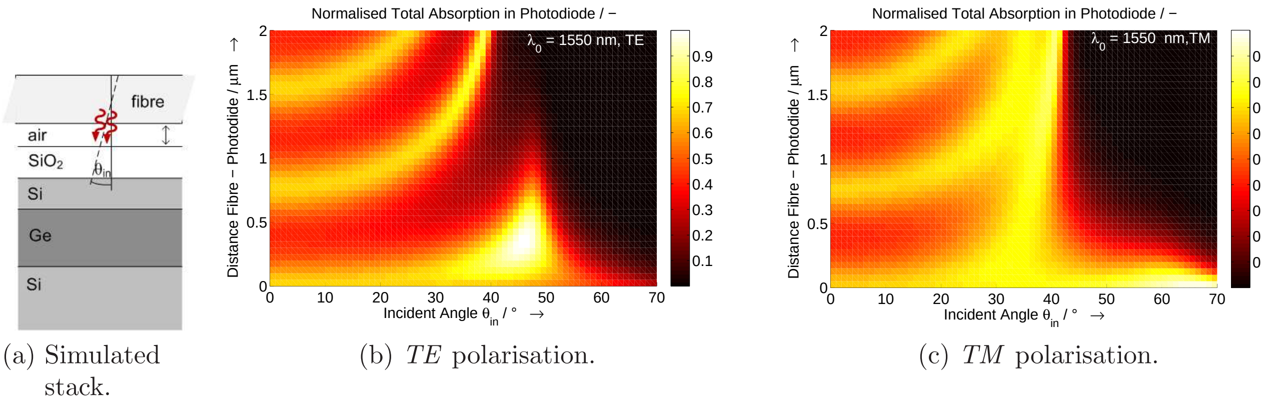

(a) Simulated stack.

(b) *TE* polarisation.

(c) *TM* polarisation.

Figure 4.34: Normalised total absorption in photodiode versus fibre distance with incident angle θ_{in} swept. The fibre is angle cleaved. The wavelength is $\lambda_0 = 1550\,\text{nm}$, the polarisation is *TE* (a) and *TM* (b).

Both polarisations, *TE* and *TM*, are considered separately. The layers of the photodiode are planar, and the influence of the metallic contact is not considered. The photodiode has similar dimensions as sample *A*2045_2.

As shown in Fig. 4.34a, the fibre is angle cleaved. Thus, the surface of the fibre tip is always parallel to the surface of the photodiode stack. Simulations of the same photodiode stack without fibre above are made for reference with vertical light incidence. They reveal that the absorption in this case is only about 54% of the absorption for the case where the influence of the fibre is included. The higher absorption that is gained with the fibre is due to Fabry-Pérot resonances.

In Fig. 4.35, the simulated normalised absorption is plotted versus the distance between fibre and surface of the photodiode for *TM* polarisation and two incident angles θ_{in}. Again, the fibre is angle cleaved. It can be seen that, depending on the angle, the variation of the absorption can be quite large ($\theta_{\text{in}} = 0°$) or quite smooth ($\theta_{\text{in}} = 35°$) for changing fibre-to-surface distance. This means that the polarisation of the incident light and the tilt of the fibre must be controllable and kept fixed if the increase of absorption by Fabry Pérot resonances shall be positively exploited. Under such optimsied conditions, the distance between fibre and surface of the photodiode is not critical anymore.

4.5.3 Evaluation of DC Circuit Model

In Fig. 4.36, measurements of dark current and measurements under illumination are shown together with the results of the *DC* circuit model implemented in *ADS*. In both cases, model

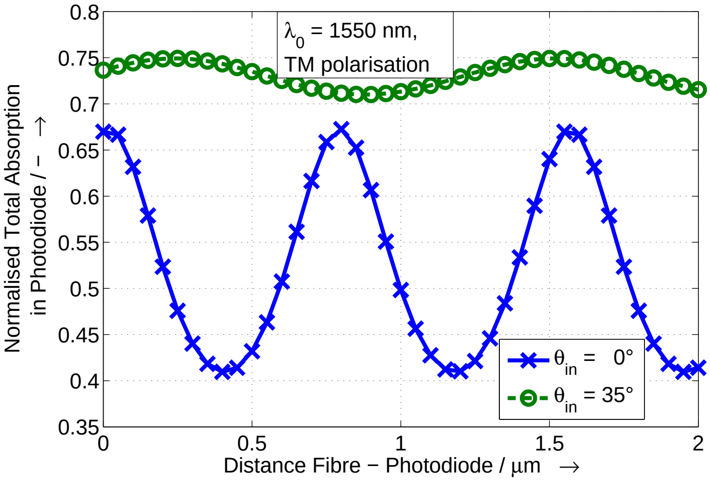

Figure 4.35: Normalised total absorption in photodiode with $\theta_{\text{in}} = 0°$ and $\theta_{\text{in}} = 35°$. The wavelength is $\lambda_0 = 1550\,\text{nm}$, the polarisation is TM. The fibre is angle cleaved.

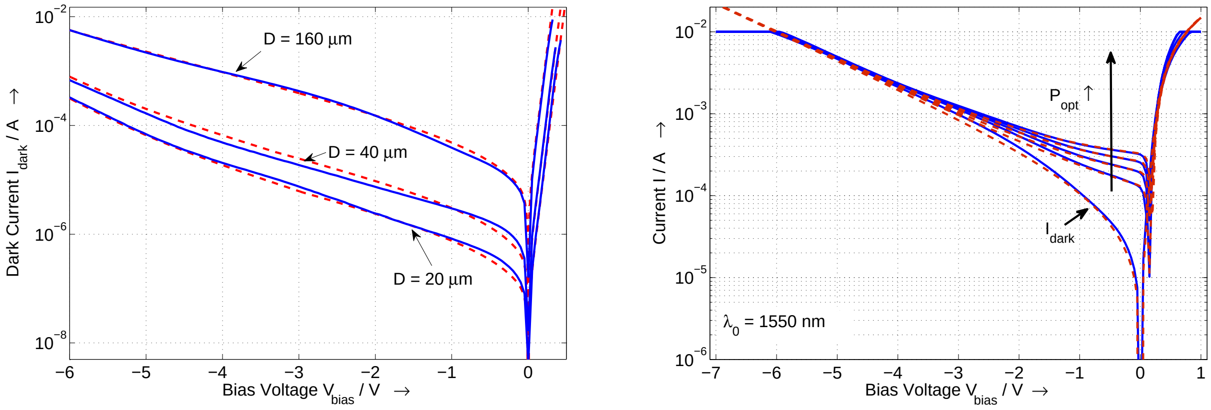

(a) *DC* dark current model.

(b) *DC* model including responsivity.

Figure 4.36: Dark current I_{dark} (a) and current under illumination I (b) versus bias voltage V_{bias}. Both, measurement (solid line) and simulation results (dashed line) are shown. The examined sample is $A2045\_2$. - For the dark current, results for three different diameters are displayed. For the case of illumination, the wavelength λ_0 is set to 1550 nm and the optical power P_{opt} is 2, 3, 4 and 5 mW. The diameter of the diode is $D = 160\,\mu\text{m}$.

Table 4.4: Extracted parameters of dark current measurements for $d_\mathrm{i} = 330\,\mathrm{nm}$ as implemented in the *ADS* model.

d_i nm	J_SD1 mA/cm^2	n_D1 -	J_SD2 mA/cm^2	n_D2 -	n_3 -	V_crit V
330	20	1.5	166	46	20	-2.95 ($D = 20\,\mu\mathrm{m}$) to -4.8 ($D = 160\,\mu\mathrm{m}$)

and measurements fit very well.

Table 4.4 summarises the extracted values for the dark current characterisation. The voltage V_crit increases with increasing diameter D (almost linearly with area A_j), but for some diodes, the effect of an additional exponential increase before the proper breakdown voltage is not seen. This is why V_crit is set manually for each diameter.

4.6 Small Signal Characterisation

For measurements in the frequency domain, different measurement setups are used: scattering parameters measured with the vector network analyser (*VNA*) provide information about the input impedance of the photodiode and its opto-electrical transfer function up to 50 GHz. With an optical heterodyne measurement setup (*HET*), the bandwidth of the photodiodes can be determined up to 65 GHz. Additionally, measurements of the opto-electrical transfer function of the smallest (and fastest) photodiodes are made with a lightwave component analyser (*LCA*) *N4373B* from Agilent Technologies. The *LCA* allows for measurements up to 67 GHz.

Before measurement results are presented, some important aspects about scattering parameters are highlighted first.

4.6.1 Scattering Parameters

Scattering parameters have already been introduced in terms of light propagation through layers with varying refractive index. They are considered now in the context of electric N-port networks, with $N \in \mathbb{N}$. The scattering parameters express the ratio between reflected (transmitted) waves b_i at the input (output) of the N-port to incident waves a_i at the input of the N-port, with $i = 1..N$. For a 2-port, this relation can be written as:

$$\begin{pmatrix} \underline{b}_1 \\ \underline{b}_2 \end{pmatrix} = \begin{pmatrix} \underline{S}_{11} & \underline{S}_{12} \\ \underline{S}_{21} & \underline{S}_{22} \end{pmatrix} \cdot \begin{pmatrix} \underline{a}_1 \\ \underline{a}_2 \end{pmatrix}, \tag{4.6}$$

with

$$\begin{pmatrix} \underline{S}_{11} = \frac{\underline{b}_1}{\underline{a}_1}|_{\underline{a}_2=0} & \underline{S}_{12} = \frac{\underline{b}_1}{\underline{a}_2}|_{\underline{a}_1=0} \\ \\ \underline{S}_{21} = \frac{\underline{b}_2}{\underline{a}_1}|_{\underline{a}_2=0} & \underline{S}_{22} = \frac{\underline{b}_2}{\underline{a}_2}|_{\underline{a}_1=0} \end{pmatrix}. \tag{4.7}$$

Like other N-port parameters, e.g. admittance or chain parameters, the scattering parameters completely describe the N-port network. In contrast to other N-port parameters, matched loads are used as terminations rather than open or short circuits. This load usually has a value of 50 Ω.

For the photodiode, which is the network under consideration, two different N-ports have to be studied as depicted in Fig. 4.37. According to this figure, the photodiode is a simple 1-port if no illumination takes place, and a simple 2-port under illumination.

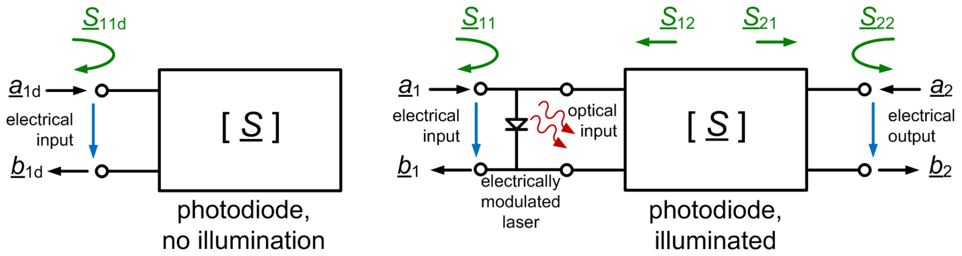

(a) Photodiode without illumination: 1-port with electrical input.

(b) Illuminated photodiode: 2-port with optical in- and electrical output.

Figure 4.37: 1-port representing photodiode without illumination (a) and 2-port representing photodiode under illumination (b). The incident and reflected waves are as well indicated as the scattering parameters.

It can be seen that, for the measurements which are relevant for this work, two scattering parameters are important: the input reflexion coefficient $\underline{S}_{11d}$[1] at the electrical port of the photodiode (Fig 4.37a), which is the output reflexion coefficient $\underline{S}_{22}$ of the overall network, and the forward transmission factor $\underline{S}_{21}$ (Fig 4.37b). Both parameters, the measurement setup used to retrieve them and the obtained measurement results are dealt with more closely in the following.

4.6.2 Input Reflexion Coefficient

For a 1-port circuit with the input impedance $\underline{Z}_{\text{in}}$ that is connected to a transmission line with the characteristic impedance $\underline{Z}_0$, the input reflexion coefficient $\underline{S}_{11}$ is given by:

$$\underline{S}_{11} = \left(\frac{\underline{Z}_{\text{in}} - \underline{Z}_0}{\underline{Z}_{\text{in}} + \underline{Z}_0} \right). \tag{4.8}$$

This results directly from Eq. 2.43, using for non-magnetic material

$$\underline{Z}_0 = \sqrt{\frac{\mu_0}{\varepsilon_0 \underline{\varepsilon}_{\text{r},0}}}, \quad \underline{Z}_{\text{in}} = \sqrt{\frac{\mu_0}{\varepsilon_0 \underline{\varepsilon}_{\text{r,in}}}} \tag{4.9}$$

and $\underline{n} = \sqrt{\underline{\varepsilon}_{\text{r}}}$.

As the photodiode without illumination is an electrical 1-port as shown in Fig. 4.37a, the measurement of its input reflexion coefficient makes it possible to determine its input impedance [22]. The according equivalent circuit of the photodiode with parasitics has been introduced

---

[1] The "d" in the lower position of $\underline{S}_{11d}$ indicates that measurements in the dark, without illumination, are referred to.

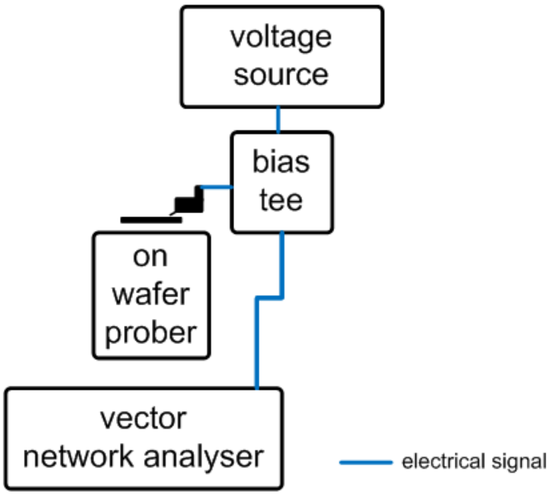

Figure 4.38: Measurement setup based on *VNA* to retrieve the electrical input reflexion coefficient $\underline{S}_{11\mathrm{d}}$ of the photodiode.

in Fig. 4.7. The measurement setup in Fig. 4.38 consists of the *VNA HP8510C* from Agilent Technologies that measures the scattering parameters up to 50 GHz, a source measurement unit (*SMU*) to set the bias point of the photodiode via the internal bias tee of the *VNA* and to simultaneously monitor the diode current, and an on-wafer prober on which the *DUT* is held by a vacuum pump. The *DUT* is contacted via *RF* probes with *GSG* configuration and a pitch of $100\,\mu$m.

The measured and simulated input reflexion coefficient of the entire photodiode structure is plotted in Fig. 4.39 in the Smith chart. The frequency ranges from 45 MHz to 40 GHz, and the reference impedance is $\underline{Z}_0 = 50\,\Omega$. The input reflexion coefficient is shown for three different mesa diameters D. The oscillations of the measurement results at higher frequencies stem from the calibration that is slightly degraded at these measurement points.

The fitting of simulated and measured values in the Smith chart is quite good. Results for both representations of the contact structure (*SC*-*OC* and *OC*-*SC*) are displayed. In order to better evaluate this matching, real and imaginary part of the reflexion coefficient are also depicted separately in Fig. 4.40. The agreement between measured and simulated data is equally fine here, for all three diameters D under consideration.

The extracted values of the junction capacitance C_j are plotted versus the diameter D and the area A_j in Fig. 4.41 for sample *A*2045_1 and a bias voltage $V_\mathrm{bias} = -1\,\mathrm{V}$. Again, both arrangements of the contact structure are applied for the parameter extraction. For C_j, a dependence on the junction area A_j is derived as expected if a parallel plate capacitor is assumed. The constant factor with which A is multiplied in Fig. 4.41b corresponds to $\frac{\varepsilon_0 \varepsilon_\mathrm{r}}{d_\mathrm{i}}$, with $\varepsilon_\mathrm{r} = 16$ the relative permittivity of *Ge* for frequencies in the GHz range.

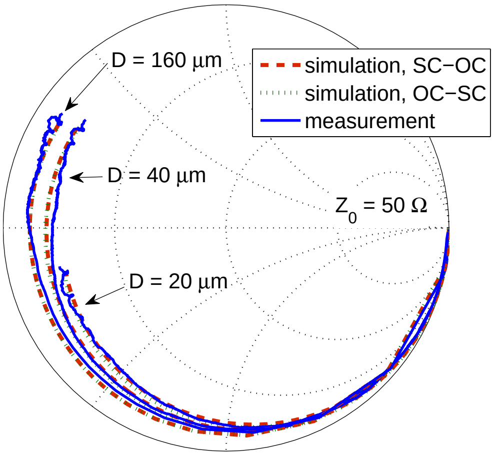

Figure 4.39: The input reflexion coefficient as represented in the Smith chart: measurements with *VNA* (solid line) and simulations with *ADS* (dashed line: *SC-OC* extraction, dotted line: *OC-SC* extraction) are shown. The frequency is swept from 45 MHz up to 40 GHz, and the bias voltage is $V_{\text{bias}} = -1\,\text{V}$. The sample in use is *A2045_1*. Results for three different diameters D are depicted: $D = 20\,\mu\text{m}$, $D = 40\,\mu\text{m}$ and $D = 160\,\mu\text{m}$.

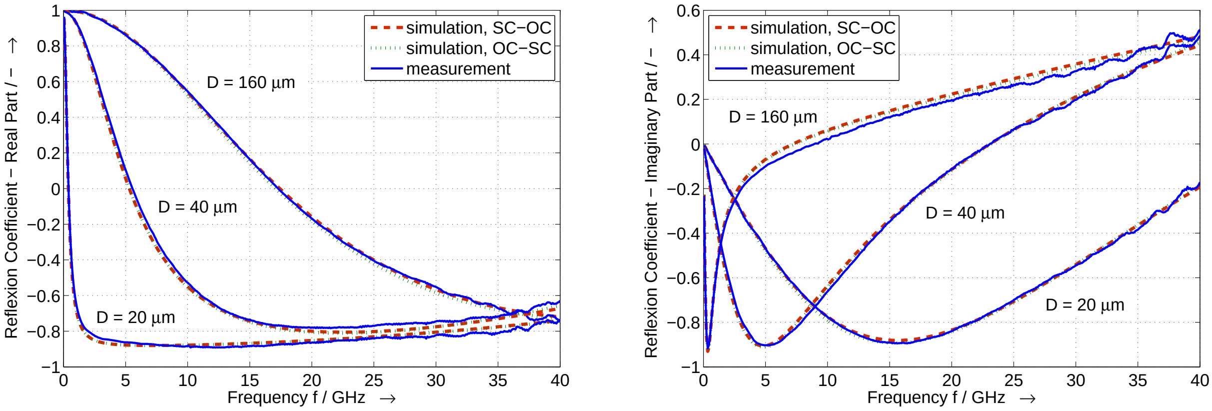

(a) Real part of input reflexion coefficient.

(b) Imaginary part of input reflexion coefficient.

Figure 4.40: Input reflexion coefficient, represented as real and imaginary part: measurements with *VNA* (solid line) and simulations with *ADS* (dashed line: *SC-OC* extraction, dotted line: *OC-SC* extraction) are shown. The frequency is swept from 45 MHz up to 40 GHz, and the bias voltage is $V_{\text{bias}} = -1\,\text{V}$. The sample in use is *A2045_1*. Results for three different diameters D are depicted: $D = 20\,\mu\text{m}$, $D = 40\,\mu\text{m}$ and $D = 160\,\mu\text{m}$.

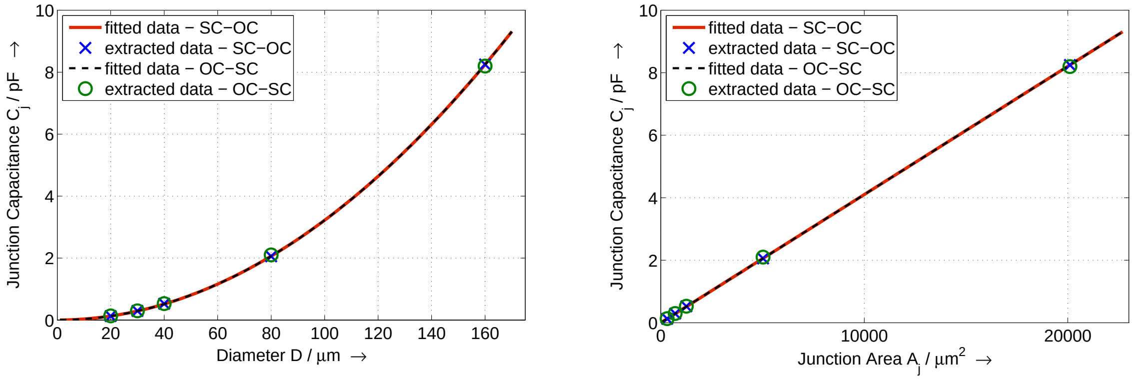

(a) Junction capacitance C_j versus D.

(b) Junction capacitance C_j versus A_j.

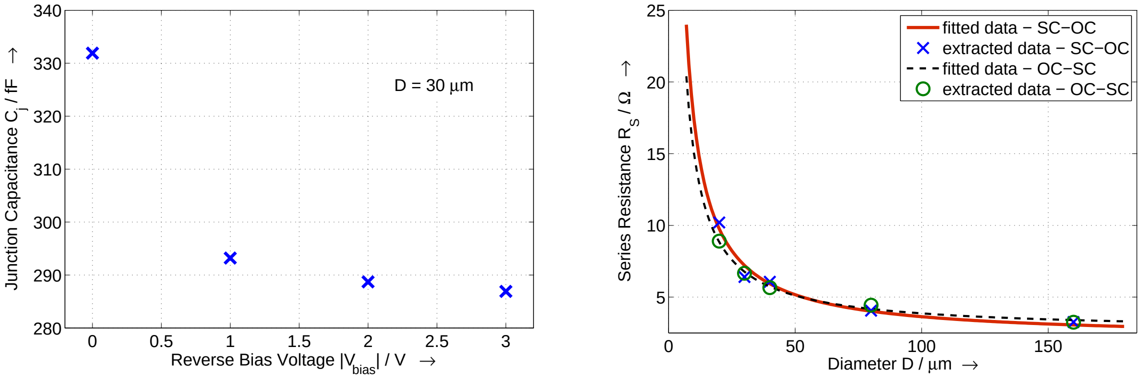

(c) Junction capacitance C_j versus V_bias for a photodiode with $D = 30\,\mu$m.

(d) Series resistance R_S versus $1/D$.

Figure 4.41: Dependence of extracted junction capacitance C_j on geometry at $V_\mathrm{bias} = -1\,$V (a-b) and on the bias voltage for $D = 30\,\mu$m (c). - Dependence of the series resistance R_S (b) on geometry at $V_\mathrm{bias} = -1\,$V. - All measurements are done on sample *A*2045_2.

The assumption that the *SCR* is not completely depleted at zero bias is backed up by comparison of the theoretical and extracted value for the depletion capacitance: the theoretical value, normalised to area, is $\frac{C_\mathrm{j}}{A} = \frac{\varepsilon_0 \varepsilon_\mathrm{r}}{d_\mathrm{i}} = 420\,\mathrm{F}\mu\mathrm{m}^{-2}$. The extracted value at zero bias is about $480\,\mu\mathrm{Fm}^{-2}$, while at $-1\,$V, it is $417\,\mu\mathrm{Fm}^{-2}$ and, thus, closer to the expected value. This means that at larger reverse bias voltage, the *SCR* is more thoroughly depleted. An example for the bias dependence of C_j is shown in Fig. 4.41c for $D = 30\,\mu$m.

The series resistance R_S and its dependence on geometry is also contained in Fig. 4.41. According to the fitting results, R_S depends on $D^{-\mathrm{m}}$, where m lies in between 1 and 2. In Fig. 4.41d, $m = 1$ is chosen. With the help of the fitting curve, the series resistance of smaller structures can be estimated and used then for the calculation of the corresponding theoretical 3 dB frequency limit. For a diameter of $10\,\mu$m, R_S is e.g. approximately $15\,\Omega$.

Table 4.5: Extracted parameters for small signal circuit elements (sample: *A2045_1*). The contact configuration *OC-SC* is applied.

D μm	R_{diff} kΩ	C_{j} fF	R_{S} Ω	L_{S1} pH	C_{P1} fF	R_{P1} Ω	C_{P2} fF	R_{P2} Ω
20	380	132	8.9	79.9	11.0	4.55	8.8	15.2
30	223	298	6.7	78.9	11.2	4.55	14.5	15.0
40	140	527	5.7	78.5	11.2	4.55	21.8	14.8
80	29	2101	4.4	75.4	10.8	4.55	48.9	15.0
160	5.5	8196	3.3	48.7	6.0	4.55	106.7	15.0

Table 4.6: Extracted parameters for small signal circuit elements (sample: *A2045_1*). The contact configuration *SC-OC* is applied.

D μm	R_{diff} kΩ	C_{j} fF	R_{S} Ω	L_{S1} pH	C_{P1} fF	R_{P1} Ω	C_{P2} fF	R_{P2} Ω
20	380	128	10.2	74.8	10.7	4.55	8.5	15.2
30	223	293	6.4	77.8	11.1	4.55	14.4	15.0
40	140	527	6.1	77.8	11.2	4.55	22.3	14.8
80	29	2057	4.1	72.5	11.0	4.55	46.7	15.0
160	5.5	8247	3.3	50.8	6.1	4.55	107.0	15.0

In Table 4.5 and Table 4.6, the parameters extracted from measurements of the input reflexion coefficient are summarised for sample *A2045_1*. Table 4.5 applies the *OC-SC* configuration of the contact structure for extraction, and Table 4.6 the *OC-SC* configuration.

4.6.3 VNA - Opto-Electrical Transfer Function

The absolute value of the forward transmission factor $\underline{S}_{21}$ represents the relative opto-electrical transfer function of the overall network; the phase information of $\underline{S}_{21}$ is not further examined in this work. The measurement setup in Fig. 4.42 is the same as in Fig. 4.38 for the electrical port. At the optical input, the *CW* signal of a 1550 nm laser is modulated by an optical intensity modulator which is driven by the *RF* signal of the *VNA RF* source. An erbium doped fibre amplifier (*EDFA*) amplifies the modulated optical signal if this becomes necessary for the smaller photodiodes.

The following calibration steps have been developed in [51] for the measurement of photodiodes as examined in this work. The measurement setups as described so far contain frequency dependent elements, like the *RF* cables connecting the port of the *VNA* to the *RF* probe, and the *RF* probe itself. In order to move the reference level for the measurements to the tips of the *RF* probe, known structures on a calibration substrate, the impedance

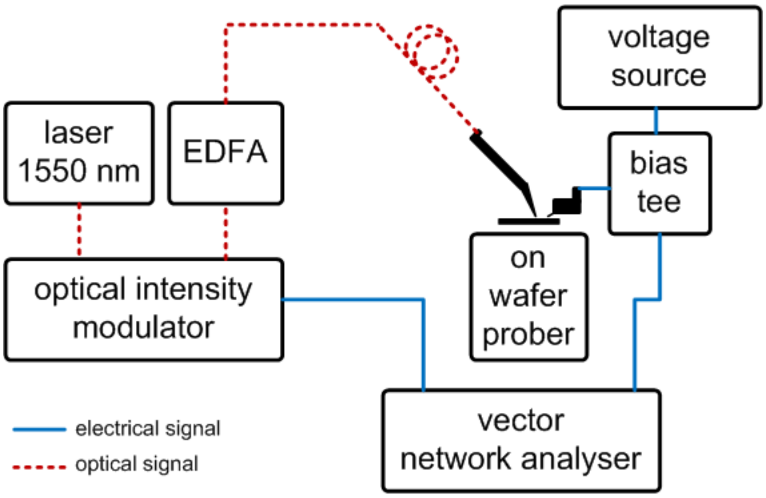

Figure 4.42: Measurement setup based on *VNA* to retrieve the opto-electrical forward transfer function $\underline{S}_{21}$ of the photodiode.

standard substrate (*ISS*) from Cascade for *GSG* configuration with 100 μm pitch, are measured. With the help of an algorithm based on 12-term-error correction, the impact on the frequency behaviour of all cables and connectors, positioned in front of the *RF* probe tips, is cancelled out. The software *WinCal* is used for this calibration with the inbuilt calibration method line-reflect-reflect-match (*LRRM*). This is a full 2-port calibration method where six calibration standards have to be measured.

This calibration is sufficient for the measurement of the reflexion coefficient $\underline{S}_{11\mathrm{d}}$. Regarding the transmission factor $\underline{S}_{21}$, additionally the frequency response of the modulator has to be considered. This is done with a reference measurement using the broadband photodiode *XPDV2020R* from u^{2}t Photonics that has a 3 dB bandwidth of 50 GHz. The frequency response of this detector must also be taken into account. Hence the final frequency response of the *DUT* $\left|\underline{S}_{21,\mathrm{DUT}}(f)\right|$ becomes [51]:

$$\left|\underline{S}_{21,\mathrm{DUT}}(f)\right| = \frac{\frac{\left|\underline{S}_{21,\mathrm{MEAS}}\right|}{\left|\underline{S}_{21,\mathrm{MEAS}}(0)\right|}}{\frac{\left|\underline{S}_{21,\mathrm{REF,MEAS}}\right|}{\left|\underline{S}_{21,\mathrm{REF,MEAS(0)}}\right|}\cdot\frac{1}{\left|\underline{S}_{21,\mathrm{REF,DATA}}(f)\right|}}. \tag{4.10}$$

$\left|\underline{S}_{21,\mathrm{MEAS}}\right|$ is the absolute value of the measured transfer function with $\left|\underline{S}_{21,\mathrm{MEAS}}(0)\right|$ the value at $f = 0$ GHz used for normalisation. $\left|\underline{S}_{21,\mathrm{REF,MEAS}}\right|$ and $\left|\underline{S}_{21,\mathrm{REF,DATA}}\right|$ are the frequency responses of the reference photodiode, measured in the specified setup and taken from data sheet, respectively. The measured frequency response of the reference photodiode is also normalised to its value at $f = 0$ GHz.

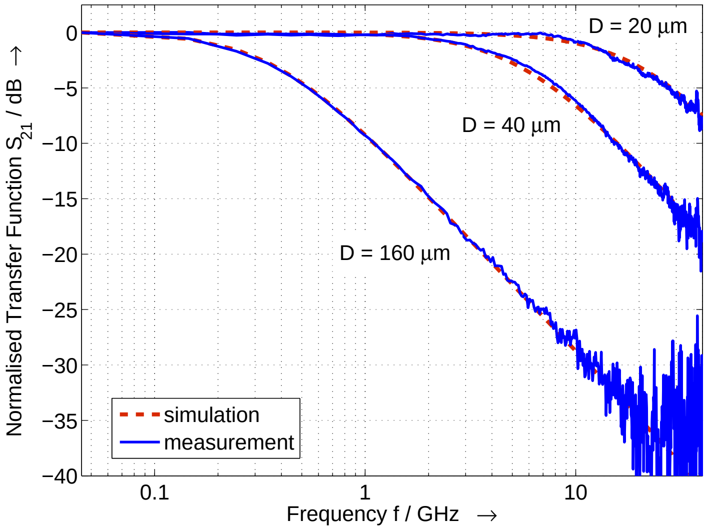

Figure 4.43: Opto-electrical transfer function measured with *VNA* (solid line) and simulated with *ADS* in the *OC-SC* configuration (dashed line) at $V_{\mathrm{bias}} = -2\,\mathrm{V}$. The wavelength is 1550 nm. Three different diameters D are shown: $D = 20$, 40 and 160 μm.

The results obtained from *VNA* measurements are summarised in the following. In Fig. 4.43, the normalised opto-electrical transfer function for sample *A*2045_1 is depicted for both, measurement with *VNA* setup and *ADS* simulation. For the small signal simulation, the *OC-SC* configuration is chosen for the contact structure. Results are shown for three different diameters. Again, the matching between measurement and model is satisfying. For the largest diameter $D = 160\,\mu\mathrm{m}$, the signal has reached the noise floor at higher frequencies.

In Table 4.7, values for measured, extracted and theoretical 3 dB frequency $f_{3\mathrm{dB}}$ are summarised for different diameters D. The corresponding values of the extracted series resistance are also listed, because they are required for the calculation of the theoretical 3 dB frequency.

Measurements are executed at a bias voltage of $V_{\mathrm{bias}} = -1\,\mathrm{V}$ on sample *A*2045_1.

For the theoretical considerations, $d_{\mathrm{i}} = 330\,\mathrm{nm}$ and $d_{\mathrm{i}} = 345\,\mathrm{nm}$ are both listed. This is done as the thickness of the intrinsic *Ge* region, if calculated back from the extracted junction capacitance, is about 345 nm instead of 330 nm.

For the extracted values, there are two columns reserved in the table: in the first one, the extracted 3 dB frequency of the overall photodiode, including the contact structure, is itemised. In the second column, the contact structure is removed in the simulated circuit. Thus, only the inner diode and the *VCCS* representing the transit frequency f_{TT} are considered.

Table 4.7: Measured, theoretical and extracted 3 dB frequency of photodiode. Measurements are done at $V_{\mathrm{bias}=-1\,\mathrm{V}}$. For the extracted 3 dB frequency, the contact structure is once included in the extraction, once only the inner diode is considered. For the theoretical values, once $d_\mathrm{i} = 330\,\mathrm{nm}$ are assumed, once $d_\mathrm{i} = 345\,\mathrm{nm}$. The extracted series resistance is always taken into account for the calculation.

D / μm	R_S / Ω	$f_{3\mathrm{dB}}$ / GHz				
		measured	extracted with contact structure	extracted without contact structure	theory, $d_\mathrm{i} = 330\,\mathrm{nm}$	theory, $d_\mathrm{i} = 345\,\mathrm{nm}$
20	8.9	18.2	19.6	19.4	19.5	20.2
30	6.7	9.2	9.2	9.3	9.2	9.6
40	5.7	5.8	5.3	5.4	5.3	5.5
80	4.4	1.3	1.4	1.4	1.4	1.4
160	3.3	0.36	0.37	0.37	0.35	0.36

For the smaller diodes, the impact of the transit frequency becomes more significant. As the modelling of the transit frequency is only a simple approximation, it is assumed that the difference observed between theoretical and extracted values stems from this part of the model. In addition, the impact of the contact structure increases for smaller diodes, and resonance effects take place. This is observed for the diode with diameter $D = 20\,\mu\mathrm{m}$. If both extracted transfer functions are compared as done in Fig. 4.44, the slope of the one which still includes the contact structure has a steeper negative slope at increasing frequencies. This indicates some resonant behaviour. Both curves intersect later on. This is why the 3 dB frequency for the extraction with contact structure is higher than for the one without, though for even higher frequencies, the latter one falls down much more slowly.

4.6.4 HET - Opto-Electrical Transfer Function

With the *VNA* of the laboratory, measurements can be carried out up to 50 GHz. In order to increase the measurement range up to 65 GHz, a heterodyne measurement setup is installed with the kind support of the Fraunhofer Institute for Applied Solid State Physics (*IAF*). It should be stated that the minimum achievable frequency is limited by the precision with which the wavelength can be set at the laser. It is about 200 MHz in this setup. The maximum achievable frequency only depends on the tunable wavelength range of the lasers. Thus very high *RF* frequencies can be obtained if only regarding the optical components of the setup. But the complete heterodyne measurement setup as used in this work also contains electrical components that reduce the available frequency range. The setup is shown in Fig. 4.45.

Two tunable laser sources *81682A* from Agilent Technologies with a wavelength range from

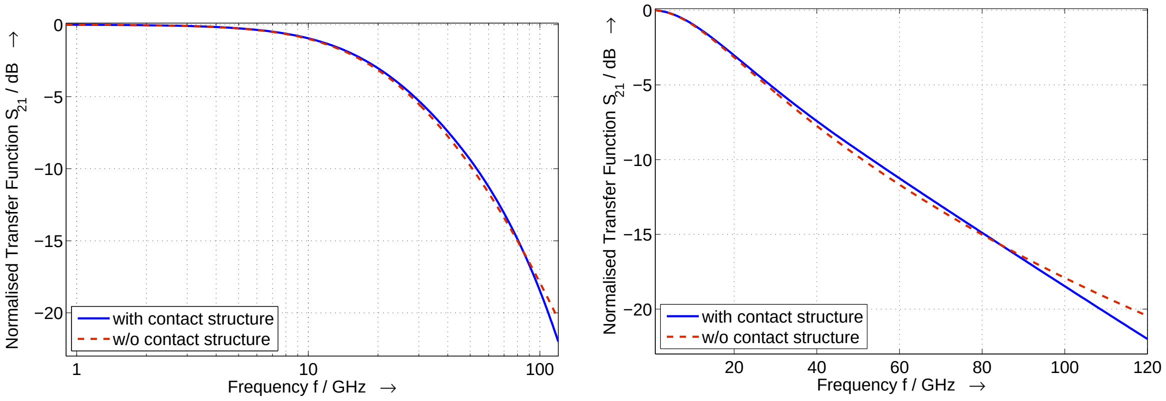

(a) Logarithmic scale. (b) Linear scale.

Figure 4.44: Extracted normalised opto-electrical transfer function, with contact structure (solid) and without (dashed) for sample *A*2045_1 and diameter $D = 20\,\mu$m. In logarithmic (a) and linear (b) representation.

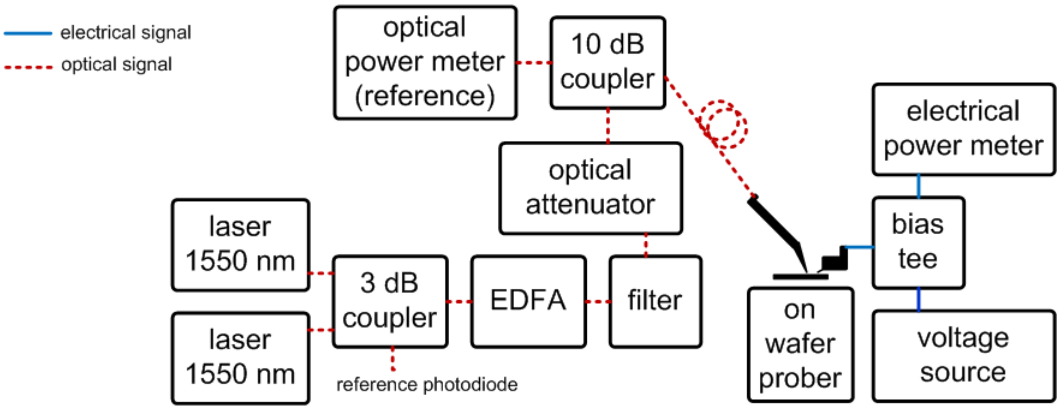

Figure 4.45: Optical heterodyne measurement setup.

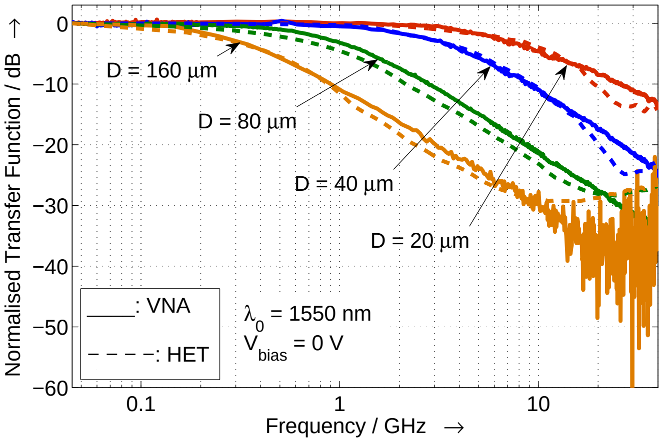

Figure 4.46: Opto-electrical transfer function measured with *HET* and *VNA* at $V_{\mathrm{bias}} = 0\,\mathrm{V}$. The wavelength is 1550 nm. Four different diameters D are shown: $D = 20\,\mu\mathrm{m}$, $D = 40\,\mu\mathrm{m}$, $D = 80\,\mu\mathrm{m}$ and $D = 160\,\mu\mathrm{m}$.

1510 nm to 1580 nm are used. These two laser sources are detuned in their wavelengths in respect to each other to get a difference frequency lying in the GHz range. Their output signals are combined in a 3 dB coupler. One of the outputs of this coupler is connected to a reference photodiode that provides the input signal of an electrical spectrum analyser to control the generated frequency. The other output signal of the coupler first goes to an *EDFA* with an adjacent filter to reduce the noise floor. Afterwards the signal passes an optical attenuator. This allows for the sweep of the optical input power. Behind the attenuator, the signal is split again, this time in a 10 dB coupler. One tenth of the power is brought to a reference optical power meter, 90% of the power is delivered to the *DUT* via an *SMF* that is placed in a fibre holder. The electrical output of the *DUT* is connected to the electrical power meter via a Picoprobe *RF* probe in *GSG* configuration, a male-to-male *RF* connector (V style) and a broadband bias tee. A *SMU* provides the bias voltage for the *DUT*.

In terms of optical calibration, one has to ensure that both lasers provide the same optical output power for the heterodyne principle to work properly. In addition, the optical power at the fibre tip is first measured via an optical power meter before the fibre is placed above the *DUT*. With the help of an internal correction factor, the power displayed at the reference optical power meter is adapted to show the same value as measured at the fibre tip. Thus, the power at the *DUT* can be indirectly monitored during measurements.

For the electrical calibration, the transfer function of the whole chain of electrical elements - *RF* probe, *RF* connector, bias tee and electrical power meter - must be taken into account.

In an *HP VEE* measurement routine provided by the *IAF*, the frequency dependence of all components is implemented in form of scattering parameters, except for the *RF* connector. The overall calibration is done inside this routine.

Measurement results retrieved with the optical heterodyne measurement setup are shown next. A comparison of the opto-electrical transfer function measured with *VNA* and *HET* is graphically done in Fig. 4.46 for sample *A*2045_1. It can be seen that the agreement is quite good up to 10 GHz. Above this frequency, however, the transfer function measured with the heterodyne measurement setup has a steeper negative slope than the measurements done with the *VNA*. It is assumed that this behaviour is due to the frequency dependent electrical components of the heterodyne measurement setup: the data of these elements which is used in the correction routine of the measurement software might be out of date and have to determined once again. Furthermore, additional elements like the *RF* male-to-male connector (V style) between *RF* probe and bias tee are not yet included in the software calibration routine.

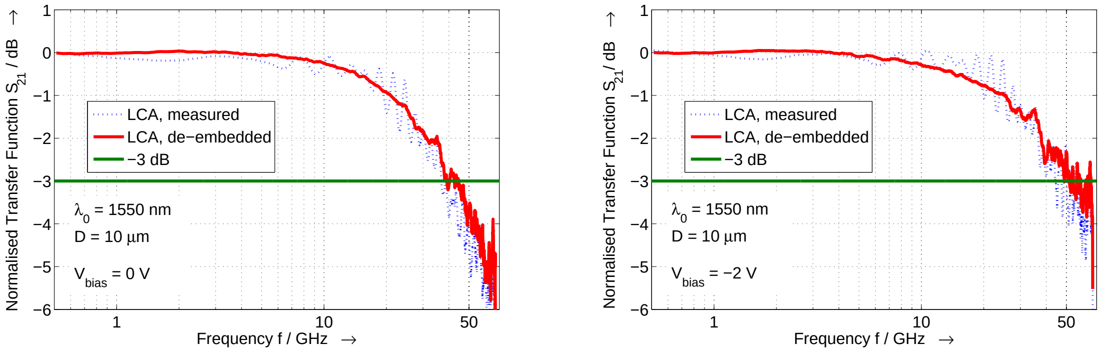

(a) Opto-electrical transfer function measured with *LCA*. $V_{\text{bias}} = 0\,\text{V}$.

(b) Opto-electrical transfer function measured with *LCA*. $V_{\text{bias}} = -2\,\text{V}$.

Figure 4.47: Opto-electrical transfer function measured with *LCA* up to 67 GHz at $\lambda_0 = 1550\,\text{nm}$. The bias voltage is $V_{\text{bias}} = 0\,\text{V}$ (a) and $V_{\text{bias}} = -2\,\text{V}$ (b).

4.6.5 LCA - Opto-Electrical Transfer Function

Due to the restrictions of the *VNA* and the heterodyne measurement setup, a third setup is used to determine the 3 dB frequency of the smallest *DUTs* of wafer *A2045_2*. These devices have a diameter $D = 10\,\mu\text{m}$, and a theoretical 3 dB frequency of 54 GHz is expected to be achievable. The setup consists of the lightwave component analyser *N4373B* from Agilent Technologies and allows bandwidth measurements up to 67 GHz. The wavelength at which measurements are carried out is again $\lambda_0 = 1550\,\text{nm}$. Fig. 4.47a shows the measured opto-electrical transfer function for zero biasing. A bandwidth of 39 GHz is found. The transfer function in Fig. 4.47b yields a 3 dB bandwidth of 49 GHz at $V_{\text{bias}} = -2\,\text{V}$, the highest one reported so far for vertical *Ge* on *Si* photodiodes [91] and close to the calculated value. The contact structure is not de-embedded for this result, so the intrinsic bandwidth is expected to come even closer to the theoretical limit.

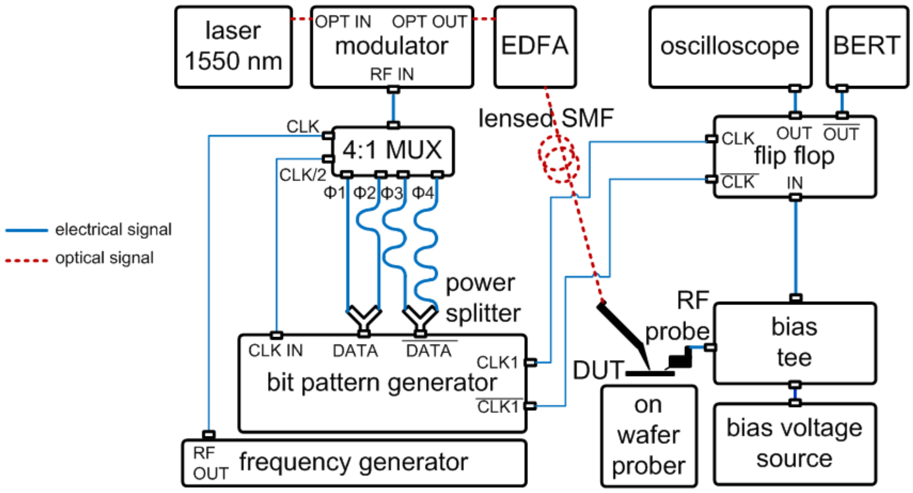

Figure 4.48: Time domain measurement setup for photodiodes using an *EDFA* to provide sufficient optical input power.

4.7 Time Domain Characterisation

The measurement setup shown in Fig. 4.48 is used to determine the eye diagram and the bit error ratio (*BER*) of the electrical output signal of the photodiode. The available bit pattern generator (*BPG*) works up to 12.5 Gbit/s. To provide a bit rate of the input signal of up to 50 Gbit/s, the 4:1 multiplexer (*MUX*) *SHF404MUX* is used: the inverted and non-inverted output signal of the *BPG* is split into four data streams by power splitters, and the four data streams are de-correlated by transmission lines of different lengths. This provides for different phase differences $\phi_{1..4}$ at the input of the *MUX*. Thus, a pseudo random bit sequence (*PRBS*) data stream with bit rates up to 50 Gbit/s can be generated. The clock signal for the $4:1$ *MUX* is generated by a frequency generator working up to 50 GHz. The corresponding frequency is set to half of the desired data rate. The output of the *MUX* drives the optical intensity modulator. The wavelength of the laser at the optical input of the modulator is set to 1550 nm. The optical output signal of the modulator is amplified by an *EDFA*. The optical power at the fibre tip is about 40 mW, which results in a photo current of approximately 5 mA at a bias voltage $V_{\text{bias}} = -2\,\text{V}$.

A flip flop that had been developed at the *INT* [92] is connected to the *RF* port of the bias tee. The *BPG* provides the clock signal for this flip flop. It samples each fourth bit of the incoming data stream. One of the differential outputs of the flip flop is connected to a sampling oscilloscope, the other one to a bit error ratio tester (*BERT*). The clock signal for oscilloscope and *BERT* also stem from the *BPG* (connection line not drawn in Fig. 4.48 for the sake of clarity).

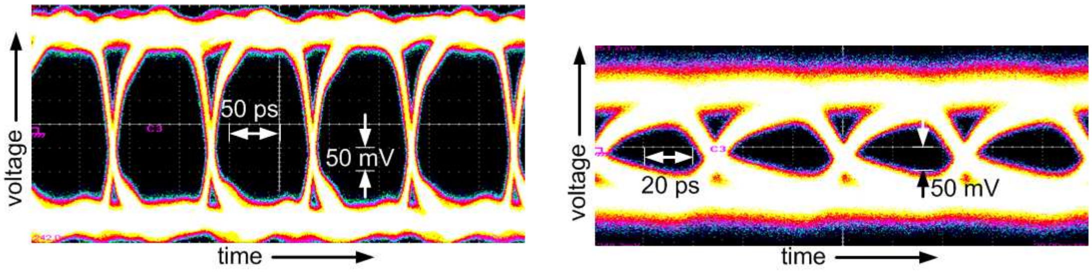

(a) Bit rate: 10 Gbit/s. (b) Bit rate: 20 Gbit/s.

Figure 4.49: Eye diagram of a photodiode with $D = 10\,\mu\mathrm{m}$ and $d_\mathrm{i} = 330\,\mathrm{nm}$ at a bit rate of 10 Gbit/s (a) and 20 Gbit/s (b), and a *PRBS* length of $2^7 - 1$ and $BER < 10^{-12}$.

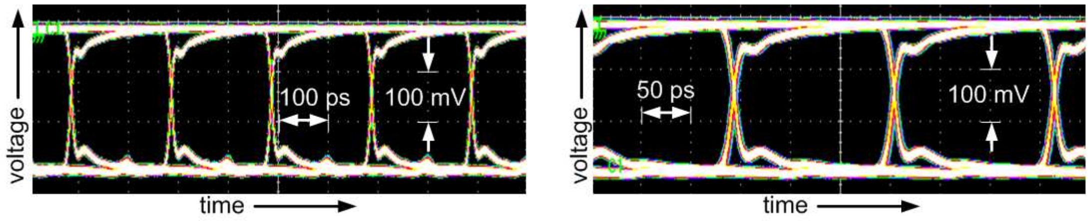

(a) Bit rate: 20 Gbit/s. (b) Bit rate: 25 Gbit/s

Figure 4.50: Eye diagram of photodiode ($D = 10\,\mu\mathrm{m}$ and $d_\mathrm{i} = 330\,\mathrm{nm}$) and flip flop for a bit rate at the photodiode of 20 Gbit/s (a) and 25 Gbit/s (b), a *PRBS* length of $2^7 - 1$ and $BER < 10^{-12}$.

Table 4.8: Data rate, *PRBS* length and *BER* achieved with the examined photodiode of sample *A*2045_2 and flip flop [92]. The wavelength is $\lambda_0 = 1550\,\mathrm{nm}$, the bias voltage $V_{\mathrm{bias}} = -2\,\mathrm{V}$.

bit rate	*PRBS* length	*BER*
10 Gbit/s	$2^{31} - 1$	$< 10^{-12}$
20 Gbit/s	$2^{7} - 1$	$< 10^{-12}$
20 Gbit/s	$2^{31} - 1$	$< 10^{-10}$
25 Gbit/s	$2^{7} - 1$	$< 10^{-12}$

The photodiode for which measurement results are presented has a diameter $D = 10\,\mu\mathrm{m}$ and a thickness of the intrinsic *Ge* region of $d_{\mathrm{i}} = 330\,\mathrm{nm}$ (sample: *A*2045_2).

For a photodiode without an adjacent flip flop [92], the eye diagram is shown in Fig. 4.49a for a bit rate of 10 Gbit/s and in Fig. 4.49b for 20 Gbit/s. The results with flip flop are presented in Fig. 4.50a for a bit rate of 20 Gbit/s and in Fig. 4.50b for 25 Gbit/s. The according *PRBS* length and the *BER* are listed in Table 4.8 as published in [93]. All measurements are done at a wavelength of $\lambda_0 = 1550\,\mathrm{nm}$ and a bias voltage of $V_{\mathrm{bias}} = -2\,\mathrm{V}$. In the following, these results are shortly compared with the results of two other publications: high data rates of up to 19 Gbit/s at a bias voltage of $-1.8\,\mathrm{V}$ across the photodiode are achieved at a wavelength of 850 nm [94]. The lateral *Ge* on *Si* photodiode is bonded to a *CMOS* amplifier stage. At 1550 nm [11], a monolithic optical receiver in 130 nm *CMOS* integrating a *Ge* waveguide photodiode obtains 10 Gbit/s. The *PRBS* length is $2^7 - 1$ and the *BER* $< 10^{-12}$ in both cases. For the 40 Gbit/s at 1550 nm reported in [3], no value for the *BER* is published for comparison.

In this work, it is the optical signal that is amplified to provide sufficiently high signals at the output of the photodiode. With an appropriate broadband amplifier stage for the photodiode current, the *EDFA* could be replaced, and the task of amplification would be mitigated to the electrical regime.

As no de-embedding is done, the frequency response of all passive electrical elements involved deteriorates the overall frequency response. These are the cables connecting the bias tee to the photodiode, the bias tee itself and the cables and adapters connecting the bias tee to the flip flop. For example, the cables in use have a loss of above 1.5 dB at 10 GHz. Thus, even higher bit rates are expected for an optimised setup where signal paths are kept as short as possible. This can be done by mounting the photodiode and the electrical complement (e.g. amplifier and/or flip flop) on the same *RF* substrate and connecting them with short bond wires.

5 Limiting Amplifier

In this chapter, a fast limiting amplifier (*LA*) that has been developed throughout this work is described. The *LA* is designed to be suitable for the amplification of the electrical output signal of the photodiode, which is thought to reduce the required optical input power of the photodiode. The *LA* is realised in a *SiGe* bipolar technology from Infineon (B7HF200) with a gate length of 180 nm. The transit frequency of the *npn* transistor is 200 GHz, the maximum oscillation frequency 250 GHz. In the first section, the boundary conditions for the design are outlined together with the circuit topology and layout of the *LA*. Then, measurement techniques and measurement results in the time domain are presented to evaluate the performance of the *LA*.

5.1 Circuit Topology

At an optical input power of 1 mW, the output voltage of the photodiode of sample *A*2045_2 with a diameter $D = 10\,\mu$m is approximately 1 mV at a 50 Ω load and a bias voltage of −2 V. The *LA* must be able to drive an undersampling flip flop if measurements are done with the setup explained in Section 4.7. Therefore, the *LA* has to provide a voltage gain of 300 for a differential output voltage swing of ±300 mV. The photodiodes have a 3 dB bandwidth of 49 GHz [91]. Hence the minimum targeted bit rate for the *LA* is 50 Gbit/s.

Fig. 5.1 shows the circuit topology and layout of one amplifier stage, here with a current source of 4 mA. One driver stage consists of a differential amplifier (*DA*) and an emitter follower (*EF*) in front of the *DA*. The *EF* operates as a level shifter and prevents that the *DA* gets into saturation. To increase the bandwidth of each amplifier stage, inductive peaking (*IP*) in the collector path is applied. As the values for the inductances are very small (15 pH to 45 pH), the inductors are realised by metal strips on the top metal layer.

The whole circuit is shown in Fig. 5.2: six driver stages with preceding *EFs* are series-connected in total, each with a gain of 3. The first 4 stages work at 4 mA, the 5th at 6 mA and the 6th at 12 mA to drive 50 Ω loads differentially with a voltage swing of ±300 mV.

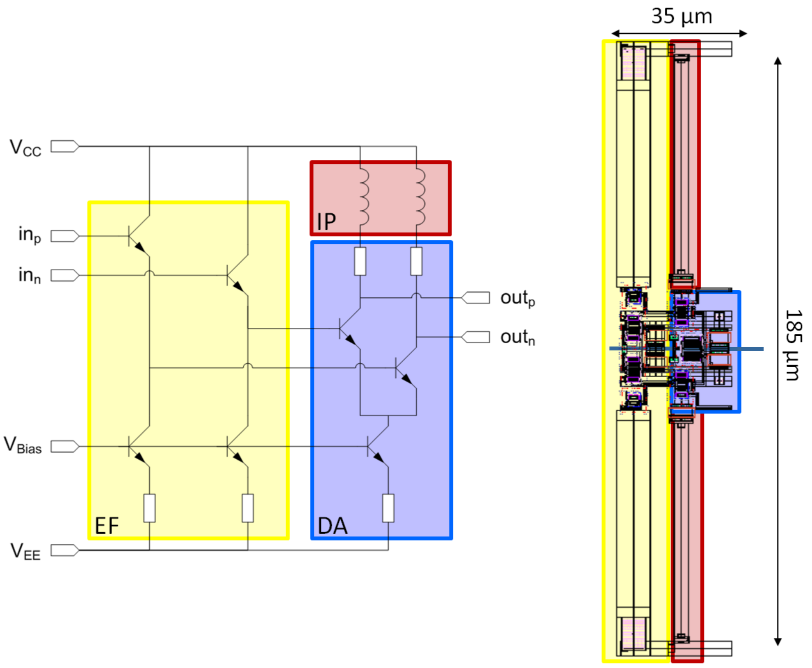

Figure 5.1: Circuit topology and layout of one 4 mA-stage of the *LA*.

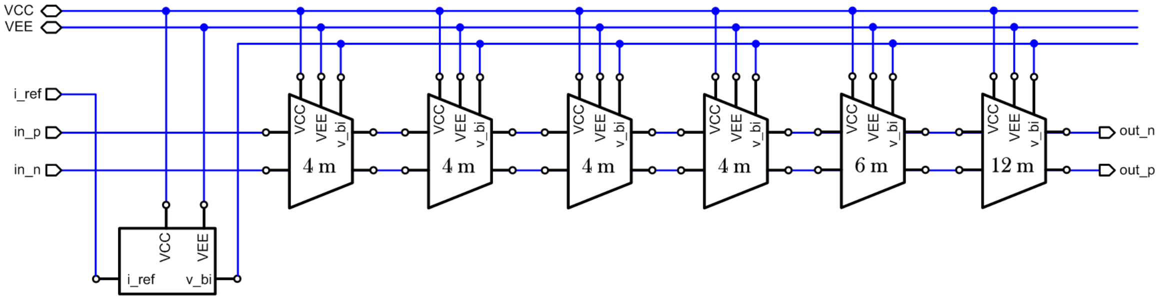

Figure 5.2: Block diagram of the whole *LA* with reference source and six driver stages.

The current of the current sources is provided via a bias current and current mirrors. The overall layout of the core of the *LA* is shown in Fig. 5.3. The core has an approximate size of $270 \times 300\,\mu\text{m}^2$.

In Fig. 5.4, the simulated eye diagram of the *LA* schematic is shown at a bit rate of 50 Gbit/s for one of the differential outputs. The temperature T is set to 45°C, which is the assumed junction temperature of the device. The eye is clearly open at these conditions.

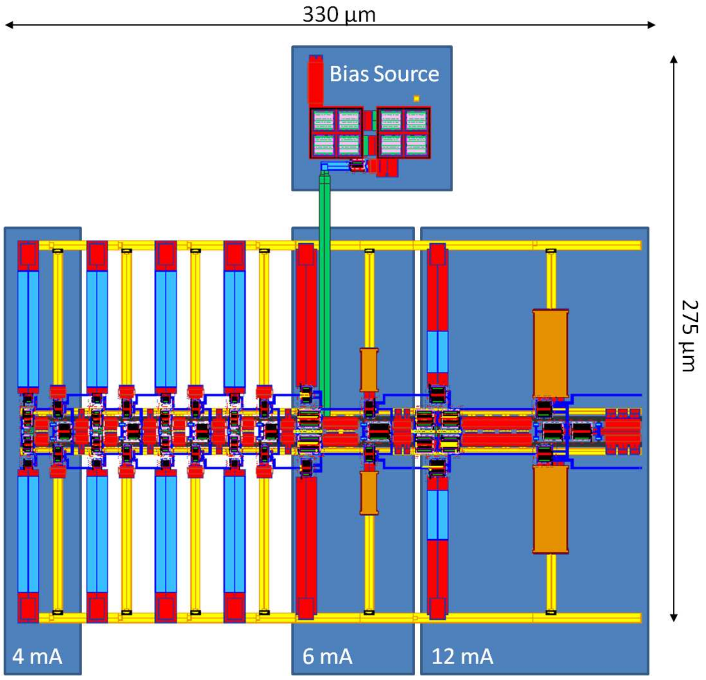

Figure 5.3: Layout of the whole *LA* core.

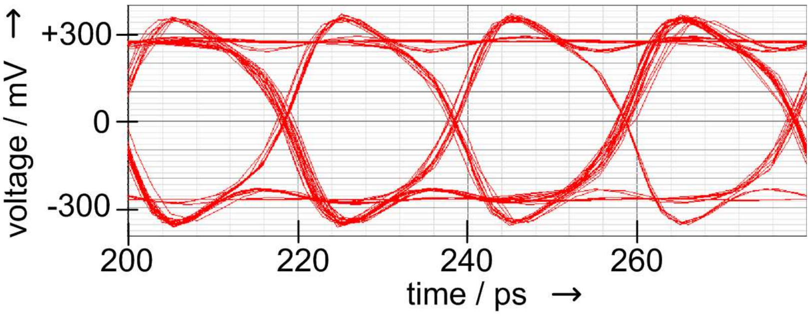

Figure 5.4: Simulated eye digaram of the *LA* schematic at a bit rate of 50 Gbit/s and a temperature of $T = 45°\text{C}$.

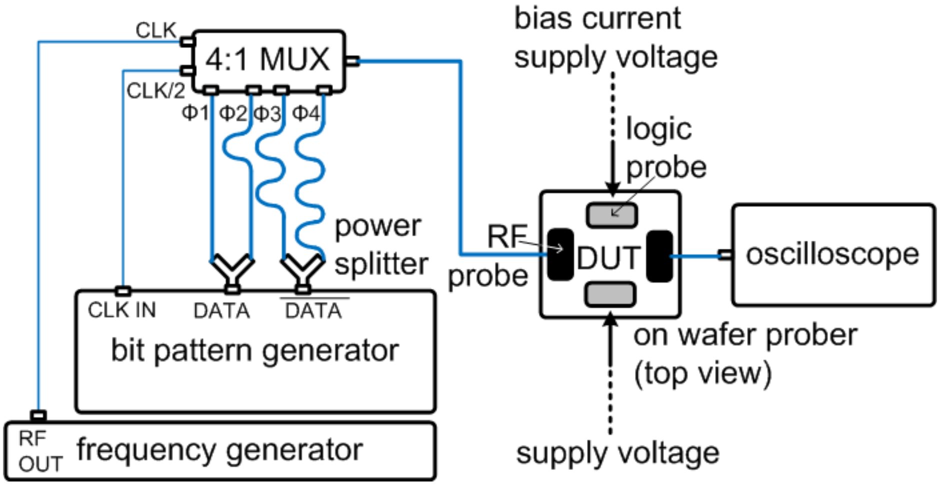

Figure 5.5: Time Domain Measurement Setup for *LA*.

5.2 Time Domain Characterisation

The measurement setup to characterise the *LA* in the time domain is depicted in Fig. 5.5. The high-speed data stream is generated in the same way as explained in Section 4.7. The output signal of the *MUX* is connected to the input of the *LA*. Both configurations, single-ended input and differential input, are examined. One output port is connected to the oscilloscope or *BERT*, the other one is terminated with 50 Ω.

In Fig. 5.6, a photograph of the final chip is shown. The chip has a total size of $580 \times 580\,\mu\text{m}^2$ and a differential input and output, both designed for *RF* probe contacting with a 100 μm pitch. Measurements with single-ended and differential input are taken. The circuit draws 100 mA at a supply voltage of −3.1 V. The input voltage of the *LA* is 45 mV and ±45 mV for single-ended and differential signals, respectively, which results as expected in an output voltage swing of ±300 mV. A lower input voltage cannot be provided by the measurement setup due to bandwidth-limited attenuators. The eyes are open for both, single-ended and differential input, at the maximum bit rate of the setup of 50 Gbit/s. This is shown in Fig. 5.7 with a *PRBS* length of $2^{31} - 1$ for both cases.

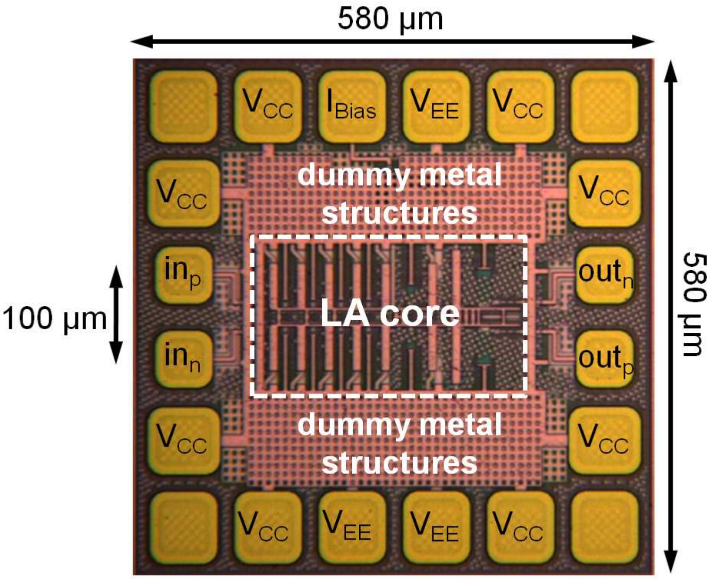

Figure 5.6: Photograph of the overall chip.

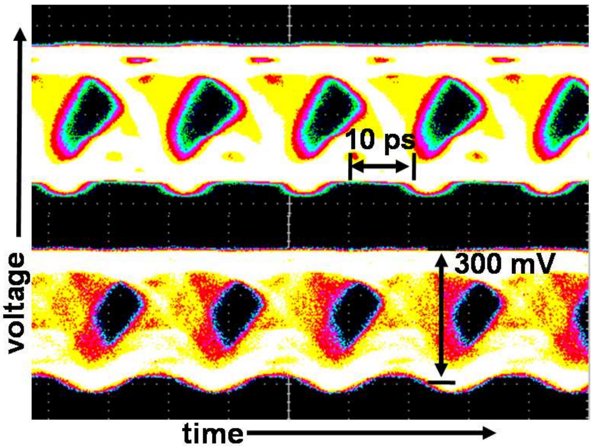

Figure 5.7: Eye diagram of the output signal of the *LA* for single-ended (top) and differential (bottom) input at a bit rate of 50 Gbit/s. The *PRBS* length is $2^{31} - 1$.

6 Grating Couplers

For the fabrication of the *PIC* structures, the *imec04* process accessible via *ePIXfab* is chosen for these investigations. The *imec04* process is suitable for passive photonic circuits and provides one crystalline *Si* layer. The description of this process can be found in [95]; it is outdated by now, and information about the current standard *imec* process is available on the *ePIXfab* homepage. The cross section of the *SOI* wafer used for the processing is shown in Fig. 6.1, together with the relevant dimensions. The process provides two etch depths for the crystalline *Si* layer: a partial one that is used in this work to define grating structures and the rib of rib waveguides, and a full one where the *Si* is etched down to the SiO_2 *BOX* layer. This etch step is used to define strip waveguides and grooves. The structures are realised with a 248 nm ultra-violet (*UV*) lithography. Additionally illustrated in Fig. 6.1 is the simulated field distribution in the *yz* plane of a grating coupler designed for the considered material system. The field plot is depicted for the E_x component for the case that the launch field is *TE* polarised. This simulation is based on *3D FDTD*.

Basic structures are designed to gain a deeper understanding of the *Si* photonic components and to evaluate the process for further applications. Of the structures that have been fabricated, grating couplers are described in this chapter. Important design parameters and their influence on the coupling efficiency are presented. Measurement setup and results are discussed afterwards.

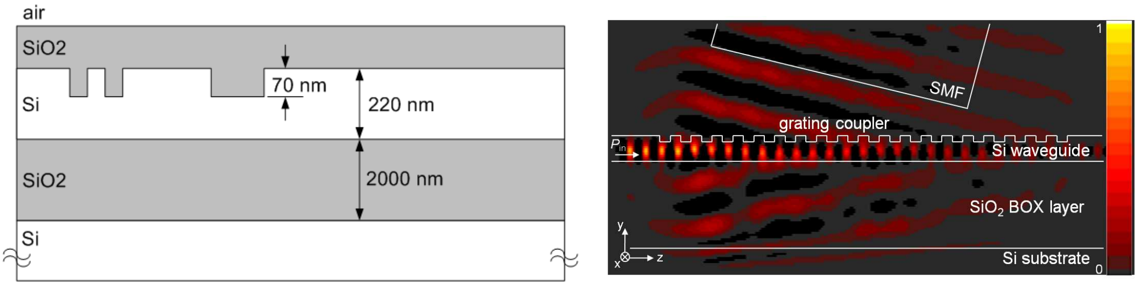

(a) Cross section of *imec04* layer stack. (b) Field plot for *TE* polarisation.

Figure 6.1: Cross section of the *SOI* wafer used in the *imec04* process as applied in this work. The passivation layer is chosen to be 500 nm thick.

6.1 Design of Grating Couplers

As two etch depths are available in the lithography process in use, simple binary gratings can be fabricated together with strip or rib waveguide structures. In terms of the coupler design, degrees of freedom are the period of the grating, g, and its duty cycle, dc. Furthermore, the influence of the fibre has to be examined: its position relative to the grating plays an important role as well as its tilt, defined relative to the surface normal. The impact of these parameters is investigated at the two wavelengths of interest, namely 1310 nm and 1550 nm. Investigations at the wavelength 1550 nm for a stack without SiO_2 passivation and a BOX thickness of $2\,\mu$m can be found in [96], based on [68]. In [68], the BOX thickness is $1\,\mu$m. The calculations in this work at hand are based on *2D EEM*, using source code for *CAMFR* from [68], pp. 147. The gratings are designed for *TE* polarisation.

In the following, optimised geometric parameters in terms of a high coupling efficiency for grating couplers at $\lambda_0 = 1310\,\text{nm}$ and $\lambda_0 = 1550\,\text{nm}$ are shown for the *SOI* stack in Fig. 6.1a. The optimum incident angle is also retrieved from simulations. For these simulations, an additional layer on top of the considered layer stack is applied like in [68]. It has a refractive index of 1.46 for refractive index matching with the glass fibre. This layer represents a glue that can be used to fix the fibre onto the grating coupler. According to [68], p. 47, simulations become less precise if no refractive index matching is applied, which is the case if applying air as surrounding material. This is why all simulations displayed here are done with this matching layer. Results for the coupling efficiency are assumed to be higher in this case compared to results with air between fibre and stack, as reflexions are reduced.

As already stated, the coupling efficiency that is determined for different geometric parameters is based on *2D* simulations. If additionally the width of the grating and thus the underlying waveguide comes into play, a correction factor has to be applied [68]: the smaller the width of the grating, the lower is the coupling efficiency for a fibre with fixed beam waist. For a grating with a width of $10\,\mu$m, the correction factor is $\zeta = 0.93$ according to [68], p. 48.

The parameters that are examined first and foremost are the grating period g and the duty cycle dc. For the optimum combination of these two parameters in the given stack and the corresponding optimum incident angle, the minimum number of grating periods is defined. The influence of the thickness of different layers on the simulation results is checked afterwards. For all simulations, *TE* polarisation of the incident light is assumed. The position of the fibre along the waveguide is additionally swept in all simulations; for the optimum position, the coupling efficiency is presented.

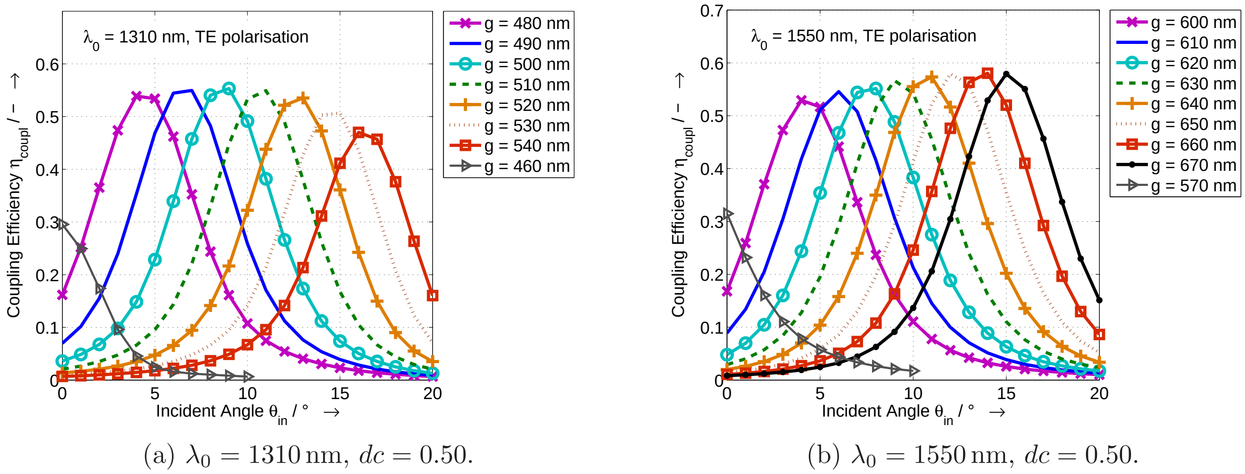

(a) $\lambda_0 = 1310\,\mathrm{nm}$, $dc = 0.50$. (b) $\lambda_0 = 1550\,\mathrm{nm}$, $dc = 0.50$.

Figure 6.2: Coupling efficiency η_{coupl} versus incident angle θ_{in} for different grating periods g. The incoming light is *TE*-polarised at a wavelength of $\lambda_0 = 1310\,\mathrm{nm}$ (a) and $\lambda_0 = 1550\,\mathrm{nm}$ (b). The duty cycle is $dc = 0.50$ for both wavelengths.

6.1.1 Grating Period

The grating period mainly determines the wavelength range for which the grating couples best into the waveguide mode. In Fig. 6.2, the coupling efficiency η_{coupl} is plotted versus the incident angle θ_{in} for different periods g. This is done for $\lambda_0 = 1310\,\mathrm{nm}$ and $\lambda_0 = 1550\,\mathrm{nm}$. The layer thicknesses correspond to Fig. 6.1a. The duty cycle is $dc = 0.50$, and the incident light is *TE*-polarised for both wavelengths. It can be seen that at small incident angles close to 0°, the smaller periods provide a higher coupling efficiency than the larger periods, which is vice versa at higher incident angles around 20°. Hence the coupling efficiency for a given period can be increased by adjusting the incident angle properly. However, Fig. 6.2 shows that the respective optimum combination of g and θ_{in} yields different maximum values for η_{coupl} at both wavelengths. From this figure, the best combination of angle and period is $\theta_{\mathrm{in}} = 9°$ and $g = 500\,\mathrm{nm}$ for $\lambda_0 = 1310\,\mathrm{nm}$. For $\lambda_0 = 1550\,\mathrm{nm}$, the best result is achieved for an angle of $\theta_{\mathrm{in}} = 14°$ and a period of $g = 660\,\mathrm{nm}$. Only integer values for the incident angle are considered for this choice. The coupling efficiency reaches values of about 55% for $\lambda_0 = 1310\,\mathrm{nm}$ and 58% for $\lambda_0 = 1550\,\mathrm{nm}$ in the *2D* simulations.

As vertical coupling is very attractive in terms of the assembly of fibre and photonic chip, Fig. 6.2 also displays the maximum coupling efficiency for an incident angle of $\theta_{\mathrm{in}} = 0°$ with corresponding optimum grating period g. In these *2D* simulations, only about 30 % coupling efficiency can be obtained for both wavelengths at vertical light incidence.

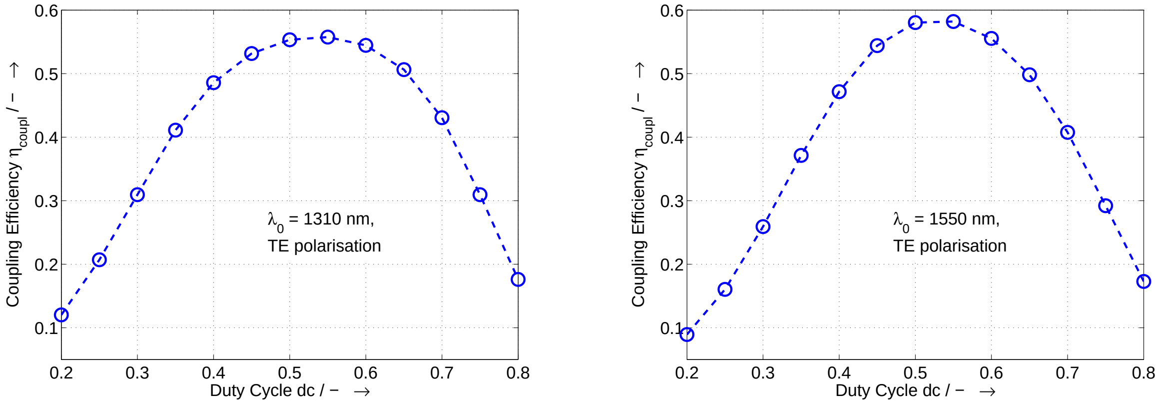

(a) $\lambda_0 = 1310\,\mathrm{nm}$, $g = 500\,\mathrm{nm}$, $\theta_{\mathrm{in}} = 14°$.

(b) $\lambda_0 = 1550\,\mathrm{nm}$, $g = 660\,\mathrm{nm}$, $\theta_{\mathrm{in}} = 9°$.

Figure 6.3: Coupling efficiency η_{coupl} versus duty cycle dc at a wavelength of $\lambda_0 = 1310\,\mathrm{nm}$ (a) and $\lambda_0 = 1550\,\mathrm{nm}$ (b) for optimum grating period g and incident angle θ_{in}.

6.1.2 Duty Cycle

The duty cycle dc primarily has an influence on the effective refractive index of the grating. In Fig. 6.3, the coupling efficiency η_{coupl} is plotted versus dc for $\lambda_0 = 1310\,\mathrm{nm}$ and $\lambda_0 = 1550\,\mathrm{nm}$. It can be seen that the optimum duty cycle is 0.55 for both wavelengths for optimum grating period g and incident angle θ_{in} as chosen in the last subsection.

If variations in the etch process occur such that the designed structures become wider or smaller than intended, the grating period remains constant, whereas the duty cycle changes. Therefore, it is interesting to observe the change in the coupling efficiency if the duty cycle deviates from its optimum value $dc = 0.55$: for a deviation of $\pm 9\%$, one loses 5% of the maximum coupling efficiency. For a deviation of $\pm 18\%$, 15% of the maximum η_{coupl} are lost. Small deviations from the optimum value of the duty cycle can be compensated for the fabricated structure by readjusting the tilt of the fibre. This is revealed in Fig. 6.4, where η_{coupl} is plotted versus the incident angle and dc is swept.

6.1.3 Number of Periods

Depending on the incident beam shape, the grating needs a certain extension along the waveguide to collect all the light that is incident on the structure. In Fig. 6.5, the coupling efficiency η_{coupl} is plotted versus the number of periods for the derived optimum period, duty cycle and tilt at $\lambda_0 = 1310\,\mathrm{nm}$ and $\lambda_0 = 1550\,\mathrm{nm}$. As can be seen from this figure, the coupling efficiency starts to saturate at a number of about 20 periods. If the number of

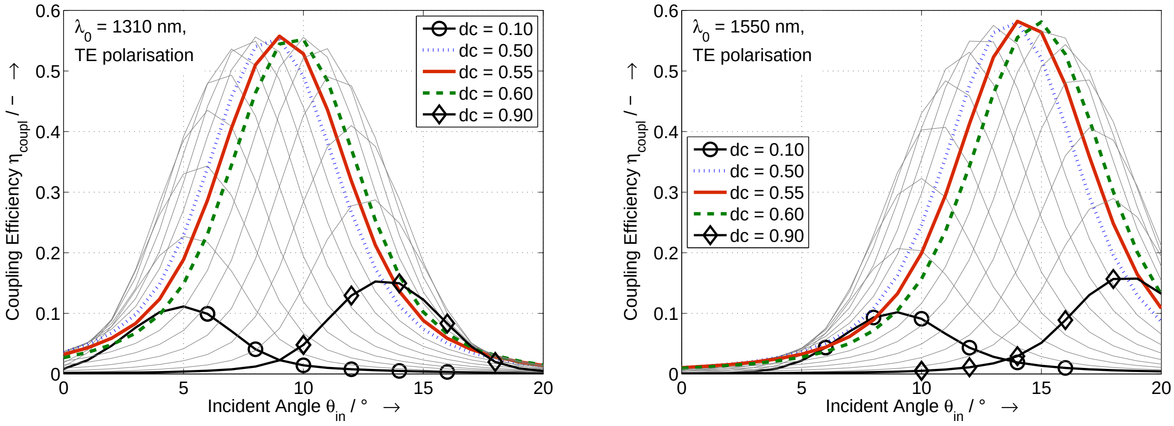

(a) $\lambda_0 = 1310\,\text{nm}$, $g = 500\,\text{nm}$.

(b) $\lambda_0 = 1550\,\text{nm}$, $g = 660\,\text{nm}$.

Figure 6.4: Coupling efficiency η_{coupl} versus incident angle θ_{in} for different duty cycles dc. The incoming light is TE-polarised at a wavelength of $\lambda_0 = 1310\,\text{nm}$ (a) and $\lambda_0 = 1550\,\text{nm}$ (b).

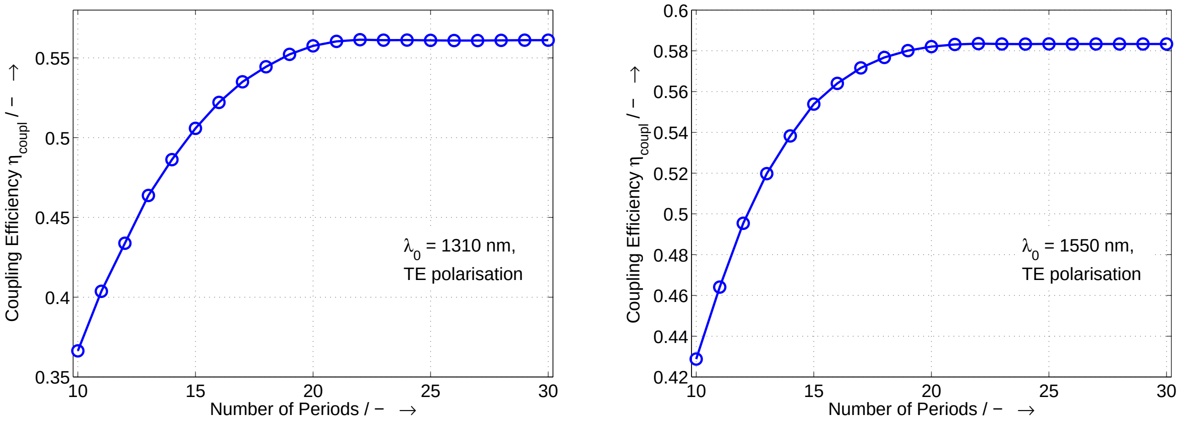

(a) $\lambda_0 = 1310\,\text{nm}$, $g = 500\,\text{nm}$, $dc = 0.55$, $\theta_{\text{in}} = 9°$.

(b) $\lambda_0 = 1550\,\text{nm}$, $g = 660\,\text{nm}$, $dc = 0.55$, $\theta_{\text{in}} = 14°$.

Figure 6.5: Coupling efficiency η_{coupl} versus number of grating periods for an optimised grating at $\lambda_0 = 1310\,\text{nm}$ and $\lambda_0 = 1550\,\text{nm}$.

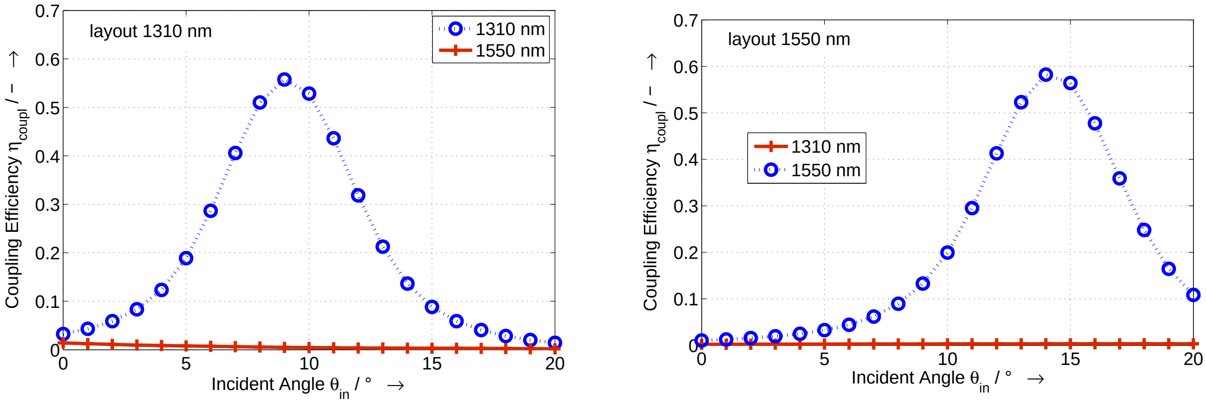

(a) Optimised grating for 1310 nm.

(b) Optimised grating for 1550 nm.

Figure 6.6: Coupling efficiency η_{coupl} versus incident angle θ_{in} for optimised grating at 1310 nm (a) and 1550 nm (b) and *TE* polarisation. For each grating, both wavelengths are considered.

periods becomes too high, the light might be coupled out again. Hence a number of periods close to the saturation point should be chosen, which is 21 in the given case.

6.1.4 Wavelength Diversity and Bandwidth

The optimised grating couplers for $\lambda_0 = 1310$ nm and $\lambda_0 = 1550$ nm are now examined regarding their diversity in terms of the wavelength. In Fig. 6.6, their coupling efficiency η_{coupl} is plotted versus the incident angle θ_{in}. The wavelength is set once to $\lambda_0 = 1310$ nm and once to $\lambda_0 = 1550$ nm for both gratings. The figure shows that the grating lets only pass the desired wavelength, independent of the chosen angle of incidence in the examined range of angles. In Fig. 6.7, the coupling efficiency for both optimised gratings is plotted versus the wavelength λ_0 for a wavelength range from 1290 nm to 1580 nm. The corresponding optimum tilt is set. It can be seen that the grating works well for the target wavelength range while the other wavelengths are suppressed. This low cross talk is important for applications where both wavelengths are sent over the same fibre.

From these considerations, the coupling efficiency of the optimised gratings is 55.8% and 58.2% for $\lambda_0 = 1310$ nm and $\lambda_0 = 1550$ nm, respectively, for *2D* simulations. Taking into account the finite width of the grating (10 μm) by the correction factor $\zeta = 0.93$, the coupling efficiencies become 51.9% and 54.1%, respectively. The corrected coupling efficiencies are displayed in Fig. 6.7 for $\lambda_0 = 1310,$ nm and $\lambda_0 = 1550,$ nm together with the corresponding 1 dB and 3 dB bandwidths. The 1310 nm grating provides a 1 dB (3 dB) of 35 nm (> 50 nm), the 1310 nm grating has a 1 dB (3 dB) bandwidth of 43 nm (> 68 nm).

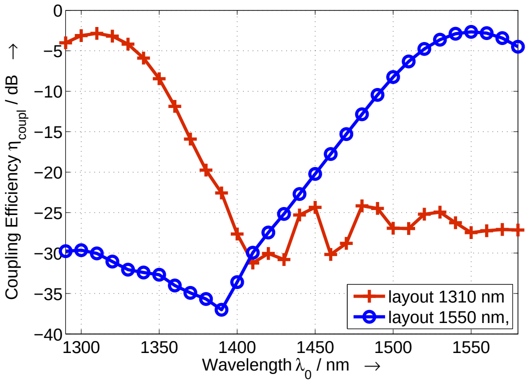

(a) Optimised grating for 1310 nm/1550 nm versus wavelength λ_0.

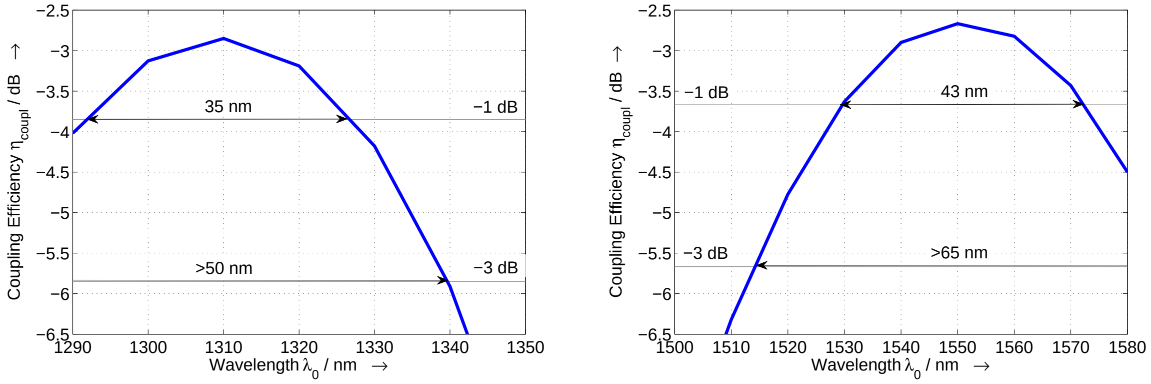

(b) Optimised grating for $\lambda_0 = 1310$ nm: 1 dB/3 dB bandwidth.

(c) Optimised grating for $\lambda_0 = 1550$ nm: 1 dB/3 dB bandwidth.

Figure 6.7: Coupling efficiency η_{coupl} versus wavelength λ_0 for optimised grating parameters and optimum incident angle θ_{in}. The grating designed for $\lambda_0 = 1310$ nm and $\lambda_0 = 1550$ nm is considered for a grating width of 10 μm (a). For this corrected coupling efficiency, the 1 dB and 3 dB bandwidth are shown for $\lambda_0 = 1310$ nm (b) and $\lambda_0 = 1550$ nm (c).

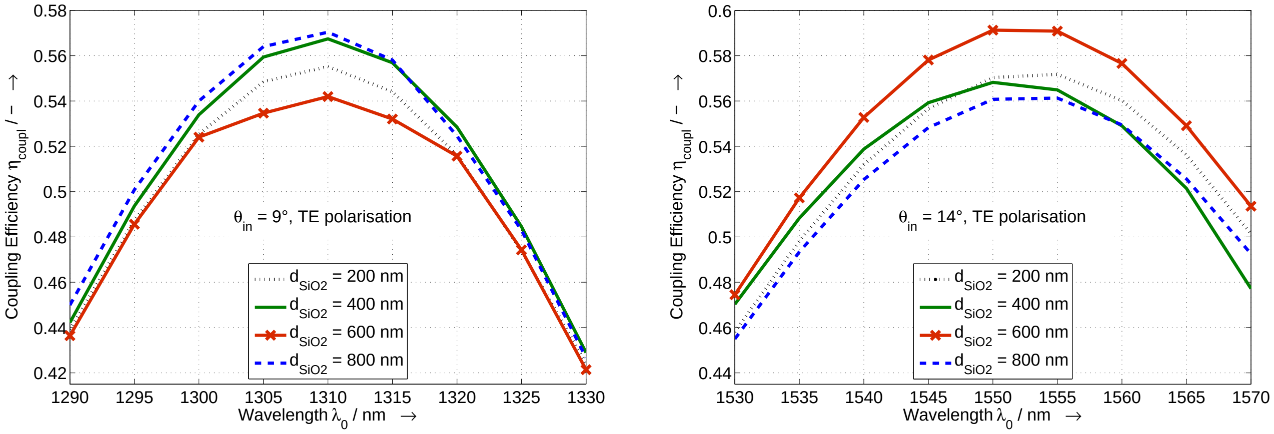

(a) $g = 500\,\text{nm}$, $dc = 0.55$, $\theta_{\text{in}} = 9°$.

(b) $g = 660\,\text{nm}$, $dc = 0.55$, $\theta_{\text{in}} = 14°$.

Figure 6.8: Coupling efficiency η_{coupl} versus wavelength λ_0 around 1310 nm (a) and 1550 nm (b). The optimised grating period g, duty cycle dc and incident angle θ_{in} are applied for both wavelengths. The thickness of the top SiO_2 layer is swept. The Si top layer is 220 nm thick and the BOX layer 2 μm.

6.1.5 Thickness of Layers

The last pages of this section highlight the influence of the thickness of layers on the grating properties. Not all of these thicknesses can be influenced by the designer in the given technology run, as the wafers are provided by *imec*. However, by varying these geometric parameters in the design process, the effect of fabrication tolerances on the coupling performance is reflected. Furthermore, more suitable wafer dimensions for future designs can thus be found.

6.1.5.1 Thickness of SiO_2 Passivation Layer

In the given process, an SiO_2 passivation layer is deposited after the lithograpy steps. For the sake of simplicity, the passivation is assumed to be planarised in the *2D* simulations, which is not the case for the fabricated structures. The thickness of the passivation layer is swept in Fig. 6.8 for the optimised grating coupler at $\lambda_0 = 1310\,\text{nm}$ and $\lambda_0 = 1550\,\text{nm}$, and the coupling efficiency is plotted versus the wavelength. According to this figure, the thickness of the passivation layer influences the achievable coupling efficiency η_{coupl}, most probably due to thickness dependent reflexion losses. However, a wavelength shift of the maximum value of the coupling efficiency is not observed for varying top SiO_2 thickness.

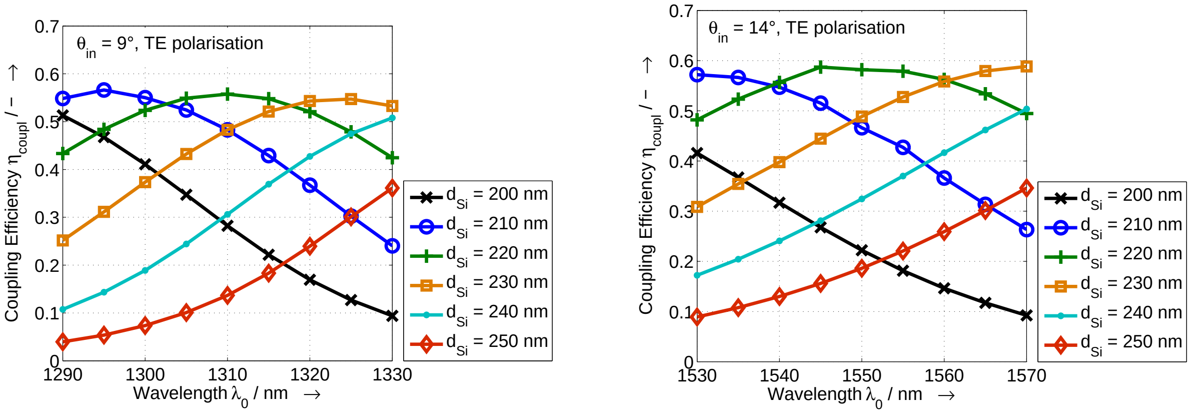

(a) $g = 500\,\mathrm{nm}$, $dc = 0.55$, $\theta_{\mathrm{in}} = 9°$.

(b) $g = 660\,\mathrm{nm}$, $dc = 0.55$, $\theta_{\mathrm{in}} = 14°$.

Figure 6.9: Coupling efficiency η_{coupl} versus wavelength λ_0 around 1310 nm (a) and 1550 nm (b). The optimised grating period g, duty cycle dc and incident angle θ_{in} are applied for both wavelengths. The thickness of the top *Si* layer is swept. The passivation layer is 500 nm thick and the *BOX* layer $2\,\mu$m.

6.1.5.2 Thickness of Si Top Layer

The thickness of the top *Si* layer of the *SOI* wafers has a fabrication tolerance of ±20 nm. The influence of a change of this thickness becomes obvious in Fig. 6.9 where η_{coupl} is plotted versus λ_0 for optimised gratings and the *Si* thickness swept: for increasing thickness, the maximum of η_{coupl} is shifted to higher wavelengths and vice versa. In Fig. 6.10, the influence on the incident angle θ_{in} is revealed if the wavelength is kept fixed ($\lambda_0 = 1310\,\mathrm{nm}$ and $\lambda_0 = 1550\,\mathrm{nm}$): with increasing thickness of the *Si* top layer, the maximum of η_{coupl} is shifted to larger incident angles. A change of 10 nm in thickness corresponds to a change of approximately 20 nm in the wavelength.

6.1.5.3 Thickness of SiO_2 Buried Oxide Layer

Next, the thickness of the SiO_2 *BOX* layer is swept for $\lambda_0 = 1310\,\mathrm{nm}$ and $\lambda_0 = 1550\,\mathrm{nm}$. The other grating parameters are set to their optimum values. According to Fig. 6.11, the coupling efficiency changes periodically with the thickness of the *BOX*. This is to be expected as the *SOI* wafer represents a Bragg reflector. For a change in the *BOX* thickness of $\frac{\lambda_0}{4n_{\mathrm{SiO2}}}$, η_{coupl} varies between minimum and maximum value. For $\lambda_0 = 1310\,\mathrm{nm}$, the $\frac{\lambda_0}{4n_{\mathrm{SiO2}}}$-thickness of the SiO_2 *BOX* is 220 nm, for $\lambda_0 = 1550\,\mathrm{nm}$, it is 270 nm, which is confirmed by the figure. It can also be observed that the coupling efficeincy is zero if the *BOX* layer becomes too thin, as then the light is lost to the substrate.

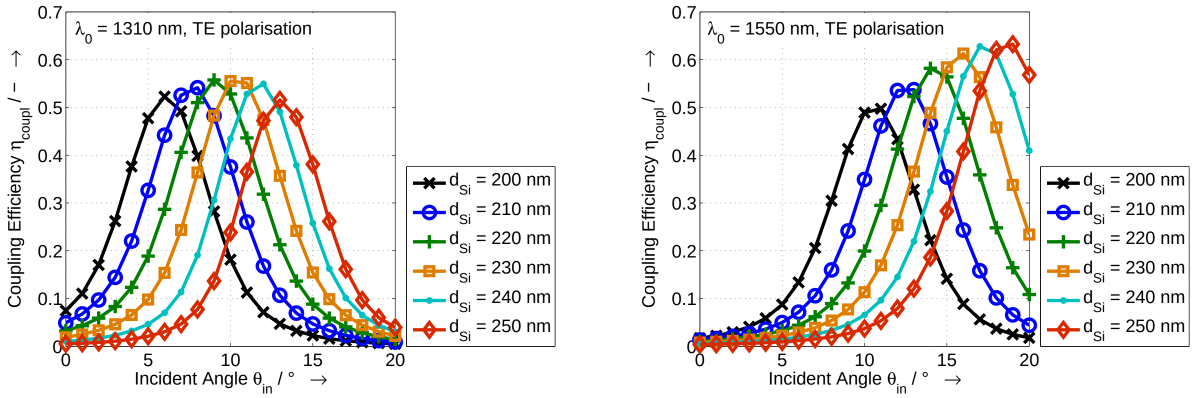

(a) $\lambda_0 = 1310\,\text{nm}$, $g = 500\,\text{nm}$, $dc = 0.55$. (b) $\lambda_0 = 1550\,\text{nm}$, $g = 660\,\text{nm}$, $dc = 0.55$.

Figure 6.10: Coupling efficiency η_{coupl} versus incident angle θ_{in} at $\lambda_0 = 1310\,\text{nm}$ (a) and $\lambda_0 = 1550\,\text{nm}$ (b) for optimised grating period g and duty cycle dc for both wavelengths. The thickness of the top Si layer is swept. The passivation layer is 500 nm thick and the BOX layer $2\,\mu\text{m}$.

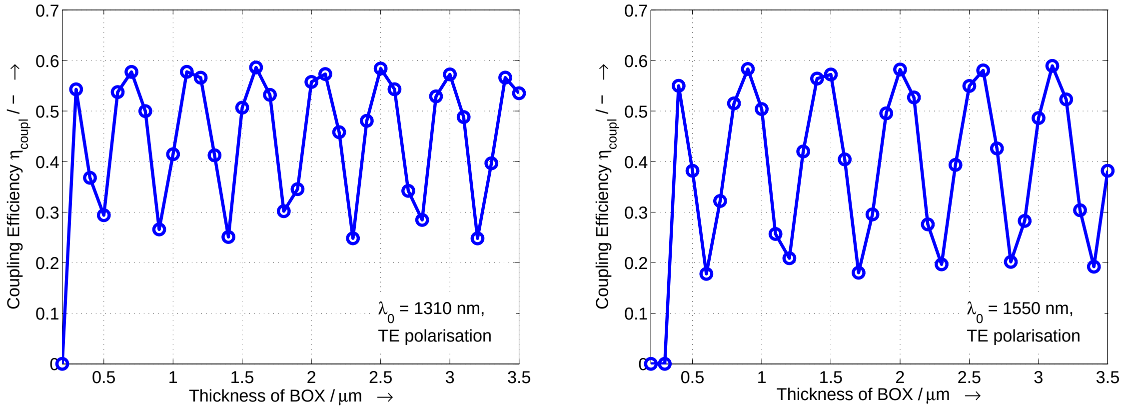

(a) $\lambda_0 = 1310\,\text{nm}$, $g = 500\,\text{nm}$, $dc = 0.55$, $\theta_{\text{in}} = 9°$.(b) $\lambda_0 = 1550\,\text{nm}$, $g = 660\,\text{nm}$, $dc = 0.55$ $\theta_{\text{in}} = 14°$.

Figure 6.11: Coupling efficiency η_{coupl} versus the thickness of the SiO_2 BOX layer for $\lambda_0 = 1310\,\text{nm}$ and $\lambda_0 = 1550\,\text{nm}$ and corresponding optimised grating period$g$, duty cycle dc and θ_{in}. The passivation layer is 500 nm thick and the Si top layer 220 nm.

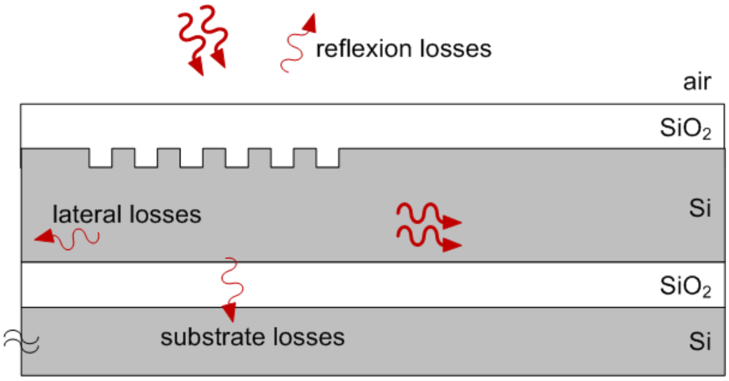

Figure 6.12: *SOI* grating coupler, cross section: latera losses, reflexion losses and losses down to the substrate.

6.1.6 Measures to Increase Coupling Efficiency

The simple *1D* binary grating examined in this work has three important loss factors which are inherent to the structure itself. They are shown in Fig. 6.12: the light coupled into the waveguide propagates in both directions of the waveguide, not only into the desired one. These are the lateral losses. Part of the light is also reflected back if the refractive indices of fibre, index matching glue and SiO_2 are not completely identical. Finally, a large portion of the light is lost to the substrate, even if the thickness of the *BOX* layer is optimised.

Some means to improve this structure and face the described losses are announced in literature: lateral losses are suggested to be reduced by a rear reflector [68]. This reflector is realised by another grating placed next to the grating coupler but on the unused side of the waveguide. To minimise reflexion losses at the surface of the coupler, mirror layers above the waveguide are applied [68]. Furthermore, apodised gratings emulate better the Gaussian beam shape of the incident beam [68]. To reduce the substrate losses, a bragg mirror below the waveguide is proposed [68]. Even better results are achieved with a gold mirror using bonding techniques [97].

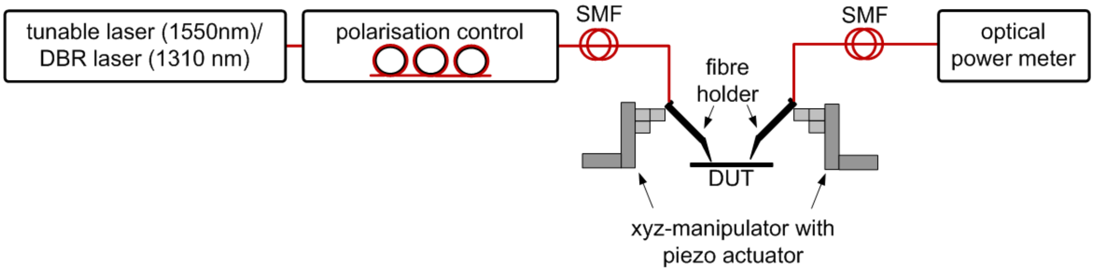

Figure 6.13: Measurement setup to characterise the optical transmission behaviour of the *PICs*.

6.2 Optical Transmission Characterisation

The *PICs* fabricated in the *imec04* process are measured with the setup shown in Fig. 6.13. The polarisation of the *CW* light provided by a tunable 1550 nm or a fix 1310 nm laser source is adjusted by a polarisation controller. Via a *SMF* or *PMF* in a fibre holder it enters the *PIC*. The *xyz*-position of the fibre holder can be changed by manipulators that are steered with the help of piezo elements and a control unit. The tilt of the fibre can be changed by rotating the fibre holder manually. Due to mechanical restrictions, not all angles can be set. With a second fibre, assembled in the same way, the light that is coupled out of the *PIC* is directed to an optical power meter. This output power together with the input power that is provided by the laser have to be known to calculate the overall losses of the transmission system.

Fig. 6.14a shows the test structure that is used to characterise the transmission behaviour of the grating couplers, based on [95]. The linar taper is responsible for the mode conversion between 10 μm wide and 500 nm wide single-mode waveguide. Losses of taper and waveguide are neglectable, all measured losses are attributed to the grating couplers. In Fig. 6.14b, the photograph of one grating coupler is depicted (top view). The grating itself has a size of approximately $15 \times 10\,\mu\text{m}^2$; the dimensions of the underlying waveguide are $50 \times 10\,\mu\text{m}^2$.

In Fig. 6.15, the measured transmission and the resulting coupling efficiency of the reference grating coupler for $\lambda_0 = 1550\,\text{nm}$ [95] is plotted versus the wavelength λ_0. The incident angle is chosen to be 13° as here maximum coupling efficiency has been measured for grating couplers in one area of the wafer [98]. The expected optimum angle for this grating period is, however, $\theta_{\text{in}} = 9°$ for this wavelength, see Fig. 6.2. The resulting coupling efficiency is $\eta_{\text{coupl}} = 35\%$, assuming the same coupling efficiency for input and output grating coupler and neglectable losses of tapers and waveguides. The 1 dB bandwidth results to be at leat 35 nm while the 3 dB bandwidth is at least 45 nm.

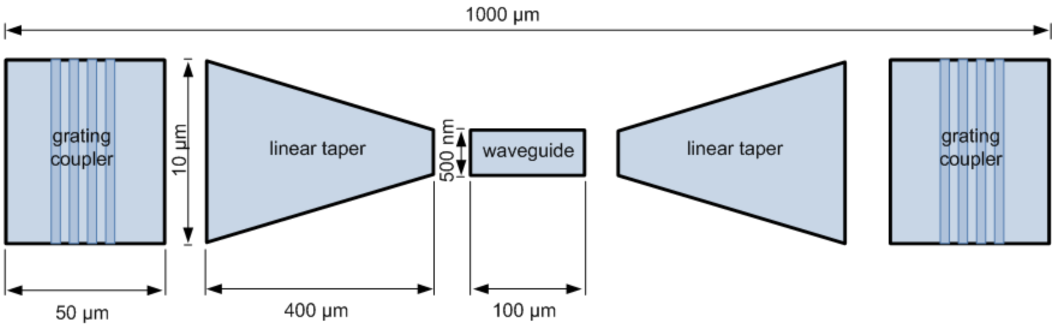

(a) Schematic of test structure to characterise grating coupler.

(b) Top view of fabricated grating coupler.

Figure 6.14: Characterised grating couplers: schematic of test structure (a) and photograph of one coupler (b).

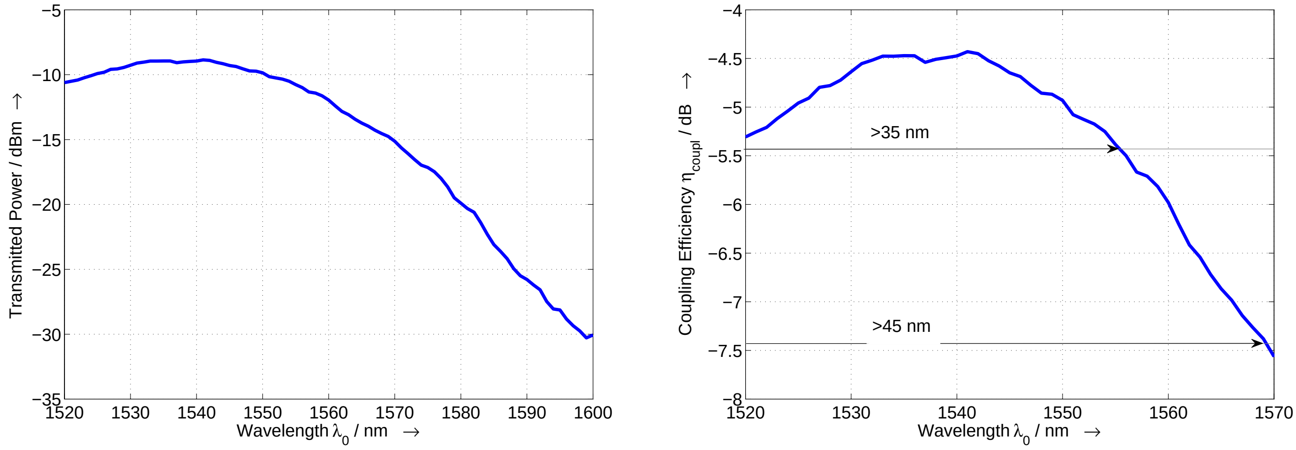

(a) Measured transmitted power.

(b) 1 dB and 3 dB bandwidth.

Figure 6.15: Measured transmitted power versus wavelength λ_0 of a 1550 nm grating coupler with a period of $g = 630\,\text{nm}$ and a duty cycle of $dc = 0.50$ (a). The incident angle is $\theta_{\text{in}} = 13°$, the polarisation is TE and the optical input power is 1 mW. The measured 1 dB and 3 dB bandwidth of this coupler is also indicated (b).

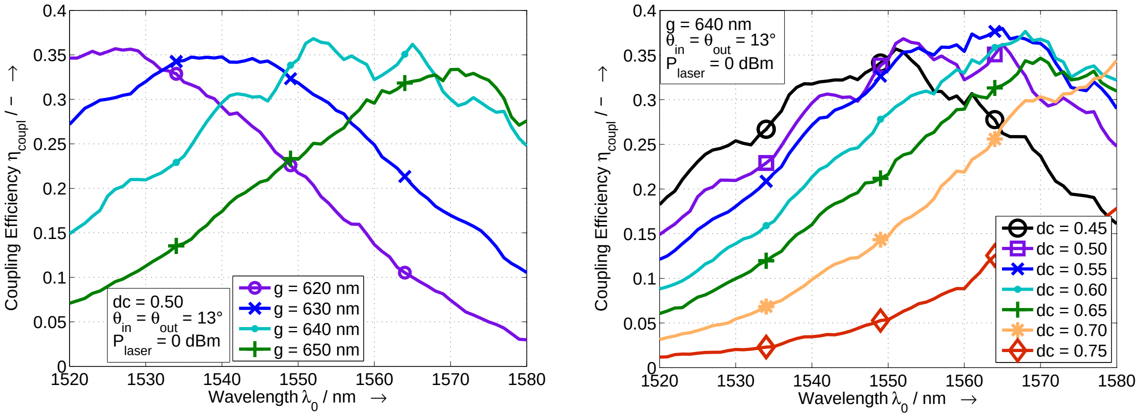

(a) Sweep g, $dc = 0.5$

(b) Sweep dc, $g = 640\,\text{nm}$.

Figure 6.16: Measured transmitted power versus wavelength λ_0 for a 1550 nm-grating coupler with period g (left) and duty cycle dc (right) swept. The incident angle is $\theta_{\text{in}} = 13°$, the polarisation is TE and the optical input power is 1 mW.

Table 6.1: Critical dimensions of the wafer processed at *imec*.

Iso Line / nm	Actual Width / nm (left to right on wafer)						
	col. −3	col. −2	col. −1	col. 0	col. +1	col. +2	col. +3
500	482	463	451	438	431	413	394

The period and duty cycle are used as parameters for the sweep over the wavelength in Fig. 6.16. The according simulation results are shown in Fig. 6.17. The comparison of Fig. 6.16 with Fig. 6.17 shows that the general behaviour of measurements and simulations agrees well. However, the maximum values of the measurement results are shifted to longer wavelengths compared to the simulations. Additionally, the coupling efficiency is lower for the measured results, namely about 35% (simulated and corrected $\eta_{\text{coupl}} \approx 50\%$).

For the explanation of these effects, the actual width of an iso line with a nominal width of 500 nm is listed in Table 6.1 for the wafer processed at *imec*. This iso line is equivalent to the standard strip waveguide that is used to characterise the grating couplers. According to these values, the width increases from the right side of the wafer (column +3) to the left of the wafer (column −3). It never exceeds the predefined value of 500 nm. The ridges of the grating are affected in the same way as the waveguides: the width of the ridges decreases from left to right on the wafer. The grating period does not change due to this fact. The duty cycle, however, decreases from left to right. According to Fig. 6.17a, the maximum value of η_{coupl} moves to shorter wavelengths for decreasing duty cycle. However, the measured structures lie on the very left side of the wafer; hence the thickness of the iso line should almost coincide with the specified one.

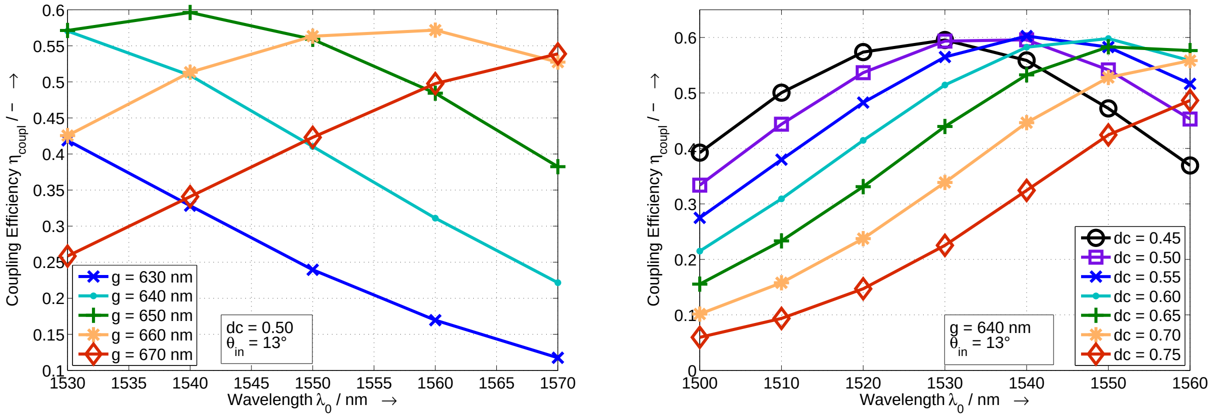

(a) Sweep g, $dc = 0.50$.

(b) Sweep dc, $g = 640\,\text{nm}$.

Figure 6.17: Simulated coupling efficiency η_{coupl} versus wavelength λ_0 for a 1550 nm-grating coupler with period g (left) and duty cycle dc (right) swept. The incident angle is $\theta_{\text{in}} = 13°$, the polarisation is *TE*.

A wavelength shift to longer wavelengths can further be explained by an increased thickness of the *Si* layer compared to the nominal thickness. For a shift from 1530 nm in simulations to 1550 nm in measurements as here observed, the actual thickness of the *Si* layer must be 230 nm instead of the nominal thickness 220 nm. This difference of 10 nm can easily be explained by fabrication variations.

Last but not least, simulations assume a refractive index matched environment around the grating: simulations are not made with air as background material. As with air additional resonances occur that are wavelength dependent, also this fact might have an impact on the overall wavelength shift. In any case, this difference between simulation and measurements accounts for the reduced coupling efficiency.

For the 1310 nm gratings, measurements can only be done at one wavelength with the given measurement setup. The actual wavelength provided by the available *DBR* laser is determined via spectrum analysis to be around 1300 nm. For the reference 1310 nm-grating coupler design from *imec*, which has a grating period of $g = 520\,\text{nm}$ and a duty cycle of $dc = 0.50$, the optimum input/output tilt of the fibre is determined as follows: the incident angle onto the input grating coupler is fixed to 15°, which is close to the expected optimum angle. The tilt of the fibre above the output coupler is swept. Results fór this sweep are shown in Fig. 6.18. After the value for the output tilt for maximum coupling efficiency is found, the input tilt is set to the same value. The maximum occuring coupling efficiency is hence about 40%.

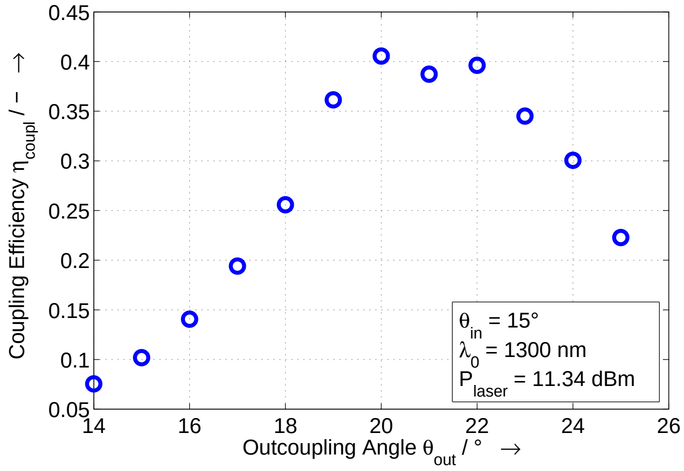

Figure 6.18: Measured coupling efficiency of a 1310 nm-grating coupler with $g = 530$ nm and $dc = 0.50$. The tilt of the output fibre is swept while the tilt of the input fibre is kept constant.

7 Conclusions

In several areas, reliable data transmission at high bit rates is needed. The applications for optical transmission go from sensors to long haul communications as well as very short interconnects heading even towards on-board links.

In this work, research is done for the build-up of such fast optical receivers. Elements in the pure optical range as well as the opto-electrical converter and devices in the electrical regime are designed and characterised.

To be able to define requirements for a fast optical receiver, the optical transmission system and its components are introduced in Chapter 2. It becomes obvious that integrated photonic circuits are crucial in the successful design of receivers. This is especially true if the receivers are based on advanced modulation formats, combined with several multiplex methods and different detection schemes. However, if a simple architecture is preferred, fast *OOK* is still an option. Thus, photodiodes suitable for vertical coupling and *OOK* are investigated here as well as photonic building blocks intended for phase detectors.

An introduction into important properties of electromagnetic waves is provided. It is demonstrated that the complex refractive index plays a decisive role in terms of absorption, reflexion and diffraction in the considered material stacks. The choice of material is justified by comparing different materials and illustrating their application in this work. As the main focus in this work lies on the opto-electrical converter with strong emphasis on characterisation and modelling, the diode and its electrical behaviour is presented.

In Chapter 3, three essential building blocks are explained in more detail. First, the photodiode is highlighted. Responsivity and bandwidth are considered as the two important ambivalent properties of the photodiode. Possible loss mechanisms due to coupling are shown.

For the design of *PICs*, the most relevant element is a waveguide. It must be designed to be single-mode, hence this property is considered for two different types of waveguides, namely strip and rib waveguide.

Different applications of diffraction gratings are examined in this work, and thus different simulation approaches are taken. The calculation methods on which the software in use is based are shortly described.

The *IHT Ge* on *Si pin* photodiodes are investigated in Chapter 4. The knowledge of the device structure provides the basis for the development of simulation models applicable in circuit simulators. The circuit simulator that is chosen to implement the models is *ADS* from Agilent Technologies. The simulation models that have been developed by M. Jutzi are the fundament for further considerations. The *DC* and small signal model are both extended in this work: the *DC* model includes an additional exponential voltage dependence of the dark current now, and the small signal model takes into account the transit time of the carriers.

The impact of different materials and the influence of zero- and one dimensional gratings on the responsivity of the photodiode are theoretically examined. The gratings prove to be very resonant solutions for which the external coupling efficiency can at least be tripled.

The central part of Chapter 4 deals with the characterisation of the photodiodes. Measurements of the dark current confirm the scalability of the *DC* model in terms of the area dependence of the dark current. The measured responsivity is higher than the expected one from simulations. One explanation found in this work is the influence of fibre position and tilt.

Different measurement setups are used to determine the frequency behaviour of the photodiodes. The input impedance and opto-electrical transfer function that are obtained from measurements with a network analyser are mainly used to evaluate the small signal model. Agreement between simulations and measurements is quite good. In this context, the influence of the contact structure on the frequency behaviour of the photodiodes with small mesa diameter is shown: this dependence can be exploited for resonance rise. The design of the contact structure has to be adapted for this purpose.

The opto-electrical transfer function is also measured with a heterodyne measurement setup. Discrepancy between results gained from the two setups are most probably explained by the calibration routine for the electrical components of the heterodyne measurement setup. Due to changes in the transmission chain, this calibration routine has to be updated.

With a commercial lightwave component analyser, a 3 dB bandwidth of 49 GHz is measured for photodiodes with a diameter of $10\,\mu$m and an intrinsic *Ge* thickness of 330 nm. The bias voltage applied is $-2\,$V. This is the highest bandwidth for vertical *Ge* on *Si pin* photodiodes published so far.

The photodiodes are also characterised in the time domain. A maximum bit rate of 25 Gbit/s is found for the same device as measured with the *LCA*. Based on the 3 dB bandwidth of the devices, higher bit rates are expected if the influence of the frequency dependent elements in the measurement setup, like cables, is reduced.

With the knowledge of the characteristics of the smallest and fastest photodiode, a limiting amplifier in *SiGe* bipolar technology is designed and electrically characterised. According to the measurement results, the limiting amplifier works up to at least 50 Gbit/s, with the available bit rate limited by the measurement setup, and amplifies the input signal by a factor of 300. This is enough to sufficiently increase the electrical output signal of the photodiode.

Based on the theoretical examination of binary grating couplers, a design with different grating periods and duty cycles is realised. A *SOI* based process from *imec* is used for this purpose. Main focus is set on the design considerations for a wavelength around $\lambda_0 = 1310\,\mathrm{nm}$, and couplers at $\lambda_0 = 1550\,\mathrm{nm}$ are examined for comparison.

A measurement setup is installed to evaluate test structures. The difference between simulated and measured coupling efficiency of the grating couplers is explained by fabrication tolerances and measurement conditions. As the fabricated *Si* layer is thicker than its nominal value, the maximum coupling efficiency shifts to longer wavelengths. The lower coupling efficiency of the measured structures is mainly attributed to the fact that no index matching glue has been applied during measurements. Maximum coupling efficiencies that have been measured for $\lambda_0 = 1310\,\mathrm{nm}$ and $\lambda_0 = 1550\,\mathrm{nm}$ are approximately 40% and 37%, respectively.

A Working Principle of Heterodyne Measurement Setup

The photo current, which is detected by the photodiode, is proportional to the optical input power and, therefore, proportional to the square of the electric field of the incident wave. This fact is exploited in the optical heterodyne setup, and the principle of the heterodyne detection is shortly presented here. Two harmonic waves with the same polarisation are considered. Their electric fields are given by:

$$E_1(t) = E_1 \cdot \cos(2\pi f_1 t) \quad \text{and} \quad E_2(t) = E_2 \cdot \cos(2\pi f_2 t)\,, \tag{A.1}$$

where E_1 and E_2 are the field amplitudes and f_1 and f_2 the frequencies of the waves. If both waves are added up and afterwards squared in the detector, one gets:

$$E^2(t) = E_1^2 \cos(2\pi f_1 t) + E_2^2 \cos(2\pi f_2 t) + 2E_1E_2 \cos(2\pi f_1 t)\cos(2\pi f_2 t)\,. \tag{A.2}$$

Applying addition theorems, the following mixing products are created:

$$E^2(t) = E_1^2 \cos(2\pi f_1 t) + E_2^2 \cos(2\pi f_2 t) + E_1E_2 \cos(2\pi (f_1 + f_2)\, t) + E_1E_2 \cos(2\pi (f_1 - f_2)\, t)\,. \tag{A.3}$$

In these considerations the frequences of both waves are about 193 THz, corresponding to $\lambda_0 = 1550\,\text{nm}$. The difference in these frequencies, $\Delta f = f_1 - f_2$, is chosen to lie in the *RF* range. Under these conditions, the first three summands in Eq. A.3 can be neglected, as their frequencies are so high that the according signals cannot be detected properly by the *RF* photodiode. The mean value of these signals is added as noise component. Hence only the fourth summand is of relevance, containing the desired difference in frequencies in the *RF* range.

The two frequencies can be defined by the following relations:

$$f_1 = \frac{c_0}{\lambda_0 + \Delta\lambda_0} \quad \text{and} \quad f_2 = \frac{c_0}{\lambda_0 - \Delta\lambda_0}, \tag{A.4}$$

where $2\Delta\lambda_0$ is the difference in the wavelengths of the two lasers. It is assumed in these considerations that the value for detuning the wavelength λ_0, namely $\Delta\lambda_0$, is the same for both lasers. The difference between the frequencies can thus be written as:

$$\Delta f = f_1 - f_2 = \frac{c_0}{\lambda_0 + \Delta\lambda_0} - \frac{c_0}{\lambda_0 - \Delta\lambda_0} = -c_0 \frac{2\Delta\lambda_0}{\lambda_0^2 - \Delta\lambda_0^2}. \tag{A.5}$$

Under the assumption that

$$\Delta\lambda_0^2 << \lambda_0^2, \tag{A.6}$$

the resulting RF frequency, Δf, and the wavelength detuning value, $\Delta\lambda_0$, become:

$$\Delta f = -c_0 \cdot \frac{2\Delta\lambda_0}{\lambda_0^2}, \quad \Delta\lambda_0 = -\frac{\Delta f}{c_0} \cdot \frac{\lambda_0^2}{2}. \tag{A.7}$$

Thus, the wavelengths that have to be adjusted at the two laser sources to get the desired difference in frequency between the two laser sources are known:

$$\lambda_1 = \lambda_0 - \frac{\Delta f}{c_0} \cdot \frac{\lambda_0^2}{2}, \quad \lambda_2 = \lambda_0 + \frac{\Delta f}{c_0} \cdot \frac{\lambda_0^2}{2}. \tag{A.8}$$

Bibliography

[1] *ITU-T Manual 2009: Optical fibres, cables and systems.*

[2] T. Veigel, M. Grözing, M. Berroth, and F. Buchali, “Design of a Viterbi Equalizer Circuit for Data Rates up to 43 Gb/s,” European Solid-State Circuits Conference (ESSCIRC) Fringe, September 2009.

[3] T. Yin, R. Cohen, M. M. Morse, G. Sarid, Y. Chetrit, D. Rubin, and M. J. Paniccia, “31GHz Ge n-i-p waveguide photodetectors on Silicon-on-Insulator substrate,” *OSA Optics Express*, vol. 15, no. 21, pp. 13965–13971, 2007.

[4] L. Vivien, D. Marris-Morini, J. Mangeney, P. Crozat, E. Cassan, S. Laval, J.-M. Fédéli, J. Damlencourt, and Y. Lecunff, “42 GHz waveguide Germanium-on-silicon vertical PIN photodetector,” pp. 185–187, 5th IEEE International Conference on Group IV Photonics (GFP), September 2008.

[5] G. Dehlinger, S. J. Koester, J. D. Schaub, J. O. Chu, Q. C. Ouyang, and A. Grill, “High-Speed Germanium-on-SOI Lateral PIN Photodiodes,” *IEEE Photonics Technology Letters*, vol. 16, no. 11, pp. 2547–2549, 2004.

[6] O. I. Dosunmu, D. D. Cannon, M. K. Emsley, L. C. Kimerling, and M. S. Ünlü, “High-Speed Resonant Cavity Enhance Ge Photodetectors on Reflection Si Substrates for 1550-nm Operation,” *IEEE Photonics Technology Letters*, vol. 17, no. 1, pp. 175–177, 2005.

[7] M. Rouvière, L. Vivien, X. Le Roux, J. Mangeney, P. Crozat, C. Hoarau, E. Cassan, D. Pascal, S. Laval, J.-M. Fédéli, J.-F. Damlencourt, J. M. Hartmann, and S. Kolev, “Ultrahigh speed germanium-on-silicon-on-insulator photodetectors for 1.31 and 1.55 μm operation,” *Applied Physics Letters*, vol. 87, no. 231109, pp. 231109–1 – 231109–3, 2005.

[8] D. Suh, S. Kim, J. Joo, G. Kim, and I. G. Kim, “35 GHz Ge p-i-n Photodetectors Implemented Using RPCVD,” 5th IEEE International Conference on Group IV Photonics (GFP), 2008.

[9] S. Klinger, M. Berroth, M. Kaschel, M. Oehme, and E. Kasper, “Ge-on-Si p-i-n Photodiodes With a 3-dB Bandwidth of 49 GHz,” *IEEE Photonics Technology Letters*, vol. 21, pp. 920–922, July 2009.

[10] M. Jutzi, M. Berroth, G. Wöhl, M. Oehme, and E. Kasper, “Ge-on-Si Vertical Incidence Photodiodes With 39-GHz Bandwidth,” *IEEE Photonics Technology Letters*, vol. 17, no. 7, pp. 1510–1512, 2005.

[11] G. Masini, G. Capellini, J. Witzens, and C. Gunn, "A 1550nm, 10Gbps monolithic optical receiver in 130nm CMOS with integrated Ge waveguide photodetector," pp. 28–30, 5th IEEE International Conference on Group IV Photonics (GFP), 2008.

[12] K. Kao and G. Hockham, "Dielectric-fibre surface waveguides for optical frequencies," in *Proceedings of the Institution of Electrical Engineers*, vol. 113, pp. 1151 –1158, 1966.

[13] M. Jetter, R. Roßbach, and P. Michler, "Red VCSELs for high-speed data communication via POF," *Photonik International*, vol. 1, pp. 33–35, 2009.

[14] *http://www.fiberoptics4sale.com/wordpress/optical-fiber-attenuation/.*

[15] *JDSU: Reference Guide to Fiber Optic Testing - Volume 1, 2007.*

[16] "Cisco White Paper: Fiber Types in Gigabit Optical Communications." 2008.

[17] P. Westbergh, J. Gustavsson, A. Haglund, A. Larsson, F. Hopfer, G. Fiol, D. Bimberg, and A. Joel, "32 Gbit/s multimode fibre transmission using high-speed, low current density 850 nm VCSEL," *Electronics Lettersj*, vol. 45, pp. 366 –368, march 2009.

[18] W. Hofmann, M. Müller, A. Nadtochiy, A. Meltzer, C.and Mutig, G. Böhm, J. Rosskopf, D. Bimberg, M.-C. Amann, and C. Chang-Hasnain, "22-Gb/s Long Wavelength VCSELs," *OSA - Optics Express*, vol. 17, no. 20, pp. 17547–54, 2009.

[19] P. J. Winzer, "Modulation and multiplexing in optical communication systems," *IEEE LEOS Newsletter*, vol. 23, no. 1, pp. 4–10, 2009.

[20] M. Seimetz, "Höherwertige Modulationsverfahren für die Glasfaserübertragung - Systemkonfigurationen und Performance-Trends," ITG-Fachbericht 214 - Photonische Netze, May 04-05 2009. ISBN 978-3-8007-3161-9.

[21] M. Seimetz, *High-Order Modulation for Optical Fiber Transmission.* Springer-Verlag Berlin Heidelberg, 2009.

[22] D. M. Pozar, *Microwave Engineering.* New York: Wiley, 3rd ed., 2005.

[23] G. Merziger and T. Wirth, *Repetitorium der höheren Mathematik.* Binomi Verlag, 1999.

[24] E. Hecht, *Optik.* Oldenbourg Verlag München Wien, 2005.

[25] E. Wolf, *Introduction to the Theory of Coherence and Polarization of Light.* Cambridge University Press, 2007.

[26] *Agilent: Basics of Measuring the Dielectric Properties of Materials - Application Note.*

[27] R. Feynman, *QED - Die seltsame Theorie des Lichts und der Materie.* Piper München Zürich, 2006.

[28] R. F. Potter, *Handbook of Optical Constants of Solids, Vol. I . Germanium (Ge).* Elsevier Science, USA, 1998.

[29] Optical Society of America, *Handbook of Optics, Vol. II . Devices, Measurements, and Properties, Second Edition.* McGraw-Hill, 2nd ed., 1995.

[30] S. Dimitrijev, *Understanding Semiconductor Devices.* Oxford University Press, 2000.

[31] H. Föll, “Online Script: Einführung in die Materialwissenschaft II,” 2010.

[32] E. Kasper, “Scriptum Bauelemente der Mikroelektronik,” 2001.

[33] S. M. Sze, *Physics of Semiconductor Devices.* John Wiley & Sons, Inc., 1969.

[34] M. Morse, “Germanium on silicon approaches III-V semiconductors in performance,” *Laser Focus World*, vol. 43, no. 5, pp. 111–113, 2007.

[35] D. F. Edwards, *Handbook of Optical Constants of Solids, Vol. I . Silicon (Si).* Elsevier Science, USA, 1998.

[36] E. D. Palik, *Handbook of Optical Constants of Solids, Vol. I . Gallium Arsenide (GaAs).* Elsevier Science, USA, 1998.

[37] L. A. Coldren and S. W. Corzine, *Diode Lasers and Photonic Integrated Circuits.* John Wiley & Sons, Inc., 1995.

[38] M. Alles, *Entwicklung und Realisierung von Wanderwellen-Photodetektoren für Hochfrequenz-Übertragungssysteme.* PhD thesis, Gerhard-Mercator-Universität - Gesamthochschule Duisburg, 2000.

[39] O. J. Glembocki and H. Piller, *Handbook of Optical Constants of Solids, Vol. I . Indium Phosphide (InP).* Elsevier Science, USA, 1998.

[40] J. Werner, M. Oehme, M. Schmid, M. Kaschel, A. Schirmer, E. Kasper, and J. Schulze, “Germanium-tin p-i-n photodetectors integrated on silicon grown by molecular beam epitaxy,” *Applied Physics Letters*, vol. 98, pp. 061108–1 – 061108–3, 2011.

[41] K. Lyutovich and E. Kasper, “Strain adjustment with thin virtual substrates,” *Solid-State Electronics*, vol. 48, pp. 1257–1263, 2004.

[42] M. Oehme, J. Werner, M. Jutzi, G. Wöhl, E. Kasper, and M. Berroth, “High-speed germanium photodiodes monolithically integrated on silicon with MBE,” *Thin Solid Films*, vol. 508, pp. 393–395, 2006.

[43] A. Matiss, R. Ludwig, J.-K. Fischer, L. Molle, C. Schubert, C. C. Leonhardt, H.-G. Bach, R. Kunkel, and A. Umbach, “Novel Integrated Receiver Module for 100 G Serial Transmission,” in *Conference on Optical Fiber Communication / collocated National Fiber Optic Engineers Conference (OFC / NFOEC)*, 2010.

[44] M. Kaschel, M. Oehme, O. Kirfel, and E. Kasper, “Spectral responsivity of fast Ge photodetectors on SOI,” *Solid-State Electronics*, vol. 53, pp. 909–911, 2009.

[45] C. R. Doerr, P. J. Winzer, Y.-K. Chen, S. Chandrasekhar, M. S. Rasras, L. Chen, T.-Y. Liow, K.-W. Ang, and G.-Q. Lo, “Monolithic Polarization and Phase Diversity Coherent Receiver in Silicon,” *IEEE Journal of Lightwave Technology*, vol. 28, no. 4, pp. 520–525, 2010.

[46] G. Roelkens, J. Brouckaert, D. Taillaert, P. Dumon, W. Bogaerts, D. Van Thourhout, and R. Baets, “Integration of InP/InGaAsP photodetectors onto silicon-on-insulator waveguide circuits,” *OSA Optics Express*, vol. 13, no. 25, pp. 10102–10108, 2005.

[47] W. Bogaerts, S. K. Selvaraja, P. Dumon, J. Brouckaert, K. De Vos, D. Van Thourhout, and R. Baets, "Silicon-on-Insulator Spectral Filters Fabricated With CMOS Technology," *IEEE Journal of Selected Topics in Quantum Electronics*, vol. 16, no. 1, pp. 33–44, 2010.

[48] K. J. Ebeling, "Bauelemente der Optoelektronik - Wellenoptik, optische Wellenleiter und -elemente, Modulatoren, Koppler," 2008.

[49] P. Bienstman, *CAMFR manual*, version 1.3 ed., September 2007.

[50] F. Landstorfer, "Scriptum Hochfrequenztechnik 1," 2001.

[51] M. Jutzi, *Photodetektoren auf Silizium-Substraten für integrierte, optische Empfänger*. PhD thesis, Universität Stuttgart, 2005.

[52] M. Berroth, "Scriptum Optoelectronic Devices and Circuits II," 2010.

[53] S. Klinger, W. Vogel, M. Berroth, M. Kaschel, M. Oehme, and E. Kasper, "Ge on Si p-i-n Photodetectors with 40 GHz bandwidth," 5th IEEE International Conference on Group IV Photonics (GFP), 2008.

[54] J. Bowers, D. Dai, W. Zaoui, Y. Kang, and M. Morse, "Resonant Si/Ge avalanche photodiode with an ultrahigh gain bandwidth product," in *The IEEE Photonics Society Winter Topicals Meeting Series, Majorca, Spain*, pp. 111 –112, 2010.

[55] D. Marcuse, *Quantum Electronics - Principles and Applications: Theory of Dielectric Optical Waveguides*. Academic Press, Inc., New York and London, 1974.

[56] K. J. Ebeling, *Integrierte Optoelektronik*. Springer-Verlag Berlin Heidelberg New York, 1989.

[57] C. Gulde, "Simulation von Wellenleiterstrukturen zum Aufbau eines Phasendetektors," study project's report, INT, Universität Stuttgart, 2008.

[58] G. Mashanovich, G. Reed, B. Timotijevic, and S. Chan, *Silicon Photonics, Chapter 2: Silicon Photonic Waveguides*. John Wiley & Sons, Ltd, 2008.

[59] T. Aalto, M. Harjanne, M. Kapulainen, P. Heimala, and M. Leppihalme, "Development of silicon-on-insulator waveguide technology," in *Proceedings of SPIE, Integrated Optics: Devices, Materials, and Technologies VIII*, vol. 5355, pp. 81–95, 2004.

[60] T. Aalto, *Microphotonic Silicon Waveguide Components*. PhD thesis, Technical Research Centre of Finland, VTT, 2004.

[61] R. A. Soref, J. Schmidtchen, and K. Petermann, "Large Single-Mode Rib Waveguides in GeSi-Si and Si-on-SiO2," *IEEE Journal of Quantum Electronics*, vol. 27, no. 8, pp. 1971–1974, 1991.

[62] S. Pogossian, L. Vescan, and A. Vonsovici, "The single-mode condition for semiconductor rib waveguides with large cross section," *IEEE Journal of Lightwave Technology*, vol. 16, no. 10, pp. 1851 –1853, 1998.

[63] P. Muellner and R. Hainberger, "Single-mode criterion for rib waveguides with small cross sections," in *Proceedings of SPIE, Physics and Simulation of Optoelectronic Devices XIV* (M. Osinski, F. Henneberger, and Y. Arakawa, eds.), vol. 6115, pp. 61152E1–8, 2006.

[64] J. Lousteau, D. Furniss, A. B. Seddon, T. M. Benson, A. Vukovic, and P. Sewel, "The Single-Mode Condition for Silicon-On-Insulator Optical Rib Waveguides With Large Cross Section," *IEEE Journal of Lightwave Technology*, vol. 22, no. 8, pp. 1923–1929, 2004.

[65] A. Yariv, "Coupled-Mode Theory for Guided-Wave Optics," *IEEE Journal of Quantum Electronics*, vol. 9, pp. 919–933, September 1973.

[66] D. Kip, "Scriptum Integrierte Optik," 2006.

[67] C. Poulton, C. Koos, M. Fujii, A. Pfrang, T. Schimmel, J. Leuthold, and W. Freude, "Radiation Modes and Roughness Loss in High Index-Contrast Waveguides," *IEEE Journal of Selected Topics in Quantum Electronics*, vol. 12, no. 6, pp. 1306–1321, 2006.

[68] D. Taillaert, *Roosterkoppelaars voor Koppeling tussen Optische Vezels en Nanofotonische Golfgeleiders - Grating couplers as Interface between Optical Fibres and Nanophotonic Waveguides*. PhD thesis, Universiteit Gent, Fakulteit Toegepaste Wetenschappen, Vakgroep Informatietechnologie, 2004-2005.

[69] T. Clausnitzer, T. Kämpfe, E.-B. Kley, A. Tünnermann, A. V. Tishchenko, and O. Parriaux, "Hocheffiziente dielektrische Transmissionsgitter - eine anschauliche Untersuchung des Beugungsverhaltens," *Photonik*, vol. 1, pp. 48–51, 2007.

[70] T. Clausnitzer, *Kontrolle der Beugungseffizienzen dielektrischer Gitter*. PhD thesis, Friedrich-Schiller-Universität Jena, 2007.

[71] P. Sheng, R. S. Stepleman, and P. N. Sanda, "Exact eigenfunction for square-wave gratings: Application to diffraction and surface-plasmon calculations," *Physical Review B*, vol. 26, p. 6, 1982.

[72] T. Clausnitzer, T. Kämpfe, E.-B. Kley, T. Tünnermann, U. Peschel, A. V. Tishchenko, and O. Parriaux, "An intelligible explanation of highly-efficient diffraction in deep dielectric rectangular transmission gratings," *OSA Optics Express*, vol. 13, no. 16, pp. 10448–10456, 2005.

[73] A. Taflove, *Computational Electrodynamics: The Finite-Difference Time-Domain Method*. Norwood, MA: Artech House, 1995.

[74] M. Moharam, E. Grann, D. Pommet, and T. Gaylord, "Formulation for stable and efficient implementation of the rigorous coupled-wave analysis of binary gratings," *OSA Journal of the Optical Society of America A (JOSA A)*, vol. 12, no. 5, pp. 1068–1076, 1995.

[75] *Manual included in RSoft Software DiffractMOD*.

[76] P. Bienstman, *Rigorous and efficient modelling of wavelength scale photonic components*. PhD thesis, Universiteit Gent, 2001.

[77] D. Taillaert, W. Bogaerts, P. Bienstman, T. Krauss, P. Van Daele, I. Moerman, S. Verstuyft, K. De Mesel, and R. Baets, "An Out-of-Plane Grating Coupler for Efficient Butt-Coupling between Compact Planar Waveguides and Single-Mode Fibers," *IEEE Journal of Quantum Electronics*, vol. 38, no. 7, pp. 949–955, 2002.

[78] M. Jutzi, M. Berroth, G. Wöhl, M. Oehme, V. Stefani, and E. Kasper, "Ge-on-Si Pin-Photodiodes for Vertical and In-Plane Detection of 1300 to 1580 nm Light," in *Proceedings of the 34th European Solid-State Device Research conference (ESSDERC), Leuven, Belgium*, pp. 345–348, September 2004.

[79] M. Oehme, J. Werner, E. Kasper, S. Klinger, and M. Berroth, "Photocurrent analysis of a fast Ge p-i-n detector on Si," *Applied Physics Letters*, vol. 91, pp. 051108–1 – 051108–3, 2007.

[80] M. Oehme, J. Werner, M. Kaschel, O. Kirfel, and E. Kasper, "Germanium waveguide photodetectors integrated on silicon with MBE," *Thin Solid Films*, vol. 517, no. 1, pp. 137–139, 2008.

[81] *Personal information from M. Kaschel and M. Oehme.*

[82] V. L. Rideout, "A Review of the Theory and Technology for Ohmic Contacts to Group III-V Compound Semiconductors," *IEEE Solid-State Electronics*, vol. 18, pp. 541–550, 1975.

[83] *Personal information from W. Sfar Zaoui and discussion with Prof. E. Kasper.*

[84] A. H. Steinbach, I. Penn, N. Chokshi, D. Martin, K. Slomkowski, W. Braun, N. Agrawal, R. Ben-Michael, and M. A. Itzler, "Equivalent Circuit Modelling of p-i-n Photodiodes for 40 Gb/s Receivers," pp. 486 – 487, The 15th Annual Meeting of the IEEE Lasers and Electro-Optics Society (IEEE/LEOS), 2002.

[85] G. Wang, "Analysis of High Speed P-I-N Photodiodes S-Parameters by a Novel Small-Signal Equivalent Circuit Model," *IEEE Microwave and Wireless Components Letters (MWCL)*, vol. 12, no. 10, pp. 378–380, 2002.

[86] K. Kato, "Ultrawide-Band/High-Frequency Photodetectors," *IEEE Microwave Theory and Techniques*, vol. 47, no. 7, pp. 1265–81, 1999.

[87] M. Jutzi, M. Berroth, G. Wöhl, M. Oehme, and E. Kasper, "40-Gbit/s Ge-Si Photodiodes," IEEE Topical Meeting on Silicon Monolithic Integrated Circuits in RF Systems, 2006.

[88] M. Oehme, J. Werner, E. Kasper, M. Jutzi, and M. Berroth, "High bandwidth Ge p-i-n photodetector integrated on Si," *Applied Physics Letters*, vol. 89, no. 7, pp. 071117–1 – 071117–3, 2006.

[89] D. Schroder, *Semiconductor Material and Device Characterization 1990.* John Wiley and Sons, Inc., 1. Auflage,, 1990.

[90] J. S. Escher, "Junction-Current-Confinement Planar Light-Emitting Diodes and Optical Coupling into Large-Core Diameter Fibers Using Lenses," *IEEE Transaction on Electron Devices*, vol. ED19, pp. 1463–1469, September 1982.

[91] S. Klinger, M. Grözing, W. Sfar Zaoui, M. Berroth, M. Kaschel, M. Oehme, E. Kasper, and J. Schulze, "Ge on Si p-i-n Photodiodes for a Bit Rate of up to 25 Gbit/s," 35th European Conference on Optical Communication (ECOC), September 20-24 2009. Paper 9.2.3.

[92] M. Grözing, M. Berroth, E. Gerhardt, B. Franz, and W. Templ, "High-Speed ADC Building Blocks in 90 nm CMOS," pp. 99–103, 4th Joint Symposium on Opto- and Microelectronic Devices and Circuits (SODC), September 2006.

[93] S. Klinger, M. Schmidt, M. Grözing, and M. Berroth, "SiGe Bipolar Limiting Amplifier with a Bit Rate of 50 Gbit/s for Optoelectronic Receivers," p. 18, GHz Symposium 2010, 2010.

[94] S. J. Koester, C. L. Schow, L. Schares, G. Dehlinger, J. D. Schaub, F. E. Doany, and R. A. John, "Ge-on-SOI-Detector/Si-CMOS-Amplifier Receivers for High-Performance Optical-Communication Applications," *IEEE - Journal of Lightwave Technology*, vol. 25, no. 1, pp. 46–57, 2007.

[95] W. Bogaerts, S. K. Selvaraja, and P. Dumon, *Technology Paper IMEC 193 01, September 2008.* ePIXfab - the silicon platform.

[96] I. E. Hosni, "2-D Design of out of plane Grating Couplers using Silicon-on-Insulator," bachelor's thesis, INT, Universität Stuttgart, 2009.

[97] F. Van Laere, G. Roelkens, M. Ayre, J. Schrauwen, D. Taillaert, D. Van Thourhout, T. F. Krauss, and R. Baets, "Compact and Highly Efficient Grating Couplers Between Optical Fiber and Nanophotonic Waveguides," *IEEE - Journal of Lightwave Technology*, vol. 25, no. 1, pp. 151–156, 2007.

[98] *Personal information from W. Sfar Zaoui.*

Curriculum Vitae

Name:	Sandra Klinger
Born:	3_{rd} June 1979 in Stuttgart Bad Cannstatt, Germany
Nationality:	German

Education:

01/2005 - now	Scientific staff at the Institute of Electrical and Optical Communications Engineering at the University of Stuttgart
09/2009 - 10/2009	Project work at Chalmers, Göteborg, Sweden, under Prof. Larsson
05/2004 - 11/2004	Diploma thesis ”Parallel Plate Patch Antenna with Horizontal Feeding Lines for DBS System” (University of Stuttgart / UPM, Madrid, Spain)
10/1999 - 11/2004	Academic studies of Electrical Engineering and Information Technology with diploma, University of Stuttgart
1990 - 1999	Christoph-Schrempf-Gymnasium, abitur
1986 - 1990	Primary school, Walheim

Acknowledgment

This thesis was carried out during my work as scientific staff at the Institute of Electrical and Optical Communications Engineering (*INT*) at the University of Stuttgart.

First of all, I owe my thanks to Prof. Berroth for the opportunity to work in his institute, for the scientific supervision of my work and the confidence that he has shown me.

Thank you to Prof. Burghartz for being the co-examiner.

Best thanks to Michael Jutzi, who introduced me into the world of integrated photodiodes and who explained to me all the measurement setups related to the device characterisation.

I want to thank the *IHT*, especially Prof. Kasper, for the cooperation in our common *DFG* project, and for providing the photodiode samples. Thank you to Prof. Schulze for valuable hints considering this thesis.

Furthermore, I express my gratitude to Dr. Hurm from the *IAF* who helped me to install the heterodyne measurement setup at the *INT*, and Dr. Haisch from Agilent Technologies with whom I carried out the *LCA* measurements of the opto-electrical transfer function of the photodiodes.

Special thanks to all the students whom I supervised and who did their part to promote my work.

Thank you to all the colleagues of the *INT* for their kind help and comradeship throughout my time at the institute.

Tom, thank you for prove reading and any other kind of support.